12-14-2015

# Bio-Inspired Design of Mechanical Band Pass Sensor with the Ability to Scavenge Energy

Md Riaz Uddin Ahmed
*University of South Carolina - Columbia*

# BIO-INSPIRED DESIGN OF MECHANICAL BAND PASS SENSOR WITH THE ABILITY TO SCAVENGE ENERGY

by

Md Riaz Uddin Ahmed

Bachelor of Science
Khulna University of Engineering and Technology, 2004

Master of Science
University of South Carolina, 2010

---

Submitted in Partial Fulfillment of the Requirements

For the Degree of Doctor of Philosophy in

Mechanical Engineering

College of Engineering & Computing

University of South Carolina

2015

Accepted by

Sourav Banerjee, Major Professor

Victor Giurgiutiu, Committee Member

Tony Reynolds, Committee Member

Lingyu Yu, Committee Member

Juan Caicedo, Committee Member

Lacy Ford, Senior Vice Provost and Dean of Graduate Studies

# DEDICATION

This dissertation is dedicated to my parents Mr. Nur Ahmed and Mrs. Jahanara Begum. I would also like to dedicate this work to my lovely wife Nabila Mahjabeen and my little angle Rahma Nawar Ahmed.

# ACKNOWLEDGEMENTS

I would like to thank my honorable advisor Dr. Sourav Banerjee for his cordial support and valuable advice in my PhD studies. I also would like to thank all iMAPS members for their continuous help. I want to express my gratitude to Dr. Tony Reynolds and Dr. Juan Caicedo for their support in my experimental studies. Finally I am grateful to my wife, Nabila Mahjabeen for her selfless support throughout her existence in my life.

# ABSTRACT

Primary objective of this work is to introduce the multi-scale computational model for the bio-inspired acousto-ultrasonic band pass sensor that are capable of mechanically sense and/or filter wide range user defined frequencies. Selecting a particular and/or a distinct band of frequencies is essential for many applications in science engineering and technologies. For example design of sensors in chemical, biomedical and biological applications; device application for acoustic modulation by breaking the acoustic reciprocity and the sensors used in precision manufacturing applications requires sensing and/or filtering of wide range of acousto-ultrasonic frequencies. Presently, electronic devices are widely employed in commercial applications for selecting the target frequencies. Concurrent to the electronics sensors mechanical sensors with smart materials are significantly contributing to the sensing technologies, especially where electronic sensors are not compatible. Mechanical sensors are traditionally made of cantilever beams and use the resonance phenomenon to select the target frequencies. Considering the required size of the sensors, the above physics limits the design of these sensors for only the high frequency (> ~3 KHz) applications. Hence, to employ such sensors, it is apparent that for the low (sonic) frequency operations humungous geometrical size will be required. Thus, in order to sublime the wide applicability of the mechanical sensors, in this work, a physics bases mechanical band pass frequency selection mechanism is proposed that is

universal can be adopted for selecting extremely wide range of frequencies with controlled geometric configurations.

To model the envisioned band pass frequency sensors, in this work, principles and the mechanics of the human cochlea are studied. Human cochlea is the most advanced and sophisticated band pass frequency sensor in nature, where it selects the sonic frequency band (20 Hz – 20 KHz) and filters all the infrasonic and ultrasonic frequencies using a device length of only ~ 35 mm (sub-wave length scale device). Inside the cochlea, the Basilar Membrane (BM) is naturally designed based on the variable stiffness model, starting from the base to the apex of the cochlea. During selecting and filtering the desired frequencies, the BM performs four major operations; (a) it create local resonances; (b) it captures only the chosen frequencies and remain unresponsive to the other frequencies; (c) it senses the input frequencies with a sensory medium (called hair cells); and in turn (d) it spatially selects the frequencies. Inspired by the cochlear mechanics, mimicking the functionalities of the basilar membrane, in this PhD dissertation, a mechanical frequency selection mechanism is proposed exploring two diverse innovative designs (1) Acousto-Elastic MetaMaterial (AEMM) model and the (2) Basilar Membrane (BM) model.

Two approaches are adopted in designing the AEMM based mechanical sensor; (a) stop band technique, (SBT) and the (b) band pass technique, (BPT). The proposed AEMM consists of a heavy core mass encapsulated in a matrix inside a stiff frame. AEMM's are recently proposed for stopping the acoustic frequencies and create the acoustic band gaps. Using SBT method, several AEMM models are studied to create very large stop band, such that, all unwanted frequencies in the environment can be filtered and user defined

frequencies can be passed through the device, automatically. However, it was found to be challenging. After several unsuccessful attempts using SBT, the new BPT method is adopted where local resonance is the key in selecting a specific frequency. Using BPT, by filtering the other possible frequencies, automatically, it is intended to develop a model which is only able to select the target frequency. Using BPT, it has been found that the proposed AEMM structure is able to mimic the functionalities of the basilar membrane and a distinct frequency can be selected by efficiently placing a smart material capable of electromechanical transduction (e.g. piezoelectric material) inside a unit cell AEMM. It has also been reported that a broadband frequency is possible to be sensed using a multi-cell structure with a systematic selection of model parameters. Comprehensive studies with analytical, numerical and experimental approaches are performed to establish the hypothesis.

AEMM model uses geometric configuration and the physics of local resonance by mimicking the functionalities of the basilar membrane. However, the mechanical frequency sensor based on exact BM model is not available. Hence, in this dissertation a real geometric configuration of the basilar membrane is adopted to serve the central objective. Using BM model, two designs are proposed; the plate model and the beam model. The plate model is preferred over the beam model, where a continuous frequency band is necessary to select without losing the intermediate frequencies. Alternatively, beam model is preferable for the precise selection of the discrete frequencies within a target frequency band. In the plate model, a trapezoidal membrane is designed, whereas, in the beam model, a series of beams supported at the ends with linearly varying lengths are proposed to fit the trapezoidal basilar geometry.

In recent years, notable attempts were made to fabricate the broadband frequency sensors. Although, few experimental studies have been reported to fabricate band pass sensors mimicking the mechanics of the basilar membrane, a true predictive model to design these sensors is missing. An ultra-fast and versatile model is necessary such that it could be used for the optimization of the model parameters. Non availability of such predictive model hinders the optimized design of the cochlea type sensors tailored to specific applications. Hence, in this research, two novel predictive models (plate type, beam type) for the band pass frequency sensors are proposed, mimicking the tapered geometry of the basilar membrane. It is aimed in this dissertation to develop the most flexible/versatile predictive models with all possible variable parameters that contribute to the frequency selection process. The models are developed in such a way that they can be employed for the optimized design of the sensors for wide varieties of scientific applications, respectively. Hence, the predictive models developed herein not only capable of handling the homogeneous model parameters but also capable of managing the functionally graded model parameters. This study reports that using the proposed predictive models, it is also possible to manipulate the attributes of the target frequency band using the functionally graded model parameters. The model flexibility based on the functionally graded parameters will allow the used to alter the geometric configuration of the envisioned sensor for a selected specific designed frequency band. Studies, using the finite element method (FEM) confirm the outcome of the proposed predictive models and prove that the innovative proposed model presented in this dissertation is even couple of orders (~ at least 3 times in a conventional personal computer) faster than its counter FEM model.

In addition to the introduction of bio-inspired mechanical band pass sensor, in this research, few novel applications of the proposed sensors are identified and envisioned, discussed herein. Two major applications in Mechanical and Biomedical engineering are identified, respectively. Mechanical application is in the realm of energy harvesting using the AEMM model and the biomedical application using the BM model is identified in the realm of pathogen identification where it is possible to sense and detect the presence of mycotoxins, a carcinogenic metabolite excreted by the fungal pathogens. . In this work, very promising power densities were recorded using the AEMM energy scavengers. This motivates the harvesters to be employed for powering the low power electronic gadgets. On the other hand the characterization and the genus identification of the fungal pathogens can be achieved by classifying their secondary metabolites called mycotoxins. A BM based cantilever beam design is proposed to detect the presence of the type of the mycotoxins in the environment.

# TABLE OF CONTENTS

# LIST OF TABLES

# LIST OF FIGURES

# CHAPTER 1: INTRODUCTION

## 1.1 Problem Statement

In recent years the band pass sensors and the single frequency sensors are increasingly used in various applications of science engineering and technology. For example such sensors are used in the micro mechanical devices, manufacturing instrumentation, 3D printing, micro-electronics devices, photonics and phononic devices and overall in many chemical and biological applications. Frequency sensors are highly demanded in the above mentioned applications with the rapid advancement of the technologies that leads to the complex measurements / operations with the high level of accuracy. Our consumer driven market demands these sophisticated devices with the highest standards of quality but with uncompromised reliability.

The in-process sensors plays significant role in assisting the industrial systems producing the near accurate outputs. In-process sensors are used to generate control signals to improve both the control and the productivity of the engineering systems. For example, acoustic emission (AE) sensors are used in many precision metal cutting processes to monitor the degree of tool wear, chip formation, surface features, etc., and in precision grinding,

acoustic emission sensors are used to detect both the near approach of the grinding wheel to the work surface, and the initial wheel contact with the work [1]. In particular, in-process sensors are needed in engineering systems, because human oversight of the industrial process is inadequate to achieve the necessary level of performance.

Traditionally, electronic and mechanical sensors are widely employed in industrial applications. Mechanical sensor covers a large area of the sensor technology due to its wide compatibility in many engineering domains. However, mechanical sensors are typically limited for high frequency applications due to its design constraints. Resonance phenomenon is the key in mechanical sensors to select a specific frequency. Because of its operating principle, large geometry is essential to employ the traditional mechanical sensors for low frequency applications. Hence, a novel but universal frequency selection process is necessary which can be adopted for sensing almost any wide range of frequencies with controlled geometric configurations.

## 1.2 Background

Frequency sensors can be classified into two categories; 1) Distinct single frequency sensor, where a unique frequency is the frequency of interest and the sensors are devised to sense only one peak of a frequency; 2) Band frequency sensor (also termed as Band Pass sensor), where a band of frequencies are sensed when the rest of the frequencies are filtered. Creating an ability of the band frequency sensing, using multiple distinct frequency sensors is a common practice. Cantilever beam (CB) model is the most popular approach in designing such sensors. Exploring the resonance frequencies, it is possible to select a unique frequency from a specific beam. These types of sensors monitor and detect

the resonance frequency shift in order to facilitate the analysis of the target parameters [2-8].

Battiston et al. [9, 10] presented a chemical sensor based on an array of eight silicon cantilever beams. All cantilevers are glazed on one side with a sensor coat that displays a distinct response to the target analyte molecules. Because of the change in surface stress or the beam mass the cantilevers mechanically respond to the bending of the beams, when the sensor layer is exposed to the analyte. Similar class of bio-chemical sensors are also presented by Moulin et al. [7] that can absorb bio-chemical species on the functionalized surface of a microfabricated cantilever and cause surface stress. Biosensors have attracted substantial attention in the last few years since the monitoring of a specific matter/molecules are crucial aspect in many applications ranging from the clinical analysis to the environmental control and to the monitoring of numerous industrial processes [6, 11-13]. Zhu et al. [14] proposed a piezoelectric microcantilever sensor for detection of humidity through resonance frequency shift due to the change in the young's modulus of the cantilever beams. Hodnett et al. [15] describes a broadband acoustic sensor to evaluate the acoustic emissions from the cavitation produced by a typical commercial 20 kHz sonochemical horn processor.

### 1.3 Objectives

Cantilever beam based frequency sensors use the resonance phenomenon to select a target frequency. Operating principle of cantilever beam limits these sensors to only high frequency applications due to their humungous size to achieve the resonance behavior at the lower frequencies. Hence a universal approach is essential to select the low frequencies,

mechanically. In this work, we intend to introduce an innovative frequency selection mechanism that can be employed at the both low and high frequency applications. After rigorous study, it has been found that, in nature, the human cochlea performs similar operation where it senses only a specific range of frequency (20 Hz to 20 KHz) and filters all the other frequencies, mechanically. Basilar membrane is the key component in the cochlea in selecting and filtering acoustic frequencies using the varying stiffness of the membrane from base to apex end [16]. The basilar membrane is stiff and narrow (about 100 μm) near the base, and flexible and wide (about 500 μm) near the apex, with a smooth logarithmic transition along its length. During operation as a broadband / band pass sensor, human cochlea performs four major operations (a) it create local resonances; (b) it captures only the chosen frequencies and remain unresponsive to the other frequencies; (c) it senses the input frequencies with a sensory medium (called hair cells); and in turn (d) it spatially selects the frequencies. Note that, human cochlea uses the local resonance phenomenon, which allows the ~35 mm long cochlea to select very low frequencies (< ~3 KHz) which is impossible using the cantilever beam design. *In this research, we aimed to propose a universal bio-inspired mechanical band pass sensing technique, mimicking the functionalities of the human cochlea that can be employed for selecting both the low and the high frequencies.*

### 1.4 Approaches

In this dissertation, based on their respective capabilities to introduce local resonance in the structure, two innovative models are proposed, a) Acousto-Elastic MetaMaterial (AEMM) model and b) Basilar Membrane (BM) model. AEMM's are

typically composed of multiple constituent with different material properties and are traditionally used for filtering acoustic waves by creating frequency band gaps. Considering the wave filtration capabilities of the acoustic metamaterial, several AEMM models are studied to create very large stop bands such that the remaining possible frequencies can be filtered other than the targeted frequency band.. This process is named 'stop band technique (SBT)', where the targeted frequency band can be passed automatically and sensed with a sensory medium. Upon successful attempts using SBT, an alternate process, named 'pass band technique (PBT)' is adopted. In PBT, it is aimed to sense only the targeted frequencies, so that the remaining frequencies can be filtered automatically. Local resonance phenomenon is the key in PBT to select a specific frequency from a unit cell AEMM. At local resonance frequency wave energy is trapped inside the soft constituent of the AEMM as an oscillatory motion. It is hypothesized that using a smart material capable of electromechanical transduction, it could be possible to recover the trapped energy and select a specific frequency from the unit cell AEMM. Hence, a multi-cell AEMM with systematic selection of model parameters is expected to result selection of the band of frequencies.

In BM approach, it is intended to mimic the geometric configuration of the basilar membrane to replicate its operating principals. In recent years, several studies are performed to develop the broadband mechanical frequency sensors mimicking the mechanics of basilar membrane. Although few experimental studies have been reported to design the band pass sensors, a universal predictive model to predictively design the sensors is missing. Although few attempts were made in the past to analytically model the cochlea [17-23], those studies are not easily transferable to fabricate artificial cochlea due

to their simplified assumptions. Hence, in this work, a comprehensive predictive model for the BM based mechanical sensor is proposed. Using the proposed BM model any frequency bands can be selected as the target parameter and the respective design parameters can be obtained, predictively for fabrication. It is intended to develop the most flexible predictive model that not only capable of handling the homogeneous model parameters but also capable of managing the functionally graded model parameters.. Two design methods for the BM sensors are proposed i) the plate model and ii) the beam model. The plate model is necessary if a continuous frequency band is required to be sensed without losing any intermediate frequencies, while the beam model can be useful where precise selection of some distinct frequencies are essential. Finite different (central) scheme is implemented to develop the proposed predictive models.

## 1.5 Inspiration

Nature is the best source of ultimate scientific references. Hence, to advance the existing state-of-the-art knowledge, scientists are not only digging hard in their associated areas, but also taking inspiration from the natural systems. In science and engineering these unique natural behaviors are possible to be considered or mimicked by the researchers with different backgrounds to achieve the desired design objectives. Hence in this study we adopted a unique bio-inspired behavior to introduce a novel mechanical band pass frequency sensing mechanism. It is known that the nature is the most important source of inspiration for engineering materials, processes, methods, structures, tools, devices, mechanisms, and systems to foster engineering creativity and innovations to its zenith. Structural and operational perfections of the biological systems are achieved through

evolution and since the primitive age of the mankind all the discoveries have been inspired by the nature. Thus it can be said that the nature has been an experimental platform for all the major scientific and technological discoveries. In recent years the idea of inspiration, mimicking and/or imitation of the natural systems in more orderly fashion, have initiated the biomimetic and/or bioinspired research and design (BIRD) practice for the engineering designers. It is known that the creative and innovative products are emerged during the conceptual design phase of the engineering design process. Thus a bioinspired conceptual design process can be treated as the first step of the BIRD process and existing engineering design phases can be applied for the succeeding phases of the BIRD.

## 1.6 Outline

Primary objective of this work is to introduce the multi-scale computational model for the bio-inspired acousto-ultrasonic band pass sensor that are capable of mechanically sense and/or filter wide range user defined frequencies. The proposed method not only overwhelms the inabilities of the respective state-of-the-art, but also suggests its few novel applications. This report is organized in such a way that it can deliver both the importance and the capabilities of the proposed band pass mechanism. The organization of the study is given below:

Chapter 1: Describes the target and the necessities of this work. This chapter also describes the corresponding background and the state-of-the-art technologies.

Chapter 2: Two models are proposed in this research to introduce mechanical band pass sensing mechanism, AEMM and BM models. In AEMM model, two approaches are

attempted, Stop Band Technique (SBT) and Band Pass Technique (BPT). In chapter 2, SBT is briefly described.

Chapter 3: Upon unsuccessful attempt using SBT method, BPT is adopted. This chapter describes the development of the unique frequency selection approach using the AEMM model and referring to the bio-inspiration demonstrated in chapter 6. Analytical, numerical and experimental studies are presented to concrete the hypothesis as discussed in section 1.4.

Chapter 4: Demonstrates the development of BM based mechanical broadband sensor. Under the umbrella of BM approach, two designs are proposed. Plate model and the Beam model. In chapter 4, development of the comprehensive predictive model for the plate design is demonstrated.

Chapter 5: This chapter describes the development of the predictive model for the BM beam model.

Chapter 6: Describes the bio-inspired background of the proposed hypothesis as referred in chapter 3. Human cochlea is considered as the reference structure. Summarizes the key features of the cochlea in designing the novel frequency selection mechanism.

Chapter 7: In this research, in addition to the proposed mechanical models for novel frequency selection mechanism, few innovative applications of the proposed models are also presented. Chapter 7, covers the key limitations of the state-of-the-art technologies for low frequency energy scavenging in powering low power electronic devices, demonstrates

the development of energy harvester using the AEMM model and Power optimization approaches are suggested in this chapter.

Chapter 8: Inspired from the energy harvester presented in chapter 7, three additional novel applications of the AEMM model are proposed (Highway noise barrier, Mobile energy harvester and the energy harvester for pacemakers).

Chapter 9: Inspired from the BM beam model, mycotoxin classification sensor is proposed using cantilever beam model. Existing detection methods are covered. Guidelines to conceal the inabilities of the existing techniques are described using Infrared Photoacoustic Spectroscopy.

Chapter 10: Beside primary objectives of this research, I was involved in couple of other projects (e.g. energy scavenging using patterned piezoelectric layer, phonon confinement using spirally oriented elastic resonators, precursor damage state quantification). Chapter 10 describes the energy scavenging procedure using patterned piezoelectric wafer.

Chapter 11: Demonstrates phonon confinement process using elastic resonators, where resonators are oriented spirally.

Chapter 12: Summarizes the contributions of this work and finally conclude the dissertation with future prospects and development of this research.

# CHAPTER 2: AEMM MODEL (STOP BAND TECHNIQUE)

In this study, the principal aim is to demonstrate the feasibility of designing a mechanical band pass frequency sensor that can predictively sense, pass, or actuate acoustic waves with desired specific frequencies or a band of frequencies, mechanically. Two approaches can be adopted to model the targeted mechanical sensor using the acousto-elastic metamaterial (AEMM).

1. Create a model that can introduce extremely wide frequency band gaps[a] by stopping all unwanted available frequencies and target frequencies can be passed/sensed automatically. This approach is termed as the stop band technique (SBT).
2. Create a model that can sense only desired frequencies, and hence automatically filters the available remaining frequencies, called the band pass technique (BPT).

[a]*Band gap is defined as the band of frequency where the energy transmission coefficient is very low and almost no energy can pass through the structure.*

As of date, the SBT is widely used and probably the only method to filter the acoustic wave. Additionally, since the Band Pass Technique is not adopted earlier by any

researcher and doesn't have any mathematical/physical background, we adopted the Stop Band Technique as our initial step to achieve our objectives.

## 2.1 Literate Review

Traditionally, researchers use stop band technique for filtering or stopping acoustic waves. It has been found that conventional materials do not possess the ability to provide such frequency stop bands. Hence, researchers proposed a system of material, called Metamaterial[b], to perform the objective.

[b]***Metamaterials*** *are artificial materials engineered to have properties that have not yet been found in nature. They are assemblies of multiple individual elements fashioned from conventional materials, such as metals or plastics, but the materials are usually constructed into repeating patterns. Metamaterials derive their properties not from the compositional properties of the base materials, but from their exactingly-designed structures. Their precise* shape, geometry, size, orientation *and arrangement can affect acoustic or* electromagnetic waves *in a manner not observed in natural materials. These metamaterials achieve desired effects by incorporating structural elements of sub-wavelength sizes, i.e. features that are actually smaller than the wavelength of the waves they affect.*

***Acoustic metamaterials*** *are kinds of metamaterials designed to control, direct, and manipulate* sound waves *as these might arise in* gases, liquids, *and* solids. *The acoustic* metamaterial *follows the theory and outcome of* negative index material *[24]. Since the acoustic metamaterial is one of the branches of the* metamaterials, *the basic*

*principle of the acoustic metamaterials is similar to the principle of metamaterials. These metamaterials usually gain their properties from structure rather than composition, using the inclusion of small inhomogeneities to enact effective macroscopic behavior. A negative refractive index of acoustic materials can be attained by altering the* bulk modulus *and* mass density *[25]. The* bulk modulus *of a material reflects the substance's resistance to uniform compression, whereas* mass density *of a material is defined as mass per unit volume. For acoustic metamaterials, both bulk modulus and mass density are component parameters, which define its* refractive index.

*In certain* frequency bands*, the effective mass density and bulk modulus may become negative. This results in a negative refractive index [24]. Neither negative mass density nor negative bulk modulus are found in naturally occurring materials; they are resulting from the* resonant frequencies *of an artificially fabricated metamaterial, and such negative responses are anomalous responses. Negative mass density or bulk modulus means that at certain frequencies the medium expands when experiencing* compression *(negative modulus), and accelerates to the left when being pushed to the right (negative density) [26].*

Resonating with the idea of acoustic metamaterial, numerous researchers have improved the concept of wave filtration capabilities by designing new and innovative materials [27-35]. El-Bahrawy [36, 37] and Banerjee et.al. [38, 39] studied wave propagation in periodic wave guides where surfaces of elastic media (wave guides) were proposed to be perturbed sinusoidally without creating any inclusions inside the material. Thus surface perturbations (surface etching) and volume perturbations (inclusions) are

completely different genres of metamaterials. Here the metamaterials with volume perturbation is discussed. On the other hand, photonic researchers are engaged in designing electromagnetic metamaterials [40-42] to explore photonic band gaps, a range of frequencies where electromagnetic waves cannot propagate [43]. Physical understanding of stress (elastic) wave propagation in phononic crystals and electromagnetic wave propagation in photonic crystals are similar [44-46]. Thus the concepts of designing new engineered materials are commutable between electrodynamics and elastodynamics. As a thumb rule, mass-in-mass systems are frequently proposed under a elastodynamic problem to predicatively manipulate the frequency band gaps in metamaterials with engineered volume inclusion. Application of such acoustic metamaterials have been envisioned for acoustic cloaking, vibration control, sound isolation, etc. [47, 48].

It is well-established that in any acoustic metamaterial, frequency band gaps are the results of either local resonance or Bragg scattering [49, 50]. Low frequency sound can be controlled by introducing locally resonant components into a unit metamaterial (known as, sonic crystal) [30, 34, 35, 49, 51], whereas conventionally high frequency stop bands can be formed by multiple scattering (Bragg) of the periodic inclusion of the sonic crystals [29, 31-33, 35, 50]. A acoustic metamaterial offers some exceptional properties (e.g. negative bulk modulus, negative effective mass density), which are not achievable using natural materials. Bragg scattering, formation of negative bulk modulus, negative effective mass density or both simultaneously, result in formation of band gaps and resonance bands with a high density of states $(DOS)^c$ in periodic structures [28, 52-55]. Negative effective mass density arises from the negative momentum of the unit cell with positive velocity field [56, 57]. In a mass-in-mass unit cell, the effective mass of the cell becomes negative at

frequencies near the local resonance frequency of the resonators due to special decay of wave amplitude [27]. Usually, a locally resonant medium consists of a heavy core embedded into a soft matrix. Local resonance of stiff materials (like, heavy core) in the system leads to the formation of frequency band gaps and can be manipulated by altering the size of the corresponding stiff component [31]. However, local resonance in matrix material allows a weakly dispersive band with a high density of states. It has been established that in any metamaterial system, additional stop bands can be introduced by adding additional local resonators in the system [27, 28].

[c]*Density of states (DOS) is calculated from the obtained dispersion relation. DOS of the system is the number of states (modes) that exist at each frequency level. A high DOS at a specific frequency level means that there are multiple modes available for occupation. Maximum DOS can be obtained where the frequency band is almost straight in the dispersion curve, which means the group velocity is close to zero and the wave energy is trapped inside the structure. A DOS of zero at any frequency means that no modes can be occupied at that frequency level and termed as stop band. For highly dispersive unimodal wave motion, the DOS is very small but not zero. The DOS is calculated from the dispersion relation by applying the following equation. In calculating the DOS, total wave number* $(\sum dk)$ *is computed for each frequency*$(d\omega = 1\ Hz)$.

$$DOS(\omega) = \frac{1}{\pi}\frac{dk}{d\omega}$$

Band gap manipulation was found in tremendous interest in the recent past, due to its diversified application capabilities. In this study, sonic bands (0-10 kHz) are analyzed

to extensively improve the wave filtering ability by using the acoustic metamaterial. In 2003, Hirsekorn et al. [51] performed a numerical simulation of acoustic wave propagation through sonic crystals consisting of local resonators using the local interaction simulation approach (LISA). They found three strong attenuation bands at frequencies between 0.3 and 6.0 kHz, which do not depend on the periodicity of the crystal. An extremely low frequency band gap for the Lamb waves can be obtained by periodically depositing single-layer or two-layer stubs on the surface of a thin homogeneous plate [30]. Caballero et al. [49] showed that absolute sonic band gaps produced by two-dimensional square and triangular lattices of rigid cylinders in air can be increased by reducing the structure symmetry. Based on the idea of localized resonant structures, Liu et al. [58] fabricated sonic crystals that exhibit spectral gaps with a lattice constant of two orders of magnitudes smaller than the relevant wavelength.

In early works, researchers were able to filter small ranges of frequency bands either in low or high frequency regions though their proposed metamaterials. However, this study is focused on isolating a very wide range of frequencies, both in low and in high frequency regions. If by any means, higher numbers of closely spaced band gaps are obtained, they can be eventually manipulated to be merged. Such multiple band gaps could potentially form wider band gaps. Such possibilities were not demonstrated by any previous models. Thus in this study, several models are envisioned to achieve the objective. Since resonator size and shape plays an important role in forming frequency band gaps [31], at first we envisioned a novel split ring metamaterial model with different size and shaped resonators. The concept of split rings is inspired by the studies on electromagnetic waves in photonics. Guenneau et al. [59] proposed a double ‘C’ resonator for wave

focusing and confinement. Movchan et al. [60] used split-ring resonators to control electromagnetic bands in two-dimensional photonic structures. Many other photonic researchers found split ring useful in manipulating electromagnetic waves for a specific purpose. To the best of the author's knowledge, split-ring resonators are introduced into an acoustic wave arena for the very first time in this study. Since Bragg scattering plays an important role in forming wider frequency band gaps, in the next model, the previously envisioned unit cell is placed in such a way that each unit cell is a mirror image of its neighboring cell.

Huang et al. [27, 28] showed that the number of band gaps in a system increases with the increase of the number of resonators in the system. In past research, mostly one or two heavy core resonators were used to generate low frequency sonic band gaps. Hence in next model, the conventional heavy core is divided into small circular resonators. Initially the small resonators are placed in a random order by keeping the same volume fraction within a unit cell. However, it is hypothesized that resonator orientation may have a considerable impact on band gap formation. Hence, two new models are visualized where resonators oriented circularly and logarithmic spirally. The spiral orientation came to mind since significant research has been performed in the field of photonics, where guiding of the electromagnetic wave by using spiral resonators [61-68] was demonstrated. For most cases, Archimedean spiral orientation was adopted. He et al. [69] proposed a three-dimensional chiral metamaterial consisting of arrays of the multi-layered mutually twisted metallic spirals which can exhibit negative refractive index at terahertz frequencies. Isik et al. [70] determined the electromagnetic response of the particles arranged in Archimedean spiral by using point group symmetry and the methods of crystallography. In 2011, Elford

et al. [71] proposed a Bernoulli type spiral coil resonator to attenuate sound pressure level at a low frequency region. They found three attenuation areas within the frequency range 0-2.2 kHz. A seashell resonator was also proposed, which is quite similar to a naturally obtained nautilus shell that can attenuate sound pressure levels at a wide range of frequencies. Since it is established that Bragg scattering depends on the periodicity of the unit cell and has significant impact on band gap formation, in the next model, the spiral resonating system is placed in a hexagonal unit cell to make the structure periodic from three directions.

Since the spiral structure is not symmetric about the unit cell, it is plausible to enhance the directional sensitivity of the spiral and result alteration of a wide range of wave modes, simultaneously. It is hypothesized that by using spiral rotation, the existing band structures can be manipulated and/or possible to introduce new band gaps, keeping the direction of wave propagation constant.

The envisioned models to extensively filter acoustic waves and introduce remarkably wide and continuous stop bands on both low and high frequency regions are listed below:

1. Split ring metamaterial

    a) With continuous periodicity
    b) With mirror periodicity

2. Multiple mass-in-mass system

a) With random resonator orientation

b) With circular resonator orientation

c) With spiral resonator orientation and square periodicity

d) With spiral resonator orientation and hexagonal periodicity

## 2.2 Numerical Implementation

It is extremely challenging to perform a mathematical formulation of the proposed complicated material systems, and thus the analysis is performed using the Finite Element Method [72]. In order to calculate the dispersion relation, the complete structure is considered infinite in both x- and y- directions by arranging the unit cell periodically. The Bloch-Floquet periodic [73] boundary condition is applied at all boundaries of the unit cell. The Bloch-Floquet boundary conditions are based on the Floquet theory, which can be applied to the problem of small-amplitude vibrations of spatially periodic structures. The theory states that the solution can be sought in the form of a product of two functions. One follows the periodicity of the structure, while the other one follows the periodicity of the excitation. The problem can be solved on a unit cell of periodicity by applying the corresponding periodicity conditions to each of the two components in the product. The generalized wave equation in a composite material can be written as:

$$C_{ijkl}(x_m)\left[1/2\left(u_{k,lj}(x_m,t)+u_{l,kj}(x_m,t)\right)\right]+1/2\left(u_{k,l}(x_m,t)+u_{l,k}(x_m,t)\right)C_{ijkl}(x_m)_{,j}+f_i(x_m)=\rho(x_m)\ddot{u}_\iota(x_m,t) \quad (2.1)$$

where, the constitutive matrix containing material properties and the density of the system are the functions of space $(x_1, x_2)$. $i, j, k, l \,\&\, m$ takes values 1, 2 & 3. Standard index notation is used throughout this manuscript. Let the body force $f(x_m)$be constant.

The unit cells are repeated in both directions and the solution can be assumed in terms of the Bloch-Floquet [74] solution, as discussed in the previous paragraph. Assuming there is no periodicity along $x_3$ direction & decoupling the phase component, the displacement solution can be viz.

$$u_i(x_m, t) = \sum_{n2}\sum_{n1} A^i{}_{n1n2} \exp(ik_m x_m) \,.\, \exp(iG_m x_m) .\exp(ik_3 x_3) \,.\, \exp(-i\omega t) \qquad (2.2)$$

where,$k_m$ is wave number along $m$-th direction and $G_m$ is component of the reciprocal lattice vector along $m$-th direction. Here, $m$ takes values 1 & 2. $G_m$ can be expressed as $G_m = 2\pi n_m / D_m$, where, $D_m$ is the periodicity of the cells in $m$-th direction. The $A^i{}_{n1n2}$is amplitude of the wave modes for particle displacement along $i$ and $n_1 \& n_2$ are the integer numbers between $-\infty \; to \; +\infty$. After substituting equation (2.2) in equation (2.1) the Bloch equation with the Bloch operator can be obtained as follows:

$$\left[\omega^2 \rho(x_m) \sum\nolimits_{n2} \sum\nolimits_{n1} A^i_{n1n2} \exp(i(k_m + G_m)x_m)\right] +$$

$$\left[\frac{1}{2} C_{ijkl}(x_m)(k_m + G_m)^2 \delta_{mj} - \frac{i}{2}(k_m + G_m)\frac{\partial C_{ijkl}(x_m)}{\partial x_j}\right] \times$$

$$\left[\sum_{n1}\sum_{n2} {A^k}_{n1n2}\exp(i(k_l+G_l)x_l)+\sum_{n1}\sum_{n1} {A^l}_{n1n2}\exp(i(k_k+G_k)x_k)\right] = 0 \qquad (2.3)$$

The above equation is a Bloch eigen value problem. The equation (2.3) is then multiplied with Bloch operator, with Bloch transformed weighting factor and integrated over the whole domain of the body and the equation was transformed to its weak form. Periodic boundary conditions are applied around the unit cell and the weak form of Bloch equation is solved only within the irreducible Brillouin Zone [74]. Further number of amplitude in the equation (2.3) is reduced for each wave number (k) point. Thus the $n_1 \& n_2$ are reduced from infinity and the truncated set of Bloch mode expansions [73] were used in the solution method. A suitable choice of reduced order basis was made based on the high symmetry points that characterize the periodic lattice. Next the Finite Element discretization was performed. Triangular isoparametric elements were used in the simulation. Element sizes were determined based on a series of convergence studies and the minimum wave length occurred in the material. The sizes of the elements were kept to a minimum of 1/10 of the corresponding minimum wave length occurred in any material type, respectively. The Bloch displacement amplitudes were discretized using the isoparametric shape function ($N_i(\boldsymbol{x})$) suitable for triangular elements for each combination of $n_1 \& n_2$ in their truncated series as follows:

$$\mathbf{A}_{n1n2} = \sum_{\boldsymbol{i=1}}^{\mathbf{3}} N_i(\mathbf{x})\Lambda_{\boldsymbol{i}} \qquad (2.4)$$

Applying the discretization equations and periodic boundary conditions, the weak form of Bloch equation reduces to an algebraic eigenvalue problem$[\mathbf{K}(k) - \omega^2\mathbf{M}]\tilde{\mathbf{V}} = \mathbf{0}$, where $\tilde{\mathbf{V}}$ is the discrete Bloch amplitude vector, which are periodic within the unit cell. The **K**(*k*) and **M** are the global stiffness and mass matrices, respectively obtained by integrating the element level matrices in proper order. Detail expressions for **K** and **M** can be found in reference [73]. The solution of the eigen value problem provided the dispersion curves for the proposed periodic media.

## 2.3 Validation of Solution Methodology

Since the investigation is conducted using FEM tool, validation of the solution methodology is essential. It is challenging to perform the mathematical formulation for the proposed models due to their increasing complexity. Hence, the simple mass-in-mass system (Ref. Figure 2.1) which is well established in literature is studied to validate the solution methodology.

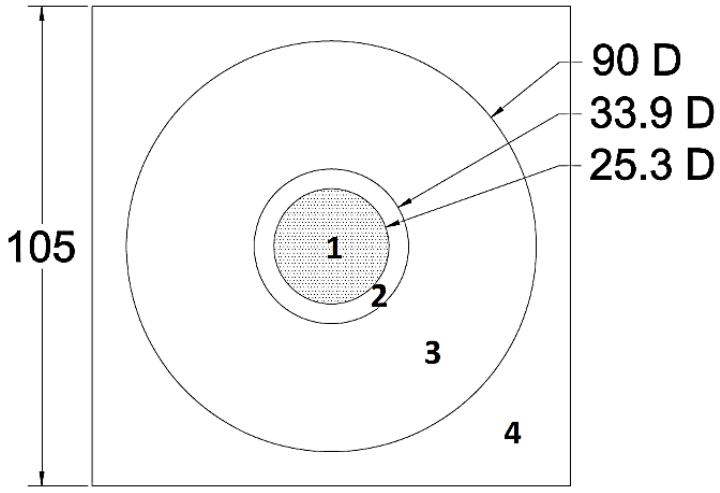


Figure 2.1: Single-resonator mass-in-mass system with square periodicity (dimensions are in mm).

The unit cell is composed of four components. A significantly stiff material, lead (component 1), is chosen as circular resonator [44, 58]. To avoid evanescent wave modes, the core resonator is coated with softer rubber like material (component 2). The rubber-lead arrangement is then embedded into a relatively stiffer component (epoxy). The lead-rubber-epoxy combination is synonymous to well-known mass-in-mass engineered material system proposed by the earlier researchers [28]. It is mathematically proven that, such engineered system provides frequency band gaps (stop bands) virtually creating negative bulk modulus and negative mass density in the structure. In engineered material system, the negative responses happen due to the mismatch of material properties between adjacent components. Hence, to allow extreme property mismatch, the mass-in-mass system is placed inside a square unit element and the gap is filled with a relatively softer material (polyethylene plastic).

Table 2.1: Properties of the components enclosed in unit cell.

| | Lead | Rubber | Epoxy | Polyethylene |
|---|---|---|---|---|
| Young's Modulus (Pa) | 13e9 | 10e6 | 3.5e9 | 0.7e9 |
| Density (kg/m$^3$) | 11310 | 980 | 1250 | 1050 |
| Poisson's Ratio | 0.435 | 0.49 | 0.38 | 0.49 |

The complete lead-rubber-epoxy-polyethylene setup is considered as the Representative Volume Element (RVE) in this section. The unit cell is a 105 mm square and diameters for lead, rubber and epoxy components are considered as 25.4 mm, 33.9 mm and 90 mm, respectively. Material property of the unit cell components are listed in Table 2.1.

It is well known that, frequency band gap occurs due to negative mass density [75] and resonance of local microstructures in metamaterials [27, 28, 30, 31, 49, 51-53, 56, 58]. To validate the above statement and adopted FEM solution methodology, multi-layered mass-in-mass model (Ref. Figure 2.1) is considered. This study is carried out for a frequency range of 0 to10 KHz. For illustration purpose, the response is reported between 0 to 4 KHz in Figure 2.2. Computed effective mass densities are normalized by the density of the stiffest component (lead) of the cell. The effective mass density of the unit cell is calculated by using the following formula under the long wavelength assumption.

$$\rho_{\alpha\beta} = \frac{\int \sigma_{\alpha\beta} d\Gamma}{\int \ddot{u}_{\alpha\beta} d\Gamma} \qquad (2.5)$$

where $\alpha, \beta = 1, 2$ and $\sigma_{\alpha\beta}$ and $\ddot{u}_{\alpha\beta}$ are the local stress and acceleration quantities. $\Gamma$ denotes the external boundary of the unit cell.

Dispersion curve for the single resonator metamaterial within the first Brillouin zone is shown in Figure 2.2a. Using the definition of mass density in equation 2.5, it has been found that the mass density of the system stays negative between the frequency range 2.27 – 2.71 KHz (Ref. Figure 2.2b). Alternatively, a stop band is observed (Ref. Figure 2.2a) at frequency range between 2.28 - 2.74 kHz (considering Γ-X directional waves). Same band gap exist for all ΓXMΓ directional waves as well. Since the mass density of the metamaterial stayed negative between the same frequency bands apparent from the stop bands indicated by the dispersion curves, the computational methodology is thus validated. This phenomenon is well reported in the literature [27, 28, 30, 31, 49, 51-53, 56, 58, 76, 77].

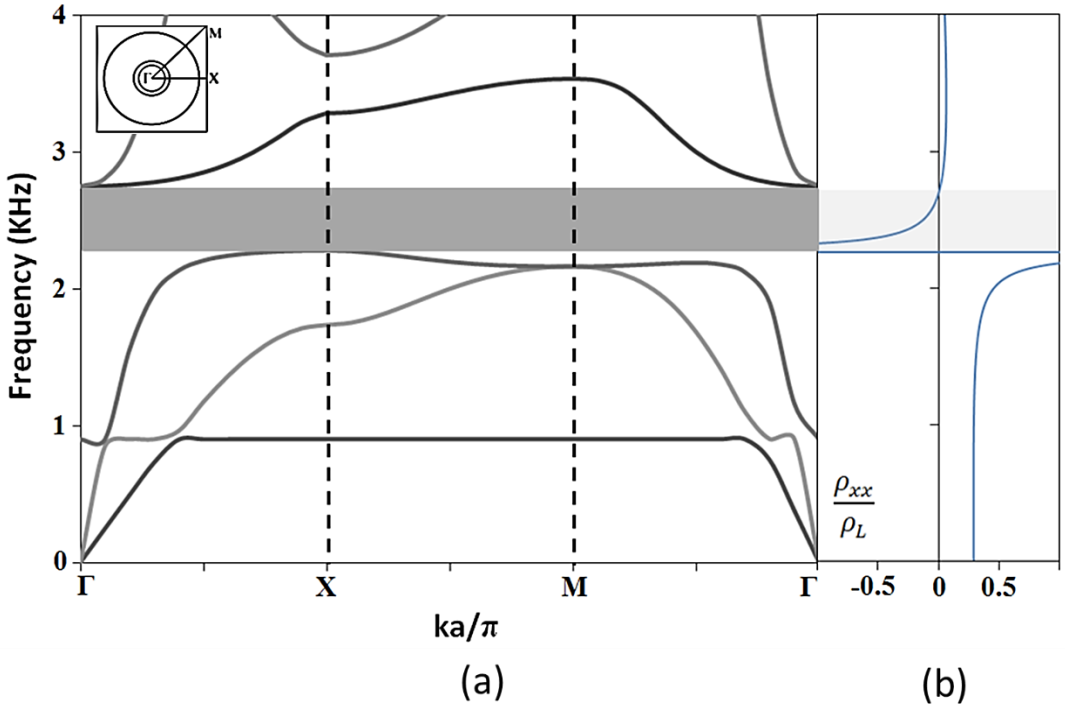


Figure 2.2: (a) Dispersion relation (b) Mass density plot for the single-resonator mass-in-mass system.

## 2.4 Split Ring Metamaterial

**Model Description**

A two dimensional structure (25.4 mm X 25.4 mm) with split ring resonators is proposed in this model. Figure 2.3 illustrates the schematic of the unit cell. The unit cell is composed of a steel core of diameter 3.6 mm embedded in a circular ring of outside diameter 7.18 mm. A softer material (Epoxy) is used to seal the space between the steel ball and the circular ring. Similar mass-in-mass system was also proposed by Huang et al. [27]. However, in this study, one additional set of semicircular rings are placed symmetrically about the core to increase the number of band gaps. To generate access to

new portal to manipulate further frequency bands, another pair of elliptical split rings are positioned symmetrically but orthogonally to the previously positioned semicircular rings. All rings are made of steel with thickness 0.94 mm and are included is a softer material. For simplicity, the steel cores, elastic coating and the split rings are considered embedded in an epoxy matrix. Material properties of the unit cell are listed in Table 2.2.

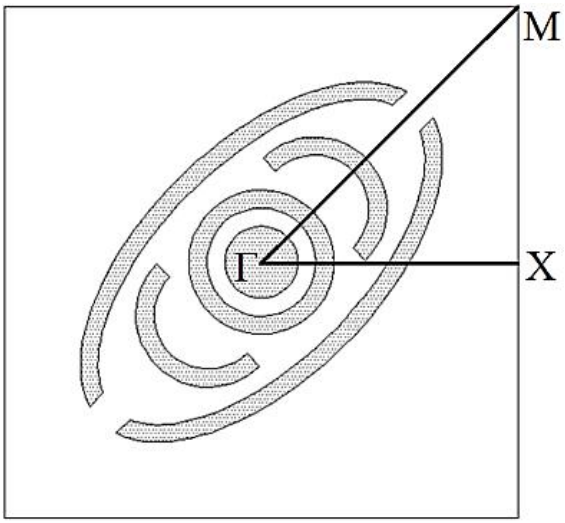


Figure 2.3: Proposed unit split-ring metamaterial with first Brillouin zone representation.

Table 2.2: Material properties of the components of the split-ring metamaterial

| Material | Young's Modulus (GPa) | Density (kg/m$^3$) | Poisson's Ratio |
|---|---|---|---|
| Steel | 205 | 7850 | 0.28 |
| Epoxy | 2.35 | 1110 | 0.38 |

**Dispersion Relation Analysis**

Split ring metamaterial with two types of periodicity (Continuous and Mirror) is discussed. A wider frequency range (0-50 KHz) is studied. Figure 2.4 describes the dispersion relation of the split ring metamaterial with continuous periodicity, where repetition of identical unit cell (Ref. Figure 2.3) in both (x- and y-) directions is considered as the continuous periodicity. The total band structure is computed for ΓXMΓ boundary (see Figure 2.3). Three band gaps are observed from 20.83 to 22.07 KHz, 27.22 to 29.94 KHz and 36.72 to 37.47 KHz with band widths of 1.24 KHz, 2.72 KHz and 0.74 KHz, respectively.

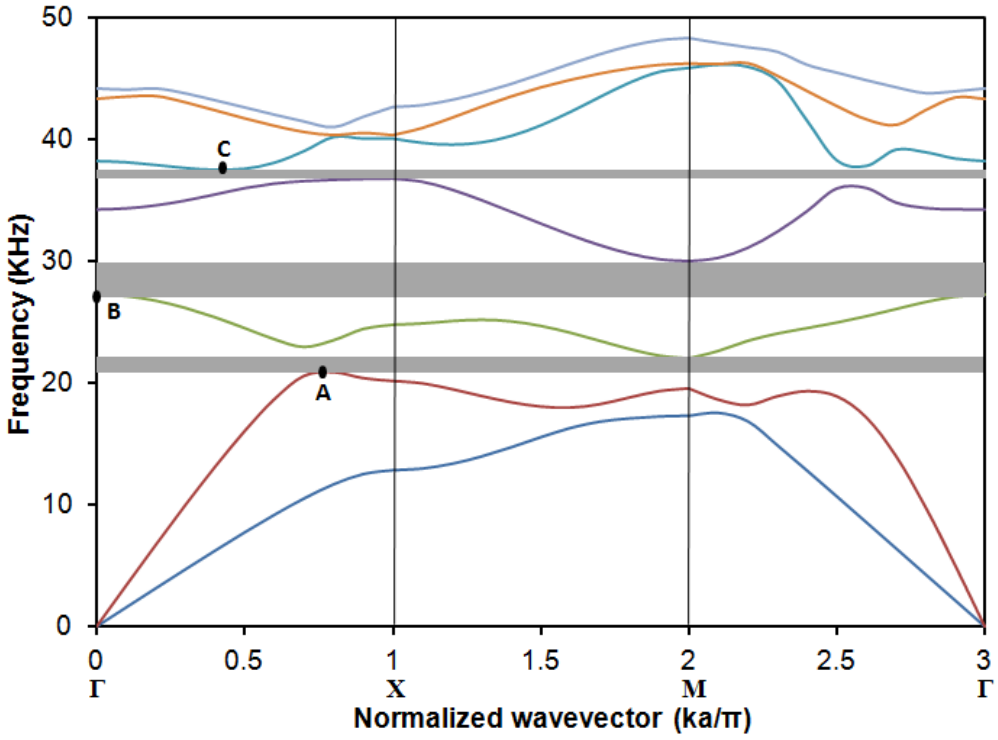


Figure 2.4: Dispersion relation for Split ring metamaterial with continuous.

To understand the explanation of band gap formation in gap frequencies, a frequency domain analysis is performed. A uniformly distributed compressive load of unit magnitude (P in Figure 2.5a) is applied on both opposite ends of the unit cell along x-direction. According to load-deformation laws, it is expected to witness compressive deformation in the unit cell along x-direction upon such input loading. At an arbitrary frequency 28.5 KHz (a frequency within band gap 27.22 to 29.94 KHz) it is observed that the unit cell is tending to elongate even though a compressive load is applied (Ref. Figure 2.5b). Such unusual phenomenon signifies the formation of negative bulk modulus at frequencies where band gap exists and hence verifies the established hypothesis on creation of frequency band gaps.

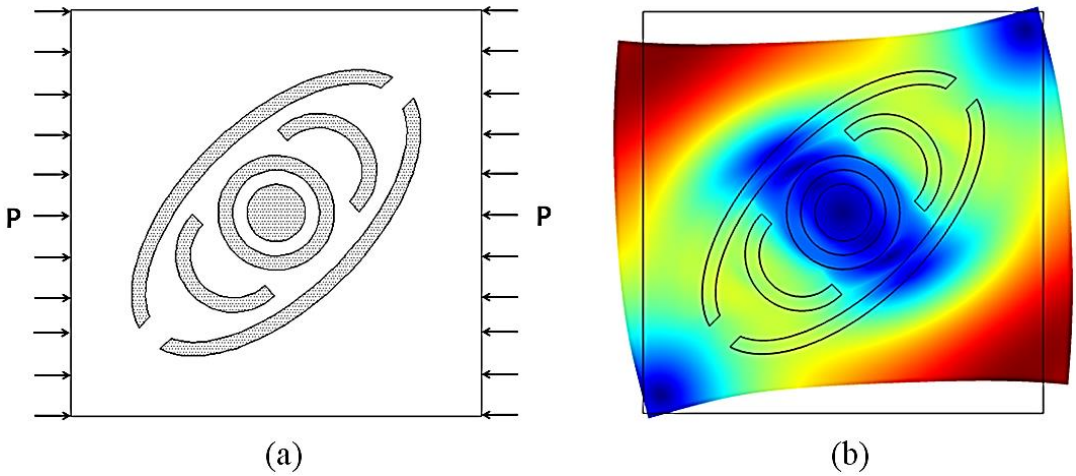


Figure 2.5: (a) Loading setup in unit cell (b) Displacement mode at f = 28.5 kHz.

The split ring metamaterial is found an improved model compared to previously studied metamaterials in considering number of stop bands within the studied frequency level. Inspired from the outcome, split ring model with mirror periodicity is studied to expand the width of the frequency band gaps and merge neighboring bands so that

extensive filtering of the acoustic frequencies can be possible. The proposed configuration is shown in Figure 2.6a. With the mirror periodicity, it is possible to widen the second band gap significantly (9 KHz, between 24 KHz and 33 KHz). In the contrary, the 1st and 3rd band gap disappeared with the modification in the periodicity (Figure 2.6b).

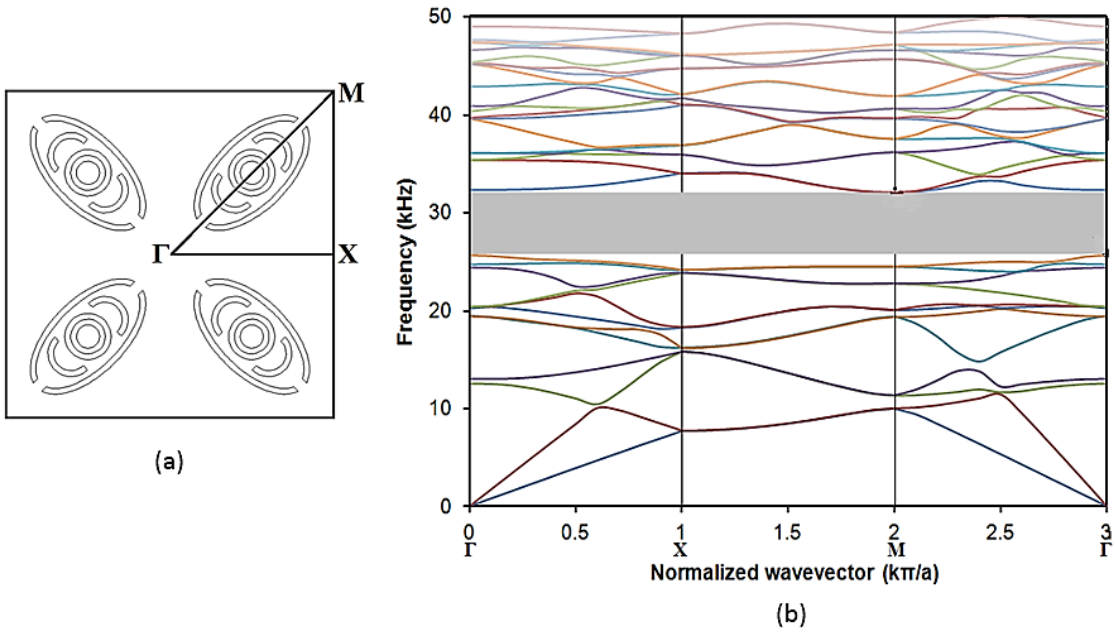


Figure 2.6: (a) Split ring metamaterial with mirror periodicity (b) Corresponding dispersion relation.

**Subsection Summary**

Using split ring metamaterial with continuous periodicity, number of stop band is improved compared to previously studied models. The proposed models could be a good choice for wave isolation study where several stop bands are required with small band widths. However, the model is not a good argument for the targeted study since continuous stop band for a very wide range of frequency is required. With mirror image periodicity

fairly wider frequency stop band is obtained with a band width of 9 kHz (24 kHz to 33 kHz) compared to previous model (maximum band width 2.7 kHz), however some of the previously obtained bands are disappeared. Though the second model is an improved version of model-1 compared to stop band width, but it is still not close enough to our required model which can stop very large range (maybe 100 KHz or more) of frequency.

## 2.5 Multiple Mass-in-Mass (MMM) System

Since formation of frequency band gap is strongly dependent on number of resonators used in a metamaterial system, several multiple mass-in-mass models are considered to extensively increase the wave filtering capability of the system.

**Envisioned Models**

To create the MMM models, the mass-in-mass system referred in Figure 2.1 is used but the central lead resonator with rubber coating is divided into thirty-two (arbitrarily chosen) small resonators such that the diameter of small resonators can be maintained as 4.5 mm. To study the effect of multiple resonators in host matrix, first a random orientation (see Figure 2.7a) of the resonators in the unit cell is studied. The random configuration hasn't shown noticeable improvement toward the desired goal and thus the small resonators are placed systematically in a circular orientation (see Figure 2.7b). Inspired from the outcome, the resonators are then placed in a logarithmic spiral pattern (Figure 2.8) to extensively manipulate the frequency bands in both low and high frequency region.

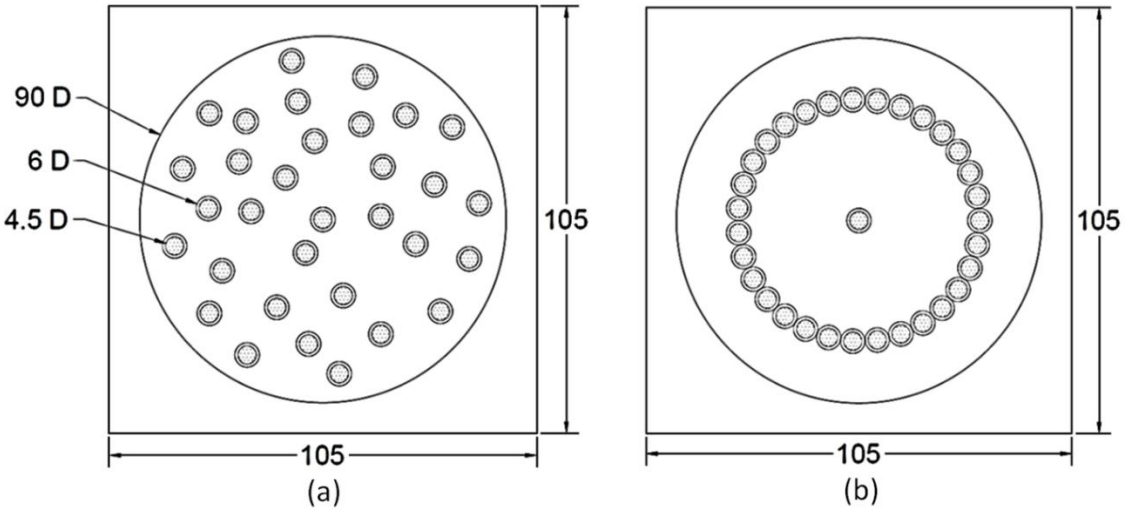


Figure 2.7: (a) Random and (b) Circular orientation of the resonators in unit cell (Dimensions are in mm.)

Both square and hexagonal periodic cells are considered for the spiral configuration. The hexagonal unit cell is 105 mm wide with 60.62 mm long faces. Logarithmic spiral was chosen such a way that the small resonator (4.5 mm) could cover at least two full turn (i.e. $4\pi$). Following a logarithmic equation in polar coordinate system- $r(\theta) = ce^{b\theta}$, where c and b are two arbitrary positive real constants, it was found that c = 10/3 and b = 0.2 could fit the proposed geometry in order to keep the overall configuration and number of resonators consistent (Figure 2.7 and Figure 2.8). Effect on wave modes could possibly be altered by changing the parameters c and b and could result different outcomes.

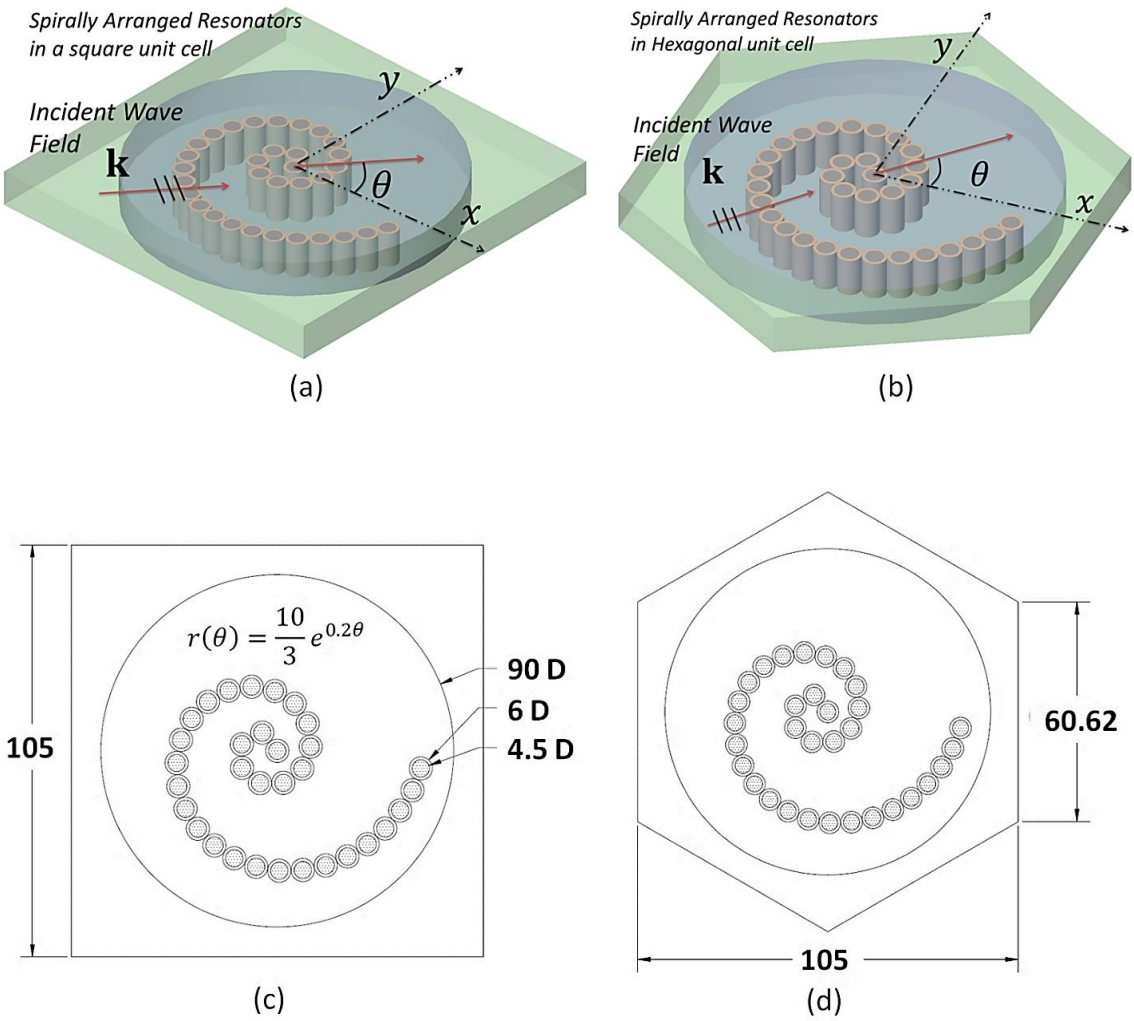


Figure 2.8: Proposed spiral resonator with (a) Square (b) Hexagonal periodicity

Since the spiral setup is not symmetric about the origin, incident wave on spiral can be altered by rotating the spiral orientation. Such rotation alters the amount of energy scattered through the material. In order to manipulate the existing band widths and introduce new band gaps, the spiral arrangement is rotated (Figure 2.9), systematically.

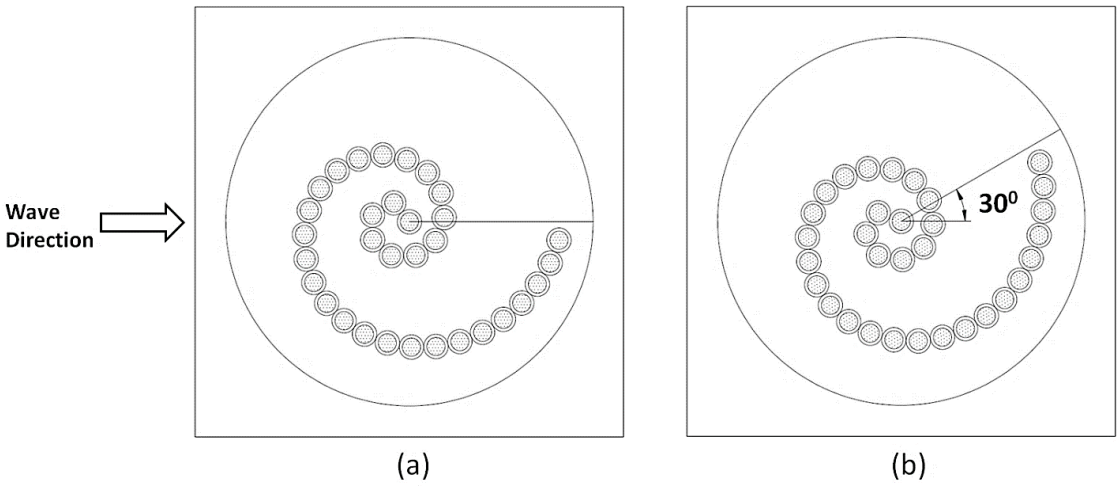


Figure 2.9: Rotation of spiral resonators about the direction of wave propagation (a) $0^0$ (b) $30^0$.

**Section Result and Discussion**

Numerical analyses are performed using the same numerical approach discussed in section 2.2. The proposed complex configurations were analyzed by using the validated computational technique presented in section 2.3. All reported results in this section are obtained between frequency ranges of 0-10 KHz. Since the numbers of frequency bands depend on the numbers of degrees of freedom of the system, splitting the big resonator may allow more band gaps at same frequency range. It has been noticed that random orientation (Ref. Figure 2.7a) of the small resonators isn't a good choice to improve the number of band gaps and only two band gaps are obtained, while five band gaps are listed when the resonators are systematically oriented in a circular orientation (Ref. Figure 2.7b). It is also visually apparent that at around 5 KHz the nondispersive zone (where frequency bands are straight) of the wave modes is broaden by employing the circular orientation where the

density of states are significantly increased. Dispersion curves for both random and circular orientations are shown in Figure 2.10.

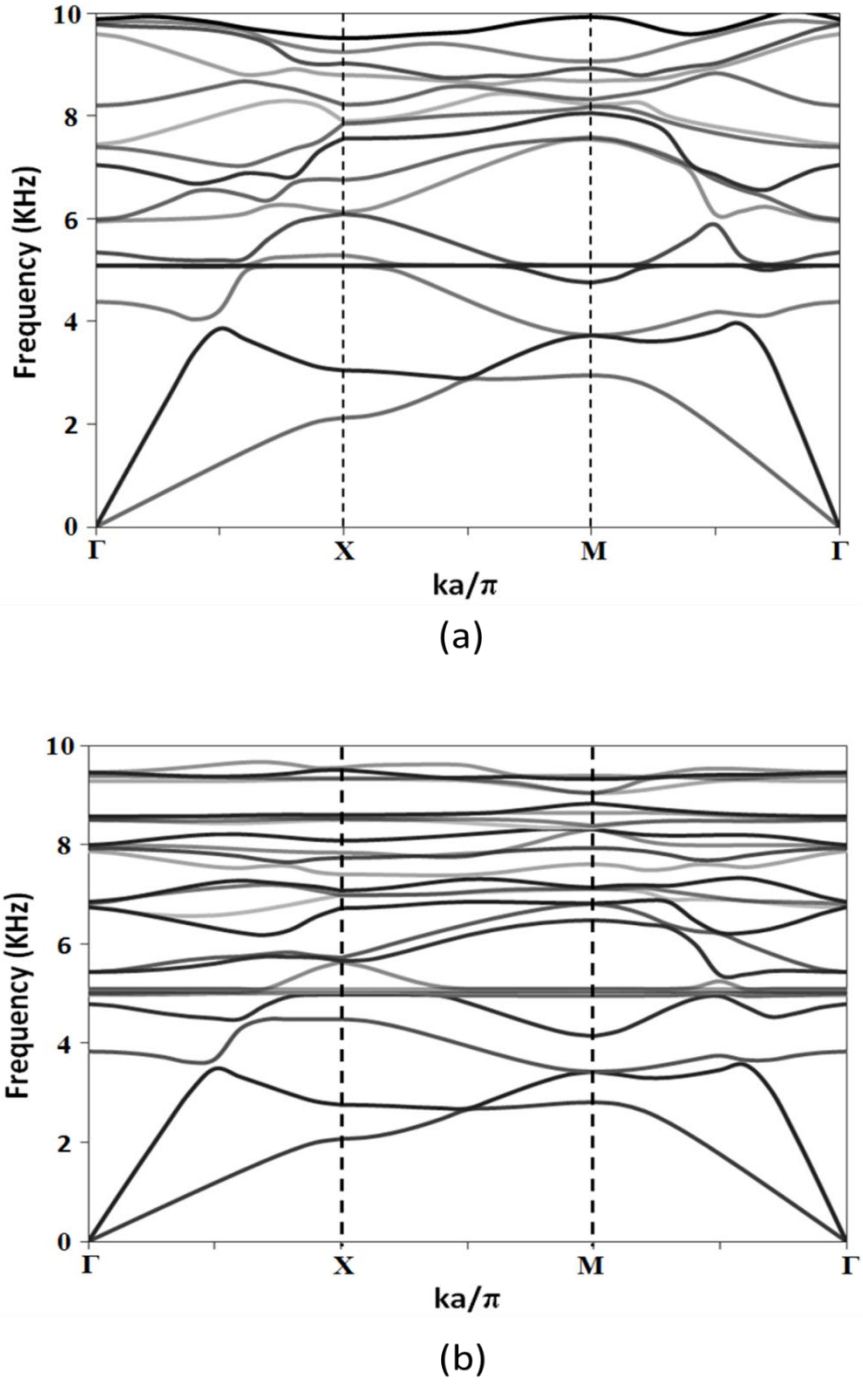


Figure 2.10: Dispersion curve for (a) Random orientation (b) Circular orientation

It is difficult to perceive the exact location and range of the stop bands from Figure 2.10. Thus, the band gaps obtained from all configurations are listed in Table 2.3. The band gaps above 100 Hz are only reported in Table 2.3. Note that, for band gap comparison Γ-X directional waves are considered.

Table 2.3: List of stop bands in Γ-X direction for random orientation, circular orientation and spiral configuration

| Orientation | Band Start (Hz) | Band End (Hz) | Band Gap (Hz) | # of Band Gaps |
|---|---|---|---|---|
| Random Orientation | 3866.691 | 4051.225 | 184.534 | 02 |
| | 8673.753 | 8805.328 | 131.575 | |
| Circular Orientation | 3482.235 | 3616.836 | 134.6014 | 04 |
| | 5836.571 | 6176.112 | 339.5419 | |
| | 7287.709 | 7415.066 | 127.3569 | |
| | 8218.752 | 8437.614 | 218.8627 | |
| Spiral Orientation (Sq. Cell) | 3454.667 | 3703.175 | 248.5084 | 07 |
| | 4756.028 | 4910.274 | 154.2455 | |
| | 5155.613 | 5288.248 | 132.6351 | |
| | 7588.973 | 7753.167 | 164.1935 | |
| | 9246.151 | 9367.912 | 121.7604 | |
| | 9549.62 | 9663.73 | 114.1109 | |
| | 9728.052 | 9837.955 | 109.9026 | |
| Spiral | 4734.045 | 4510.483 | 223.562 | 10 |
| | 7293.706 | 7175.432 | 118.2731 | |

| | | | | |
|---|---|---|---|---|
| Orientation<br><br>(Hx. Cell) | 7570.903 | 7434.122 | 136.7811 | |
| | 7736.459 | 7604.774 | 131.6848 | |
| | 7981.432 | 7819.903 | 161.5284 | |
| | 8422.138 | 8275.442 | 146.6963 | |
| | 8812.458 | 8541.347 | 271.1107 | |
| | 8963.19 | 8827.699 | 135.4912 | |
| | 9100.463 | 8999.008 | 101.4544 | |
| | 9663.074 | 9535.885 | 127.1886 | |

Since systematic (circular) orientation of the resonators showed some improvement, next the resonators are placed in a logarithmic spiral orientation. Significant improvement was observed with seven band gaps (see Figure 2.11 and Table 2.3) by orienting the resonators in spiral pattern in a square periodic unit and keeping the spiral setup at $45^0$ with the direction of wave propagation. Similarly, using spiral resonator in a hexagonal periodic unit and keeping the spiral setup at $45^0$ with the direction of wave propagation, 10 stop bands are observed (Figure 2.12 and Table 2.3). Although the extent of the band gaps are smaller, many band gaps at close proximity provide flexibility to alter them by rotating the spiral.

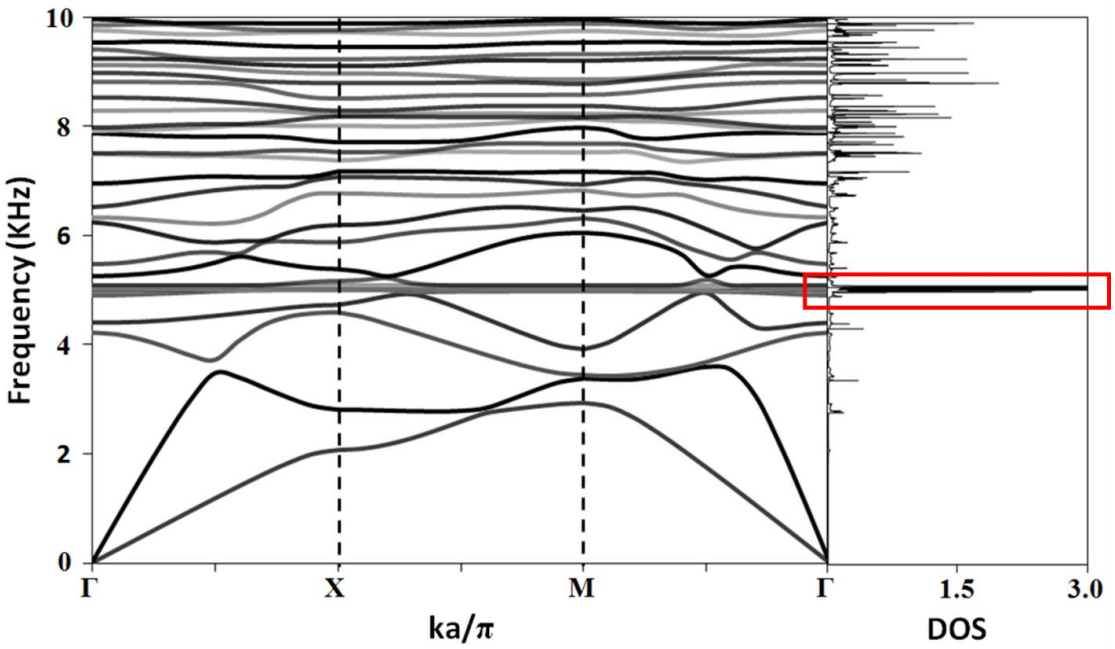


Figure 2.11: Dispersion curve for spiral orientation in square cell by keeping the spiral 450 with the horizontal. Associated density of states on right.

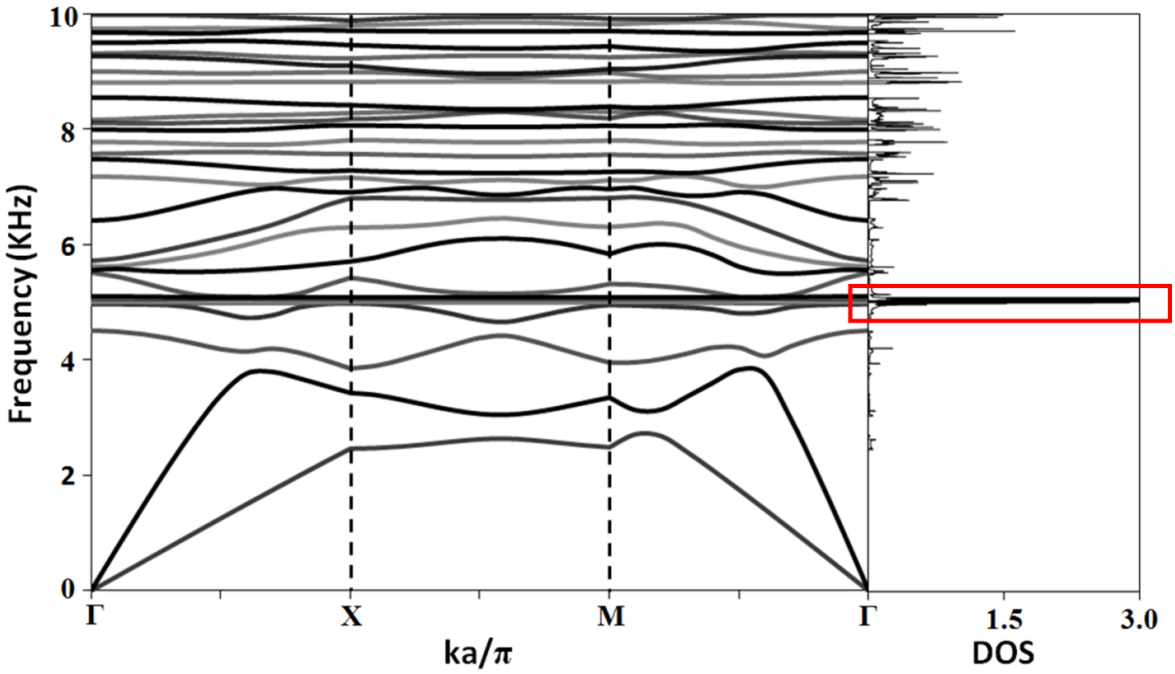


Figure 2.12: Dispersion curve for spiral orientation in hexagonal cell and corresponding density of states.

From the proposed analysis and dispersion curves presented in Figure 2.11 and Figure 2.12, it is difficult to visualize the location and width of the band gaps. Thus, Figure 2.13b and Figure 2.13d are introduced to demonstrate the band gaps corresponds to square and hexagonal cell, respectively. It has been noticed that, keeping the same volume fraction in the unit cell and positioning the resonators in a circular and logarithmic spiral orientation, larger number of band gaps can be obtained compared to the single resonator metamaterial and random orientation of the resonators.

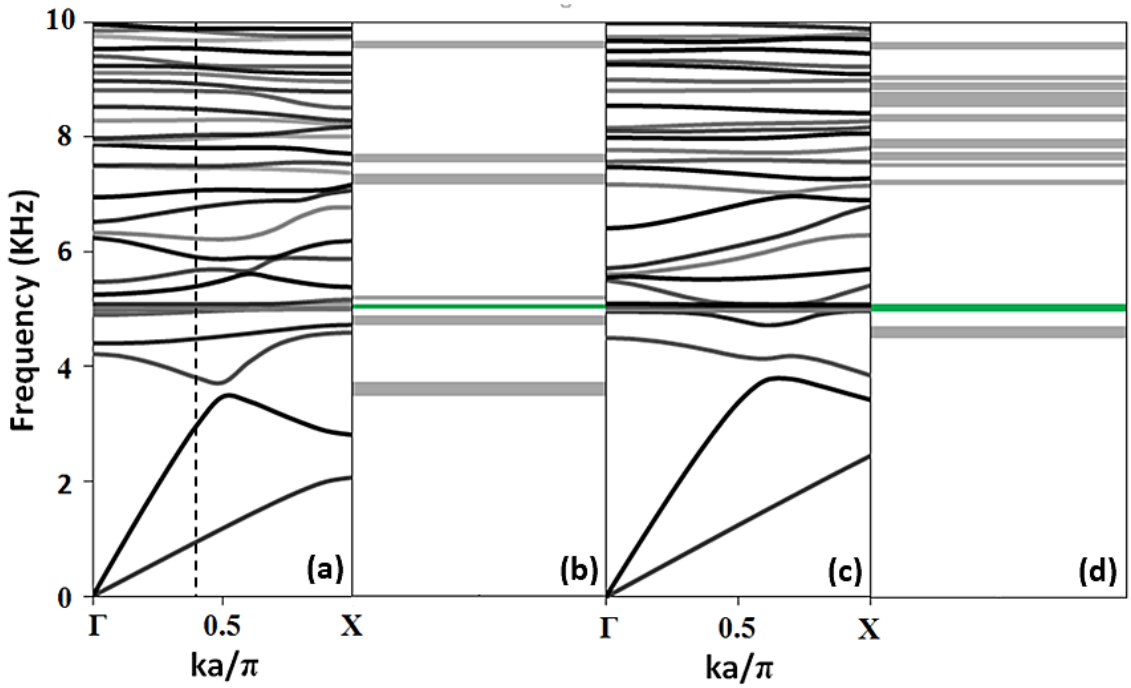


Figure 2.13: Dispersion relation and band gap representation for Square (a - b) and Hexagonal (c-d) cell, respectively, for Γ-X directional wave by keeping the spiral $0^0$ with horizontal.

Large numbers of band gaps were observed for both types of periodicity (square and hexagonal). At 7.8 - 9.7 Hz, no band gap is noticed in square unit cell, however significantly large stop bands are observed for hexagonal cell at that region. Usually low frequency band gaps are associated with the local resonance of the cell constituents,

whereas high frequency band gaps are results from Bragg-scattering in any periodic structure. The hexagonal cells are periodic in three directions, hence allows extended scattering of wave energy compared to the square cell periodicity, which leads to the formation of increased number of band gaps at high frequency regions (Figure 2.13d).

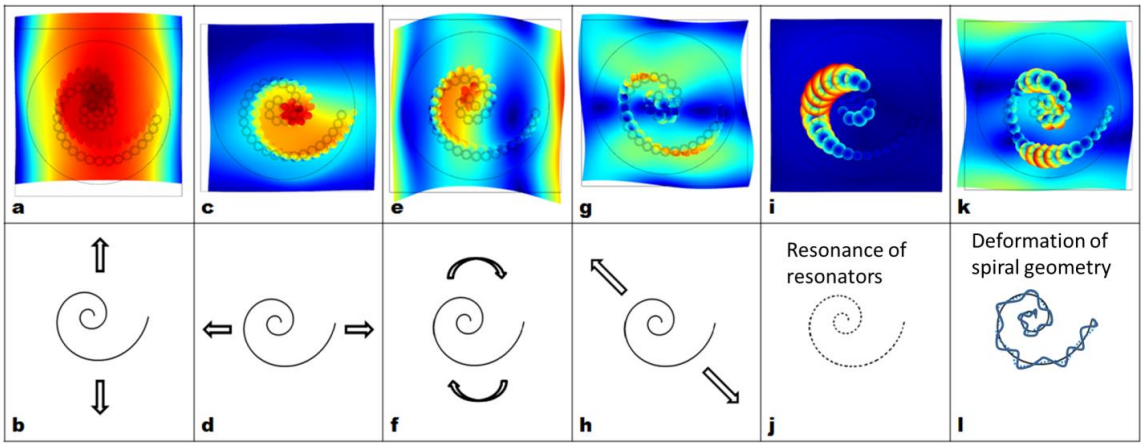


Figure 2.14: Displacement/vibration patterns of the spiral resonators in 1st (a-b), 2nd (c-d), 3rd (e-f), 4th (g-h), 7th (i-j) and 37th (k-l) modes.

Vibration/Displacement patterns of unit cell at different frequency modes are described in Figure 2.14. First and second modes in Figure 2.13a are the two axial vibration modes of the complete spiral setup as shown in Figure 2.14(a-b) and Figure 2.14(c-d). Displacement patterns of these modes are presented at $ka/\pi = 0.4$ (dashed line in Figure 2.13a). Rotation of the spiral is noticed in third mode (Figure 2.14(e-f)), whereas shear stretching of spiral took place in the fourth mode (Figure 2.14(g-h)). Next thirty-two (mode $5^{th}$ – $36^{th}$) frequency modes are strongly dominated by the softest component (Rubber) of the cell, where the energy is trapped inside and the frequency modes are almost straight (coined as Weakly Dispersive Modes (WDM)). Ripple in spiral orientation in different directions are observed in the modes from $37^{th}$ mode and onward. Such alteration of spiral

structure created the high frequency modes leaving some new band gaps at high frequency region.

The WDM refer to the modes where distinct wave modes exists but $d\omega$ along the wave number axis between $0 - ka/\pi$ are less than 20 Hz. The bands that are exhibiting the Weakly-Dispersive Zone (WDZ) are shown in Figure 2.13b & Figure 2.13d with marking. It is well understood that the WDZ are the response of vibration trapped inside the softest component of the cell. No geometric dependency of such modes was reported. It was found that using random, circular and spiral orientation these WDZ modes can be altered or broadened. Width of the WDZ is very narrow (~ 8 Hz) for random orientation and around 25 Hz for circular orientation. But it can be extended up to 57.5 Hz & 73.5 Hz (Figure 2.13) by using the spiral orientation in square and hexagonal unit cells, respectively. It is also noticed that the dense zone, where density of WDM is maximum, can be shifted by arranging the resonators in a systematic order. WDZ's can be significantly advantageous in stopping low frequency acoustic waves composed of multivalued wavenumbers through a structure. Note that the numbers of resonators in the unit cell are exactly equal to the number of weakly dispersive wave modes found from the dispersion curves. Nearly zero group velocities ($C_g = \Delta\omega/\Delta k$) were observed for weakly-dispersive modes, which signifies roughly no energy dissipation on those modes and will result very low to zero transmission. As a result the density of states at any frequency is significantly high. A close up view of the density of states presented in Figure 2.11 and Figure 2.12 are presented in Figure 2.15 between the frequencies 4970 Hz – 5120 Hz. Figure 2.15 shows the envelop obtained from Hilbert transform of the data on density of states at certain frequency. There is an indication of enhanced weakly dispersive zone by employing spiral packing of local

resonators. Moreover the zone is enhanced by hexagonal periodicity of unit cell over rectangular unit cells.

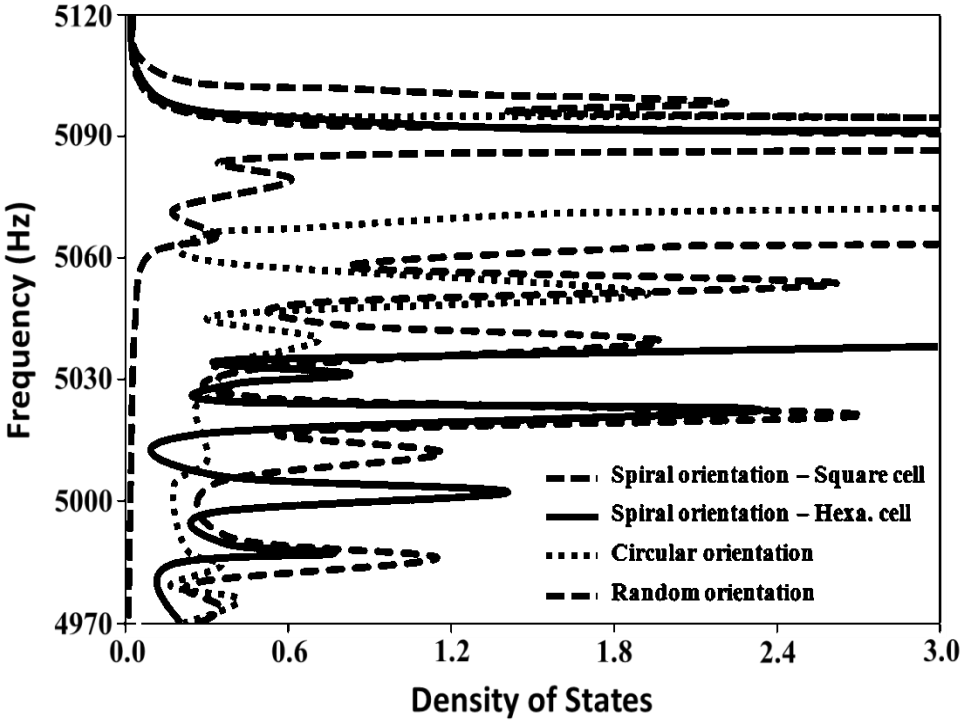


Figure 2.15: Envelop of density of states within the weakly dispersive zone for different resonator configurations

At WDZ, frequency modes are trapped inside the softest component of the structure (Figure 2.16) [58]. Displacement patterns at 5086.12 Hz and 5086.13 Hz, selected arbitrarily, are presented for #14 and #17 weakly-dispersive modes in Figure 2.16a and Figure 2.16b, respectively, with group velocities of 0.10971 m/s and 0.02058 m/s. Since the displacements of the resonators were found very small but nonzero, negligible amount of energy is absorbed by the stiffest part of the structure at WDZ. Similar pattern is also observed for randomly distributed resonators of same volume fraction. Hence, in this context of weakly dispersive zone, a definite geometrical pattern is not imperative as long as the local resonators (stiff materials inside a soft matrix) are present in the wave paths.

**Rotation of Spiral Resonator System**

As discussed earlier, band gaps above 100 Hz are only reported in this section, however, with spiral orientation, there exist a large number of band gaps which are very close to 100 Hz (e.g. 99 Hz, 98 Hz etc.), unlike random and circular orientation where the next band gap after 100 Hz is only 8.5 Hz. Since the spiral resonators are not symmetric about the unit cell, those frequency band gaps can be easily improved by rotating the spiral setup and it also might be possible to connect two adjacent band gap and form a wider stop band. However due to symmetricity circular resonator setup does not allow such improvements.

As the spiral setup is not symmetric about the origin of the unit cell, orientation of the spiral opening (Ref. Figure 2.9a) or the long arm about the wave direction exhibit considerable impact on wave propagation. Since the waves along Γ-X direction are studied, the spiral opening is oriented parallel to the wave direction. Hence, to analyze the directional sensitivity, the spiral setup is rotated about the direction of wave propagation with $30^0$ increments (Figure 2.9b). In addition, $45^0$ and $135^0$ rotations are also considered as they are synonymous to M-Γ directions (Ref. Figure 2.6a) for the square unit cell. Since, $180^0 \geq \theta \geq 360^0$ is a mirror representation of $0^0 \leq \theta \leq 180^0$, hence shows expected similar response.

In the following figures, maximum band widths of the frequency bands beyond 100 Hz are reported. As expected and discussed earlier the weakly-dispersive zones (Figure 2.16) are found to be uninfluenced by the spiral rotation, whereas frequency band gaps above weakly-dispersive zones can be manipulated significantly by altering the spiral orientation. It has been noticed that new band gaps are introduced for both square and

hexagonal unit cells and widths of the preexisting band gaps can be considerably altered (Figure 2.16). Six band gaps were noticed at $0^0$ orientation for the square periodic cell with no band gaps in between 7.8 KHz and 9.5 KHz. But three narrow stop bands are introduced after rotating the spiral to $30^0$.

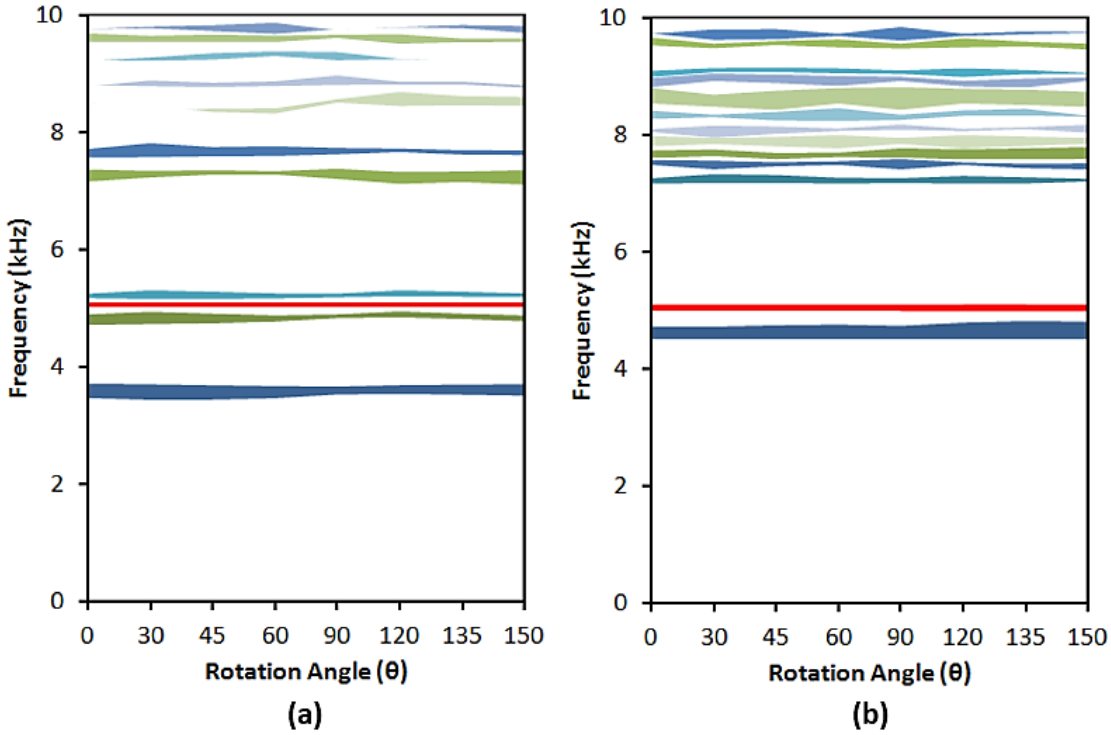


Figure 2.16: Band gap plot at different rotation of single spiral resonator with (a) Square (b) Hexagonal periodicity.

Rotating the spiral may introduce more stop bands and as a consequence, ten band gaps are listed when the spiral is rotated to $45^0$ - $60^0$. For the hexagonal periodic cell, ten band gaps are observed at $0^0$ orientation and a maximum of twelve band gaps can be achieved with the modification of spiral orientation. It is also found that width of a particular band can be extensively manipulated by rotating the spiral in the unit cell, however merging of adjacent stop bands hasn't achieved using the proposed spiral rotation technique.

**Subsection Summary**

Spiral structures show important characteristics in filtering sound waves. Though, Archimedean spiral resonators are familiar in photonics research community, however spiral resonators are novel in phononic research area. In this section, a set of circular resonators are placed in a logarithmic spiral orientation to filter and guide sonic acoustic waves. Two types of periodic cells (Square and Hexagonal) are considered. Significantly larger number of frequency band gaps can be achieved by placing the resonators in a logarithmic spiral orientation, rather than using single heavy resonator or placing the resonators in a random or circular pattern. Since high frequency band gaps are function of Bragg-scattering in any periodic structure, hexagonal unit cell provides additional band gaps compared to square cell due to its three directional periodicity. Coined weakly-dispersive modes (WDM) are noticed for the first time in this section. In weakly-dispersive zone, the vibration modes are get entrapped into the softest material of the cell, while the resonating material kept vibrationless. Nearly zero group velocities are computed for the propagated wave which leads to negligible dissipation of wave energy. The concept of WDM can be very useful for later studies where energy trapping or nearly zero energy transmission is essential. It is also reported that, introduction of new band gaps and extensive alteration of band widths can be possible by rotating the spiral setup about the direction of propagating wave. Since number of stop band increased extensively by using the spiral resonator setup, it was expected that significantly large and continuous stop band can be created through widening and merging existing neighboring stop bands by rotating the spiral setup. Unfortunately, the expectation isn't fully fulfilled with the spiral rotation. It can be conclude that proposed MMM models are capable to significant number of frequency band gaps, but unable to create very wide and continuous stop bands.

## 2.6 Chapter Summary

Both Split ring metamaterials and Multiple Mass-in-Mass systems are significantly improved models for wave filtration studies in considering the capacity of forming frequency band gaps. Band width can also be improved by using the spiral resonating setup. However, both the models are quite off in achieving the objective of the study by generating very large stop bands. Weakly dispersive phenomenon is observed, which can be useful for future studies where energy trapping or nearly zero transmission is necessary. Since the Stop Band Technique hasn't found a good enough choice for this study, it is essential to adopt the novel Band Pass Technique.

# CHAPTER 3: AEMM MODEL (BAND PASS TECHNIQUE)

Since the Stop Band Technique (SBT) found not good enough for the targeted objective, novel Band Pass Technique (BPT) is adopted. The Band Pass Technique is an opposite method compared to the Stop Band Technique. Principal objective in this chapter is to propose a mechanical model that is capable of passing/actuating only the desired frequencies and stopping/filtering all other available frequencies in the system. Following the objective, in SBT, we aimed to propose a model that can filter all unwanted system frequencies, hence allows to pass through the desired frequencies. On the contrary, in BPT, we intent to develop a model that is only capable of sensing/passing the required frequencies and remain unresponsive for other frequencies, hence filtered automatically.

After rigorous study it has been found that, nature offers similar sort of operation through human hearing system. It is well known that, hearing range of a normal human is 20 Hz to 20 KHz, known as sonic frequency. Human hearing organ can't capture below and beyond the sonic frequency range. This means, human ear can only sense and pass 20 Hz to 20 KHz and isolate all other frequencies exist in nature. In human ear, cochlea is the principal part in selecting sonic frequencies. Since we are inspired from the functionality of the cochlea in modeling our system, it is critical to clearly understand the working principle of human cochlea (Refer chapter 6 for more details).

Here we implemented the concept of hair cell mimicking the functionality using a smart material. As a first trial we first embedded the piezoelectric material inside the acoustoelastic metamaterial for selecting a specific frequency.

To design a bio-inspired band pass sensor/filter it is critical to model a system that is able to perform the principal operations (Perform local resonance; Sense desired frequency and filter all other frequencies in environment; Sense input frequency with some kind of sensory medium and Select frequency spatially) of the basilar membrane (Refer chapter 6). Resonance in a system is a common mechanical phenomenon, however local resonance seems an unusual feature where only a part of the system exhibits resonance characteristic whereas remaining parts stay vibrationless. From our previous study for stop band technique, it has been found that acoustic metamaterial has the ability to introduce local resonance in structure. Hence in this section acoustic metamaterial is considered to investigate whether it can perform all principal operations of human cochlea and can develop a mechanical band pass sensor.

## 3.1 AcoustoElastic MetaMaterial Model

Acousto-elastic metamaterials (AEMM) are traditionally used for filtering acoustic wave using bragg scattering and local resonance. As mentioned earlier, AEMM are typically made as periodic structure where bragg scattering takes place due to the periodicity of the unit AEMM and local resonance it the result of mechanical property mismatch in unit structure. Since local resonance is the targeted phenomenon is this section, hence unit AEMM is studied in developing the band pass sensor. At local resonance frequencies, the frequency bands are almost straight in dispersion curve (Ref.

Figure 2.13), which was termed as weakly dispersive zone (WDZ). In process of filtering acoustic wave, AEMM's are either guide the acoustic energy in other directions (called scattering) or traps the energy inside the structure as local resonance (see Figure 3.1).

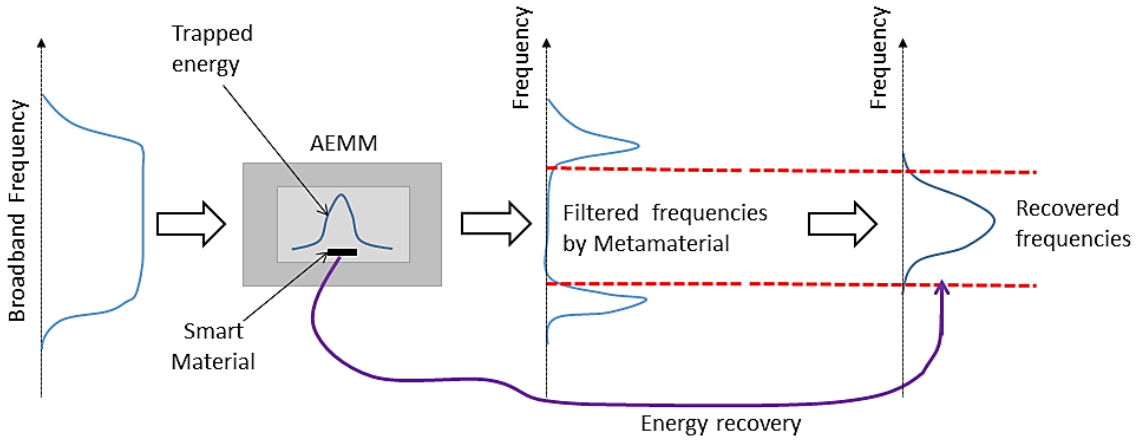


Figure 3.1: Wave filtering using AcoustoElastic MetaMaterial through energy trapping in addition with energy recovering scope using smart material.

Since at local resonance frequencies, wave energy with specific frequency contents is trapped inside the structure as dynamic strain energy, it is hypothesized that using a smart material (converts mechanical vibration to electrical signal) the trapped frequencies can be recovered. However it is essential to have a proper design of the AEMM to place smart materials and recover the trapped frequencies. To illustrate the concept, a three-dimensional unit-cell AEMM model is considered as shown in Figure 3.2. The unit cell is a rectangular ~36.5 mm X ~36.5 mm X ~14 mm prism consisting of a rectangular aluminum frame with a cylindrical matrix inside. A spherical heavy core made of lead (Pb) is encapsulated inside the matrix. Diameter of the core mass ($D_m$) and the matrix ($D_M$) are ~12.5 mm and ~25 mm, respectively. Material properties of the unit cell is listed in Table 3.1.

Table 3.1: Properties of the components enclosed in the AEMM unit cell.

| | Lead | Rubber | Aluminum |
|---|---|---|---|
| Young's Modulus (Pa) | 13.5e9 | 0.9942e6 | 68.9e9 |
| Density (kg/m$^3$) | 11340 | 1600 | 2700 |
| Poisson's Ratio | 0.435 | 0.47 | 0.33 |

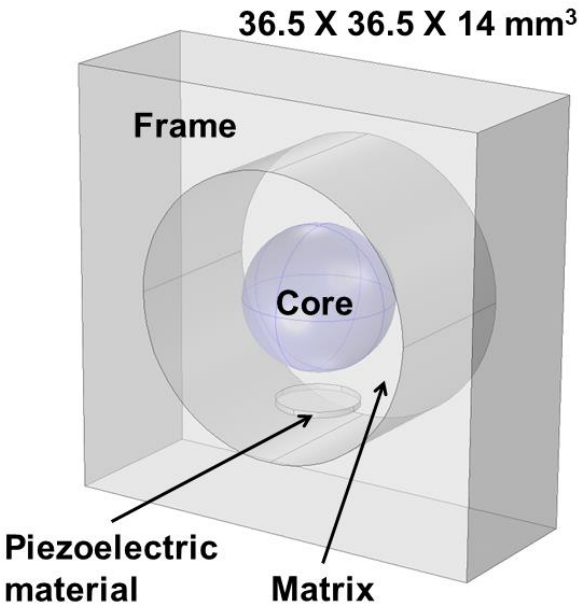


Figure 3.2: Unit cell AcoustoElastic Metamaterial (AEMM)

It is hypothesized that, at local resonance frequencies wave energy will trap and stay as dynamic strain energy inside the soft constituent (Rubber) of the unit cell. Hence a piezoelectric material (PZT 5H) is placed in between the lead core and aluminum inside wall to convert trapped strain energy into electrical potential. Analytical, numerical and experimental studies are performed to validate the hypothesis.

## 3.2 Analytical Development

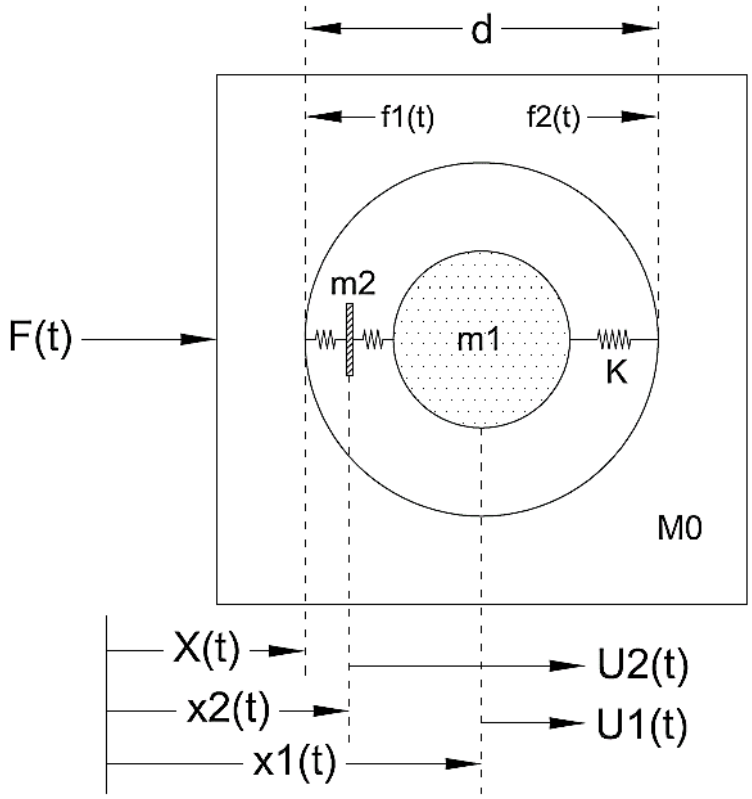


Figure 3.3: Spring-mass representation of unit cell AEMM

The unit cell AEMM (Ref. Figure 3.2) can be represented as spring-mass system as shown in Figure 3.3. For computational simplicity, the analytical model is developed for 2-dimensional domain. Considering the outer frame (Aluminum) is rigid with a cylindrical void of diameter d. The void contains a spherical ball of mass $m_1$ and radius $r_1$. Another mass $m_2$ (piezoelectric material) is placed in between the mass $m_1$ and inner wall of the outer frame. Since it is assumed that the cylindrical void is filled with soft rubber, hence it can be represented as an elastic spring with spring constant K. A force F(t), where t is the time, is applied on the left side of the rigid frame.

**Effective Dynamic Mass Calculation**

Let us consider a balance of linear momentum in the composite system. Assume that all quantities depend harmonically on time and that a one-dimensional approximation of the problem is adequate. The spring attached to the left wall of the cavity exerts a force $f_1(t)$ on the wall while the spring attached to the right wall exerts a force of $f_2(t)$ on the wall. Then the internal and external forces acting on the unit cell of the bar are given by

$$F(t) = \mathrm{Re}\left(\hat{F}e^{-i\omega t}\right)$$

$$f_1(t) = \mathrm{Re}\left(\widehat{f_1}e^{-i\omega t}\right)$$

$$f_2(t) = \mathrm{Re}\left(\widehat{f_2}e^{-i\omega t}\right)$$

where the amplitudes $\hat{F}$, $\widehat{f_1}$ and $\widehat{f_2}$ are generally complex. Let the time-dependent position of the left side of cavity is given by

$$X(t) = X_0 + U_0(t) = X_0 + \mathrm{Re}\left(\widehat{U_0}e^{-i\omega t}\right)$$

where $X_0$ is the initial position and $\widehat{U_0}$ is the complex valued displacement of the bar. Then the velocity of the rigid bar is

$$V_0(t) = \frac{dX}{dt} = \mathrm{Re}\left(-i\omega\widehat{U_0}e^{-i\omega t}\right) = \mathrm{Re}\left(\widehat{V_0}e^{-i\omega t}\right)$$

where $\widehat{V_0} = -i\omega\widehat{U_0}$. Assume that the rigid frame has mass $M_0$. Therefore, the linear momentum of the rigid bar is

$$P_{\mathrm{frame}} = M_0V_0(t) = M_0\mathrm{Re}\left(\widehat{V_0}e^{-i\omega t}\right)$$

If $U_1(t)$ is the relative displacement of the ball, the position of the ball is given by

$$x_1(t) = X(t) + \frac{d}{2} + U_1(t) = X_0 + U_0(t) + \frac{d}{2} + U_1(t)$$

$$x_1(t) = X_0 + \frac{d}{2} + [U_0(t) + U_1(t)] = X_0 + \frac{d}{2} + u_1(t)$$

where $u_1(t) = U_0(t) + U_1(t)$. For harmonic motions, we can write

$$x_1(t) = X_0 + \frac{d}{2} + \mathrm{Re}\left(\widehat{u_1} e^{-i\omega t}\right) \qquad (3.1)$$

where $\widehat{u_1}$ is the complex valued displacement of the core ball. Therefore, the velocity of the ball is

$$v_1(t) = \frac{dx_1}{dt} = \mathrm{Re}\left(-i\omega\widehat{u_1} e^{-i\omega t}\right) = \mathrm{Re}\left(\widehat{v_1} e^{-i\omega t}\right)$$

where $\widehat{v_1} = -i\omega\widehat{u_1}$. The linear momentum of the ball is given by

$$P_{\mathrm{ball}}(t) = m_1 v_1(t) = m_1 \mathrm{Re}\left(\widehat{v_1} e^{-i\omega t}\right)$$

If $U_2(t)$ is the relative displacement of the piezoelectric material, the position of the piezoelectric material is given by

$$x_2(t) = X(t) + \frac{d}{4} + U_2(t) = X_0 + U_0(t) + \frac{d}{4} + U_2(t)$$

$$x_2(t) = X_0 + \frac{d}{4} + [U_0(t) + U_2(t)] = X_0 + \frac{d}{2} + u_2(t)$$

where $u_2(t) = U_0(t) + U_2(t)$. For harmonic motions, we can write

$$x_2(t) = X_0 + \frac{d}{4} + \mathrm{Re}\left(\widehat{u_2} e^{-i\omega t}\right) \qquad (3.2)$$

where $\widehat{u_2}$ is the complex valued displacement of the piezoelectric material. Therefore, the velocity of the piezoelectric material is

$$v_2(t) = \frac{dx_2}{dt} = \mathrm{Re}\left(-i\omega\widehat{u_2} e^{-i\omega t}\right) = \mathrm{Re}\left(\widehat{v_2} e^{-i\omega t}\right)$$

where $\widehat{v_2} = -i\omega\widehat{u_2}$. The linear momentum of the piezoelectric material is given by

$$P_P(t) = m_2 v_2(t) = m_2 \mathrm{Re}\left(\widehat{v_2} e^{-i\omega t}\right)$$

Then the total linear momentum of the system is

$$P(t) = P_{\mathrm{frame}} + P_{\mathrm{ball}} + P_P$$

$$P(t) = M_0 \mathrm{Re}\left(\widehat{V_0} e^{-i\omega t}\right) + m_1 \mathrm{Re}\left(\widehat{v_1} e^{-i\omega t}\right) + m_2 \mathrm{Re}\left(\widehat{v_2} e^{-i\omega t}\right)$$

$$P(t) = \mathrm{Re}\left(\widehat{P} e^{-i\omega t}\right)$$

where $\widehat{P} = M_0\widehat{V_0} + m_1\widehat{v_1} + m_2\widehat{v_2}$. From Newton's second law, the applied force equals the rate of change of linear momentum,

$$F(t) = \frac{d}{dt}[P(t)]$$

Hence, considering harmonic forces, we have

$$\mathrm{Re}\left(\hat{F}e^{-i\omega t}\right) = \frac{d}{dt}\left[\mathrm{Re}\left(\hat{P}e^{-i\omega t}\right)\right]$$

$$\hat{F} = -i\omega\left(M_0\widehat{V_0} + m_1\widehat{v_1} + m_2\widehat{v_2}\right)$$

Let us now consider the free-body diagram of springs inside the cavity those are connected to the piezoelectric material as shown in Figure 3.4.

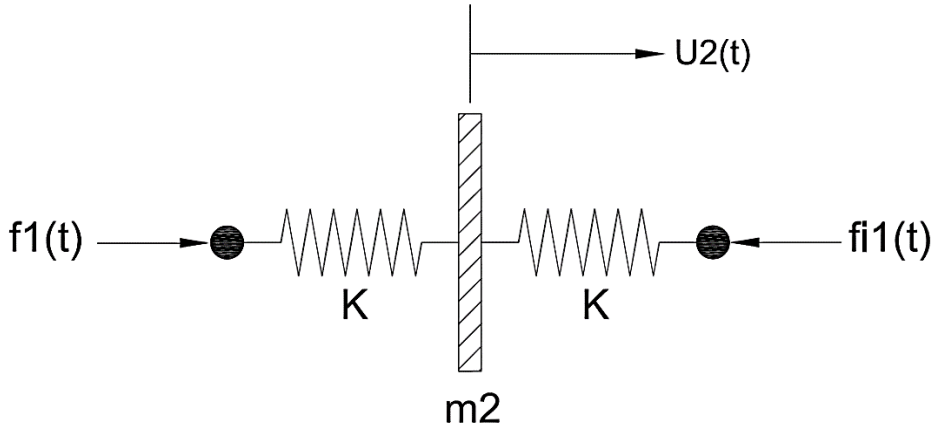


Figure 3.4: Free-body diagram for the spring-mass system those are connected to the piezoelectric material

Hooke's law for each spring implies that

$$-f_1(t) = KU_2(t) = f_{i_1}(t) \qquad (3.3)$$

where K is the complex spring constant. Recall that the displacement of the spring is given by

$$u_2(t) = U_0(t) + U_2(t)$$

$$U_2(t) = u_2(t) - U_0(t) = \mathrm{Re}\left(\widehat{u_2}e^{-i\omega t}\right) - \mathrm{Re}\left(\widehat{U_0}e^{-i\omega t}\right) \qquad (3.4)$$

Using equation (3.4) in (3.3)

$$-\mathrm{Re}\left(\widehat{f_1}e^{-i\omega t}\right) = K\left[\mathrm{Re}\left(\widehat{u_2}e^{-i\omega t}\right) - \mathrm{Re}\left(\widehat{U_0}e^{-i\omega t}\right)\right] = \mathrm{Re}\left(\widehat{f_{i_1}}e^{-i\omega t}\right)$$

$$\widehat{f_1} = -\widehat{f_{i_1}} = K\left(\widehat{U_0} - \widehat{u_2}\right) \qquad (3.5)$$

Next considering the free-body diagram of the spring-mass system (see Figure 3.4 and equation (3.2)), the balance of linear momentum for the spring-mass system implies that

$$f_1(t) - f_{i_1}(t) = m_2\frac{d^2x_2}{dt^2} = m_2\mathrm{Re}\left(-\omega^2\widehat{u_2}e^{-i\omega t}\right)$$

$$\mathrm{Re}\left(\widehat{f_1}e^{-i\omega t}\right) - \mathrm{Re}\left(\widehat{f_{i_1}}e^{-i\omega t}\right) = m_2\mathrm{Re}\left(-\omega^2\widehat{u_2}e^{-i\omega t}\right)$$

$$\widehat{f_1} - \widehat{f_{i_1}} = -m_2\omega^2\widehat{u_2} \qquad (3.6)$$

Using equation (3.5) and (3.6)

$$-m_2\omega^2\widehat{u_2} = 2K\left(\widehat{U_0} - \widehat{u_2}\right)$$

$$\widehat{u_2} = \frac{2K}{2K - m_2\omega^2}\widehat{U_0} \qquad (3.7)$$

Now consider the free-body diagram of springs inside the cavity those are connected to the ball as shown in Figure 3.5.

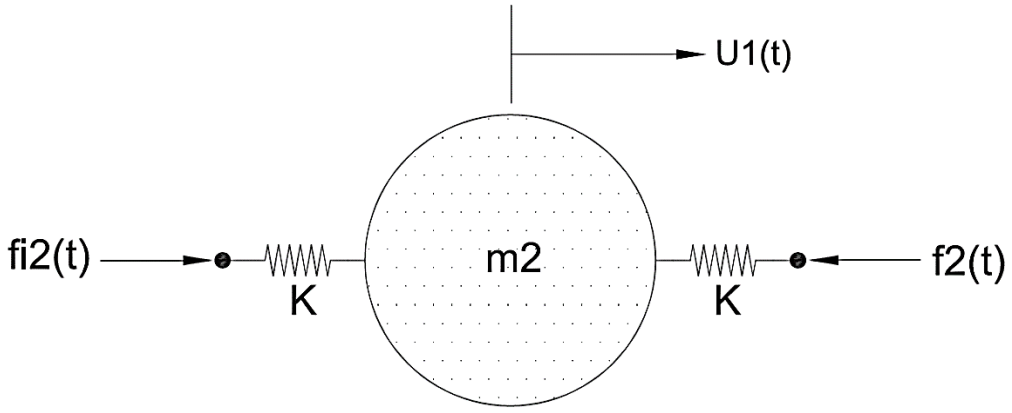


Figure 3.5: Free-body diagram for the spring-mass system those are connected to the ball

Using Hooke's law,

$$-f_{i_2}(t) = KU_1(t) = f_2(t) \qquad (3.8)$$

Recalling the displacement of the spring as,

$$u_1(t) = U_0(t) + U_1(t)$$

$$U_1(t) = u_1(t) - U_0(t) = Re\left(\widehat{u_1}e^{-i\omega t}\right) - Re\left(\widehat{U_0}e^{-i\omega t}\right) \qquad (3.9)$$

Using equation (3.9) in (3.8)

$$\widehat{f_{i_2}} = -\widehat{f_2} = K\left(\widehat{U_0} - \widehat{u_1}\right) \qquad (3.10)$$

Now considering the free-body diagram of the spring-mass system (see Figure 3.5 and equation (3.1)), the balance of linear momentum for the spring-mass system implies that

$$f_{i_2}(t) - f_2(t) = m_1 \frac{d^2 x_1}{dt^2} = m_1 \mathrm{Re}\left(-\omega^2 \widehat{u_1} e^{-i\omega t}\right)$$

$$\widehat{f_{i_2}} - \widehat{f_2} = -m_1 \omega^2 \widehat{u_1} \qquad (3.11)$$

Using equation (3.10) and (3.11)

$$-m_1 \omega^2 \widehat{u_1} = 2K\left(\widehat{U_0} - \widehat{u_1}\right)$$

$$\widehat{u_1} = \frac{2K}{2K - m_1 \omega^2} \widehat{U_0} \qquad (3.12)$$

Now, $\widehat{V_0} = -i\omega \widehat{U_0}$, $\widehat{v_1} = -i\omega \widehat{u_1}$ and $\widehat{v_2} = -i\omega \widehat{u_2}$. Hence,

$$\widehat{v_1} = \frac{2K}{2K - m_1 \omega^2} \widehat{V_0} \qquad (3.13)$$

$$\widehat{v_2} = \frac{2K}{2K - m_2 \omega^2} \widehat{V_0} \qquad (3.14)$$

Recalling the linear momentum amplitude of the system,

$$\widehat{P} = M_0 \widehat{V_0} + m_1 \widehat{v_1} + m_2 \widehat{v_2} \qquad (3.15)$$

Plugging equations (3.13) and (3.14) in (3.15)

$$\widehat{P} = M_0 \widehat{V_0} + m_1 \frac{2K}{2K - m_1 \omega^2} \widehat{V_0} + m_2 \frac{2K}{2K - m_2 \omega^2} \widehat{V_0}$$

$$\widehat{P} = \left[M_0 + \frac{2Km_1}{2K - m_1 \omega^2} + \frac{2Km_2}{2K - m_2 \omega^2}\right] \widehat{V_0} = M_{\mathrm{eff}} \widehat{V_0}$$

where $M_{eff}$ is the effective dynamic mass of the system and given by

$$\mathbf{M_{eff}(\omega) = M_0 + \frac{2Km_1}{2K - m_1\omega^2} + \frac{2Km_2}{2K - m_2\omega^2}}$$

**Voltage Output Calculation**

It is hypothesized that upon dynamic behavior of the constituents of the system, piezoelectric material will experience compressive force along its thickness direction. Referring Figure 3.4, total compressive force acting on piezoelectric material,

$$f(t) = f_1(t) + f_{i_1}(t) = f_1(t) + f_{i_2}(t) \qquad (\text{since } f_{i_1} = f_{i_1})$$

Using equations (3.5) and (3.10)

$$f(t) = K[U_0(t) - u_2(t)] + K[U_0(t) - u_1(t)]$$

$$f(t) = K[2U_0(t) - u_1(t) - u_2(t)]$$

Considering harmonic motion

$$\hat{f} = K\left[2\widehat{U_0} - \widehat{u_1} - \widehat{u_2}\right] \qquad (3.16)$$

Using (3.7) and (3.12) in (3.16)

$$\hat{f} = K\left[2\widehat{U_0} - \frac{2K}{2K - m_1\omega^2}\widehat{U_0} - \frac{2K}{2K - m_2\omega^2}\widehat{U_0}\right]$$

$$\hat{f} = \widehat{U_0}\left[2K - \frac{2K^2}{2K - m_1\omega^2} - \frac{2K^2}{2K - m_2\omega^2}\right]$$

Stress on piezoelectric material,

$$T^P = \frac{\hat{f}}{A^P} = \frac{\hat{f}}{\pi r_2^2} = \frac{\widehat{U_0}}{\pi r_2^2}\left[2K - \frac{2K^2}{2K - m_1\omega^2} - \frac{2K^2}{2K - m_2\omega^2}\right]$$

Assuming,

$$M_e = 2K - \frac{2K^2}{2K - m_1\omega^2} - \frac{2K^2}{2K - m_2\omega^2}$$

$$T^P = \frac{\widehat{U_0}M_e}{\pi r_2^2} \qquad (3.17)$$

where $A^P$ and $r_2$ are the cross-sectional area and radius of the piezoelectric material along thickness axis.

Electric charge density displacement of the piezoelectric material is given as

$$\{D\} = [d]\{T^P\} + [\varepsilon^P]\{E\}$$

where $\varepsilon^P$, d and E are defined as permittivity, piezoelectric charge constant and electric field strength.

Assuming the piezoelectric material is only polarized in thickness direction and neglecting all other effects, piezoelectric charge is given as

$$D_3 = d_{33}T_3^P + \varepsilon_{33}^P E_3 \qquad (3.18)$$

Electric field strength in thickness mode,

$$E_3 = \frac{V(t)}{h} \qquad (3.19)$$

where $h$ is the thickness and $V(t)$ is defined as the electric potential generated across the piezoelectric material.

Using equations (3.17) and (3.19) in (3.18)

$$D_3 = d_{33}\frac{U_0(t)M_e}{\pi r_2^2} + \varepsilon_{33}^P \frac{V(t)}{h}$$

Electric charge density,

$$q(t) = \int \mathbf{D}\cdot\mathbf{n}\, dA$$

$$q(t) = \int_0^{r_2}\int_0^{2\pi} D_3\, dr\, d\theta$$

$$q(t) = \int_0^{r_2}\int_0^{2\pi}\left[d_{33}\frac{U_0(t)M_e}{\pi r_2^2} + \varepsilon_{33}^P\frac{V(t)}{h}\right] dr\, d\theta$$

$$q(t) = -\frac{2d_{33}M_e}{r_2}U_0(t) + \frac{2\pi r_2\varepsilon_{33}^P}{h}V(t)$$

$$q(t) = C_1U_0(t) + C_2V(t)$$

Assuming, $C_1 = -\frac{2d_{33}M_e}{r_2}$ and $C_2 = \frac{2\pi r_2\varepsilon_{33}^P}{h}$

Electric current generated through piezoelectric material is given by

$$I(t) = \frac{dq(t)}{dt} = C_1 \frac{dU_0(t)}{dt} + C_2 \frac{dV(t)}{dt}$$

Voltage generated across the resistive load $R_0$,

$$V(t) = R_0 I(t) = R_0 C_1 \frac{dU_0(t)}{dt} + R_0 C_2 \frac{dV(t)}{dt}$$

Considering harmonic excitation,

$$V_0 = i\omega R_0 C_1 U_0 + i\omega R_0 C_2 V_0$$

$$\mathbf{V_0(\omega) = \frac{i\omega C_1 R_0 U_0}{1 - i\omega C_2 R_0}}$$

Higher acceleration is capable of harvesting higher electric potential [78], thus the output response is presented in terms of Frequency Response Function (FRF) to normalize such effect.

$$\mathbf{FRF = \left| \frac{V_0(\omega)}{\omega^2} \right|}$$

**Analytical Dynamic Response**

In this study, piezoelectric material PZT 5H is considered as energy conversion medium. Lead and Aluminum 6061 material properties are counted for core mass and outer frame. Necessary material properties for the analytical computation are listed in Table 3.2.

.

Table 3.2: Required material properties for analytical computation

| Parameter | Value | Unit |
|---|---|---|
| K | 0.9986e3 | N/m |
| $m_1$ | 11.423 | gm |
| $m_2$ | 0.183 | gm |
| $M_0$ | 31.4 | gm |
| $r_2$ | 3.4925 | mm |
| h | 0.508 | mm |
| $d_{33}$ | 593 | pC/N |
| $\varepsilon_{33}^{P}$ | 3400*8.854 | pF/m |
| $R_0$ | 10 | KΩ |
| $U_0$ | 1 | mm |

Dynamic effective mass against excitation frequency is plotted in Figure 3.6b. Dynamic effective mass of the system is found to be negative at ~0.42 KHz and ~3.3 KHz. It has been proven that, the effective mass becomes negative near the local resonance frequency of the internal masses[79]. This also implies[58] that wave energy is trapped inside the soft matrix and cannot be transmitted through the structure[27, 80]. Consequently, the embedded wafer is stressed and maximum FRF is obtained at the local resonance frequencies (Figure 3.6a). Two dominant peaks are observed, where the first peak results from the local resonance of the core mass and the second peak is due to the resonance of the wafer itself.

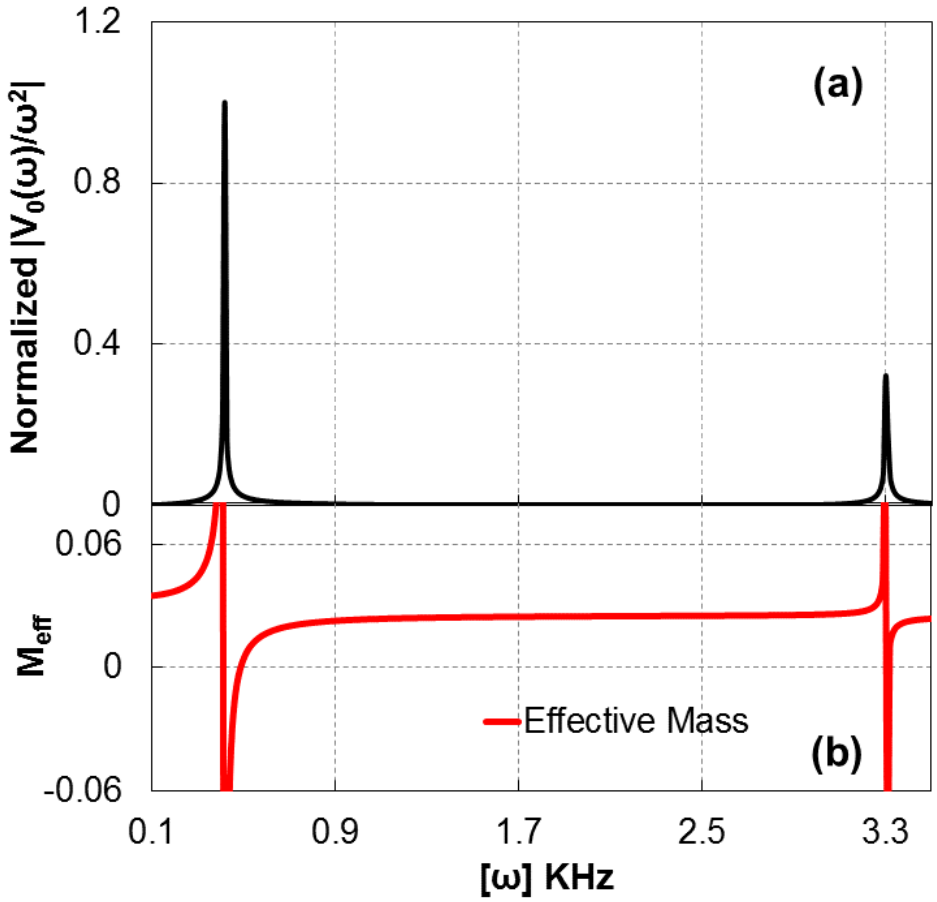


Figure 3.6: Analytically obtained dynamic (a) FRF and (b) Effective mass

### 3.3 Numerical Implementation

Analytical study suggests that using the unit cell AEMM with proposed material combinations and PZT placement, local resonance takes place at a distinct frequencies. Hence, unique frequencies has been sensed using the piezoelectric material with maximum electric potential at corresponding frequencies. Alternatively, other frequencies in the study remain unsensed (or filtered) with negligible electric potential. The above outcome strongly supports the operating principal of our targeted mechanical band pass sensor/filter. To understand and verify the dynamics behind the maximum voltage output at local

resonance frequencies, a numerical study is performed with identical unit cell AEMM. Note that, in analytical study, for computational simplicity 1-dimensional study was performed, however the numerical study is performed in 3-dimensional domain.

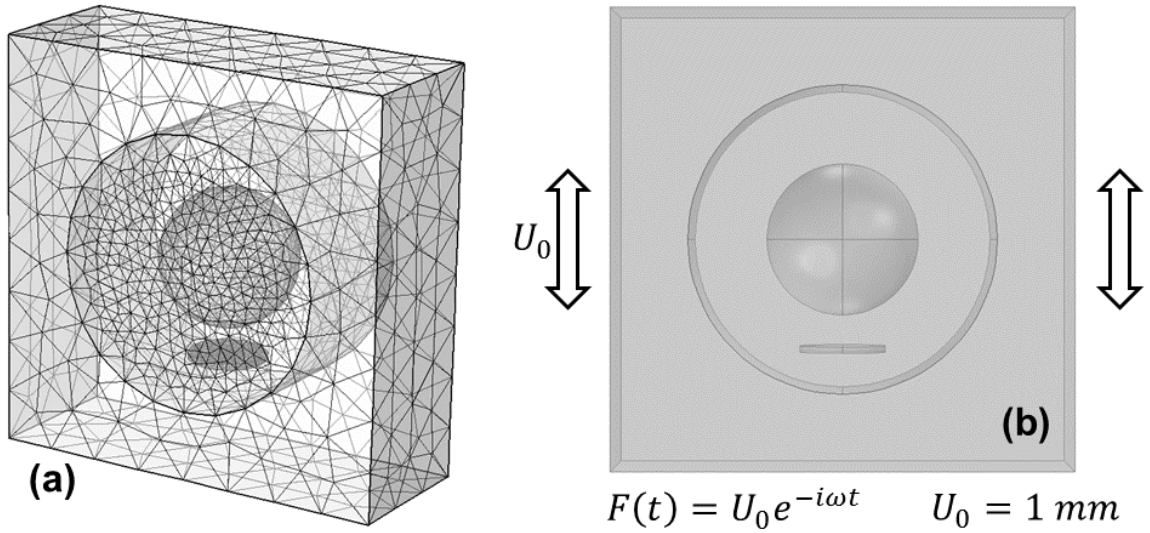


Figure 3.7: (a) Sample meshing of the unit cell AEMM (b) Harmonic excitation configuration

A frequency domain analysis is performed using computational tool COMSOL multiphysics. 4-noded tetrahedral elements are used with maximum element size is maintained 1/4 times of the wavelength of the respective constituent at the highest frequency level of the study. A sample meshing configuration of the unit AEMM is shown in Figure 3.7a. Unit displacement (1 mm) harmonic excitation is applied on two opposite sides of the unit cell (see Figure 3.7b) to find the dynamic response of the cell constituents at different frequencies.

Numerical computation supports the analytical argument with maximum FRF at ~0.43 KHz and ~3.31 KHz (see Figure 3.8). Despite the fact that the numerical analysis is performed using a 3-dimensional (3D) model and the analytical study is performed using

a 1-dimensional (1D) spring-mass model, resonance frequencies are in very close agreement. On both occasions (resonance of the core mass and the wafer) the piezoelectric material encounters high compressive stress and records maximum electric potential (see Figure 3.9).

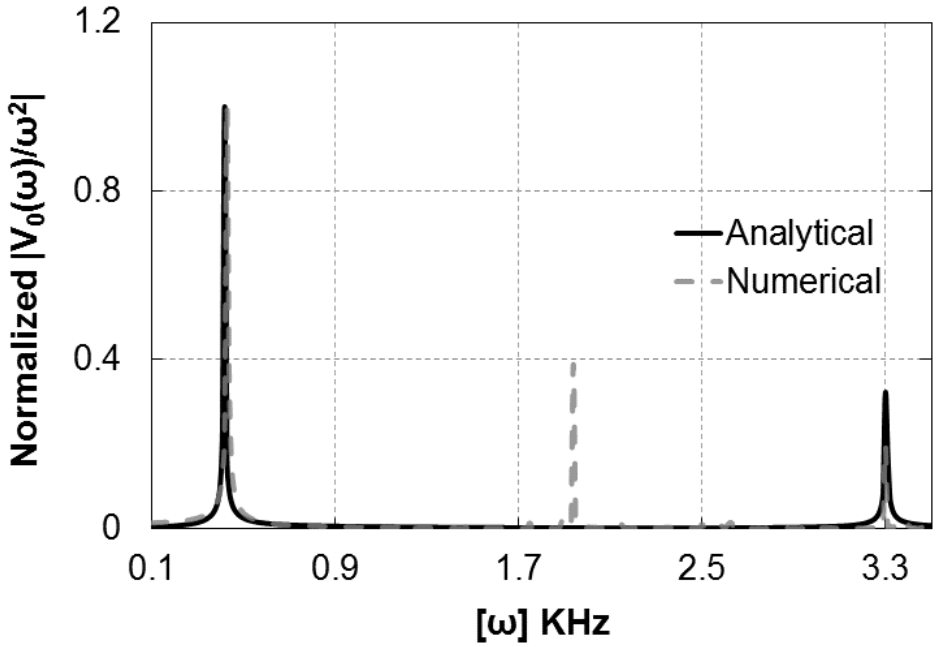


Figure 3.8: Numerical and Analytical FRF response comparison of the unit AEMM at different frequencies

At 0.43 KHz, the lead resonator is exhibiting local resonance and moving towards the piezoelectric material, following its thickness axis, which results compressive stress on PZT material. At 3.31 KHz, core mass is stationary, while PZT material is trying to resonate. Resistance force encountered by the PZT from surrounding the rubber during its resonance movement causes the FRF pick at corresponding frequency. On the contrary, two different cases of low FRF at off-resonance frequencies (e.g. ~0.98 KHz & ~1.47 KHz) are shown in Figure 3.9c & Figure 3.9d.

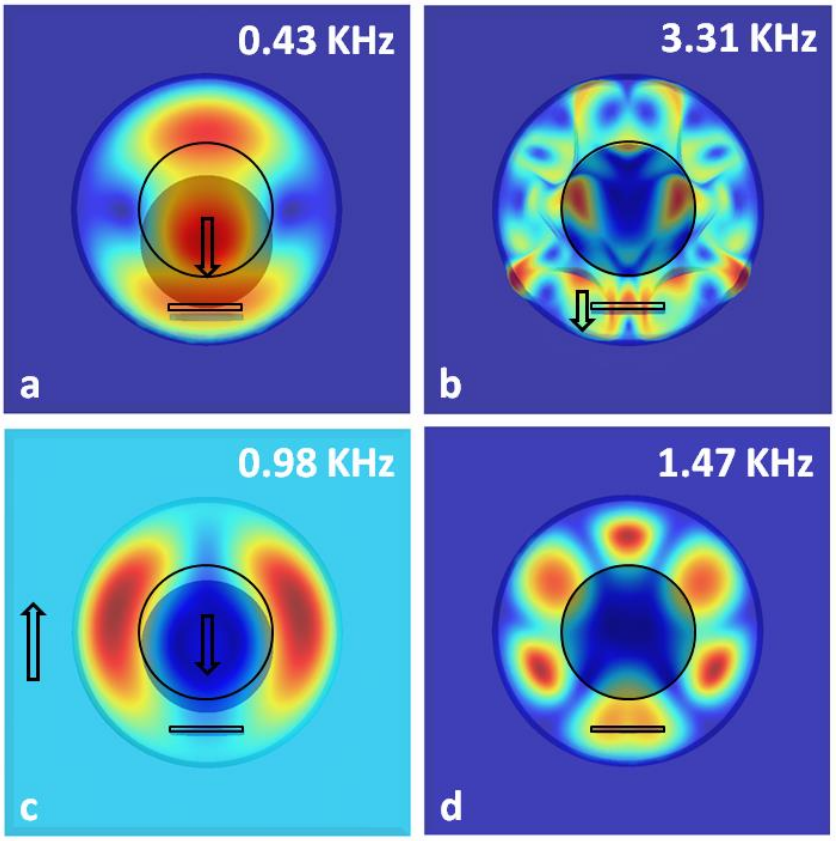


Figure 3.9: Displacement patterns in a unit cell at (a) ~ 0.43 KHz (b) ~ 3.31 KHz (c) ~ 0.98 KHz and (d) ~ 1.47 KHz.

At ~0.98 KHz, the core mass moved towards the wafer but the matrix flows along the frame. Hence, the matrix adjacent to the wafer has a tendency to stream toward fringe matrix and distance between two masses is decreased. Although there is a relative movement, the lead ball is unable to create considerable stress on the wafer and negligible power is harvested. At ~1.47 KHz, wave energy stays trapped inside the matrix as dynamic oscillation, while the core and the wafer are stationary. This phenomenon also results negligible FRF response.

An additional possibility of sensing frequency at ~1.94 KHz (Figure 3.8) was found, which is not intuitive and was also not observed from the 1-D analytical model. In

this study, it is commented that the consequence of matrix splashing, contained between the core mass and the wafer, the modal inflection between ~1.94 KHz and ~1.95 KHz causes the electric potential (Figure 3.10). Oscillation of the matrix between the wafer and the heavy mass which is stationary causes the wafer to deform and produces electric potential.

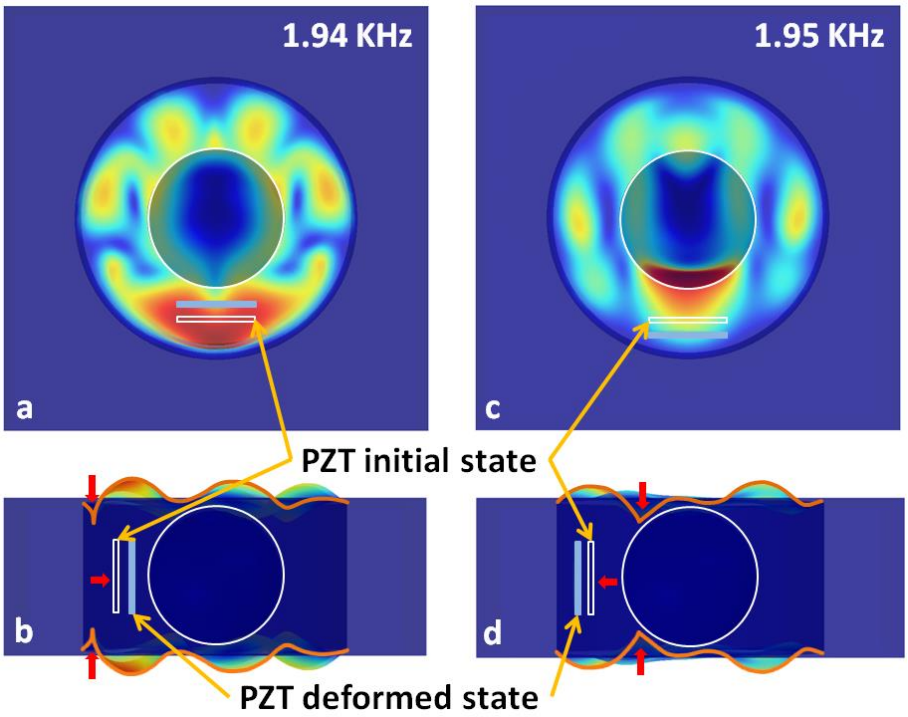


Figure 3.10: Matrix splashing phenomenon in unit cell model at the transition between ~ 1.94 KHz and ~ 1.95 KHz. Displacement plots at ~ 1.94 KHz (a) front view (b) side view with surface outlines. Displacement plots at ~ 1.95 KHz (c) front view (d) side view with

In numerical study unit displacement is applied as excitation input to evaluate the dynamic response of AEMM, however in practical case acoustic wave typically act as pressure wave on AEMM structure. Displacement excitation technique is adopted for experimental validation simplicity, however it is essential to demonstrate whether the displacement mechanism is comparable to pressure wave mechanism or not.

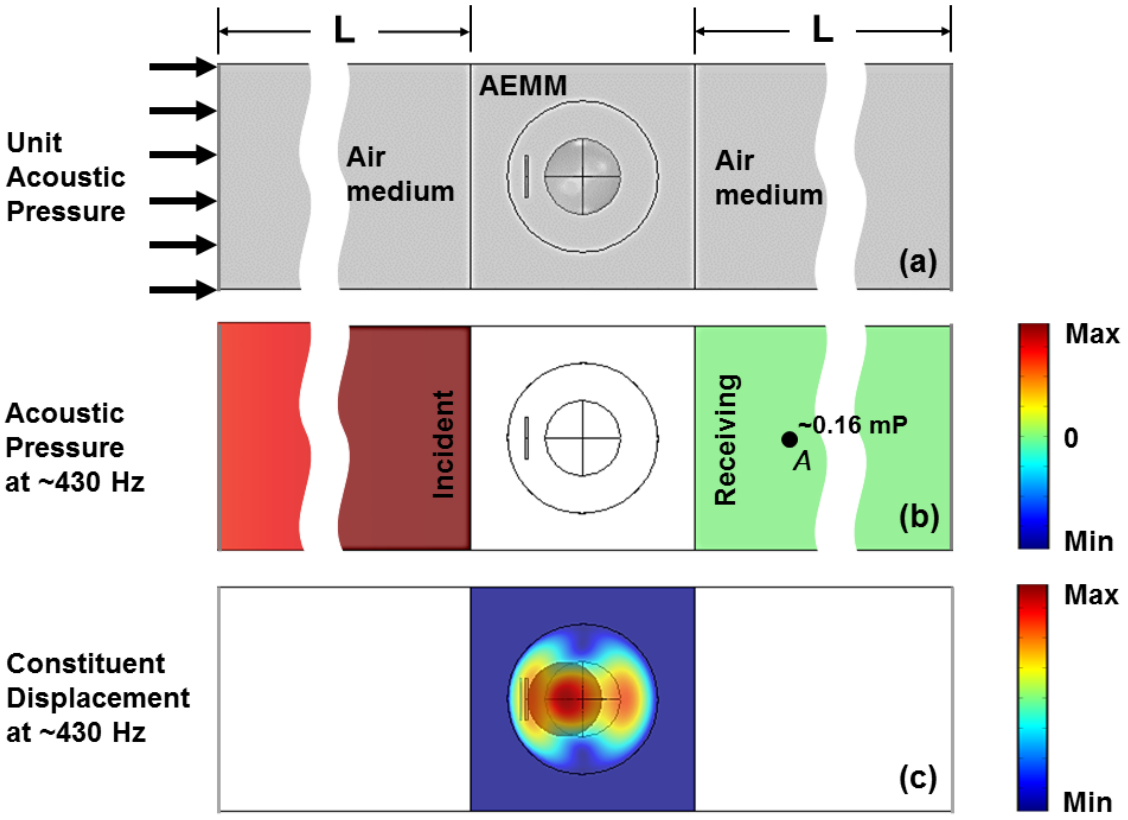


Figure 3.11: Dynamic behavior of the unit AEMM upon acoustic wave incidence. (a) Study setup with acoustic pressure input. (b) Acoustic pressure in air medium at ~430 Hz (c) Displacement modes of the constituents of the AEMM at ~430 Hz.

Hence a 3-dimensional numerical study (frequency domain) is performed applying unit pressure as the input load. To consider the input load as acoustic pressure a long air medium of length L is used in both input and receiving ends of the AEMM (see Figure 3.11). L is defined as, twice of the wavelength of the minimum studied frequency in the medium (air). Figure 3.11c shows the dynamic response of the unit cell upon unit acoustic pressure. It has been found that upon acoustic pressure, the AEMM unit cell encounters similar vibration modes compared to the displacement excitation mechanism. The resonance mode upon displacement excitation is found at ~ 430 Hz, while same displacement mode is observed at exactly the same the frequency (~ 430 Hz) with the

acoustic pressure input. Hence it can be conclude that both displacement and pressure wave mechanism provides identical dynamic response.

The study also confirms the acoustic wave filtration ability of the AEMM (Ref. Figure 3.11b). Upon any applied pressure as shown in Figure 3.11a, the AEMM structure supposed to move along the pressure of incidence, since the cell is considered free to move in all directions. However at local resonance frequency (~ 430 Hz), the structure seems almost unmoved due to the formation of negative mechanical properties at corresponding frequency (ref Figure 3.6). Such negative properties (e.g. effective mass) helped the structure to act differently than the established laws of motion and remain in position, which results very low pressure amplitude (~ 0.16 mP) in receiving end of the AEMM (Ref. Figure 3.11b). Pressure amplitude is measured at an arbitrary point 'A' in the receiving end. To further confirm the wave filtration ability of the AEMM, response at two off-resonance frequencies are investigated. At both ~340 Hz and ~480 Hz, the unit cell is exhibiting positive movement along the direction of loading (Ref. Figure 3.12(a-b)) and an acoustic pressure of ~9.57 mP and ~30.6 mP is recorded at point 'A' at corresponding frequencies, respectively (see Figure 3.12(c-d)). Note that, acoustic pressure amplitude at point 'A' at the off-resonance frequencies (~340 Hz and ~480 Hz) are ~60 and ~190, respectively, times higher than the amplitude recorded at the resonance frequency (~430 Hz). Significantly higher acoustic pressure amplitude is recorded at ~480 Hz because of the higher structural displacement amplitude at the corresponding frequency.

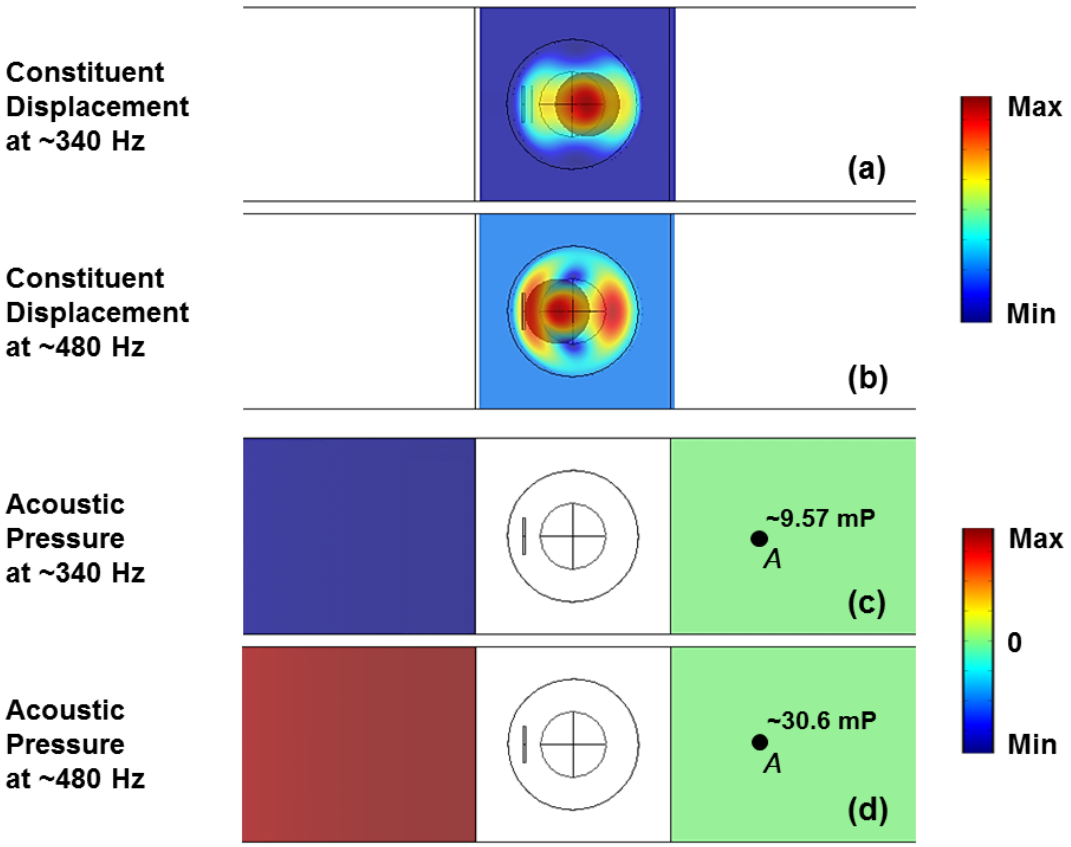


Figure 3.12: (a-b) Acoustic pressure and (c-d) cell displacement response at two off-resonance frequencies, 340 Hz and 480 Hz.

## 3.4 Experimental Approach

**Fabrication of the Model**

Both analytical and numerical approaches are in very close agreement concerning the proposal of sensing specific frequencies using unit cell AEMM. However, since the work is targeted for industrial applications, it is essential to validate the hypothesis experimentally. Hence, identical (compared with analytical and numerical) unit cell AEMM is fabricated in iMAPS (Integrated Material Assessment and Predictive Simulation) and Materials laboratory at Department of Mechanical Engineering, USC.

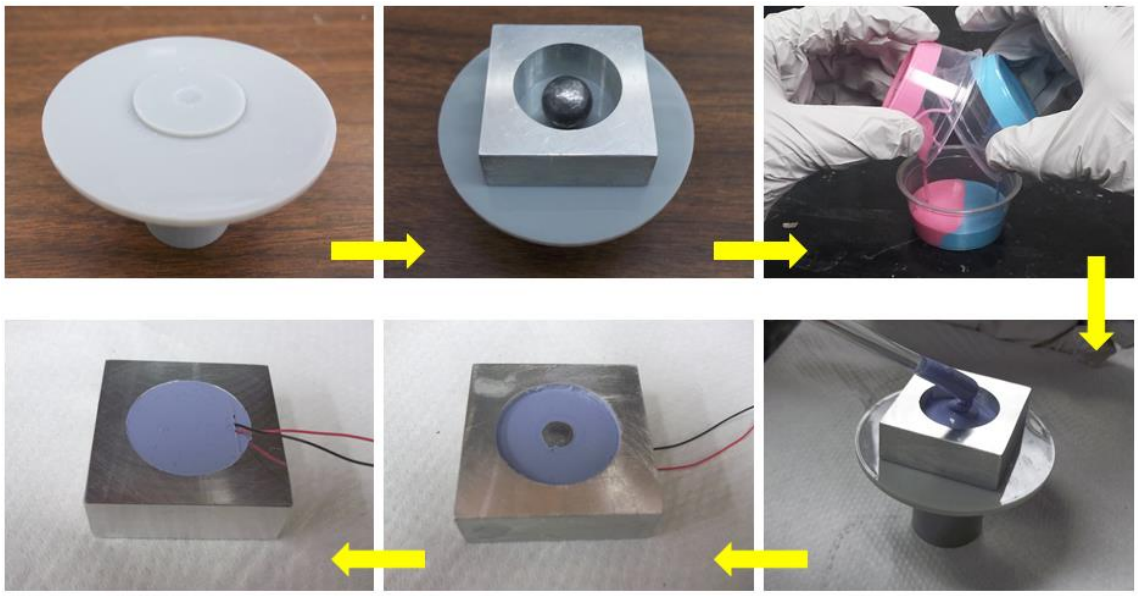

Figure 3.13: Fabrication steps of unit cell metamaterial. (a) Fabrication setup (b) Liquid rubber placement (c) Fabricated final form with embedded piezoelectric sensors to capture the vibration in the rubber only.

Machined Aluminum 6061 is considered as the frame structure with a cylindrical hole to place the rubber and lead components. Since lead ball's diameter is slightly lower than the thickness of aluminum block and it is required to place the ball at the middle (concerning all three dimensions) of the aluminum cavity, a cylindrical support is designed and fabricated using 3D printing technology (see Figure 3.13). The cylindrical support consist of three parts (Insider, Base and Handle) where diameter of the Insider portion is exactly same as the diameter of the aluminum hole. A small arc indentation is considered at the middle of the Insider, such that it can hold the lead ball at the middle. The Insider goes inside of the aluminum cavity and its dimension is set to support the lead core at the middle of the structure with high precision. Diameter of the Base is slightly higher than the width of the aluminum block, so that it can carry the whole structure.

The fabrication process is divided into two steps. First, the lead core is placed inside the middle of the aluminum block with the help of cylindrical support. A liquid rubber (OOMOO 300, contains two parts, mixed strategically for homogeneous strength) is then used to fill the cavity in aluminum block. Since it is necessary to sense / transfer signal from rubber component, a piezoelectric disk (with soldered wire) is fully submerged into the liquid rubber in such a way that it matches the identical orientation compared to the numerical or analytical study.

Usual rubber curing time is 6 hours. However, it is required to start the second step of fabrication at around 3-4 hours after the first step. During the initial steps, cylindrical support was used to hold the lead ball at the middle. Hence, an empty space has opened at the bottom of the structure after removing the cylindrical support. In the second step, the new empty space is filled with the rubber following the same procedure described above. Since it is required to have a good bonding between the rubbers, the second step is started before the full curing time of the rubber.

**Testing and Response from unit cell AEMM model**

A Vibration Exciter (type 4809, from B & K Instruments) is used in testing the harmonic response of the fabricated metamaterial. The exciter is capable of providing controlled vertical displacement excitation. It is controlled through a Sine-Random Generator (type 1024) and Power Amplifier (type 2706) from Bruel & Kjaer. An aluminum support is manufactured to hold the metamaterial system in the vibration exciter. Schematic and actual experimental setup of the AEMM model in shown in Figure 3.14. The test job is clamped in two opposite sides and a simple harmonic displacement excitation (identical

with simulation input) is applied using the Sine-Random Generator (SRG). A frequency sweep operation is not available in our used SRG, however, it is only capable of generating a single frequency excitation at a time and excitation frequency can be tuned using the SRG knob. Tuning range of SRG is limited to 20 Hz to 20 KHz. An Oscilloscope (TDS 2004C, Tektronix) is connected to the piezoelectric wafer to recover the trapped energy response from the rubber component.

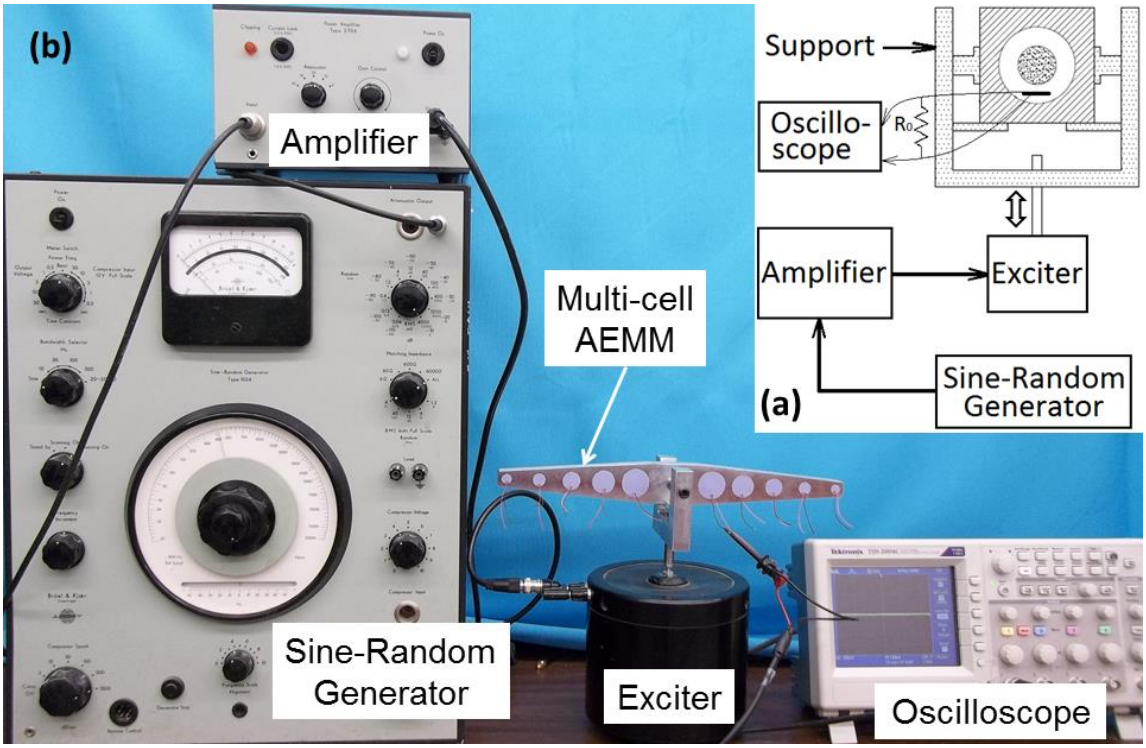


Figure 3.14: (a) Schematic diagram of test setup for unit cell (b) real test setup for multi-cell specimen.

From numerical and analytical analysis it has been noticed that excitation at around ~ 430 Hz and ~ 420 Hz, respectively, local resonance takes place in rubber-lead combination in the unit cell, which seems the best state to sense the signals from rubber through a piezoelectric sensor. The experimental approach reinforces (Figure 3.15) the analytical and numerical results with maximum potential at ~0.37 KHz and ~3.1 KHz. In

our experimental study, possible fabrication error and limitation of the instrumentation may have caused little shifts in the FRF peaks compared to the numerical and analytical solution. The FRF peak at ~1.94 KHz, suggested by the numerical computation is weakly observed in the experimental power output. Again such mismatch could be the result of imperfect alignment of the piezoelectric wafer.

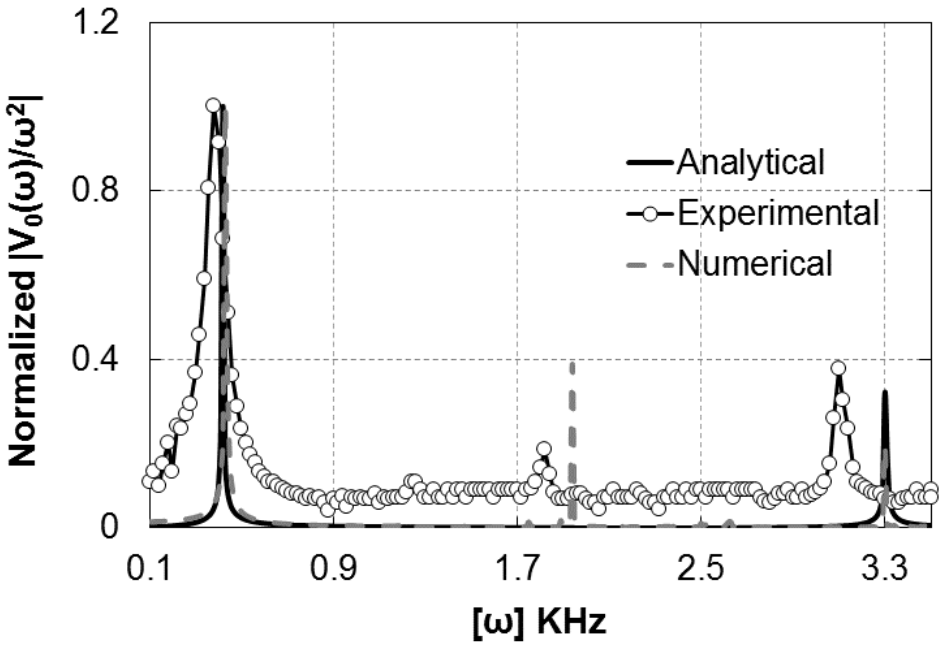


Figure 3.15: Analytical, Numerical and Experimental FRF response comparison for the proposed unit AEMM.

The above analytical, numerical and experimental analysis confirms that using a unit AEMM it is possible to model a mechanical sensor which can sense specific desired frequencies and filter unwanted system frequencies. The proposed model satisfies the three principal operations of the most developed band pass sensor, human cochlea. It can introduce local resonance, filter/remain unsensed for unwanted frequencies and select the desired frequencies employing piezoelectric material. The proposed model lacks in selecting different frequencies spatially (another principal operation of human cochlea).

However, typically in industrial operations each sensor is designed to actuate only a unique frequency to the manufacturing tool. Hence, the proposed unit AEMM sensor is an acceptable choice for industrial manufacturing applications.

## 3.5 Multi-cell AEMM Model

In some engineering applications a band of frequency input/sensing could be essential or a multipurpose sensor may find valuable, which can provide multiple specific frequency input and can be used for multiple manufacturing operations. Keeping this in mind, using the established hypothesis, a multi-cell AEMM model is proposed. The proposed model consists of multiple (five) cells with linearly varying core mass in each cell (Figure 3.16). Mirror construction of the multi-cell wings is fabricated to avoid vibration instability during the dynamic operation. The proposed model is linearly tapered toward smaller cells and center-to-center spacing between cells are constant. Here a special measure is taken to keep the wafer inside the matrix in perfect alignment.

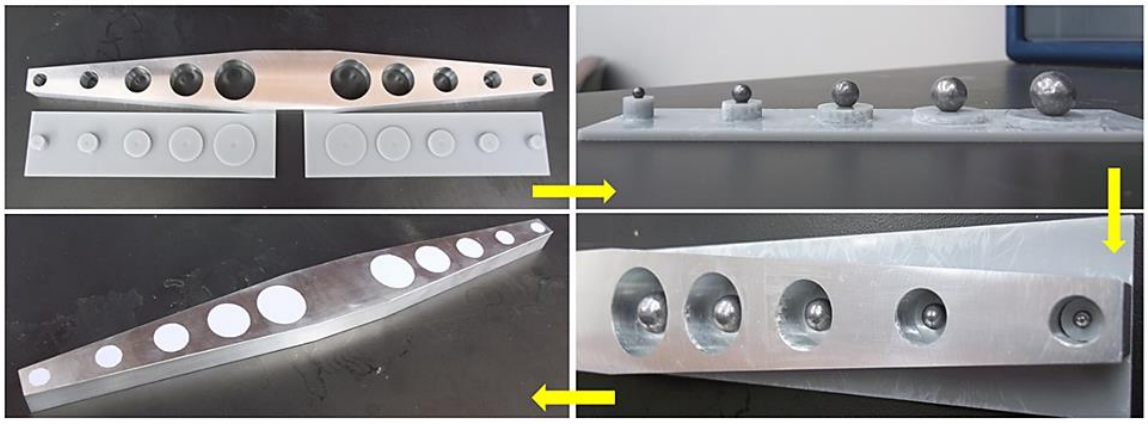

Figure 3.16: Fabrication steps of a multi-cell AEMM structure.

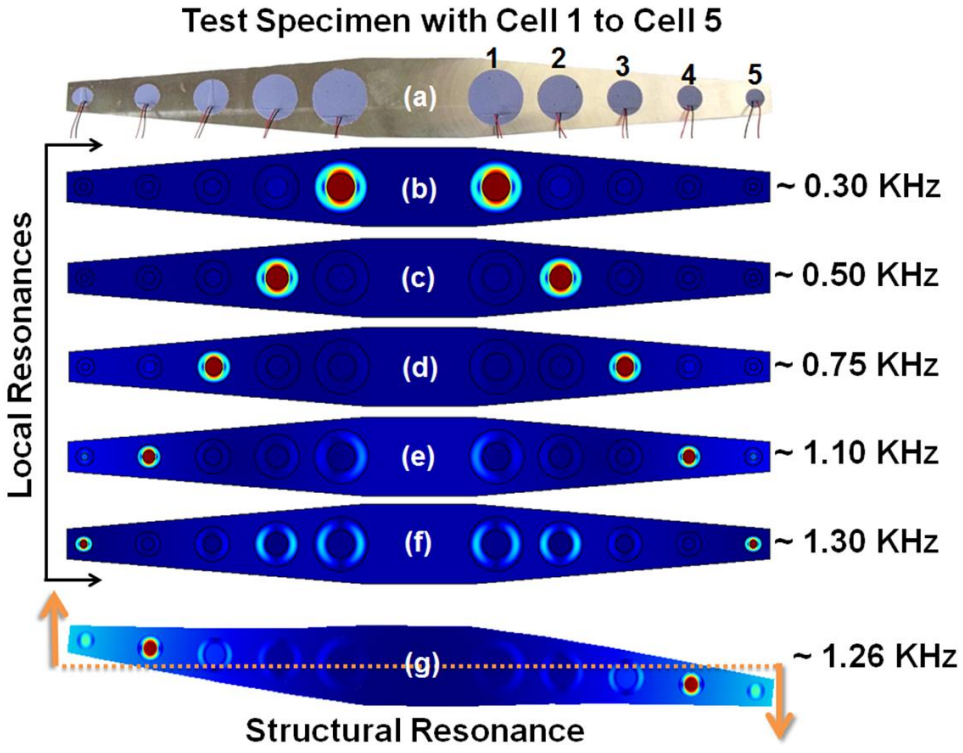


Figure 3.17: (a) Multi-cell metamaterial model. Displacement patterns obtained through numerical simulation at (b) ~ 0.30 KHz (c) ~ 0.50 KHz (d) ~ 0.75 KHz (e) ~ 1.10 KHz (f) ~ 1.30 KHz. (g) structural resonance at ~ 1.26 KHz.

Numerical and experimental investigations suggests that wave energies at different frequencies are trapped (Figure 3.17 (b-f)) and can be sensed (Figure 3.18) using the proposed model. From cell 1 with heaviest core mass (11.43 gm, $D_m$=12.5 mm, $D_M$=25 mm), the peak potential is noticed at ~0.30 KHz. Similarly, other frequencies like ~0.50 KHz, ~0.76 KHz, ~1.1 KHz, ~1.38 KHz can be selected from the cells 2-5, respectively. Mass and diameter ($D_m$) of the core masses are in cell 2: ~6.03 gm, ~10.2 mm, cell 3: ~2.86 gm, ~7.9 mm, cell 4: ~0.97 gm, ~5.6 mm and cell 5: ~0.19 gm, ~3.3 mm, respectively and in all cells $D_M$=2 $D_m$. In Figure 3.18 it can be seen that the FRF peaks between ~2.6 KHz - ~3.1 KHz are consistent among all the cells because the mass of the piezoelectric wafers

are almost similar in all the cells. In Figure 3.18, the FRF peaks are normalized with respect to each respective cell at the local resonances.

To illustrate further, the voltage output from multiple cells at ~0.30 KHz and ~1.10 KHz are plotted in Figure 3.19, which confirms that ~0.30 KHz and ~1.1 KHz frequency inputs can be selected from the cells with core mass ~11.43 gm and ~0.97 gm, respectively. Figure 3.18 shows an additional FRF peaks at ~1.26 KHz, which is consistent among all the cells. The peak can be explained from the Figure 3.17g, which shows the effect of structural resonance.

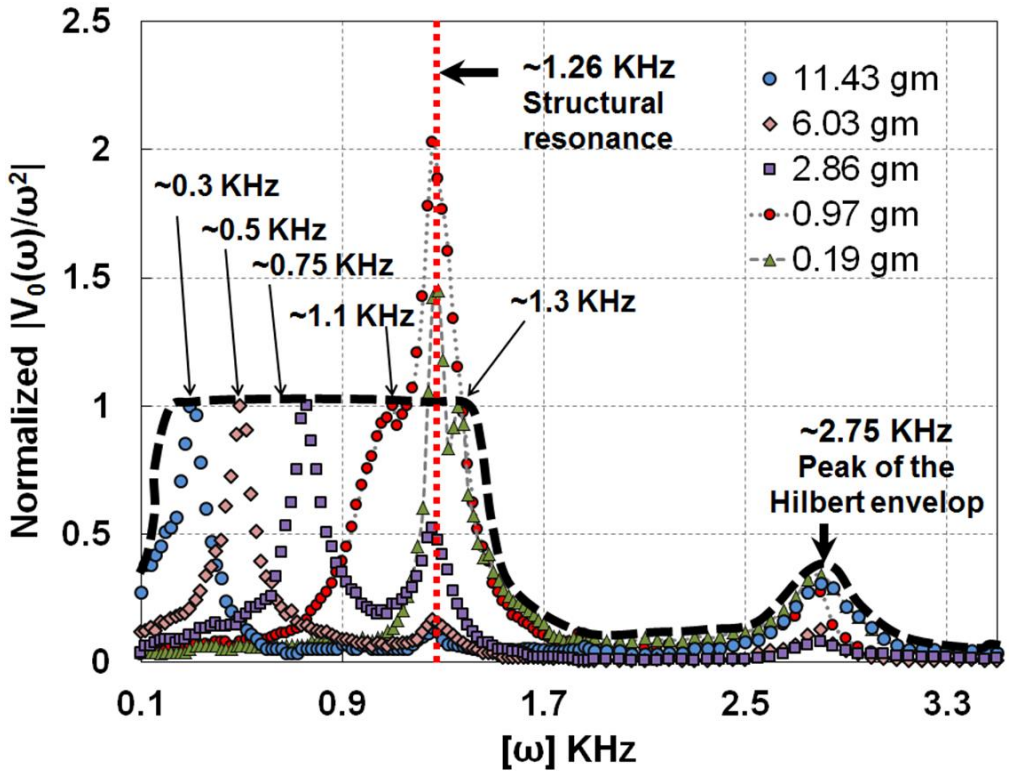


Figure 3.18: Normalized experimental response from multi-cell metamaterial model.

The above demonstration confirms that using a multi-cell AEMM with controlled parameters, multiple frequencies can be selected from different cells and can result a widely usable mechanical sensor. On the other hand, using the hypothesis and selecting the proper model parameters it is possible to introduce a broadband (or band pass) frequency sensor.

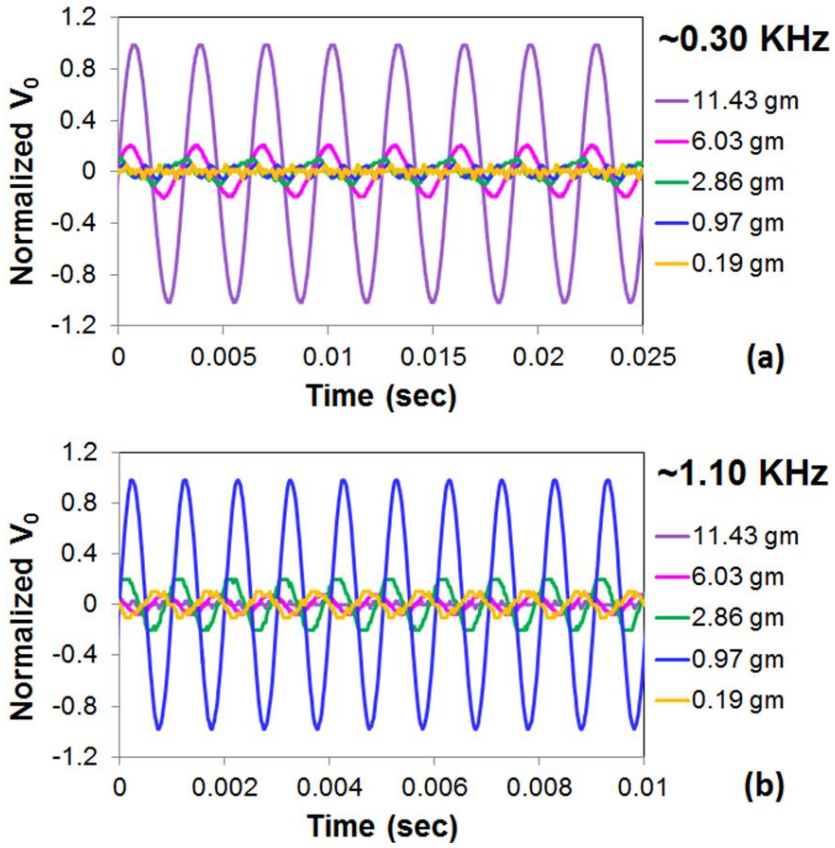


Figure 3.19: Normalized voltage output at (a) ~ 0.3 KHz and (b) ~ 1.1 KHz with different core mass in each cell.

## 3.6 Chapter Summary

Upon unsuccessful attempt of developing a mechanical band pass sensor using stop band technique, band pass technique is adopted. Inspired from the most developed band

pass sensor in nature, human cochlea, acoustoelastic metamaterial is considered to perform the principal operations of the cochlea (basilar membrane). Upon analytical, numerical and experimental it has been established that, the unit cell AEMM models is capable of performing principal operations of the human cochlea, thus, able to sense specific frequencies and filter/remain unresponsive for all unwanted frequencies in the system. Following the hypothesis, a multi-cell AEMM model is proposed with varying geometric configurations in each cell. It has been found that, the multi-cell model is capable of selecting different frequencies from each cell, which can make the model widely usable in industrial applications. The multi-cell model also opens the opportunity to introduce broadband (or band pass) sensor with appropriate cell geometry and material properties.

# CHAPTER 4: BASILAR MEMBRANE (PLATE MODEL)

Principal aim of this dissertation is to propose a novel band pass frequency sensing mechanism. Two models are envisioned, Acousto-elastic metamaterial (AEMM) model and Basilar membrane (BM) model. Chapter 2 and 3 demonstrates the possibility to introduce mechanical frequency sensor using the acousto-elastic metamaterial. In this section, basilar membrane geometric configuration is considered to model the targeted frequency sensor. Under the umbrella of BM based sensor, two models are envisioned, plate model and beam model. This chapter describes the development of the plate type band pass frequency sensor. The concept of BM based frequency sensor is not fairly new. In recent years, a notable number attempts were made to develop the broadband frequency sensors adopting the mechanics of basilar membrane. However, a true ultra-fast predictive model is missing which can be used for the optimized design of these sensors. Hence, in this research, a predictive model for the band pass frequency sensor is proposed, mimicking the tapered geometry of the basilar membrane. Most flexible predictive model is developed with variable engineering parameters that contribute to the frequency selection. Hence, the predictive model developed herein can not only to handle homogeneous but also any functionally graded model parameters. With the proposed model, it is also possible to alter

the attributes of the selected length of the designed sensor for the same targeted frequency band using functionally graded parameters. A study, using finite element method (FEM) confirms the outcome of the proposed predictive model and proves that the developed model is almost 3 times faster than its counter FEM.

## 4.1 Background

To recover the hearing deficiency, cochlea implantation is essential if the inner ear is damaged. The key functions of cochlea are not only the conversion of acoustic wave into electric signals, but also the spatial selectivity of the frequencies [81]. Basilar membrane (BM), which is a biological diaphragm, plays the most important role in a human cochlea by selecting the sonic frequencies by naturally varying the mechanical properties and the boundary conditions of the biological membrane from the basal to the apical end (please refer chapter ). Basilar membrane selects the sonic frequencies spatially since the local resonance dominates at different places of the BM with inputs with different frequencies. Recently, mimicking the basilar membrane few attempts are reported to artificially realize the frequency selectivity. Chen et al. [82] proposed an artificial basilar membrane by deposing discrete Cu beams on a piezoelectric membrane or substrate. Tanaka et al. [83] fabricated a fishbone-like structure from a thin Si plate as an equivalent mechanical model of the cochlea. A micro cochlea model is presented by Wittbrodt et al. [84] using a thin polyimide plate as basilar membrane attached over a micromachined fluid channel. Very recently Shintaku et al. [85] proposed a microbeam array with variable thickness and investigated its suitability for an acoustic sensor with wide-range of frequency selectivity. In 2013, Tanujaya et al. [86] presented an artificial basilar membrane prototype to catch

sinusoidal waves at various frequencies using Laser Doppler Vibrometer. White and Grosh [87] constructed a micro-engineered hydromechanical cochlea that has a micromachined membrane as well as a fluid-filled duct to mimic the cochlear chamber. However, the response frequencies detected by the acoustic input were above the audible frequency range. In a recent study, Kim et al. [88, 89] assessed the frequency selectivity of an artificial basilar membrane constructed using a piezoelectric beam array. Though a considerable number of studies are performed to model artificial mechanical cochlea, a predictive model is missing. A model is truly demanded that will guide and enhance the performance of the fabricated device or help design the sensors accurately/predictively with tailored target application in mind.

Since it is established that the basilar membrane possess the ability to select a specific band of frequency, thus, in this study we intend to develop a band pass frequency sensor adopting the geometry of the basilar membrane. It is expected that using the proposed model it is not only possible to design the mechanical band pass sensor parameters (e.g. geometry, bandwidth) predictively, but also it will fulfill the long standing necessity of the predictive model for an artificial mechanical cochlea. Though few attempts were made in past to analytically model the cochlea [17-23], however, those studies are not easily transferable to fabricate artificial cochlea due to their simplified assumptions. In this study mimicking the actual basilar membrane in human cochlea a trapezoidal membrane is considered. In the process of developing the predictive model, we aimed to develop as flexible as possible (through allowing functionally graded model parameters and boundary conditions) such that the proposed model can be implemented in for large varieties of scientific applications.

## 4.2 Analytical Development

Basilar membrane is a trapezoidal structure with narrower width at the base and wide at the apex. The membrane is attached to the boundary supports at the three ends except at the apex as shown in Figure 4.1. Following the configuration of the basilar membrane, a trapezoidal domain is considered in this study as the sensing device (Figure 4.1). L is defined as the length of the continuous domain, where Bi and Bf are the base and apex widths, respectively. Significantly small thickness of the domain is measured to treat the domain as a thin membrane.

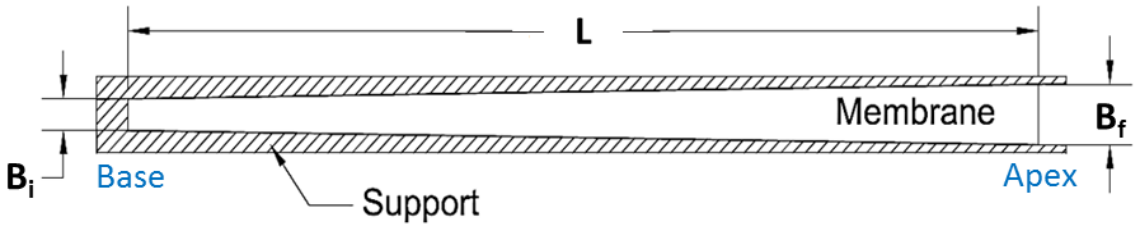


Figure 4.1: Proposed geometric configuration of the band pass sensor

To make the predictive model widely implementable or versatile, several flexibilities are incorporated in the model, for example, flexibilities in the (a) material properties (b) geometric configuration and (c) boundary conditions. A list of variable that can be handled with ease using the proposed predictive model is listed below. Apart from the listed conditions, other model parameters can be defined as a constant parameter. Flexibility of the boundary condition at the apex is not applicable as it is a free end mimicking the actual basilar membrane (e.g. right end in Figure 4.1).

1. Stiffness $[E(x, y)]$ (homogeneous / functionally graded)

2. Poissons Ratio $[\nu(x,y)]$ (homogeneous / functionally graded)
3. Density $[\rho(x,y)]$ (homogeneous / functionally graded)
4. Thickness $[h(x,y)]$ (uniform / functionally graded)
5. Boundary condition (fixed / simply supported)

Dynamic equation of the plate can be represented as shown is equation 4.1, where $\eta$ and P are the deflection of the plate and downward uniform pressure on entire plate top surface, respectively. $D = (Eh^3)/\left(12(1-\nu^2)\right)$ is defined as the bending stiffness of the membrane.

$$\frac{\partial^4\eta}{\partial x^4} + 2\frac{\partial^4\eta}{\partial x^2\,\partial y^2} + \frac{\partial^4\eta}{\partial y^4} = \frac{P}{D} - \frac{\rho h}{D}\frac{\partial^2\eta}{\partial t^2} \qquad (4.1)$$

Considering harmonic pressure $\left(P = pe^{i\omega t}\right)$ excitation and corresponding harmonic response of the domain $\left(\eta = \xi e^{i\omega t}\right)$, equation 4.1 can be modified to equation 4.2, where, $\xi = \xi(x,y)$ is the dynamic deflection of the plate and $\omega$ is the excitation frequency.

$$\frac{\partial^4\xi}{\partial x^4} + 2\frac{\partial^4\xi}{\partial x^2\,\partial y^2} + \frac{\partial^4\xi}{\partial y^4} - \omega^2\frac{\rho h}{D}\xi = \frac{p}{D} \qquad (4.2)$$

Equation 4.2 represents the deflection equation for a rectangular domain. Since in this study, the sensor domain is trapezoidal in shape, it is required to perform a coordinate transformation to make the deflection equation valid for all discretized points in a trapezoidal domain. A new coordinate system u-v is considered (see Figure 4.2) for the trapezoidal domain, while x-y is the usual Cartesian coordinate system representing the rectangular domain. New v-axis lies on y-axis, whereas u- makes an angle $\theta$ with the x-

axis. Thus, x- and y- components can be expressed as $(x = u\cos\theta)$ and $(y = u\sin\theta + v)$. Transformation of derivative terms in equation 4.2 from x-y domain to u-v domain is expressed in equations (4.3-4.5).

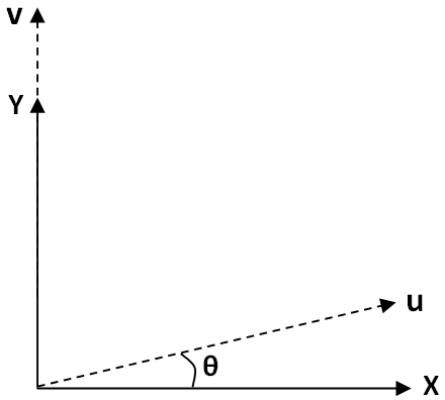


Figure 4.2: Coordinate transformation scheme for rectangular to trapezoidal domain

$$\frac{\partial^4\xi}{\partial x^4} = \frac{1}{\cos^4\theta}\frac{\partial^4\xi}{\partial u^4} - \frac{4\sin\theta}{\cos^4\theta}\frac{\partial^4\xi}{\partial u^3\,\partial v} + \frac{6\sin^2\theta}{\cos^4\theta}\frac{\partial^4\xi}{\partial u^2\,\partial v^2} - \frac{4\sin^3\theta}{\cos^4\theta}\frac{\partial^4\xi}{\partial u\,\partial v^3} + \frac{\sin^4\theta}{\cos^4\theta}\frac{\partial^4\xi}{\partial v^4} \qquad (4.3)$$

$$\frac{\partial^4\xi}{\partial y^4} = \frac{\partial^4\xi}{\partial v^4} \qquad (4.4)$$

$$\frac{\partial^4\xi}{\partial x^2\partial y^2} = \frac{1}{\cos^2\theta}\frac{\partial^4\xi}{\partial u^2\,\partial v^2} - \frac{2\sin\theta}{\cos^2\theta}\frac{\partial^4\xi}{\partial u\,\partial v^3} + \frac{\sin^2\theta}{\cos^2\theta}\frac{\partial^4\xi}{\partial v^4} \qquad (4.5)$$

Concise form of deflection equation in transformed u-v coordinate system is presented in equation (4.6), using equations (4.3-4.5) in (4.2).

$$\frac{1}{\cos^4\theta}\left(\frac{\partial^4\xi}{\partial u^4}\right) - \frac{4\sin\theta}{\cos^4\theta}\left(\frac{\partial^4\xi}{\partial u^3\,\partial v}\right) + \frac{4\sin^2\theta+2}{\cos^4\theta}\left(\frac{\partial^4\xi}{\partial u^2\,\partial v^2}\right) - \frac{4\sin\theta}{\cos^4\theta}\left(\frac{\partial^4\xi}{\partial u\,\partial v^3}\right) + \frac{1}{\cos^4\theta}\left(\frac{\partial^4\xi}{\partial v^4}\right) -$$

$$\omega^2\frac{\rho h}{D}\xi = \frac{p}{D} \qquad (4.6)$$

To find the deformation information of the trapezoidal domain upon dynamic loading, equation 4.6 is solved using elastodynamic finite (central) difference method. Traditionally, the finite difference (FD) scheme is widely used to solve the rectangular domains, while it is very rare to adopt FD method for solving trapezoidal structure. Coordinate transformation is a vital step to implement FD for tapered structure. Figurative finite difference discretization scheme of the domain is shown in Figure 4.3. Conventionally, uniform distance is measured between two node points (Δu or Δv), however, in this work, Δv is considered non uniform and increases along the length (base to apex) of the structure. Note that, Δv is unchanged across a specific width of the domain.

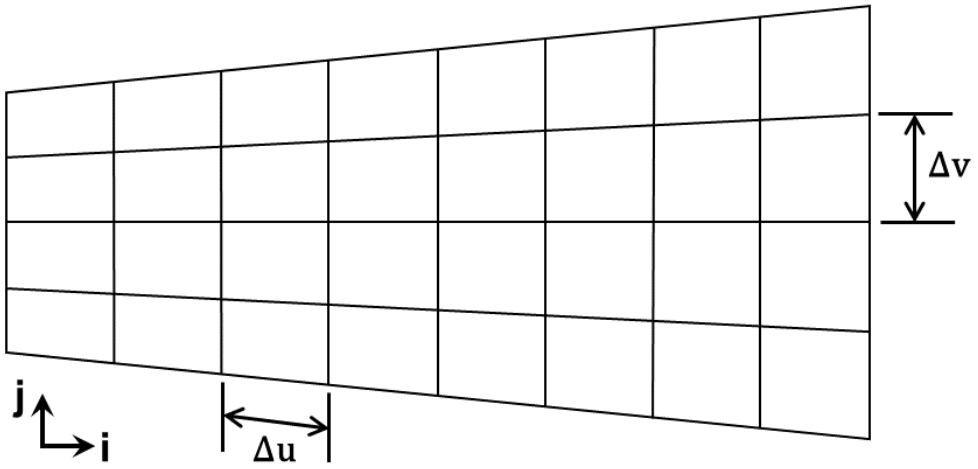


Figure 4.3: Finite difference discretization scheme

Finite difference approximation of the derivative terms in equation (4.3-4.5) are presented in equations (4.7-4.11)

$$\frac{\partial^4 \xi}{\partial u^4} = \frac{1}{\Delta u^4}\left(\xi_{i-2,j} - 4\xi_{i-1,j} + 6\xi_{i,j} - 4\xi_{i+1,j} + \xi_{i+2,j}\right) \qquad (4.7)$$

$$\frac{\partial^4 \xi}{\partial v^4} = \frac{1}{\Delta v_i{}^4}\left(\xi_{i,j-2} - 4\xi_{i,j-1} + 6\xi_{i,j} - 4\xi_{i,j+1} + \xi_{i,j+2}\right) \qquad (4.8)$$

$$\frac{\partial^4 \xi}{\partial u^2 \partial v^2} = \frac{1}{\Delta u^2 \Delta v_{i-1}{}^2}\xi_{i-1,j-1} - \frac{2}{\Delta u^2 \Delta v_{i-1}{}^2}\xi_{i-1,j} + \frac{1}{\Delta u^2 \Delta v_{i-1}{}^2}\xi_{i-1,j+1} - \frac{2}{\Delta u^2 \Delta v_i{}^2}\xi_{i,j-1} +$$

$$\frac{4}{\Delta u^2 \Delta v_i{}^2}\xi_{i,j} - \frac{2}{\Delta u^2 \Delta v_i{}^2}\xi_{i,j+1} + \frac{1}{\Delta u^2 \Delta v_{i+1}{}^2}\xi_{i+1,j-1} - \frac{2}{\Delta u^2 \Delta v_{i+1}{}^2}\xi_{i+1,j} + \frac{1}{\Delta u^2 \Delta v_{i+1}{}^2}\xi_{i+1,j+1} \qquad (4.9)$$

$$\frac{\partial^4 \xi}{\partial u^3 \partial v} = \frac{1}{4\Delta u^3 \Delta v}\xi_{i-2,j-1} - \frac{1}{4\Delta u^3 \Delta v_{i-2}}\xi_{i-2,j+1} - \frac{1}{2\Delta u^3 \Delta v_{i-1}}\xi_{i-1,j-1} + \frac{1}{2\Delta u^3 \Delta v_{i-1}}\xi_{i-1,j+1} +$$

$$\frac{1}{2\Delta u^3 \Delta v_{i+1}}\xi_{i+1,j-1} - \frac{1}{2\Delta u^3 \Delta v_{i+1}}\xi_{i+1,j+1} - \frac{1}{4\Delta u^3 \Delta v_{i+2}}\xi_{i+2,j-1} + \frac{1}{4\Delta u^3 \Delta v_{i+2}}\xi_{i+2,j+1} \qquad (4.10)$$

$$\frac{\partial^4 \xi}{\partial u \partial v^3} = \frac{1}{4\Delta u \Delta v_i{}^3}\xi_{i-1,j-2} - \frac{1}{4\Delta u \Delta v_i{}^3}\xi_{i+1,j-2} - \frac{1}{2\Delta u \Delta v_i{}^3}\xi_{i-1,j-1} + \frac{1}{2\Delta u \Delta v_i{}^3}\xi_{i+1,j-1} +$$

$$\frac{1}{2\Delta u \Delta v^3}\xi_{i-1,j+1} - \frac{1}{2\Delta u \Delta v^3}\xi_{i+1,j+1} - \frac{1}{4\Delta u \Delta v^3}\xi_{i-1,j+2} + \frac{1}{4\Delta u \Delta v^3}\xi_{i+1,j+2} \qquad (4.11)$$

Generalized final form of the membrane deflection equation in trapezoidal domain is expressed in equation (4.12), using equations (4.7-4.11) in (4.6).

$$\frac{1}{\cos^4\theta}\left(\frac{1}{\Delta u^4}\xi_{i-2,j} - \frac{4}{\Delta u^4}\xi_{i-1,j} + \frac{6}{\Delta u^4}\xi_{i,j} - \frac{4}{\Delta u^4}\xi_{i+1,j} + \frac{1}{\Delta u^4}\xi_{i+2,j}\right) - \frac{4\sin\theta}{\cos^4\theta}\left(\frac{1}{4\Delta u^3 \Delta v}\xi_{i-2,j-1} -\right.$$

$$\frac{1}{4\Delta u^3 \Delta v_{i-2}}\xi_{i-2,j+1} - \frac{1}{2\Delta u^3 \Delta v_{i-1}}\xi_{i-1,j-1} + \frac{1}{2\Delta u^3 \Delta v_{i-1}}\xi_{i-1,j+1} + \frac{1}{2\Delta u^3 \Delta v_{i+1}}\xi_{i+1,j-1} -$$

$$\left.\frac{1}{2\Delta u^3 \Delta v_{i+1}}\xi_{i+1,j+1} - \frac{1}{4\Delta u^3 \Delta v_{i+2}}\xi_{i+2,j-1} + \frac{1}{4\Delta u^3 \Delta v_{i+2}}\xi_{i+2,j+1}\right) + \frac{4\sin^2\theta + 2}{\cos^4\theta}\left(\frac{1}{\Delta u^2 \Delta v_{i-1}{}^2}\xi_{i-1,j-1} -\right.$$

$$\frac{2}{\Delta u^2 \Delta v_{i-1}{}^2}\xi_{i-1,j} + \frac{1}{\Delta u^2 \Delta v_{i-1}{}^2}\xi_{i-1,j+1} - \frac{2}{\Delta u^2 \Delta v_i{}^2}\xi_{i,j-1} + \frac{4}{\Delta u^2 \Delta v_i{}^2}\xi_{i,j} - \frac{2}{\Delta u^2 \Delta v_i{}^2}\xi_{i,j+1} +$$

$$\left.\frac{1}{\Delta u^2 \Delta v_{i+1}{}^2}\xi_{i+1,j-1} - \frac{2}{\Delta u^2 \Delta v_{i+1}{}^2}\xi_{i+1,j} + \frac{1}{\Delta u^2 \Delta v_{i+1}{}^2}\xi_{i+1,j+1}\right) - \frac{4\sin\theta}{\cos^4\theta}\left(\frac{1}{4\Delta u \Delta v_i{}^3}\xi_{i-1,j-2} -\right.$$

$$\frac{1}{4\Delta u \Delta v_i{}^3}\xi_{i+1,j-2} - \frac{1}{2\Delta u \Delta v_i{}^3}\xi_{i-1,j-1} + \frac{1}{2\Delta u \Delta v_i{}^3}\xi_{i+1,j-1} + \frac{1}{2\Delta u \Delta v^3}\xi_{i-1,j+1} - \frac{1}{2\Delta u \Delta v^3}\xi_{i+1,j+1} -$$

$$\frac{1}{4\Delta u\Delta v^3}\xi_{i-1,j+2}+\frac{1}{4\Delta u\Delta v^3}\xi_{i+1,j+2}\Big)+\frac{1}{\cos^4\theta}\Big(\frac{1}{{\Delta v_i}^4}\xi_{i,j-2}-\frac{4}{{\Delta v_i}^4}\xi_{i,j-1}+\frac{6}{{\Delta v_i}^4}\xi_{i,j}-\frac{4}{{\Delta v_i}^4}\xi_{i,j+1}+$$

$$\frac{1}{{\Delta v_i}^4}\xi_{i,j+2}\Big)-\omega^2\frac{\rho h}{D}\xi_{i,j}=\frac{p}{D} \qquad (4.12)$$

Since central difference scheme is adopted, it is required to count at least two node points on every side (top, bottom, left, right) of the node point where we intend to implement the equation 4.2 and calculate the deflection amplitude. Following the requirement, some fictitious node points are imagined outside every ends of the domain as shown in Figure 4.4.

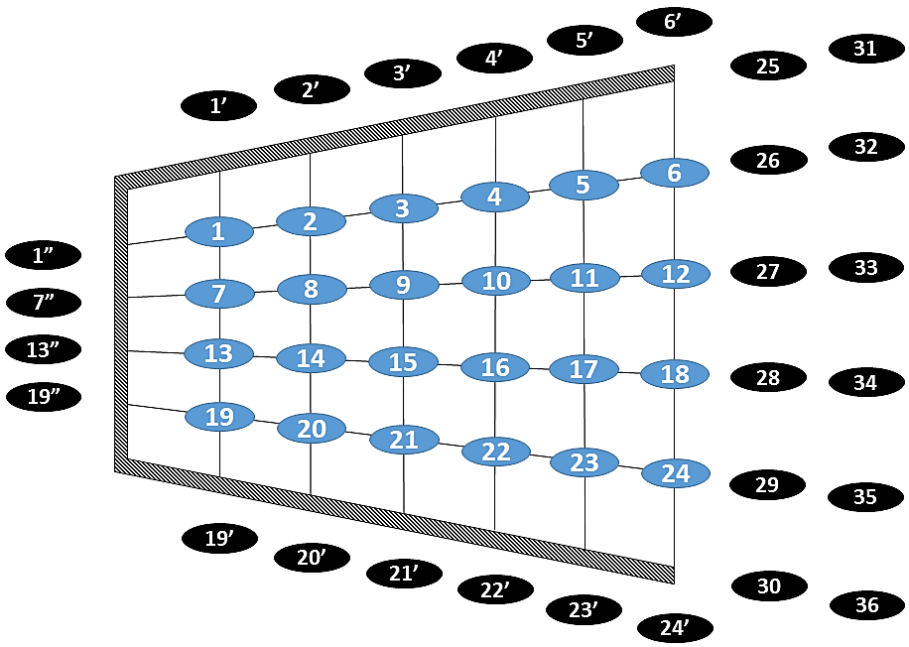


Figure 4.4: Fictitious node points (black) setting outside of the domain.

It is necessary to express the deflection equation of the fictitious node points in terms of the nodes inside the plate. Boundary conditions are counted to find the finite difference deflection equation at fictitious node points. Single row/column imaginary nodes are considered at the supported boundaries of the domain while double column is

considered at the free end (see Figure 4.4). The boundary connections can either be fixed or simply supported. In fixed connection, it is assumed that the deflection amplitude at a fictitious point is same as the deflection at the nearest node point inside the domain with '+ ve', while same amplitude with '- ve' is assumed for the simply supported connection. As an example, $\xi_{1'} = \xi_1$ or $\xi_{1''} = \xi_1$ for fixed boundary and $\xi_{1'} = -\xi_1$ or $\xi_{1''} = -\xi_1$ are for simply supported boundaries. To calculate the deflection equation for imaginary nodes at the free end, it has been assumed that bending moment and shear force at the free boundary are zero. Finite difference approximation of the bending moment and shear force at (i,j)-th node point is presented in equations (4.13) and (4.14), respectively.

$$\mathbf{M_u} = -\mathrm{D}\left[\frac{1}{\Delta u^2}\xi_{i-1,j} - \left(\frac{2}{\Delta u^2} + \frac{2\nu}{\Delta v_i{}^2}\right)\xi_{i,j} + \frac{1}{\Delta u^2}\xi_{i+1,j} + \frac{\nu}{\Delta v_i{}^2}\xi_{i,j-1} + \frac{\nu}{\Delta v_i{}^2}\xi_{i,j+1}\right] \qquad (4.13)$$

$$\mathbf{S_u} = -\mathrm{D}\left[-\frac{1}{2\Delta u^3}\xi_{i-2,j} + \left(\frac{1}{\Delta u^3} + \frac{(2-\nu)}{\Delta u \Delta v_i{}^2}\right)\xi_{i-1,j} - \left(\frac{1}{\Delta u^3} + \frac{(2-\nu)}{\Delta u \Delta u_i{}^2}\right)\xi_{i+1,j} + \frac{1}{2\Delta u^3}\xi_{i+2,j} - \frac{1}{2}\frac{(2-\nu)}{\Delta u \Delta v_i{}^2}\xi_{i-1,j-1} + \frac{1}{2}\frac{(2-\nu)}{\Delta u \Delta v_i{}^2}\xi_{i+1,j-1} - \frac{1}{2}\frac{(2-\nu)}{\Delta u \Delta v_i{}^2}\xi_{i-1,j+1} + \frac{1}{2}\frac{(2-\nu)}{\Delta u \Delta v_i{}^2}\xi_{i+1,j+1}\right] \qquad (4.14)$$

Using equation (4.13-4.14) and zero internal force at free boundary, calculated deflection equations for imaginary nodes in first (right after free end) and the second column are expressed in equations (4.15) and (4.16), respectively.

$$\boldsymbol{\xi_{i,j}} = (2 + 2\nu\alpha_{i-1})\xi_{i-1,j} - \nu\alpha_{i-1}\xi_{i-1,j-1} - \nu\alpha_{i-1}\xi_{i-1,j+1} - \xi_{i-2,j} \qquad (4.15)$$

$$\boldsymbol{\xi_{i,j}} = \xi_{i-4,j} - [4 + 2(2-\nu)\alpha_{i-3} + 2(2-\nu)\alpha_{i-1}]\xi_{i-3,j} + [4 + 4(2-\nu)\alpha_{i-1} + 4\nu\alpha_{i-2} + 6\nu(2-\nu)\alpha_{i-2}\alpha_{i-1}]\xi_{i-2,j} - [2\nu\alpha_{i-2} + 4\nu(2-\nu)\alpha_{i-2}\alpha_{i-1} + 2(2-\nu)\alpha_{i-1}]\xi_{i-2,j-1} - [2\nu\alpha_{i-2} + 4\nu(2-\nu)\alpha_{i-2}\alpha_{i-1} + 2(2-\nu)\alpha_{i-1}]\xi_{i-2,j+1} + [(2-\nu)\alpha_{i-3} + (2 -$$

$\nu)\alpha_{i-1}]\xi_{i-3,j-1} + [(2-\nu)\alpha_{i-3} + (2-\nu)\alpha_{i-1}]\xi_{i-3,j+1} + \nu(2-\nu)\alpha_{i-2}\alpha_{i-1}\xi_{i-2,j-2} +$

$\nu(2-\nu)\alpha_{i-2}\alpha_{i-1}\xi_{i-2,j+2}$ (4.16)

Where, $\alpha_i = \Delta u^2/\Delta v_i{}^2$

## 4.3 Result and Discussion

The elastodynamic equation for the basilar membrane is solved using a customized computer code written in MATLAB. To test the functionality of the proposed predictive model, initially, a homogeneous system is solved where the material properties are considered with uniform plate thickness. Next to verify (to answer are we building it right?) the proposed model is compared with the Finite Element Model (FEM) simulated in the COMSOL Multiphysics environment. Further, upon verification, functionally graded model parameters are introduced in our model to note the perturbation in the attributes of the sensing parameters. Although the developed model can manage different types of boundary supports, in this article, sensing capabilities are reported only employing the fixed boundary connections. The model properties that are considered for the homogeneous structure is listed in the Table 4.1. While selecting the dimensions of the virtual model for solution in our study, the actual geometric configurations of the basilar membrane, inside the human cochlea is mimicked which is 35 mm long.

Table 4.1: Parameters used for homogeneous model

| Beam Parameters | Value | Unit |
|---|---|---|
| Stiffness (E) | 8.963 | MPa |
| Density (ρ) | 1130 | $Kg/m^3$ |
| Poisson's Ratio (ν) | 0.48 | |
| Thickness (h) | 0.1 | mm |
| Length (L) | 35 | mm |
| Base Width ($B_i$) | 1 | mm |
| Apex Width ($B_f$) | 2 | mm |

Harmonic unit pressure is considered over the top surface of the domain as excitation input. A frequency range of 100 Hz – 10 KHz is studied. Figure 4.5 presents the deflection patterns of the sensor at three different frequencies. It can be seen that at the lower frequencies, maximum localized deflection can be measured towards the apical end of the model. Maximum deflection location is shifted towards the base with increasing excitation frequency. This phenomenon is quite evident since the bending rigidity of the structure is lower at the apical end, compared to the base, and this is due to the increase in the width of the membrane, even though a constant E is defined for computation (ref. Table 1). Apart from the maximum peak, other smaller peaks are evident at the apical end. In human cochlea, basilar membrane is submerged in a fluidic medium to achieve travelling wave phenomenon and membrane-fluid dynamic interaction is responsible for damping out these smaller fluctuations or the amplitude peaks. However, in this study, fluidic media is avoided. This is because we proposed the model to aid the design and fabrication process

simpler for the artificial basilar membrane sensors with their intended use in the air medium. However, how to damp these fluctuations or the smaller peaks using optimized design of the membrane property, but without using the fluid medium, is under rigorous study.

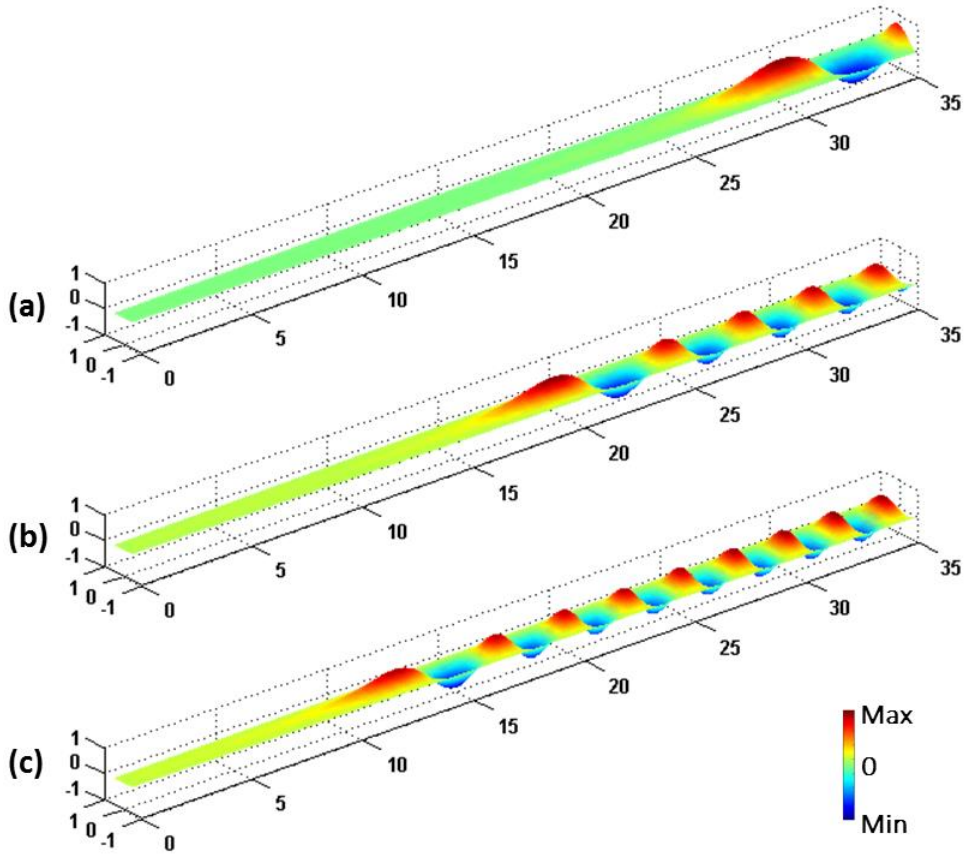


Figure 4.5: Deflection patterns of the membrane at different frequencies (a) 3 .06 KHz (b) 4.29 KHz and (c) 5.64 KHz

Figure 4.5 shows the defection pattern and the peak shifts in the membrane in relation to the incremental change in the excitation frequencies. To validate the acceptability of the proposed predictive model, a numerical study is performed using computational tool COMSOL Multiphysics. Identical model parameters, as listed in Table 1, and boundary conditions are considered compared to the predictive model. Figure 4.6

represents the numerically obtained deflection profile of the sensor at three different frequencies (~3.06 KHz, ~4.29 KHz and ~5.64 KHz), those are also counted to represent the deflection patterns in Figure 4.5.

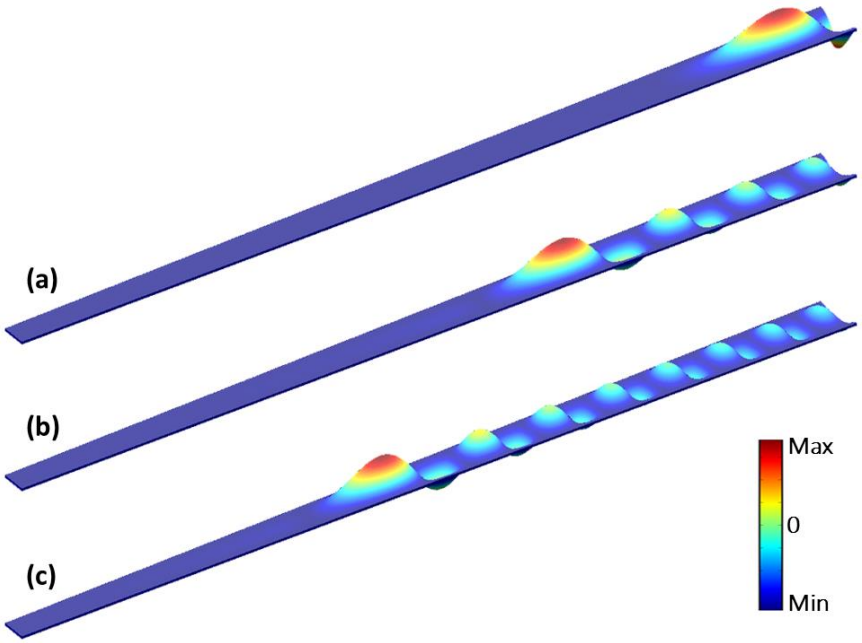


Figure 4.6: Numerically (using COMSOL multiphysics) obtained deflection profile of the sensor at (a) 3.06 KHz (b) 4.29 KHz and (c) 5.64 KHz

Comparing the Figure 4.5 and Figure 4.6, it can be seen that the response from the predictive model and the FEM analysis are in very close agreement. Using the proposed model ~3.06 KHz, ~4.29 KHz and ~5.64 KHz frequencies can be selected at X = ~29.58 mm, ~19.43 mm and ~12.25 mm, respectively, while using the FEM model same frequencies are possible to select approximately from the same location or at same X, where 'X' is the membrane length measured from the base. It has also been counted that, considering the computation time, our developed model (~ 825 sec) is almost three (3) times faster than the FEM method (~ 2436 sec). Note that, in both the approaches, the domain is discretized with the same dimension of elements. In the current technological

world, processing time plays a vital role in the selection of any technique, where our proposed model strongly overpowers the FEM technique.

Since the device is connected at the two opposite sides width of the fixed boundaries (ref Figure 4.1), maximum deflection is measured at the central points of the membrane across the length of the sensor. Absolute deflection profiles along the center line (along the length of the membrane) at the arbitrary frequencies e.g. ~4.29 KHz, ~4.33 KHz and ~4.37 KHz and ~4.41 KHz are shown in Figure 4.7. It has been found that at any specific input frequency, maximum deflection amplitude can be recorded only from a very specific location in the structure.

Figure 4.5 states that the peak deflection amplitude shifts from the apex to the base with the increasing input frequency. It has been noticed that with the incremental increase in the input frequencies, the peak deflection detected, doesn't move all the way from the apex to the base end, which is a conventional understanding [90] but a new peak generates in front of the maximum peak (Ref. Figure 4.7). Then the new peak gains amplitude with the increase in the input frequency until it suppresses the previous maximum peak. Amplitude of the previous maximum peak drops quickly and become one of those smaller tailgating coda peaks, once the new higher peak gains the maximum amplitude of deflection. Note that, at any specific frequency, maximum deflection amplitude cannot be recorded from more than one location of the structure. Interestingly, when a peak reaches the maximum amplitude, instead of moving toward the base end it shifts toward the apical end as the frequency increases (Ref. Figure 4.7), which defies our conventional understanding. This phenomenon is quite interesting itself reported herein, since bending

stiffness is lower towards the apical end. Probably the reported mechanism above is the fundamental physics that generates the peak at a very specific location at specific frequency in the basilar membrane.

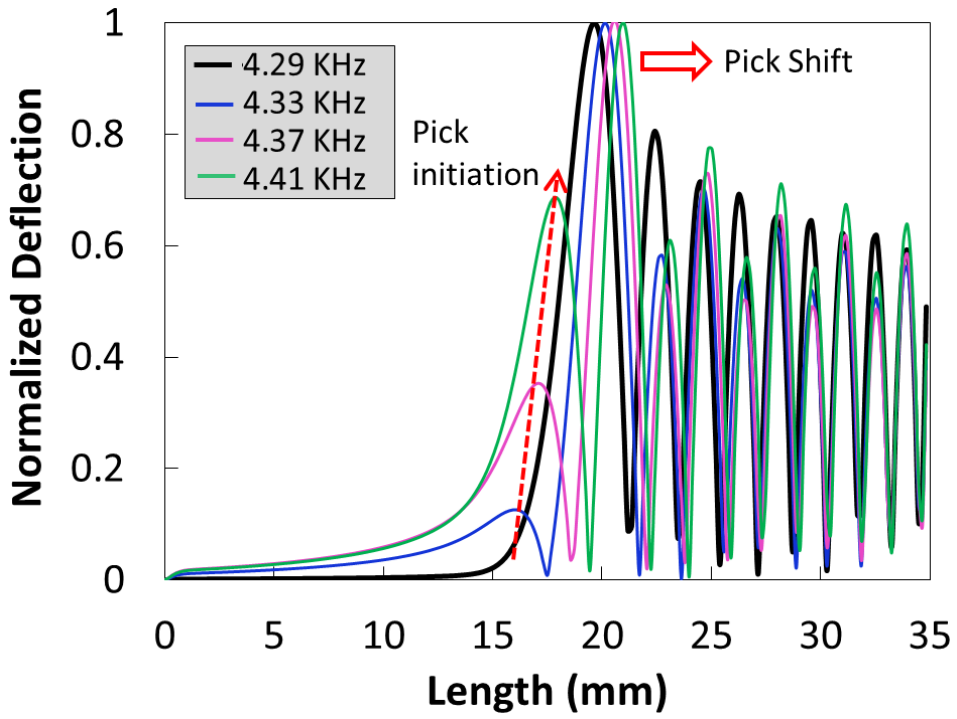


Figure 4.7: Normalized deflection of the centerline of the membrane at different frequencies

It has been reported in handful numbers of article that a band of frequency is required to be selected in many scientific disciplines (please refer Introduction section). Say for example, it may be required to design a sensor with a selected band of 4.5 KHz – 5.5 KHz frequencies for a specific engineering or acoustic application. In such scenario, how the proposed model can be used to design the band pass frequency sensor with tight resolution in the incremental frequencies (e.g. at the order of ~0.01Hz), is the fundamental question we answer herein. Deflection profile of the centerline at the targeted frequency band is plotted in Figure 4.8. Now if a threshold limit of the deflection amplitude is set to

avoid all smaller perturbations in the deflection profile as shown in Figure 4.8, it can be possible to sense only the frequency band 4.5 KHz – 5.5 KHz from the length segment ~13.3 mm to ~20.1 mm (measured from the base) of the device. Figure 4.8 confirms that it is possible to select a specific frequency band from a specific length segment of the proposed structure with only homogeneous model parameters. Further to fabricate such sensors, smart sensing mechanism proposed by the earlier researchers [85-89] can be employed to record the peak deflections of the membrane.

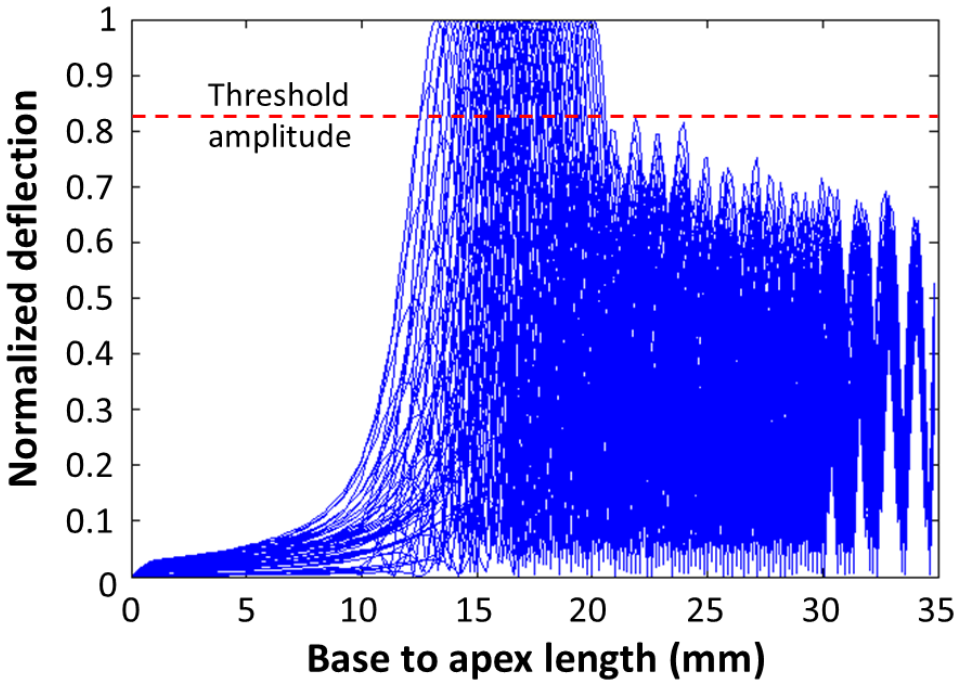


Figure 4.8: Normalized deflection profile for a frequency band 4.5 KHz – 5.5 KHz

Next, functionally graded model parameters are considered to validate the ability of the predictive model to control the band frequency sensing attributes by controlling other parameters if the designer has restrictions on some parameters, calculated earlier. Functionally graded stiffness, poissons ratio, density and membrane thickness are

considered here in this model to proceed to make the model truly versatile. Each time, only one parameter is defined as functionally graded while other parameters are constant. In this work simple linear functions are considered to define functionally graded parameters, however the predictive model is able to manage any type of complex functions (e.g. exponential, logarithmic, higher order functions or any digitized or discrete properties distributed over the entire domain). Stiffness, density and the thickness are defined such a way that at the basal end the magnitude of the specific parameter is same as it was considered for homogeneous model, however, the magnitude of the parameter increases along the model length and gained 1.5 times at the apex. Since in homogeneous model, poisson's ratio was considered 0.48 and it is not possible to get poisson's ratio above 0.5, thus poissons ratio is functionally graded in such a way that it decreases 1.5 times towards the apex end compared to the base end.

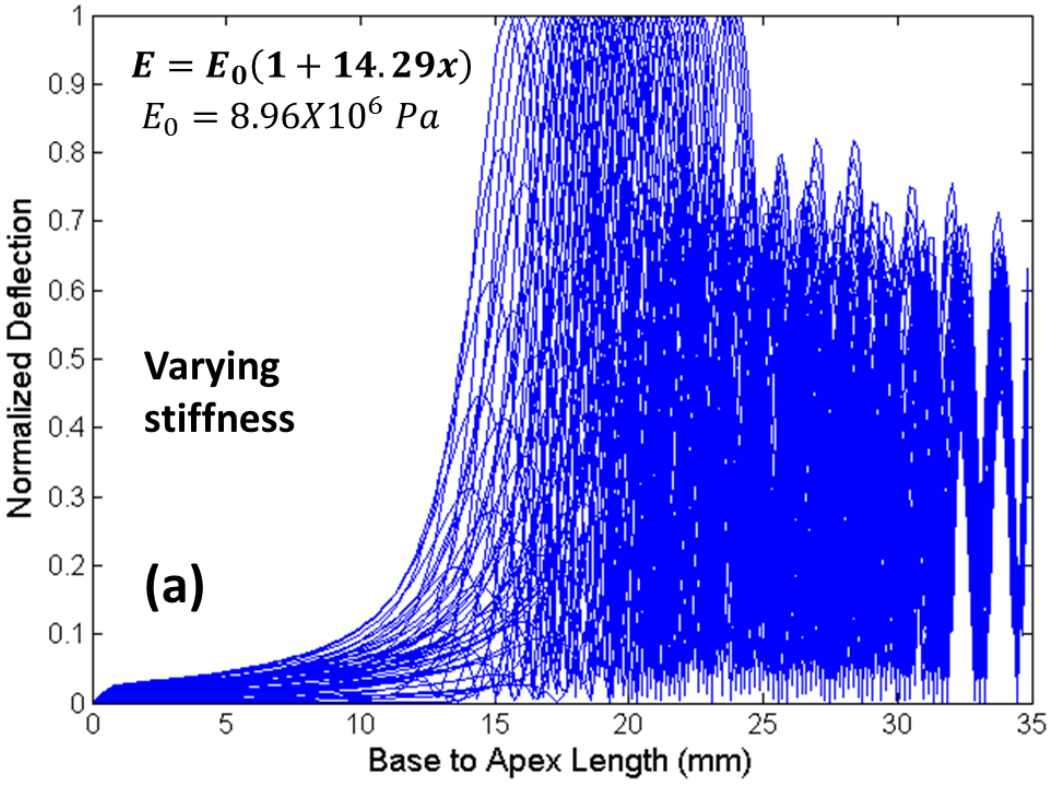

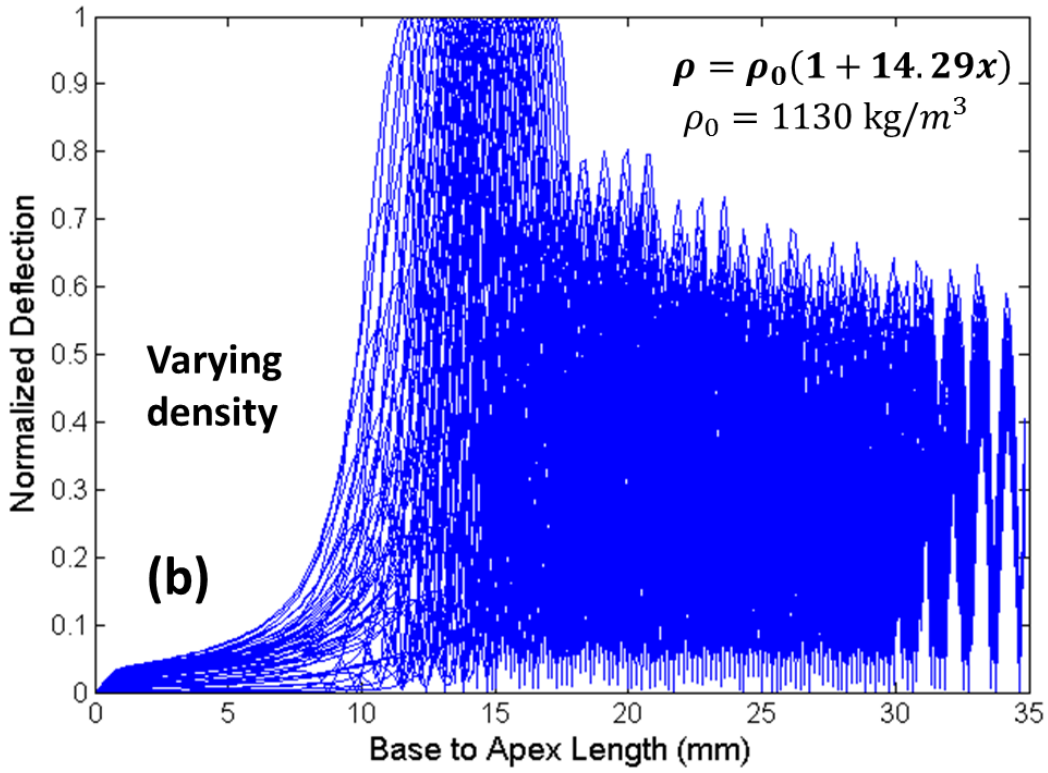
$\boldsymbol{\rho = \rho_0(1 + 14.29x)}$
$\rho_0 = 1130\ \mathrm{kg}/m^3$
Varying density
(b)
Normalized Deflection
Base to Apex Length (mm)

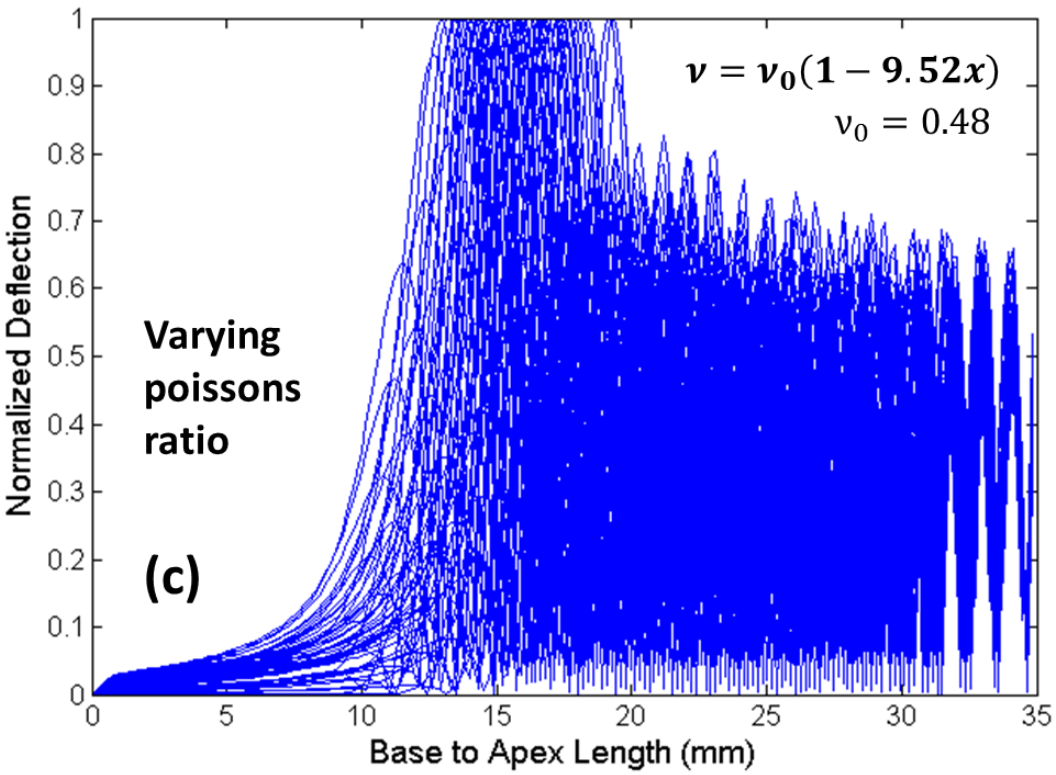
$\boldsymbol{\nu = \nu_0(1 - 9.52x)}$
$\nu_0 = 0.48$
Varying poissons ratio
(c)
Normalized Deflection
Base to Apex Length (mm)

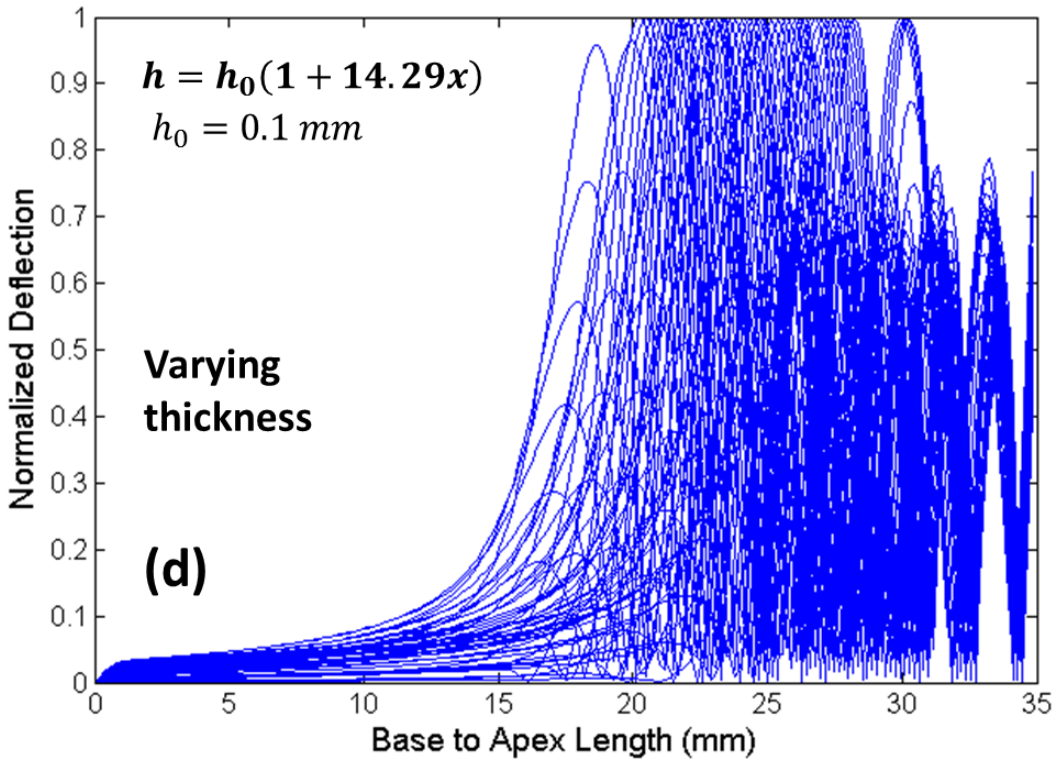


Figure 4.9: Deflection profile of the device with functionally graded (a) Stiffness (b) Density (c) Poissons ratio (d) Thickness.

Figure 4.9 shows the deflection response of the structure with different functionally graded model parameters. The same frequency band (4.5 KHz – 5.5 KHz) is considered as our reference problem like we investigated with the homogeneous model parameters. Setting a threshold deflection amplitude, while using homogeneous model parameters the required frequency band can be selected from the length segment 13.3 mm to 20.1 mm (see Figure 4.8), whereas using functionally graded stiffness same frequency band can be selected from the length segment 15.6 mm to 24.2 mm (ref. Figure 4.9a and Figure 4.10). Likewise, using functionally graded density, poissons ratio and thickness it is possible to select the 4.5 KHz – 5.5 KHz band from the length segment 11.6 mm – 17.3 mm, 13.0 mm – 19.3 mm, 20.3 mm – 30.3 mm, respectively. Figure 4.10 explicitly shows the effect of

the parameters in the selection process. Figure 4.10 suggests that poissons ratio isn't a significant parameter in manipulating the frequency band selection. However plate thickness and stiffness has substantial effect in the design parameters. Using the proposed functionally graded thickness and stiffness it is possible to select the targeted frequency band from the different section of the domain and require wider segment compared to the homogeneous model. Alternatively, narrower length section can be measured to sense the same frequency band with defined density function.

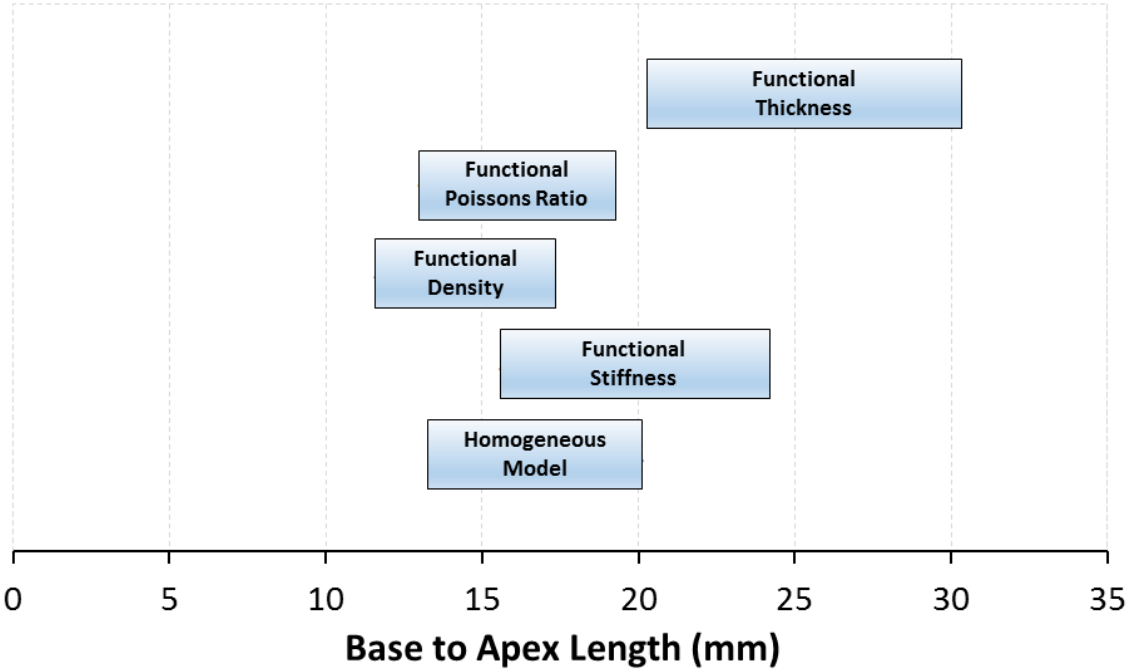


Figure 4.10: Length segment of the device from where frequency band 4.5 KHz – 5.5 KHz can be selected using homogeneous or functionally graded model parameters.

## 4.4 Chapter Summary

In summary, a cochlea-inspired predictive model for plate-type band-pass frequency sensor is developed. In many disciplines of science and technology, it is essential

to select a band of frequencies with highest resolution, named as band pass frequency sensor/filter. A considerable number of studies have been performed from last couple of decades to present mechanical broadband frequency sensors/filters. However, a comprehensive and comparatively fast predictive model is missing and utmost necessary in order to conduct an optimization study before any design proposal. In this work, a predictive model for band pass frequency sensor is developed so that the frequency band and the model parameters can be selected predictively. It is expected that the developed predictive model can boost the artificial cochlea technology since the human cochlea also performs as band pass frequency sensor, naturally. In this work, following the geometry of the basilar membrane, trapezoidal structure mimicking the basilar membrane is suggested for the sensor device. The predictive model is developed with utmost flexibility that not only can manage homogeneous but also any functionally graded model parameters. The model is flexible enough to adopt different types of boundary conditions. With homogeneous model parameters, it has been found that a specific band of frequency can be selected from a distinct segment of the model. It has been reported that it is possible to shift, wide or narrow the length segment using functionally graded structure towards selecting the same frequency band. The outcome confirms that using the predictive model it is possible to extensively manipulate the frequency selection attributes of the model, predictively. The predictive model in numerically validated using the simulation tool COMSOL Multiphysics and it has been found that our proposed model is almost 3 times faster than the FEM technique. Though, in this work, deflection amplitude is referred as sensing parameters, however the deflection amplitude can easily be converted to electrical signals through implementing smart materials, specifically piezoelectric material. The

predictive model can be linked to any optimization tool to get the user required optimized geometry for any target frequency band.

# CHAPTER 5: BASILAR MEMBRANE (BEAM MODEL)

Although in many past articles basilar membrane is considered as a continuous membrane to model the artificial cochlea, however it has been reported that, in reality, BM consists of a series of closely attached fixed beams. In this research, plate model is proposed where a specific frequency band is targeted to be sensed without losing any frequency information within the target band. A beam model is also proposed to design a broadband frequency sensor where selection of different specific frequencies is essential. As noted in chapter 4, several attempts were made in recent past to model BM based mechanical frequency selection devices, where majority of these attempts adopted the beam array structure. Though few experimental studies are performed, a comprehensive predictive model is missing to select the model parameters and target a frequency band, predictively. Hence in this research, along with the plate type, a predictive model is also developed for the BM based beam type sensor.

## 5.1 Model Description

In developing the beam model a series of thin beam are considered with linearly varying length. Beams are accommodated in a trapezoidal frame following the geometric

configuration of the real basilar membrane. A representative model of the proposed beam type sensor is shown in Figure 5.1.

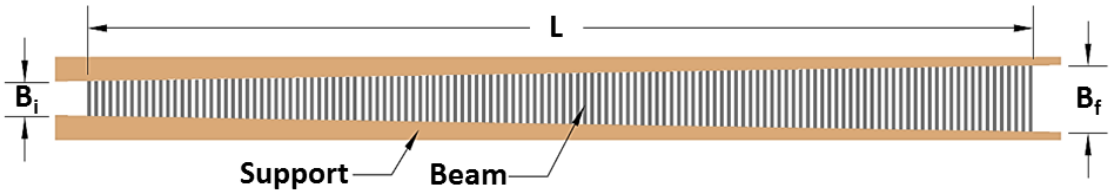


Figure 5.1: Envisioned basilar membrane beam model

## 5.2 Analytical Formulation

Likewise the BM plate model, in developing the predictive model for the beam geometry, it is intended to develop the most flexible model that can be used in manipulating the device geometry and target frequency band extensively. To achieve the objective, several flexibilities are incorporated in the proposed predictive model as listed below:

6. Stiffness $[E(x, y)]$ (homogeneous / functionally graded)
7. Beam width $[b(x, y)]$ (homogeneous / functionally graded)
8. Thickness $[h(x, y)]$ (homogeneous / functionally graded)
9. Length $[L(x, y)]$ (homogeneous / functionally graded)
10. Density $[\rho(x, y)]$ (uniform / functionally graded)
11. Boundary condition (fixed / simply supported)

Apart from the listed conditions, other model parameters are considered constant. Dynamic equation of a beam can be represented as shown is equation 5.1, where $\eta$ and P are the deflection of the beam and downward uniform pressure on beam top surface,

respectively. It is assumed that each beam is distinct and doesn't influence the deflection behavior of its neighboring beams. Also assumed that, each beam only deflects vertically. Twisting and lateral deflections are ignored. Hence, each beam can be considered as a line element. Since, each beam is independent, the dynamic equation 5.1 is applicable for each individual beam, only by adjusting the geometric configurations for each beam.

$$\frac{\partial^2}{\partial x^2}\left(EI\frac{\partial^2 \eta}{\partial x^2}\right) + \rho A\frac{\partial^2 \eta}{\partial t^2} = P \qquad (5.1)$$

$$I = \frac{1}{12}bh^3 \qquad (5.2)$$

Where, A is the cross-section area of the beam. Letting $D = EI$, equation 5.1 can be represent as

$$\frac{\partial^2}{\partial x^2}\left(D\frac{\partial^2 \xi}{\partial x^2}\right) + \rho A\frac{\partial^2 \xi}{\partial t^2} = P \qquad (5.3)$$

Considering harmonic pressure $\left(\mathrm{P} = \mathrm{p}e^{i\omega t}\right)$ excitation and corresponding harmonic response of the beams $\left(\eta = \xi e^{i\omega t}\right)$, equation 5.3 can be modified to equation 5.4, where, $\xi = \xi(x, y)$ is the dynamic deflection of the beam and ω is the excitation frequency.

$$\frac{\partial^2}{\partial x^2}\left(D\frac{\partial^2 \xi}{\partial x^2}\right) - \rho A\omega^2 \xi = p$$

$$\frac{\partial^2 D}{\partial x^2}\frac{\partial^2 \xi}{\partial x^2} + D\frac{\partial^4 \xi}{\partial x^4} - \rho A\omega^2 \xi = p \qquad (5.4)$$

Equation 5.4 is the final differential form of the beam deflection equation. Central difference method is adopted to solve the equation. Finite difference approximation of the derivative terms are shown in equation 5.5 and 5.6.

$$\frac{\partial^4 \xi}{\partial x^4} = \frac{1}{\Delta x^4}\left(\xi_{i-2,j} - 4\xi_{i-1,j} + 6\xi_{i,j} - 4\xi_{i+1,j} + \xi_{i+2,j}\right) \qquad (5.5)$$

$$\frac{\partial^2 \xi}{\partial x^2} = \frac{1}{\Delta x^2}\left(\xi_{i-1,j} - 2\xi_{i,j} + \xi_{i+1,j}\right) \qquad (5.6)$$

x- is defined as the longitudinal axis of the beam and using finite difference method each beam is discretized longitudinally. The whole sensor domain is discretized as a matrix, where each row represents an individual beam. Each beam is discretized with same number of nodes, hence $\Delta x$ may vary depending on length of the beam. $\Delta y$ is the distance between two beams and consistent throughout the model. Since central difference scheme is adopted, it is required to count at least two node points on every ends of the node point where we intend to implement the equation 5.4 and calculate the deflection amplitude. Similar to the plate model (ref. section 4), fictitious node points are imagined in both ends of each beam. Boundary conditions are considered to find the finite difference deflection equation at fictitious node points as described in chapter 4.

## 5.3 Result and Discussion

The final dynamic equation 5.4 of the basilar membrane beam model is computed using a customized computer code written in MATLAB. Initially, homogeneous model parameters are considered to test the functionality of the proposed predictive model. In the homogeneous model, all the model parameters are considered constant, except the length of each beam. In this study, length of the beams are set such that apex end beam length is 1.5 times than the beam at the base end. The model properties that are considered for the homogeneous structure is listed in the Table 4.1.

Table 5.1: Parameters used for homogeneous model

| Beam Parameters | Value | Unit |
|---|---|---|
| Stiffness (E) | 68.9 | GPa |
| Density (ρ) | 2700 | $Kg/m^3$ |
| Beam width (b) | 2 | mm |
| Beam thickness (h) | 1 | mm |
| Base beam length ($l_i$) | 20 | mm |
| Apex beam length ($l_f$) | 30 | mm |
| Total number of beams | 20 | |
| Beam distance (Δy) | 4 | mm |
| Device length (L) | 116 | mm |

In this analysis, it is considered that beams are fixed connected in both ends with the supports. Unit harmonic downward pressure is applied on top surface of the beams. Only first mode of the beam vibration is considered for frequency selection purpose. Thus, maximum beam deflection is recorded at the middle of the beams. Figure 5.2 presents the normalize deflection amplitude of the beams measured at mid-point of the beams. Since base end beams are shorter compared to the apex end beams, higher frequencies can be sensed from the base end (ref. Figure 5.2). Figure 5.3 reports that using the proposed model and homogeneous parameters listed in Table 4.1, it is possible to sense a frequency band 5.95 KHz – 12.95 KHz.

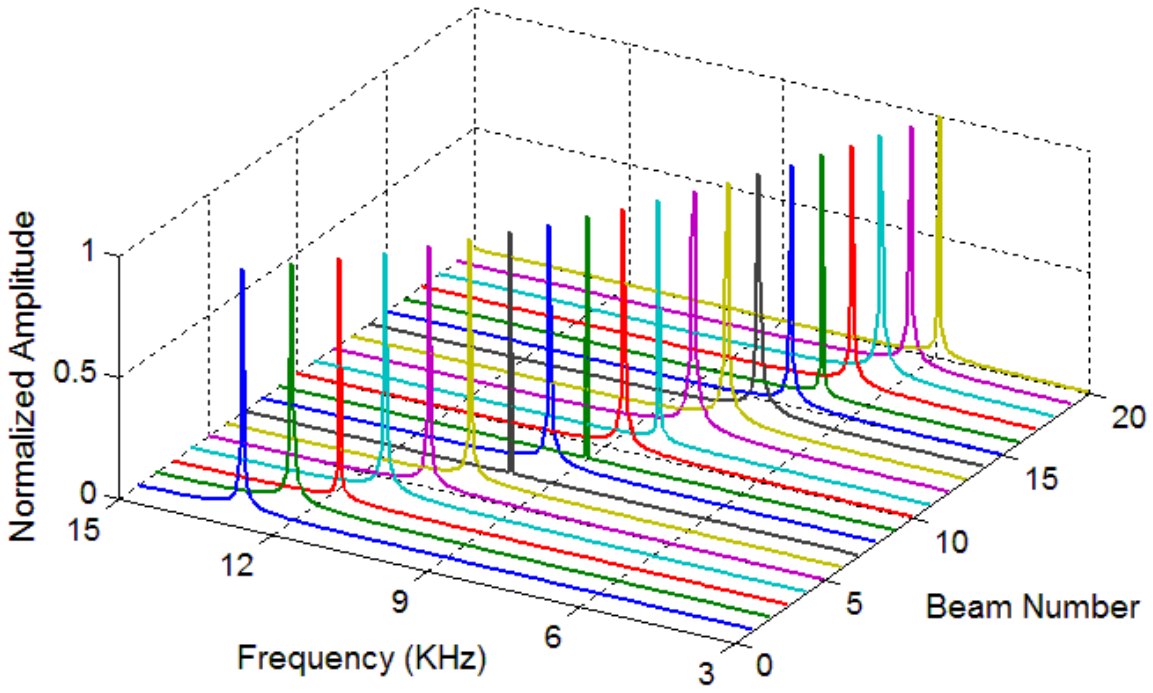


Figure 5.2: Normalized deflection amplitude at middle point of the beams for a frequency range of 3 KHz – 15 KHz. Beam number counted from the base to apex end.

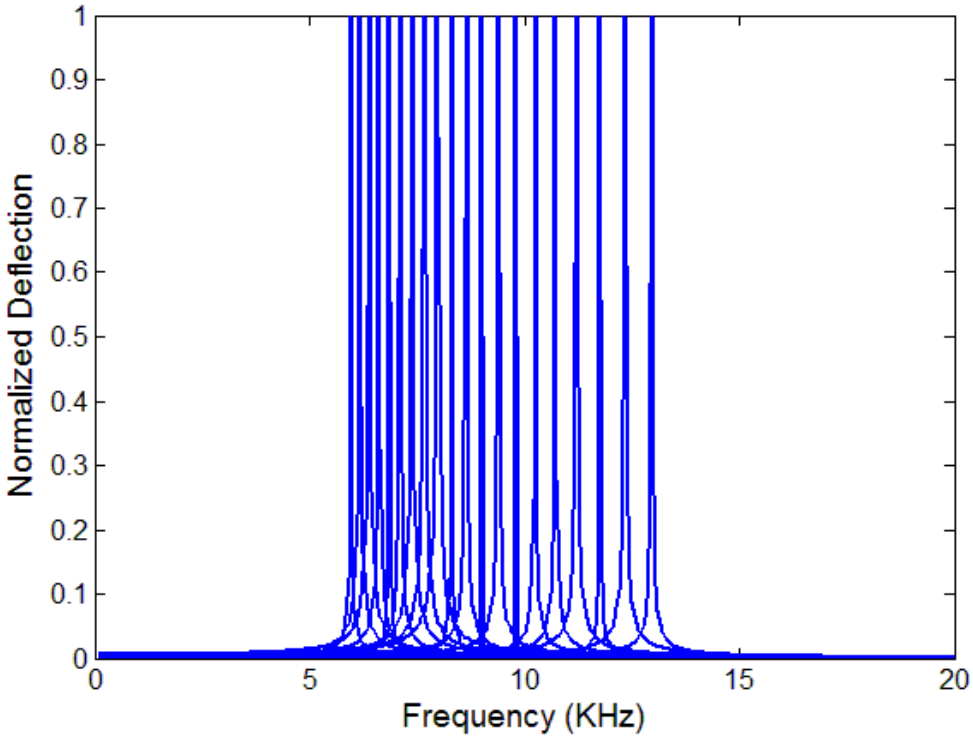


Figure 5.3: Normalized deflection of the beam center point. 2-D representation of Figure 5.2.

## 5.4 Numerical Investigation

Next, to verify, the analytically developed proposed predictive model is compared with the Finite Element Model (FEM) simulated in the COMSOL Multiphysics environment. Frequency domain analysis is performed. Similar homogeneous model parameters are considered in the FEM model as listed in Table 4.1.

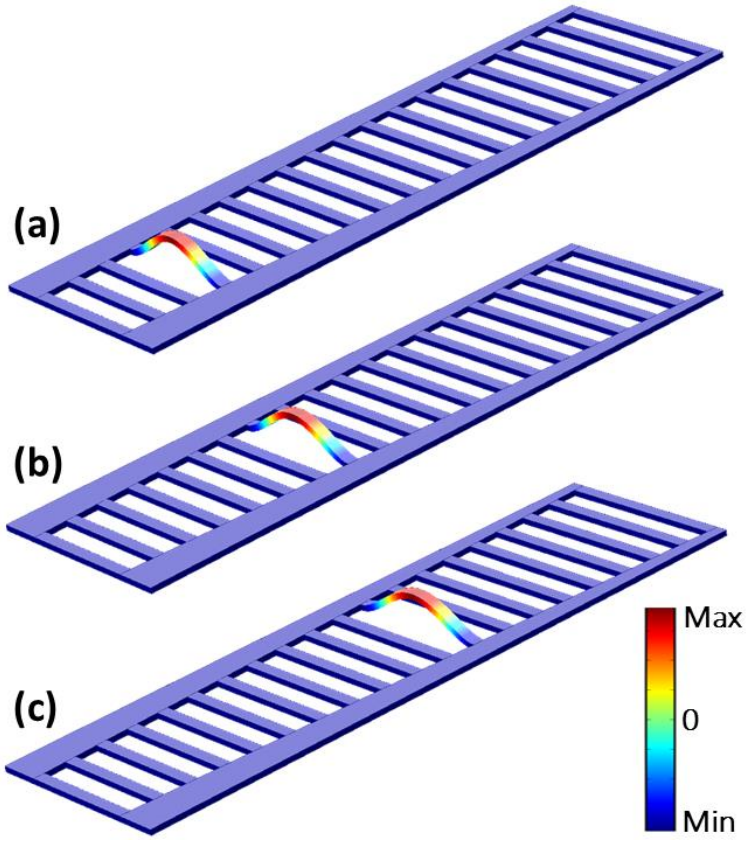


Figure 5.4: Numerically (using COMSOL multiphysics) obtained deflection profile of the sensor at (a) 11.07 KHz (b) 9.23 KHz and (c) 7.81 KHz

The analytically developed predictive model suggest that it is possible to select 11.2 KHz, 9.4 KHz and 7.95 KHz from the $4^{th}$, $8^{th}$ and $12^{th}$ beams of the device, respectively (ref. Figure 5.2). FEM study verifies the predictive model strongly by selecting 11.07 KHz, 9.23 KHz and 7.81 KHz from the $4^{th}$, $8^{th}$ and $12^{th}$ beams, respectively (see Figure 5.4).

While the predictive model reports that, 5.95 KHz – 12.95 KHz frequency band can be sensed using the proposed model, FEM study confirms the argument with 5.81 KHz – 12.82 KHz frequency selectivity. It has also been counted that, considering the computation time, our developed model is almost five (~ 3) times faster than the FEM method.

## 5.5 Frequency Band Manipulation

The predictive model is developed such that it can handle not only homogeneous, but also functionally graded model parameters to allow extensive flexibility to manipulate frequency sensing ability of the proposed model. Functionally graded stiffness, density, beam thickness and beam width are considered here in this model to proceed to make the model truly flexible. Each time, only one parameter is defined as functionally graded while other parameters are constant. In this work simple linear functions are considered to define functionally graded parameters, however the predictive model is able to manage any type of complex functions (e.g. exponential, logarithmic, higher order functions or any digitized or discrete properties distributed over the entire domain). Parameters are defined such a way that at the basal end beam the magnitude of the specific parameter is same as it was considered for the homogeneous model, however, the magnitude of the parameter increases along the model length and gained 1.5 times at the apex end beam.

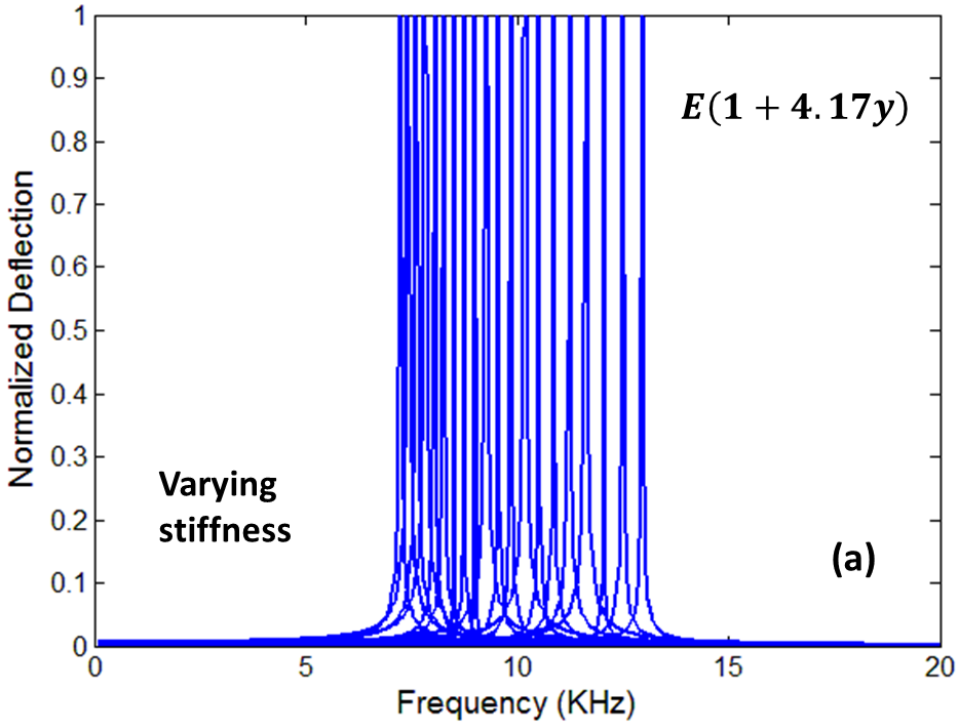
$E(1 + 4.17y)$
Varying stiffness
(a)
Normalized Deflection
Frequency (KHz)
0
0.1
0.2
0.3
0.4
0.5
0.6
0.7
0.8
0.9
1
0
5
10
15
20

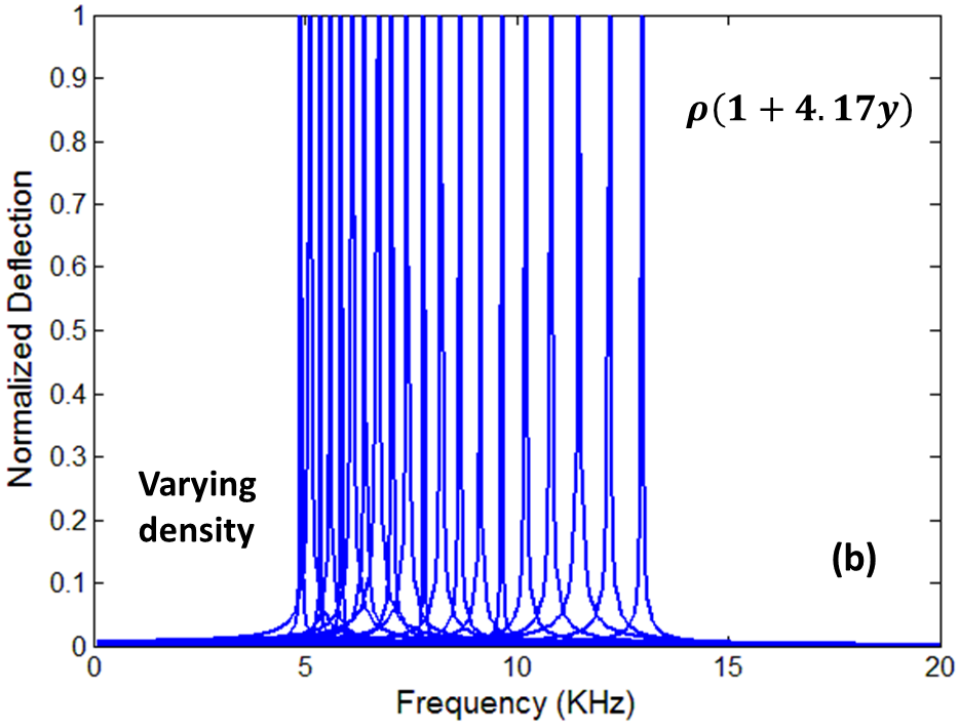
$\rho(1 + 4.17y)$
Varying density
(b)
Normalized Deflection
Frequency (KHz)
0
0.1
0.2
0.3
0.4
0.5
0.6
0.7
0.8
0.9
1
0
5
10
15
20

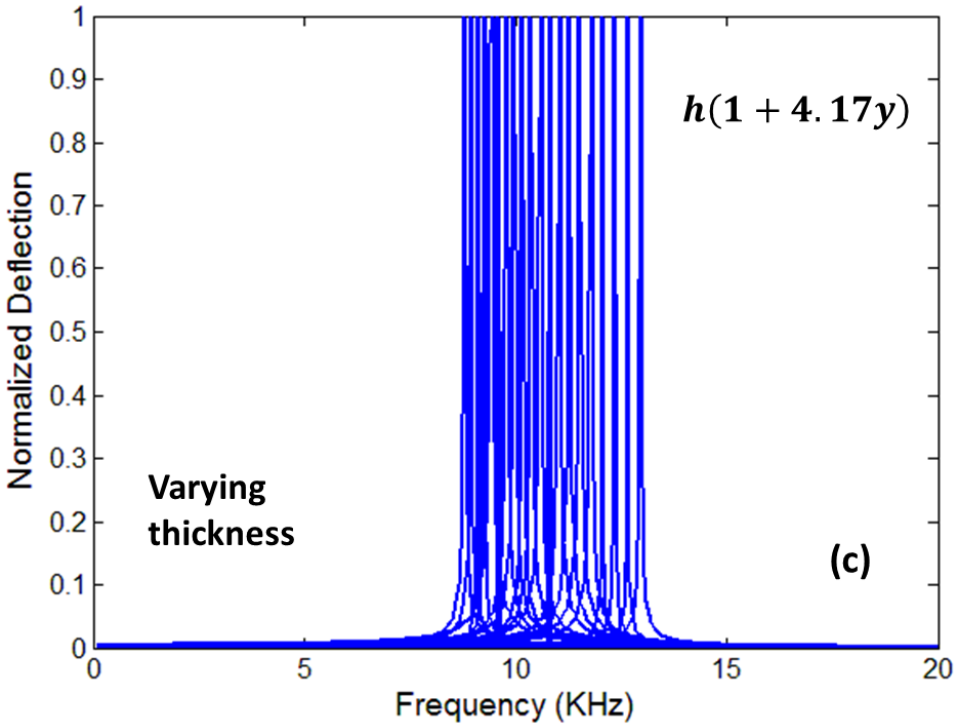


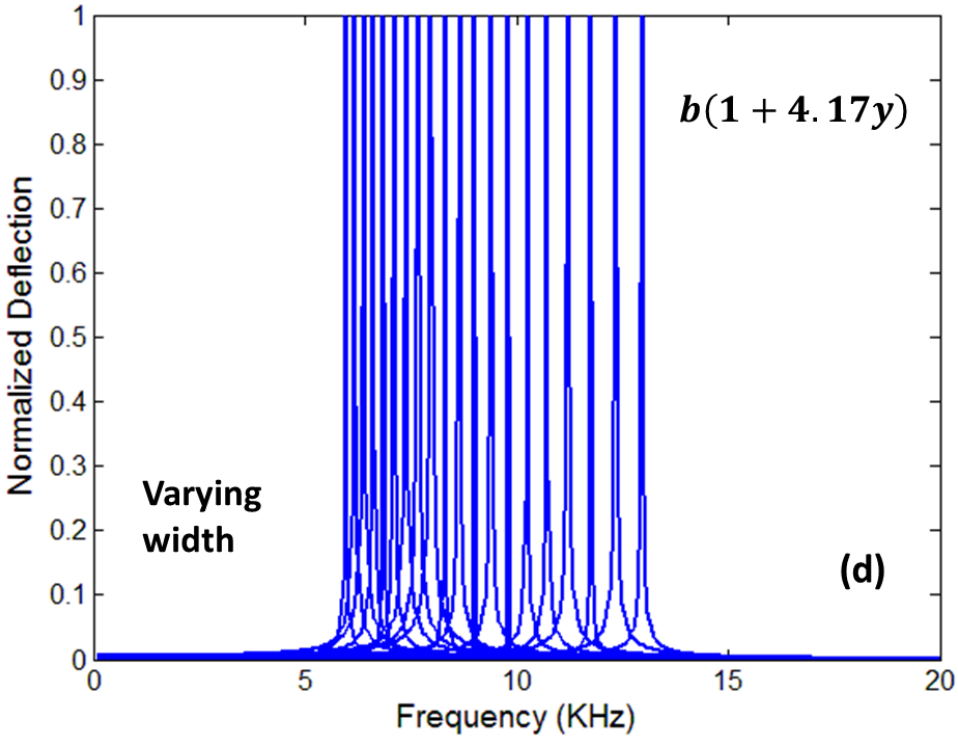


Figure 5.5: Normalized deflection amplitude of the center point of the device with functionally graded (a) Stiffness (b) Density (c) Thickness and (d) width.

Figure 5.5 shows the deflection response of the beams with different functionally graded model parameters. While using homogeneous model parameters it is possible to select a frequency band 5.95 KHz – 12.95 KHz using the envisioned beam model (ref. Figure 5.3), whereas using the proposed functionally graded stiffness the target frequency band can be narrowed down to 7.25 KHz – 12.95 KHz. Since in the base end beam stiffness stays same compared to homogeneous model, which results identical maximum limit of the target frequency band. Alternatively, minimum frequency limit shifts to higher frequency due to the increased of apex end beam stiffness using the functionally graded stiffness model. Likewise, using functionally graded density, beam thickness and width it is possible to select frequency band 4.9 KHz – 12.95 KHz, 8.8 KHz – 12.95 KHz and 5.95 KHz – 12.95 KHz, respectively.

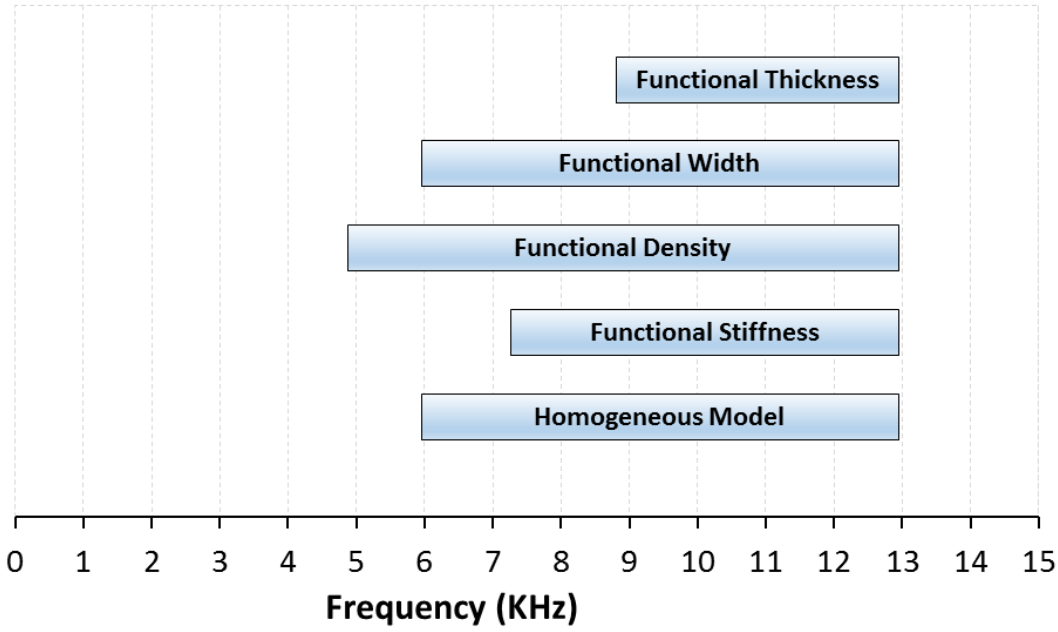


Figure 5.6: Frequency band that can be selected using homogeneous or functionally graded model parameters specific to the example presented.

Figure 4.10 explicitly shows the effect of the parameters in the selection process. Figure 4.10 suggests that beam width isn't a significant parameter in manipulating the frequency band selection. However beam thickness, density and stiffness possess substantial impact in design parameters.

## 5.6 Chapter Summary

In summary, a BM-inspired predictive model for beam-type band-pass frequency sensor is developed. In this work, following the geometry of the basilar membrane, a series of beams in a trapezoidal structure with varying beam lengths is suggested for the sensor device. The predictive model is developed with utmost flexibility that not only can manage homogeneous but also any functionally graded model parameters. The model is also flexible enough to adopt different types of boundary conditions. With homogeneous model parameters, it has been found that a specific band of frequency can be selected using the proposed beam sensor. It has also been reported that it is possible to shift, wide or narrow the target frequency band using functionally graded structure. The outcome confirms that using the predictive model it is possible to extensively manipulate the frequency selection attributes of the model, predictively. The predictive model in numerically validated using the simulation tool COMSOL Multiphysics and it has been found that our proposed model is almost ~ 5 times faster than the FEM technique. Though, in this work, deflection amplitude is referred as sensing parameters, however the deflection amplitude can easily be converted to electrical signals through implementing smart materials, specifically piezoelectric material. The predictive model can be linked to any optimization tool to get the user required optimized geometry for any target frequency band.

# CHAPTER 6: COCHLEA MECHANICS

The cochlea is a highly developed and complex mechanical sensory system. Its function is to convert a single time-varying pressure signal into a time-varying pattern of excitation on the approximately 25,000 fibers of the eighth cranial nerve. In this chapter, the anatomy and basic function of the cochlea are described, and the landmark measurements that have shaped the modern understanding of cochlear operation are quoted. Finally, a simple abstract model that captures the essential features of cochlear operation is described.

## 6.1 Anatomy

The general description of the anatomy is based on the treatments of Dallos [91], Evans [92], Kessel and Kardon [93], Moller [94], and Shepherd [95]. Figure 6.1 shows the anatomy of the human auditory periphery. Sound waves travel down the canal or external auditory meatus, and vibrate the eardrum or tympanic membrane. On the other side of the eardrum is the internal auditory meatus, an air-filled cavity that leads to the nasopharynx via the Eustachian tube, which opens during swallowing to equalize pressure across the eardrum. Vibrations of the eardrum couple into the small bones or ossicles of the middle ear, called the hammer or malleus, anvil or incus, and stirrup or stapes. The footplate of the stapes presses on the oval window, an opening in the vestibule of the inner ear. Vibration

of the stapes causes waves to travel in the fluid inside the vestibule and the cochlea. The round window allows pressure relief for the incompressible cochlear fluid.

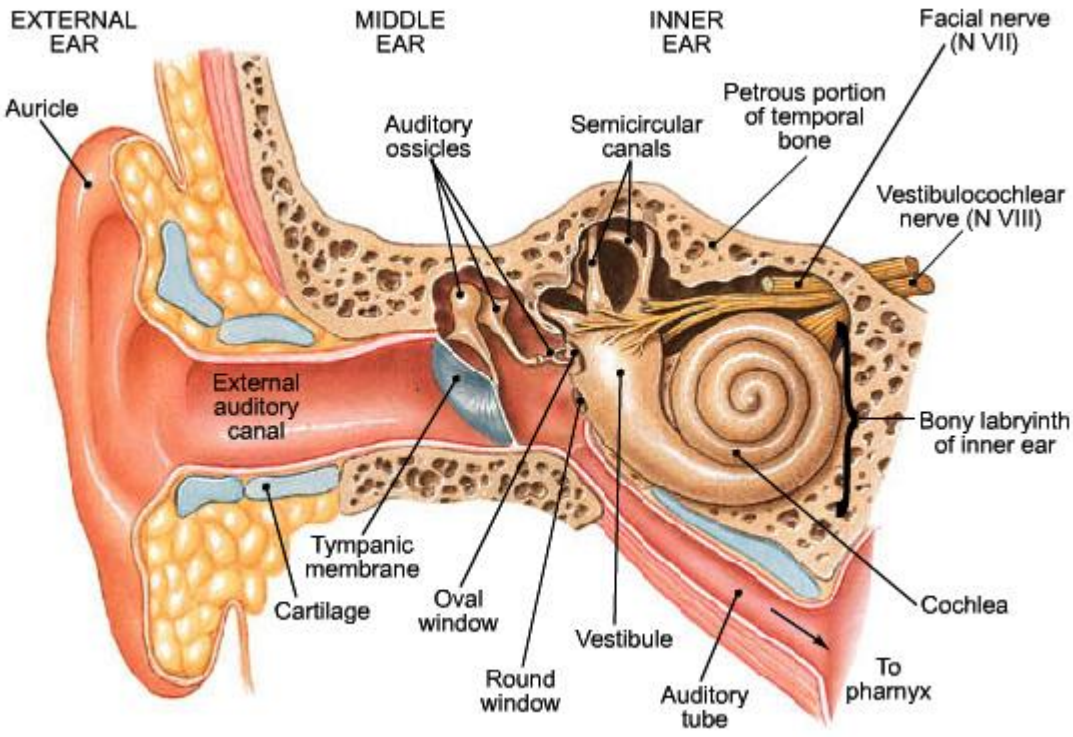


Figure 6.1: Anatomy of the human auditory periphery.

The middle ear provides a mechanical advantage to allow the pressure fluctuations of the air to couple energy efficiently into movement of the fluid-and-membrane structure of the cochlea. However, the middle ear is not a simple air-to-water impedance matcher, as is commonly believed; to characterize it as such is to assume incorrectly that acoustic (compressional) waves are propagated in the cochlear fluid. Rather, waves are propagated by the combined movement of the incompressible cochlear fluid and the membranes inside the cochlea, so the middle ear is matching the impedances of the air and the stiffest part of

the membrane. A discussion of the historical confusion surrounding this subtle point is given by Schubert [96].

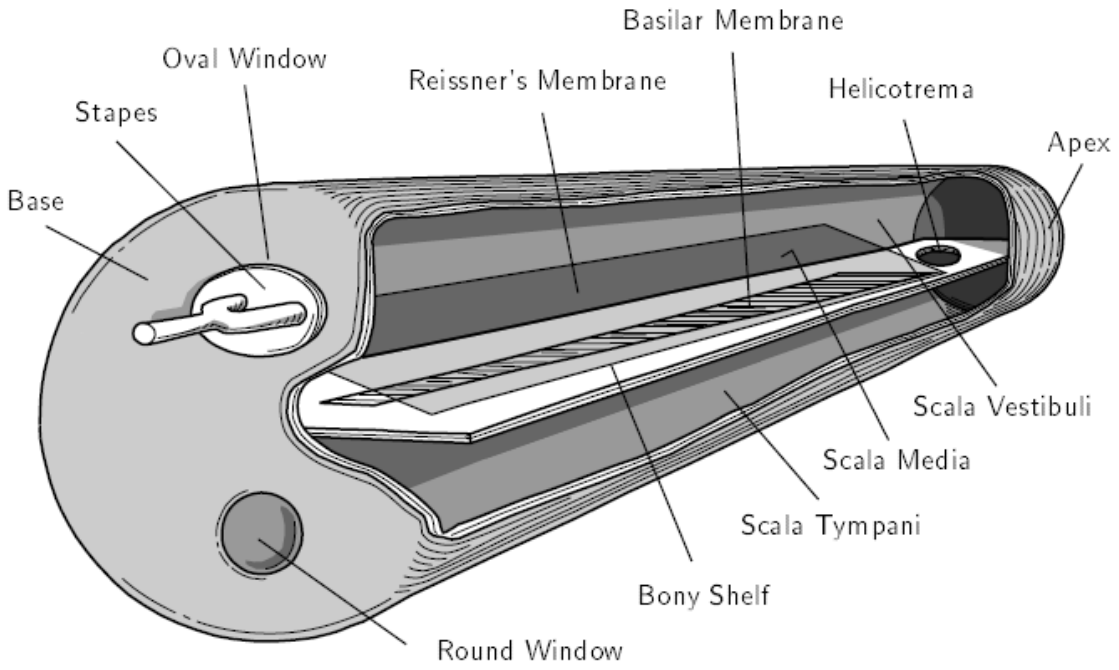


Figure 6.2: The unrolled cochlea, simplified to emphasize the bony shelf and widening of the basilar membrane [97].

The cochlea and vestibular apparatus are commonly believed to have evolved from the lateral line organ of fishes [95]. In humans, the cochlea is about 35 mm long and about 2 mm in diameter. If the spiral cochlea structure could be unrolled, it would appear as a long fluid-filled tube, with the basilar membrane and Reissner's membrane running down its length, as shown schematically in Figure 6.2. The membranes and the bony shelf or spiral osseus lamina subdivide the cochlea into three major compartments or scalae namely, the scala vestibuli, scala media, and scala tympani running from the base of the cochlea to the apex.

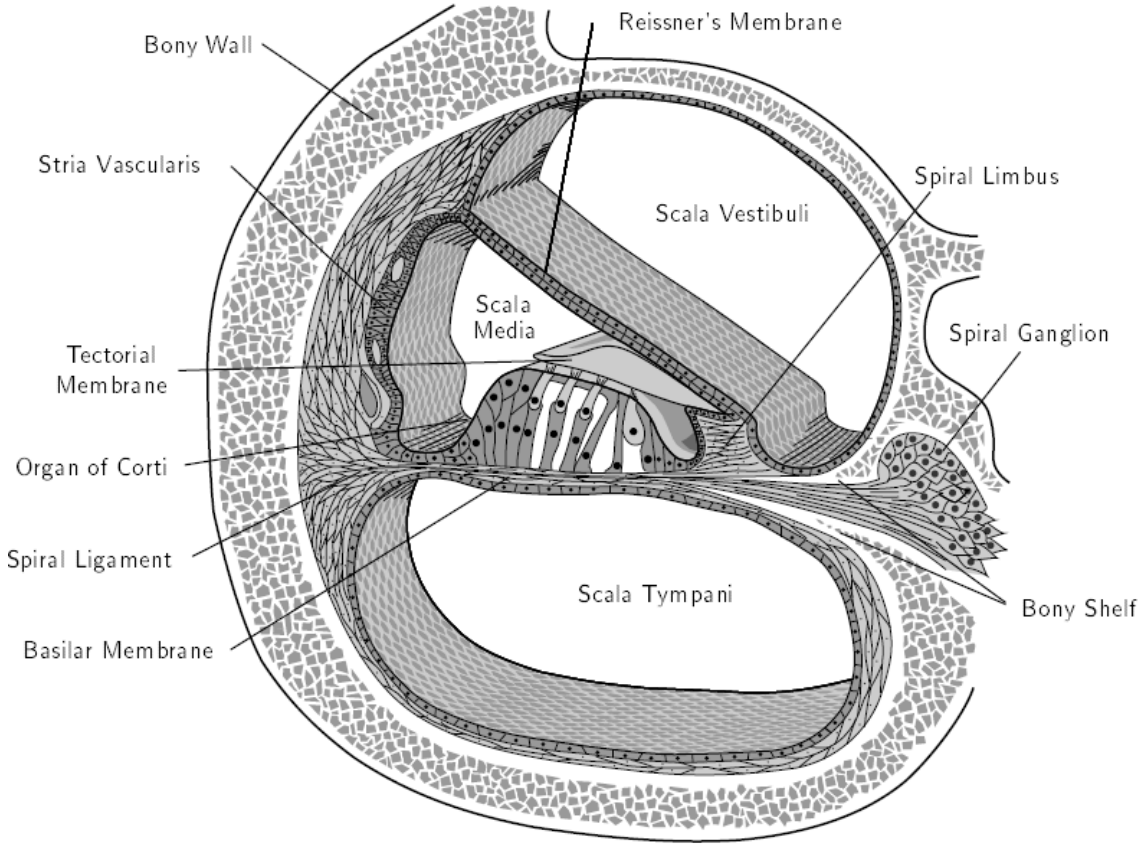


Figure 6.3: Cross-section through the cochlea [93].

The basilar membrane and Reissner's membrane run nearly the length of the cochlea. The scala media terminates near the apex of the cochlea. At the apex of the cochlea, the basilar membrane terminates, and a small hole in the bony shelf, called the helicotrema, allows the scalae vestibuli and tympani to join. The helicotrema allows for equalization of pressure and ionic concentration of the fluid in the scalae vestibuli and tympani.

The basilar membrane is not an isotropic stretched membrane; it consists of long, thin, beamlike fibers running across its width [98]. There is virtually no direct mechanical coupling from one fiber to the next. The basilar membrane is stiff and narrow (about 100

μm) near the base, and flexible and wide (about 500 μm) near the apex, with a smooth transition along its length. The stiffness of the basilar membrane decreases by at least a factor of 100 from base to apex, in an approximately exponential fashion [91]. Reissner's membrane is light, thin, and very flexible. It serves no mechanical purpose; its function is to provide ionic isolation between the scalae media and vestibuli. The fluid contained in the scalae vestibuli and tympani is called perilymph; it is high in sodium content and low in potassium content, similar to interstitial fluid. The scala media is filled with endolymph, a fluid that has a low sodium concentration but is rich in potassium. The difference in ionic concentration between the endolymph and perilymph is maintained by the dense capillary network called the stria vascularis, shown in Figure 6.3.

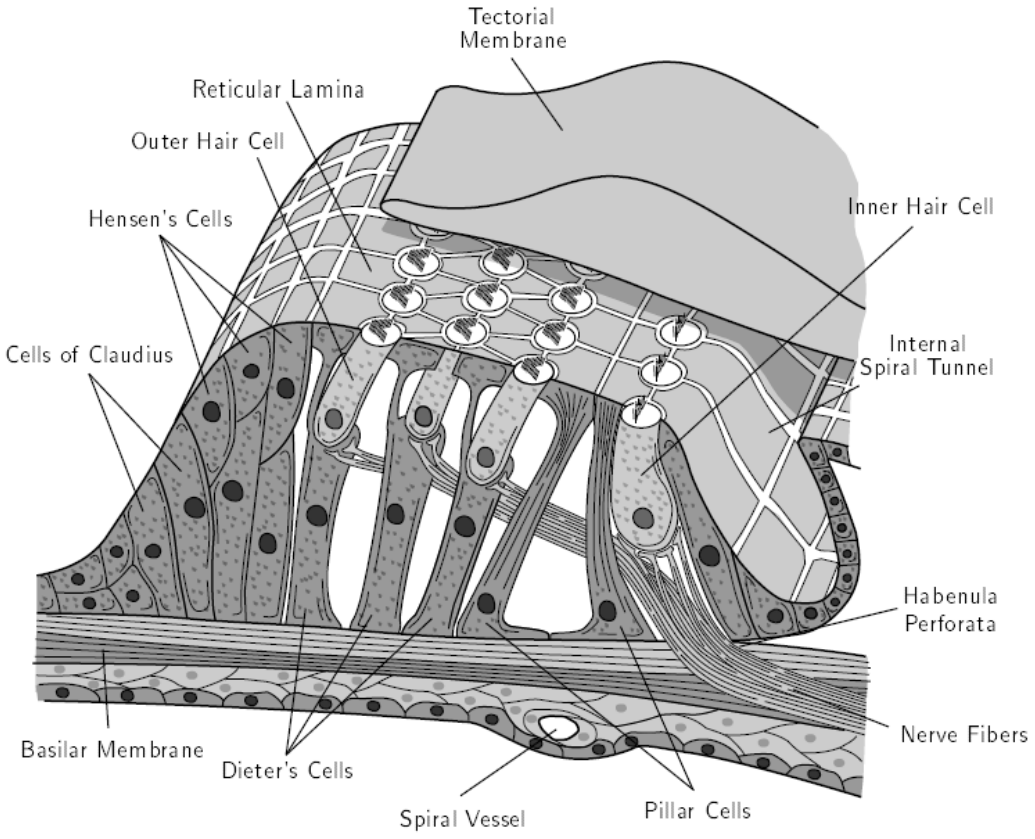


Figure 6.4: The organ of Corti, with the tectorial membrane partially cut away [93]

The stria vascularis is the site of intense metabolic activity, which necessarily requires access to the bloodstream for nutrients and waste disposal. The purpose of this sophisticated arrangement is to maintain the electrical potential difference, called the endocochlear potential, between the perilymph and endolymph. The endocochlear potential acts as a quiet power supply for the hair cells in the organ of Corti [99]; these hair cells are sensitive to tiny movements, and must be isolated from the noise of the circulatory system. A small blood vessel, called the spiral vessel, also runs beneath the basilar membrane, as shown in Figure 6.4, but no capillaries are extended into the organ of Corti.

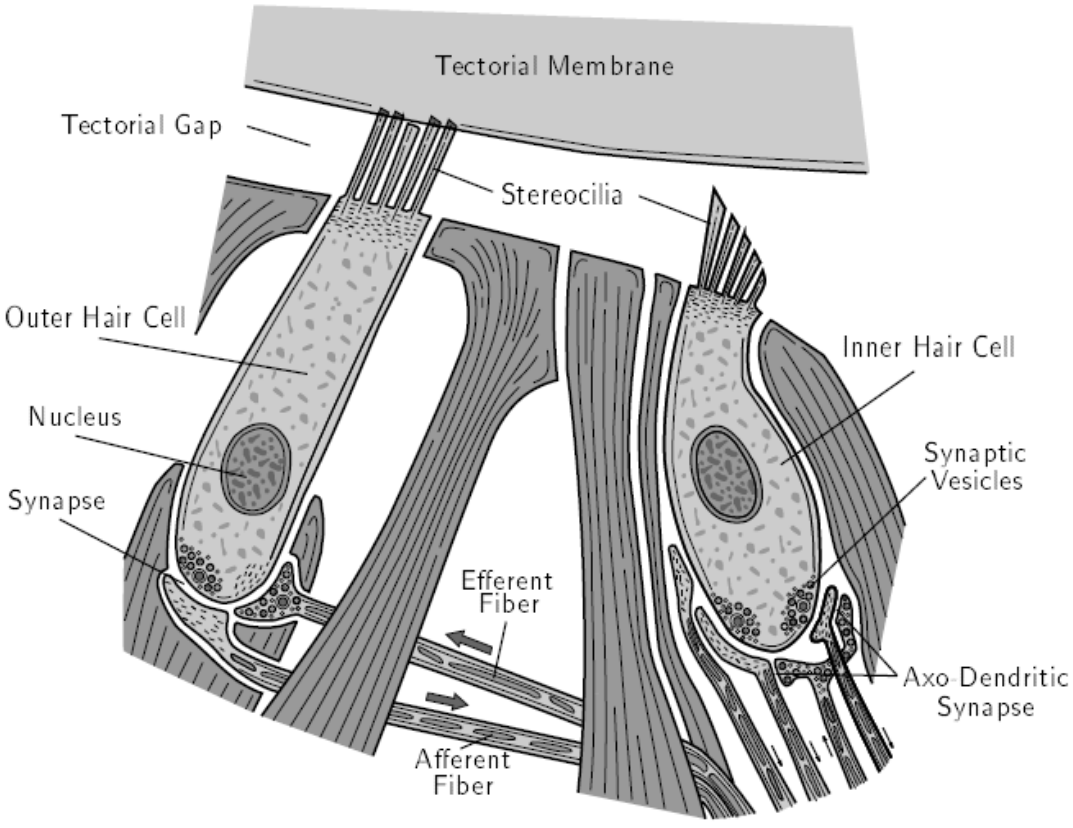


Figure 6.5: Detail of the inner and outer hair cells, showing their relationship to the tectorial membrane and to the nerve fibers [100].

When the hair cells of the organ of Corti draw power from the stria vascularis in response to an input sound, small fluctuations in the endocochlear potential can be measured. These fluctuations are called the cochlear microphonic, since the measured voltage waveform is an approximate replica of the sound itself. The tectorial membrane is a transparent, noncellular, flexible, gelatinous mass that is situated between the organ of Corti and Reissner's membrane. It is suspended above the organ of Corti from the spiral limbus, which is an enlargement of the cell lining of the cochlear interior. The fluid-filled space beneath the tectorial membrane and enclosed by the spiral limbus and organ of Corti is called the internal spiral tunnel or spiral sulcus.

The organ of Corti is shown in Figure 6.4. It resides on top of the basilar membrane, and contains one row of inner hair cells, and three to five rows of outer hair cells, so named for their position with respect to center of the spiral. There are about 3000 inner hair cells and about 9000 outer hair cells, spaced about 10 μm apart. The hair cells are rigidly attached to the basilar membrane by the supporting Dieter's cells and the pillar cells. The Dieter's cells have processes that extend upward to hold the tops of the outer hair cells; the resulting rigid upper surface of the organ of Corti is called the reticular lamina.

All the hair cells have stereocilia, or fine filaments, that extend upward into the tectorial gap from the reticular lamina. There are many important differences between the inner hair cells and the outer hair cells, as shown in Figure 6.5. The outer hair cells vary in length between about 30 μm at the base to about 70 μm at the apex. The length of the stereocilia of the outer hair cells is also graded, increasing from about 4 μm at the base to about 8 μm at the apex. The ends of the tallest stereocilia of the outer hair cells are

embedded firmly in the tectorial membrane, whereas the stereocilia of the inner hair cells are free to move in the fluid in the tectorial gap.

The stereocilia are arranged in a V or W formation (Ref. Figure 6.6) for the outer hair cells, and in a shallow curve for the inner hair cells. The outer hair cells are tall, slim, and stiff, with fine tensile filaments that wrap around the cell body, to form a kind of skeleton structure [101]. In addition, the outer hair cell walls are known to contain actin, which is the contractile protein of muscle. The outer hair cells make contact with the supporting cells only at their tops and bottoms; most of the length of the outer hair cell is free to move. By contrast, the inner hair cells are short, round, and flexible, with no tensile skeleton structure. They have an approximately uniform size, regardless of their position along the length of the cochlea, and they are bound tightly by the supporting cells.

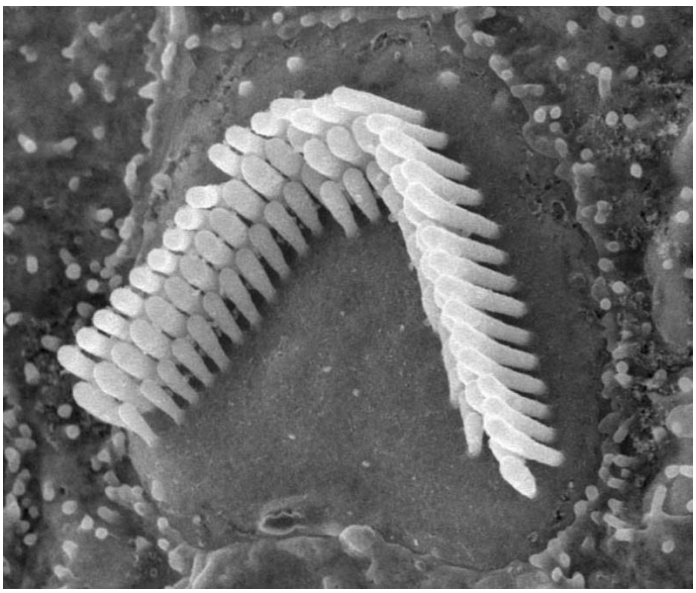

Figure 6.6: SEM image of stereocilia arranged in V-formation [102]

The relationship between the hair cells and the nerve fibers is shown in Figure 6.5. Nerve fibers that carry signals to the brain are afferent fibers, whereas those carrying signals from the brain are efferent fibers. The majority of nerve fibers that make connections to the outer hair cells are efferent, whereas the majority of nerve fibers that make connections to the inner hair cells are afferent. Connections from the hair cells to the afferent fibers are made by excitatory chemical synapses; connections from the efferent fibers to the hair cells are made by inhibitory synapses [103]. Synaptic vesicles in the transmitting cell release neurotransmitter into the synaptic cleft between the two cells, causing an influx of current into the receiving cell.

## 6.2 Function

The functional input to the cochlea is the stapes movement, which is a high-fidelity replica of the sound pressure in the air outside the ear. We are now concerned with how the cochlea performs its encoding of the input signal into nerve impulses on the cochlear nerve. Sinusoidal movement of the stapes causes waves to propagate down the fluid and membrane structure of the cochlea, as shown in Figure 6.7. The wave is not carried solely by compression of the fluid, since the cochlear fluid is essentially incompressible at audio frequencies; rather, the wave is propagated by the combined movement of the fluid and the membrane. Since the fluid cannot be compressed, conservation of fluid mass dictates that the round window must move in opposition to the stapes, as measured experimentally by von Bekesy [104].

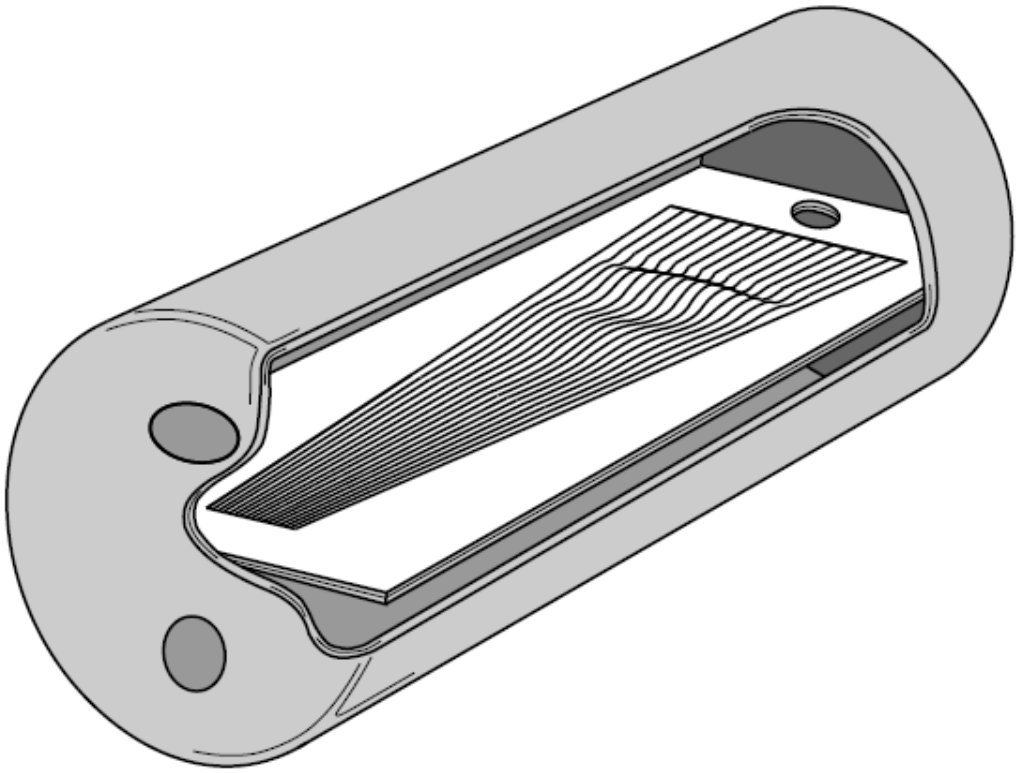

Figure 6.7: Propagation of a wave down the cochlea, for a fixed input frequency, viewed at one moment.

At the basal end of the cochlea, the basilar membrane is narrow and stiff, so the membrane-displacement waves propagate quickly with long wavelength. As the wave travels down the cochlea, the stiffness of the membrane decreases, so the waves slow down, become shorter, and increase in amplitude. At some point, called the best place for the given input frequency, the membrane will vibrate with maximum amplitude. Beyond the best place, the basilar membrane becomes too flexible and highly damped to support wave propagation at the given frequency, and the wave energy dissipates rapidly.

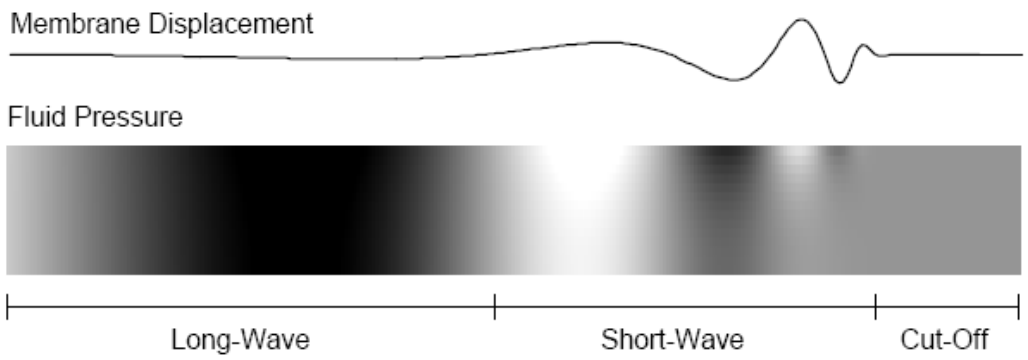


Figure 6.8: Detail of wave propagation, showing the membrane displacement and fluid pressure along a vertical slice through the lower chamber, for a sinusoidal stapes vibration.

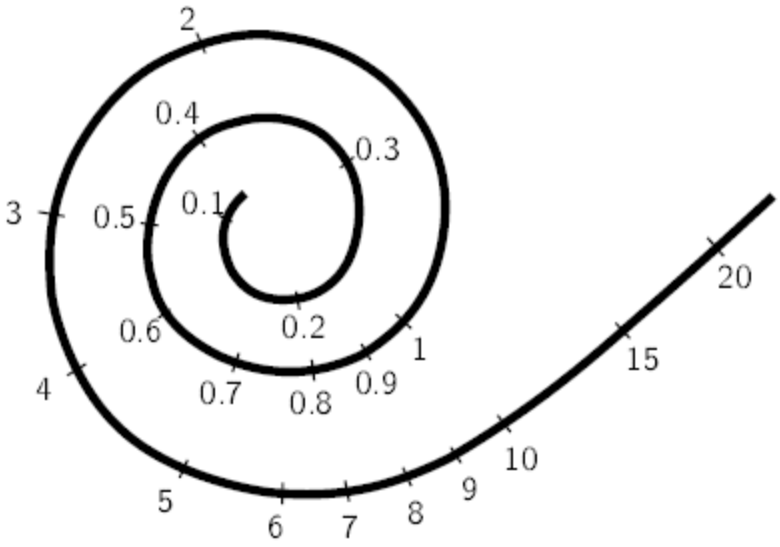


Figure 6.9: Approximate frequency map (in kHz) on the basilar membrane, inferred from noise-masking thresholds and other anatomical considerations [105].

The membrane displacement and fluid pressure in the lower chamber are shown schematically in Figure 6.8. The wave is said to be in the long-wave region when its wavelength is long with respect to the height of the duct. In this region, the fluid particle motion is constrained to be essentially horizontal, like a wall of fluid moving back and forth in a pipe. When the wavelength becomes short with respect to the height of the duct,

the wave is said to have entered the short-wave region. At this point, the wave propagates more like ripples on the surface of a deep pond, where the fluid particles trace out elliptical trajectories, with greater amplitude near the surface. Finally, the wave dies out in the highly damped cut-off region.

The position of maximum displacement of the basilar membrane varies approximately logarithmically with the frequency of the input, for frequencies above about 1 kHz [106]. Frequencies lower than 1 kHz are more compressed along the length of the cochlea, as shown in Figure 6.9. The coiling of the biological cochlea has no significant effect on the traveling wave [107, 108]. The primary purpose of the coiling appears to be to save space. The effect of basilar-membrane displacement on the stereocilia of the hair cells is shown in Figure 6.10. In this commonly accepted view, attributed to Ter Kuile [91], movement of the basilar membrane results in a shearing movement of the reticular lamina against the gelatinous tectorial membrane.

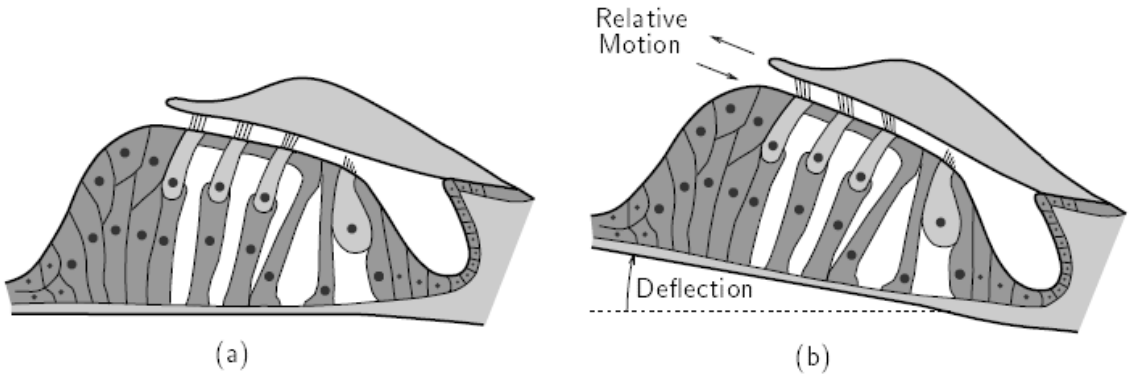


Figure 6.10: Shearing movement of the basilar and tectorial membranes, when the basilar membrane is displaced [94].

For small displacements, the degree of shear and hence the bending of the outer-hair-cell stereocilia, which are attached to the tectorial membrane is proportional to the

displacement of the membrane. Since the inner-hair-cell stereocilia are not attached to the tectorial membrane, they are bent by a force due to viscous drag as they move with respect to the fluid in the tectorial gap; this force is proportional to the velocity of basilar membrane. So, to a first order, outer-hair-cell stereocilia are stimulated in proportion to membrane displacement, whereas inner-hair-cell stereocilia are stimulated in proportion to membrane velocity.

Stimulation of the inner-hair-cell stereocilia in one direction triggers the influx of ionic currents into the hair cell, which depolarizes the membrane and leads to a release of neuro transmitter. Stimulating the inner-hair-cell stereocilia in the other direction has no effect, so it is common to model the inner hair cell as responding to a half-wave-rectified version of membrane velocity. The presence of neurotransmitter leads to an increased probability of the firing of an action potential or spike by the spiral ganglion cell. The spiking communication mechanism for an individual nerve fiber has an estimated dynamic range of 25 to 30 dB; however, the dynamic range of human hearing is on the order of 120 dB. Since as many as 10 or 20 spiral ganglion cells encode the output of a single inner hair cell, a significant part of the better performance at the system level may be due to the encoding of the output of a single inner hair cell by many spiral ganglion cells, which may have different sensitivities and spontaneous firing rates.

The behavior of outer hair cells is still a subject of research in the auditory community. Some researchers have shown that movement of the stereocilia triggers an influx of ionic current [109]; others have shown that injection of current or change in voltage triggers a change in length in vitro [101, 110, 111]. Taken together, these findings

would suggest that movement of the stereocilia triggers a change in length, although to date this mechanical-to- mechanical relationship has not been shown conclusively. Other circumstantial evidence implicates the outer hair cells as the force-generating active elements of the cochlea. The firm attachment of the outer-hair-cell stereocilia to the tectorial membrane would facilitate the generation of forces that could act between the basilar and tectorial membranes. The outer hair cells are located centrally in the organ of Corti, where the basilar membrane undergoes its largest excursion, and hence are favorably positioned to exert forces on the basilar membrane. Under the right conditions, it is likely that the outer cells act so as to add energy to the traveling wave, to amplify sounds that would otherwise be too weak to be encoded effectively by the inner hair cells and spiral ganglion cells.

Under some conditions, the active outer hair cells can become unstable, leading to oscillations. The resulting ringing in the ears is known as tinnitus. The oscillations can cause waves to travel both forward and backward along the cochlea. The backward-going waves can couple energy out through the bones of the middle ear to the eardrum, which then broadcasts sound out of the ear [112]. Other spectacular artifacts of the active processes include the Kemp echo, a reflected sound that follows stimulation by a click or tone burst [113].

Most active cochlear models assume that outer hair cells are capable of applying forces to the basilar membrane at frequencies that span essentially the entire range of hearing. The assumption of fast motility is being checked experimentally, and evidence is accumulating that the outer hair cells are capable of changing length at frequencies at least

up to 1 kHz [114], and possibly higher [115]. Note that the detailed mechanisms by which the inner hair cells are stimulated, and by which the outer hair cells may influence the wave propagation in vivo, are still unknown. This fascinating subject is known as cochlear micromechanics. Ter Kuile's shearing mechanism is one example of a micromechanical model; other interesting micromechanical models include models of viscous flow through the subtectorial gap from the spiral sulcus [116], and preferential bending of the basilar membrane in different regions [18, 117].

## 6.3 Abstraction

In human cochlea, basilar membrane is the key component in sensing sonic frequencies and filtering all other frequencies in the environment, which makes the cochlea most developed band pass filter in nature. Though in most past studies, basilar membrane is considered as plate for computational simplicity, however in reality it is made of numerous compact beams, connected through lateral ends of the basilar membrane (see Figure 6.11).

Each beam in the membrane shows flexural resonance response upon distinct sonic frequency input. Basilar membrane beams possess higher bending stiffness at its basal end, hence resonates at high sonic frequency (~ 20 KHz) excitation. Whereas beams at apical end resonates at lower frequencies due to its low bending stiffness. Hair cells in the cochlea employed to sense different frequencies with membrane resonance. As a nutshell, in developing a pass band sensor, basilar membrane performs four principal operations as listed below:

1. Perform local resonance
2. Sense desired frequency and filter all other frequencies in environment
3. Sense input frequency with some kind of sensory medium (e.g. hair cells)
4. Select frequency spatially

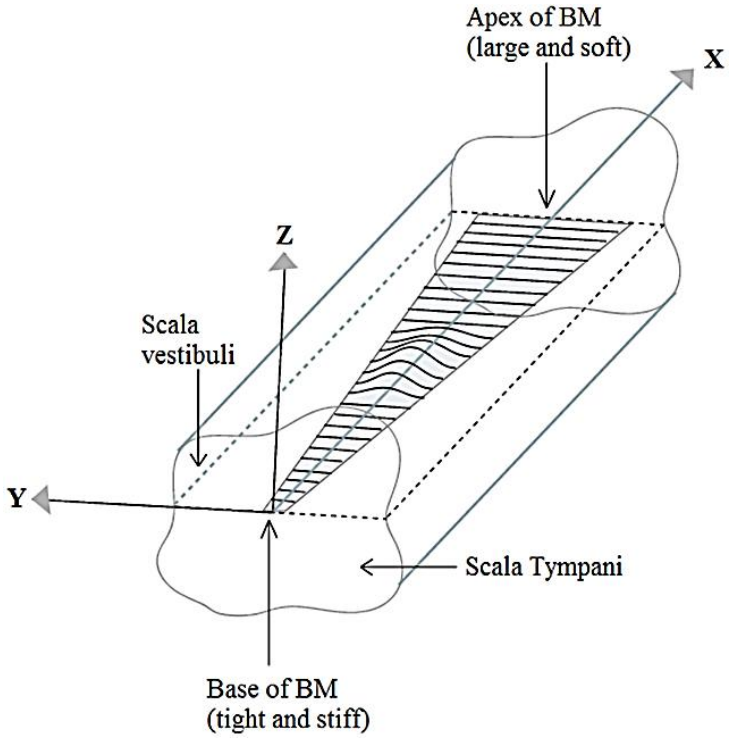


Figure 6.11: Schematic representation of the unrolled basilar membrane with fiber orientation

Hence to model a pass band sensor/filter it is critical to model a system which can perform all the principal operations of the basilar membrane. Resonance in a system is a common mechanical phenomenon, however local resonance seems an unusual feature where only a part of the system exhibits resonance characteristic whereas remaining parts stay vibrationless. From our previous study for stop band technique, it has been found that acoustic metamaterial has the ability to introduce local resonance in structure. Hence in

this section acoustic metamaterial is considered to investigate whether it can perform all principal operations of human cochlea and can develop a mechanical band pass sensor.

## 6.4 Effect of Spiral Coiling

The conventional understanding about the mammalian cochlea is that it evolved essentially and perhaps solely to conserve space inside the skull [104]. Cochlear coiling is absent in reptiles, birds, and monotreme mammals [118]. Coiling allowed the cochlea to become longer, increasing the potential octave range, whereas uncoiled cochleae have been associated with relatively limited hearing ranges. In 1976, Hinchcliffe [119] suggested that the evolution of coiling enhanced high-frequency hearing. Later on, studies on land mammal ear anatomy [120] found a strong correlation between the low frequency hearing limit of each species and the product of basilar membrane length and number of spiral turns. Steele et al. [108] also found that longitudinal curvature of the cochlear duct generates radial fluid pressure gradients; which enhances the radial movement of the hair cells [104, 121]. Recently, a new theory proposed that the cochlea's graded curvature actually enhances low frequency hearing [122], similar to a whispering gallery in which sounds cling to the concave surface of the lateral wall [123]. The cochlear spiral shape redistributes wave energy toward the outer wall, particularly along its innermost, tightest, apical turn, and thereby enhances sensitivity to lower frequency sounds. Recently, Manoussaki et al. [124] confirmed the significant influence of cochlea curvature gradient on low frequency wave propagation in cochlear canal.

# CHAPTER 7: LOW FREQUENCY ENERGY SCAVENGER

Chapter 3 described the development of the AEMM based mechanical frequency selection technique using the local resonance phenomenon. This chapter demonstrates a novel application of the AEMM model. Since voltage is the sensing parameter for designing the AEMM based frequency sensor, this chapter illustrates the possibility to harvest energy at low frequencies using the AEMM model.

## 7.1 Background

Recent advancements in low power electronic gadgets, micro electromechanical systems and wireless sensors have significantly increased the local power demand. To circumvent the energy demand, low power local energy harvesters are proposed for harvesting energy from different ambient energy sources. Energy harvesters utilize the ability of piezoelectric materials to generate electric potential in response to external mechanical deformation. Significant research activities on low power energy harvesters can be found in many literatures [125-128]. Key of these research activities are to introduce self-powered wireless electronics systems such that the maintenance, replacement of the old batteries and the chemical waste from conventional batteries could be avoided [129].

Microcantilever energy harvesters are the most common low power energy harvesters, where power outputs are in the range of micro Watts [130-135]. Recently, we have proposed plate type energy harvesters for high frequency applications[136, 137]. Most of the energy harvester uses the local resonance physics to localize and harvest dynamic energy. Acousto-elastic phononic crystal (AEPC) also has the ability to introduce local resonance in the structure, hence recently AEPC's are brought into the field of energy harvesting because of its unique ability in wave manipulation in a wide range of frequency [134, 135, 138-142]. It is well established that phononic crystals are capable of creating frequency band gaps either through Bragg scattering or local resonance [31, 58, 143]. Local resonance frequency bands are commonly used in harvesting energy from the phononic crystal since the filtered wave energy localizes in the structure at those frequencies. Hence several researchers proposed AEPC's for performing duel operations, filtering wave and harvesting filtered energy, simultaneously, which cannot be achieved using regular energy harvesters.

Carrara et al. [144] proposed a metamaterial energy harvester using a parabolic acoustic mirror where a novel method of wave guiding through an acoustic funnel was proposed. Gonella et al. [135] proposed a 20X20 hexagonally oriented phononic crystal with three cantilever beams at each joint and coated the beams with piezoelectric material to harvest energy. Both models were proposed to harvest energy at high frequencies (>50 KHz) level, however in this study we are focused on low frequency (<1 KHz) energy harvesting. Few attempts were made to model low frequency harvester in recent years. Wu et al. introduced a cavity in the phononic crystal to localize the acoustic energy at the resonance frequency and harvested the energy using a polyvinylidsenefluride (PVDF) film

[142, 145, 146]. Using the comparative methodology, Lv et al. and Yeh [140, 147] theoretically and experimentally studied an energy harvesting generator using point-defect phononic crystal coupled with piezoelectric crystals. Power output from such low frequency phononic crystal based energy harvesters (PCEH) are quite low (in the range of nano Watts (nW) or couple of micro Watts (μW)) against 10 KΩ load resistance (a reference resistance in this study to compare in a metric). However Chen et al.[134] reported a model that can harvest considerably higher electric potential using a one-dimensional phononic piezoelectric cantilever beam. In their model they proposed to utilize the Bragg scattering physics for harvesting energy instead of using the local resonance phenomenon. Although the proposed model is an efficient energy harvester, however the model length is significantly higher (1 m long) considering it for powering low power electronic devices. Also note that the unit PCEH's are limited to harvest energy only at a single frequency.

Since acousto-elastic metamaterial (AEMM) possesses similar physics as AEPC (Ref. chapter 1) and capable of introducing local resonance modes, AEMM can be an ideal choice to overshoot the incapacities of PCEH. Energy harvesting capabilities of AEMM hasn't been explored extensively. Ideally, AEMM's are represented as spring-mass combination in a mass-in-mass system. In this section, similar AEMM's are studied as proposed in chapter-1 to develop low frequency energy harvester, which is referred as sonic crystal by Liu et al. [58]. Very few attempts were made to model the energy harvester based on acousoelastic metamaterials. The idea of simultaneous wave filtering and energy harvesting using AEMM is first noted by Gonella et al. [135] in 2009. However, they didn't study the idea in detail to explore the power output capability of the AEMM. In 2013,

Mikoshiba et al. [141] introduced a 1-D spring-magnet-spring electromagnetic energy harvester model replicating the resonator lattice system proposed by Huang et al. [148]. Since the model was one dimensional, harvesting capability of the structure is limited to only at a single frequency and power output of the system is fairly low (~ 3.6 μW). Very recently, Zhang et al.[149] introduced a modified AEMM structural unit consists of a square mass connected to a square frame by four convolute folded beams. For unit input excitation, maximum 0.005 V (approx. power output in nW range against reference load resistance) can be harvested which is significantly low compared to the other harvesters. Additionally, the proposed model is quite complicated for fabrication and most importantly, the proposal lacks experimental validation. Hence, confidence on the proposed model is dubious.

In this study we present an AEMM based energy scavenger that can harvest energy from low frequency ambient vibrations for driving the low power electronic devices. In modeling the harvester, we aim to include several features in the harvester, all those are not achievable with existing designs and makes the AEMM harvester unique and employable in a variety of engineering applications.

1. **Simultaneous wave filtering and energy harvesting,** for offering dual operation at a time, allowing potential use of possible energy wastage, providing green energy and circumvent energy demand. Very rare feature. Only possible using AEPC.

2. **Operate at low frequency, <1 KHz,** since ambient vibrations usually hold low frequency contents.

3. **Maintain small (sub-wavelength) scale model (<50 mm),** since the harvester is targeted for low power electronics those are quite smaller is size. Very challenging to have feature 2 and 3 together using existing models.

4. **Significantly higher and maximized power output.** Maintaining feature 1, maximum 3.6 μW power output is reported from unit cell in early studies.

5. **Allow energy harvesting at multiple frequencies using single cell,** to alleviate the power output capacity of the model, keeping the sub-wavelength size. Single frequency harvesting was emphasized in past studies.

6. **Simplicity in design.** Essential for cost management, implementation and experimental validation.

7. **Experimental validation.** Most studies lacks experimental validation, may be for design complexity, hence unreliable for industrial implementation.

Similar to phononic crystal, acousto-elastic sonic crystal's (AEMM's) are also conventionally used for stopping acoustic waves due to their low transmissibility at certain frequency ranges [58] and as a result low frequency stop band filters are designed using mass in mass systems [150]. In chapter-1, it has been shown that at the local resonance frequencies the filtered wave energy is trapped inside the soft constituent of the metamaterial as dynamic strain energy [149] and it is possible to sense the trapped frequencies using embedded piezoelectric wafers. Since electric potential is the selecting parameter in developing mechanical sensor, conversely, employing appropriate electric circuit, the sensed potential can be converted to electric power. Adopting the process, filtered wave energy using the AEMM can be recovered and converted to electric power to develop an energy scavenger. Hence, coupling two different physics in a single

phenomenon we can make the AEMM bimodal (wave filtering and energy harvesting) in applications. In AEMM, the soft material is used as a host matrix to house the heavy mass. The trapped wave oscillates inside the matrix differently at different modes. Maximum power can be harvested while the piezoelectric wafer is strained inside the matrix due to the local resonance of the embedded mass. In addition we also intend to attain the targeted objectives listed above using the envisioned AEMM based energy harvester.

## 7.2 Modeling

To illustrate the concept, same unit AEMM model (recalled in Figure 7.1) is adopted as it is demonstrated in chapter 3. Young's modulus of aluminum, lead and matrix are ~68.9 GPa, ~13.5 GPa and ~0.98 MPa, respectively. Since local resonance phenomenon is the key in harvesting energy from unit AEMM, materials of the cell constituents are chosen in such a way that it can offer multiple low frequency local resonance modes.

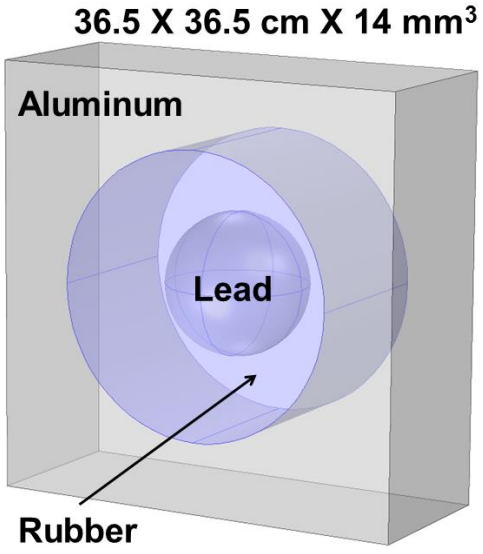


Figure 7.1: Unit cell AcoustoElastic MetaMaterial (AEMM)

## 7.3 Finding Local Resonance Modes

To illustrate the low-frequency resonances and energy distribution in the structure, dispersion relation and eigenmodes are computed using the FEA tool, COMSOL multiphysics [30]. 4-noded tetrahedral elements are used with maximum element size is maintained 1/4 times of the wavelength of the respective constituent at the highest frequency level of the study. In order to calculate the dispersion relation, the complete structure is considered infinite in both x- and y- directions by arranging the unit cell periodically.

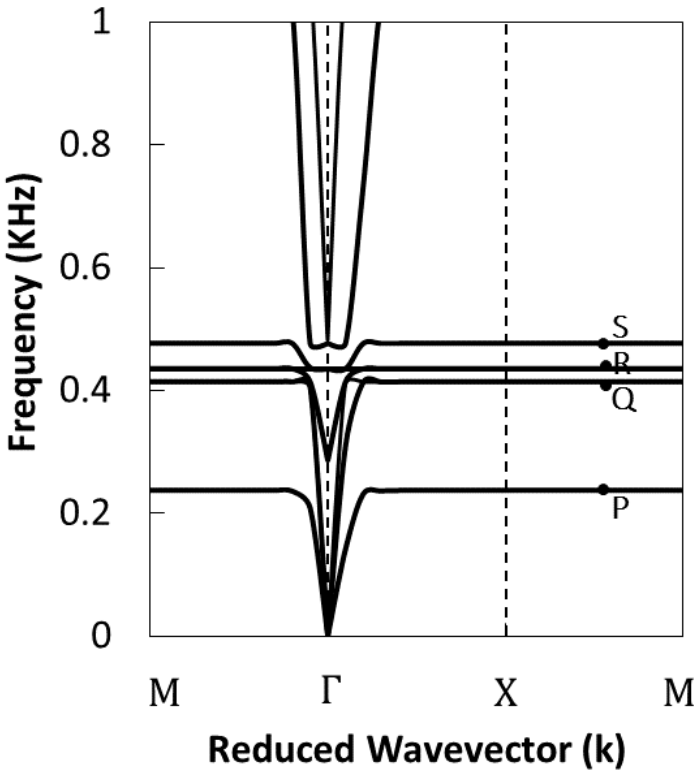


Figure 7.2: Band structure of the unit AESC

The Bloch-Floquet periodic [31] boundary condition is applied at all boundaries of the unit cell. The Bloch-Floquet boundary conditions are based on the Floquet theory which can be applied to the problem of small-amplitude vibrations of spatially periodic structures. Calculated dispersion curve of the unit cell is shown in Figure 7.2. The band structure doesn't show any dispersive mode, however it introduces a couple of flat bands within 1 KHz frequency range.

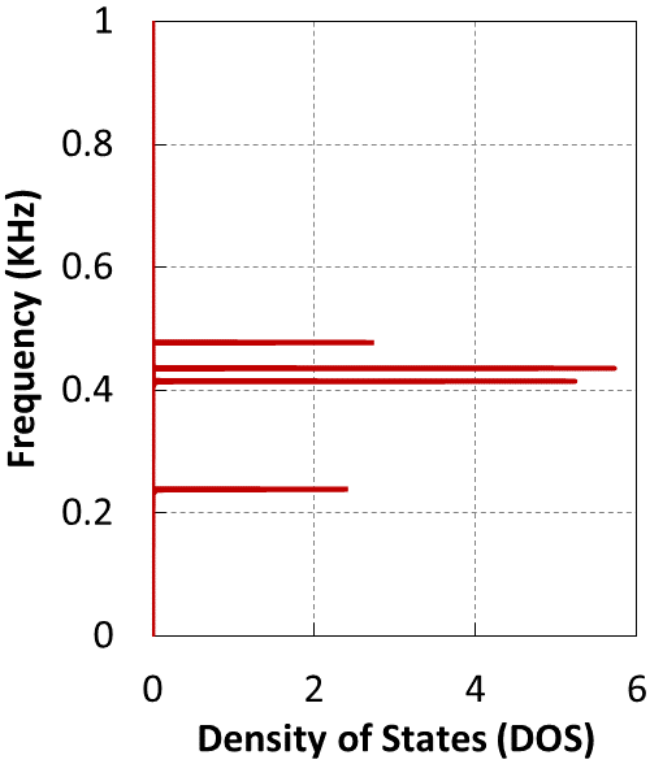


Figure 7.3: Density of States representation of the unit AESC

To clearly distinguish local resonance frequencies, Density of States (DOS) is computed for each frequency within the studied range (0-1 KHz). DOS of the system are the numbers of states (modes) exist at each frequency level. A high DOS at a specific frequency level means that there are multiple modes available for occupation. Maximum

DOS can be obtained where the frequency band is almost straight in dispersion curve, which means the group velocity is close to zero and the wave energy is trapped inside the structure. A DOS of zero at any frequency means that no modes can occupy at that frequency level (termed as stop band). For highly dispersive unimodal wave motion, the DOS is very small but not zero. DOS is calculated from the dispersion relation by applying the relation DOS ($\omega$) = $(1/\pi)(dk/d\omega)$. In calculating DOS, total wave number $\sum dk$ is computed for each frequency ($d\omega$=1 Hz).

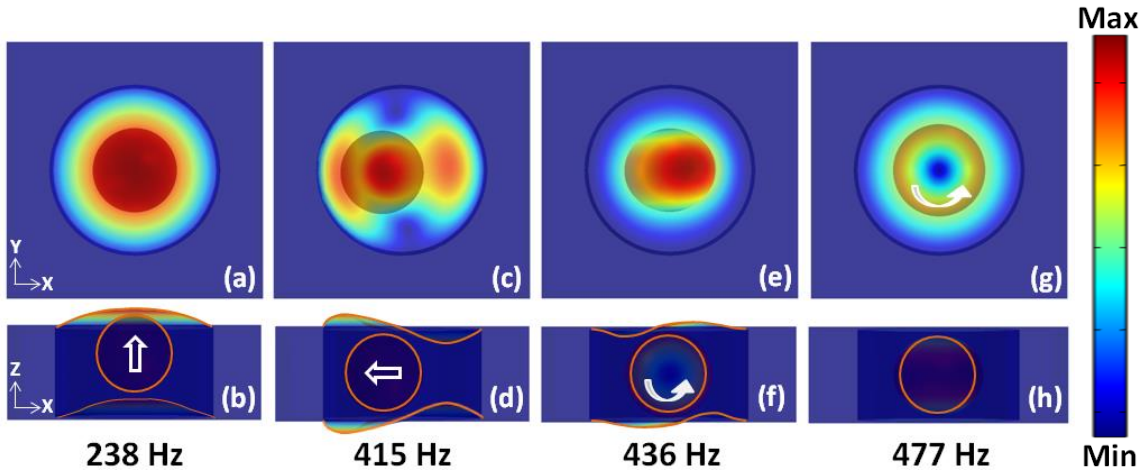


Figure 7.4: Displacement plots of the cell constituents at (a-b) 238 Hz; (c-d) 415 Hz; (e-f) 436 Hz and (g-h) 477 Hz

Figure 7.3 represents the computed DOS for the frequency range 0-1 KHz. Four DOS picks are plotted within the studied frequency limit at 238 Hz, 415 Hz, 436 Hz and 477 Hz. The DOS pick frequencies correspond to the flat bands in dispersion plot (Ref. Figure 7.2) and confirm the existence of local resonance (LR) at those frequencies. Figure 7.4 represents the displacement plots of the unit cell at LR frequencies (mode P, Q, R, S in Figure 7.2) in order to understand the vibration pattern of the cell constituents. At 238 Hz (mode P), the center mass resonates along the z- direction (thickness) of the cell, whereas

at 415 Hz (mode Q), core mass resonates along the x- direction (longitudinal). At both 436 Hz (mode R) and 477 Hz (mode S), the lead resonator is not moving sideways, however rotates counterclockwise about the y- and z- directions, respectively.

## 7.4 Acquiring LR Modes with External Loading

Figure 7.4 represents the eigen models of the unit cell, without confirmation of the excitement type or exact frequency that produce the local resonance modes within the structure. To identify this, a frequency domain analysis is performed. Different loading conditions are considered to actuate different LR modes. Inspired from the eigenmodes, similar boundary displacement excitations are considered (see Figure 7.5) to acquire corresponding LR models. Excitation along the Z- and X- axes result in the P and Q modes, respectively. Harmonic rotation about Y- and Z- axes result in the R and S modes, respectively. This study considers different loading conditions, however further studies may propose a unique loading condition to actuate all four available local resonance modes.

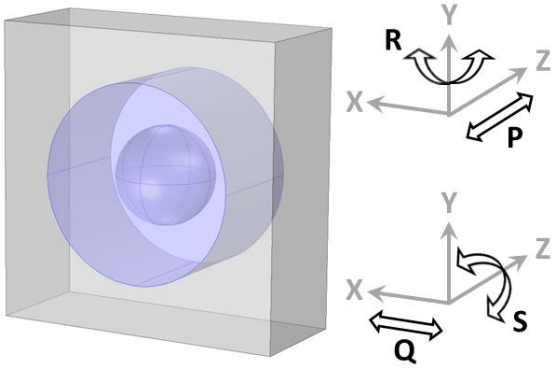


Figure 7.5: Harmonic excitation directions of the unit cell to introduce different local resonance modes (P, Q, R, S).

Figure 7.6 confirms that using specific loading condition it is possible to actuate specific local resonance modes. However, local resonance frequencies shifted slightly relative to the eigen frequency study.

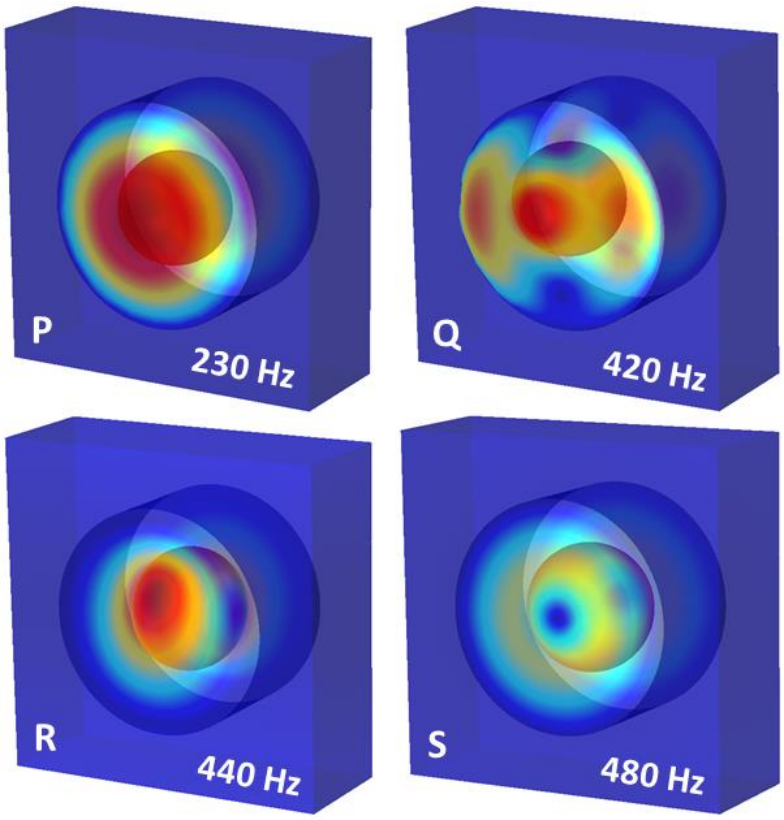


Figure 7.6: Displacement plots of the model at different loading conditions.

## 7.5 Mode Selection and Strategic PZT Placement

Each resonance mode traps dynamic wave energy inside of the matrix-resonator combination of the cell. Hence it is expected that appropriate placing of an energy conversion medium (say, piezoelectric material) with proper design inside the matrix component can provide significant electric potential at local resonance frequencies. Figure 7.6 confirms that using AESC model, multi-frequency energy harvesting is possible from

a unit cell, however for demonstration purpose mode Q (at 415 Hz) is extensively studied in this work. In mode Q, since the center mass resonates along the longitudinal direction of the cell, we expect that placing a piezoelectric disc in between center mass and aluminum frame will be good enough to harvest electrical potential. Note that, the PZT disc needs to be placed so that its thickness axis lies concentric to the center line axis of the core mass.

## 7.6 PZT placement optimization

To convert the trapped strain energy into electrical potential at the selected mode Q, a piezoelectric wafer ($\phi$~7 mm, thickness =~0.5 mm, mass =~0.16 gm) is embedded inside the matrix in between the lead core and the cavity wall (Figure 7.7b). In chapter-3, it has been reported that, distinct FRF pick can be obtained from the selected mode, Q, placing PZT at the middle of the core resonator and the cavity wall. For sensing application having a FRF pick is more important than the FRF amplitude. Whereas FRF amplitude is a key factor for an energy harvester. Hence, it is crucial to choose the exact distance of the PZT from the resonator (termed as 'h') to have the maximum voltage output. A numerical study is performed to select the best position for the PZT. Figure 7.7a suggests that the amplitude of the Frequency Response Function (FRF) follows a Gaussian function with respect to 'h' and FRF is maximum when h = 1.78 mm, which is 1/3.5 times of the distance between center mass and cavity wall (termed as 'H' = 6.23 mm). PZT position in the unit cell is finalized according to Figure 7.7a where maximum FRF response has been recorded.

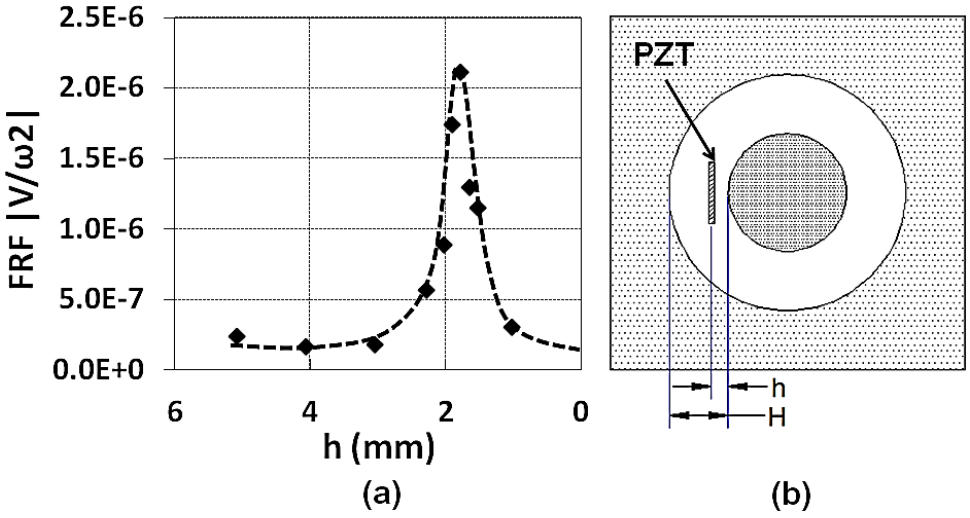


Figure 7.7: (a) FRF output with respect to distance, 'h', between PZT and core mass. (b) Final position of the PZT for maximum electric potential.

## 7.7 Result and Discussion

Since in chapter-3, possibility of receiving electric potential using unit AEMM is validated analytically, numerically and experimentally, hence in this section analytical and numerical demonstrations are not repeated, however experimental study is performed to report the power output capacity of the proposed model. Likewise chapter-3, displacement excitation ($U_0 = 1$ mm) mechanism is used and electric potential is measured against the reference load resistance ($R_0 = 10$ KΩ). Power output ($P_0$) of the system is defined as,

$$P_0(\omega) = \frac{[V_0(\omega)]^2}{R_0}$$

Resistive load affects the current and at certain load resistance, the circuit harvests maximum power [136, 151] due to resonance. In this study the fundamental possibility of

designing an AEMM based energy scavenger is presented and extensive analysis revealing the effect of ground acceleration and external load resistance are omitted.

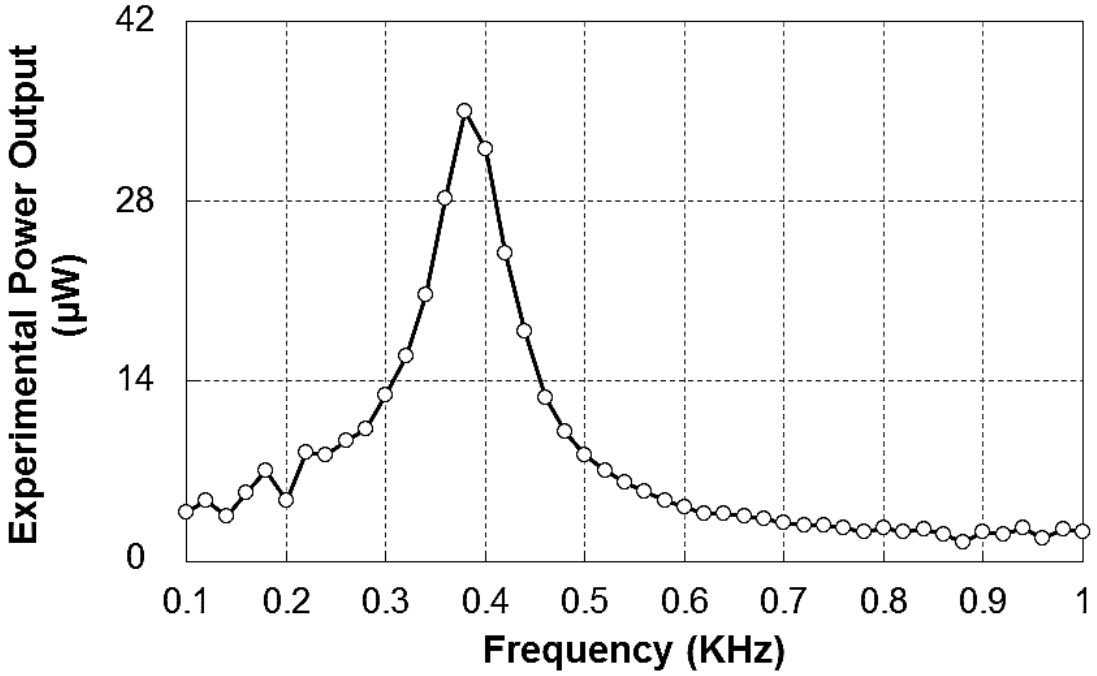


Figure 7.8: Experimentally obtained output power (μW) against 10 KΩ load resistance.

The experimental result shows that within the studied frequency limit, using the proposed AEMM model and suggested PZT placement, maximum ~36 μW power can be generated at ~0.37 KHz (see Figure 7.8). The harvested power up to ~36 μW against ~10 KΩ resistive load at low frequency region using unit cell AEMM with unit excitation and keeping the structure size in small (sub-wavelength) scale is significantly higher than the power generated by previously proposed models those can filter wave and harvest energy, simultaneously. Using the similar hypothesis and multi-cell model as suggested in chapter 3 and Figure 3.18, it is possible to introduce a broadband energy scavenger. It has been found that using our previously introduced multi-cell model (Ref. Figure 3.17a), the peak

harvested power (against 10KΩ, ~5μW) can be obtained at ~0.32 KHz from cell-1 with heaviest core mass (11.43 gm). Additionally, it was found that the peak energy can also be harvested at other frequencies, e.g., ~0.50 KHz (~34μW), ~0.76 KHz (~35μW), ~1.1 KHz (~22μW) and ~1.38 KHz (~11μW) from the cells with decreased core masses.

## 7.8 Possible Power Optimization Approaches

In any energy harvester, one of the key targets is to maximize the power output. Though the harvested power using the proposed model is significantly higher than the existing models of same kind, additionally, two approaches are suggested to further maximize the power output using the unit AEMM model,

1. Multi-frequency/multi-modal harvesting
2. Geometric optimization

**Multi-frequency Harvesting**

In current state of the art, low frequency energy harvesting at multiple frequencies is very challenging using the unit cell design. Figure 7.4 confirms that using proposed AEMM model, four local resonance (energy trapping) mode can be introduced within 1 KHz range. It has already been reported that, placing a piezoelectric material perpendicular to the loading direction in between the core resonator and the cavity wall is the appropriate orientation for harvesting energy from mode Q (Ref. Figure 7.7). It is hypothesized that, with proper placement of the piezoelectric material significant energy can be scavenged from the other modes (P, R and S) as well. To harvest energy at those modes, tentative orientation of the piezoelectric material is described in Table 7.1.

Table 7.1: Tentative orientation of the smart material to scavenge energy at different models of vibration

| Mode | Vibration Pattern | Tentative Piezoelectric Material Orientation |
|---|---|---|
| P | Core resonator is vibrating along thickness direction of the unit cell. | In between resonator and free surface of the matrix material, keeping piezoelectric material and AEMM thickness axis aligned. |
| R | Core resonator is rotating about the width axis of the structure. | In between resonator and cavity wall, keeping piezoelectric material and AEMM thickness axis parallel. |
| S | Core resonator is rotating about the thickness axis of the structure. | In between resonator and cavity wall, keeping piezoelectric material thickness axis perpendicular to the AEMM thickness axis. |

In early studies, PZT 5H is employed as energy conversion medium in harvesting energy from mode Q. It has be observed without PZT placement in the structure, mode Q is found at ~ 415 Hz, however the mode shifts to ~ 430 Hz with the PZT addition. It has also been found that, PZT orientation and placement significantly manipulates the vibration modes in the AEMM. Other vibration modes in the AEMM (P, R and S) are extinct after placing the PZT inside. We anticipate that, since the mass and stiffness of the piezoelectric material is considerable compared to the constituents of the unit cell, hence it plays significant role in vibration patterns of the constituents. By selecting the appropriate piezoelectric material, its shape and placement significant energy can be scavenged from the P, R and S modes without affecting the vibration modes due to the addition of the PZT material.

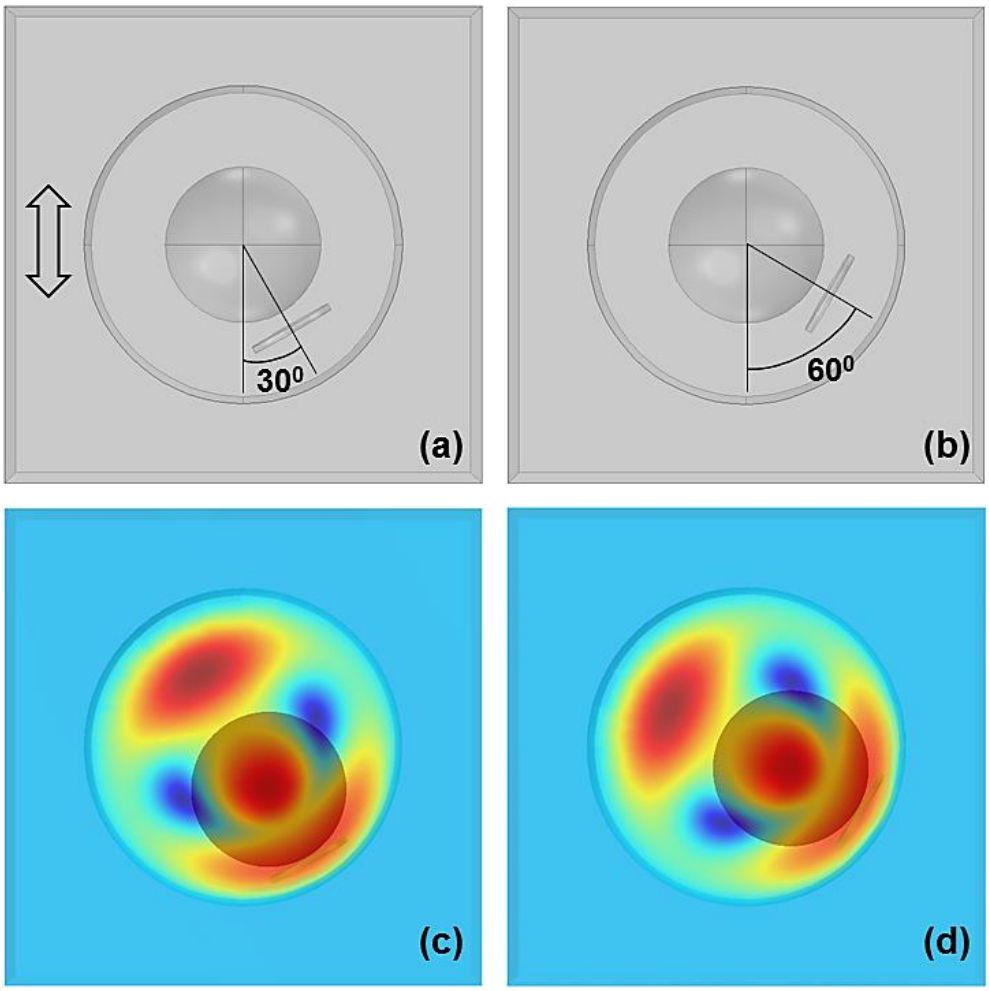


Figure 7.9: PZT rotation about the thickness axis of the unit cell (a) 300 (b) 600. Displacement plot at 500 Hz with PZT (c) 300 (d) 600 PZT orientation.

To understand the PZT effect in vibration modes in little more detail, a numerical study is performed at various orientations of the PZT in the unit cell. Keeping all other parameters constant, the piezoelectric material is rotated about the thickness axis of the cell with an interval of $30^0$. Figure 7.9 (a-b) shows two sample orientations ($30^0$ and $60^0$) of the PZT. Figure 7.9 (c-d) confirms the mode manipulation feature of the AEMM through PZT orientation. Where with $0^0$ PZT orientation only Q mode is exist, additional local resonance modes can be introduced with the rotated PZT orientation. Interestingly it has been observed that, in the proposed model, there are two local resonance modes always exists;

1) along the loading axis; and 2) along the PZT thickness axis. The loading direction is recalled in Figure 7.9a with double sided arrow. Since in mode Q, both loading and PZT thickness axis coincides, hence only one mode is exist with $0^0$ PZT orientation. Note that, the second mode doesn't exist only if the PZT thickness axis is perpendicular to the loading axis. Inspired from the outcome, additional studies (such as, using multiple PZT, using variable PZT, optimize orientation etc.) are envisioned to further introduce new local resonance modes and optimize the power output from a unit cell AEMM.

**Geometric Optimization**

Recalling the effective mass equation in chapter-3, effective mass (hence, local resonance) of the system is strongly depends on mechanical properties and geometric configuration of the cell constituents. It is hypothesized that, power output and local resonance frequency of the system can be altered significantly through the variation of cell geometry and material selection.

## 7.9 Chapter Summary

This chapter demonstrates the energy harvesting capabilities of an acousto-elastic metamaterial (AEMM) in the ground of simultaneous wave filtering and energy harvesting. In addition to wave filtering and energy harvesting the proposed model is also capable of obtaining several other objectives which are not available in previously introduced models. It is also confirmed that multi-frequency energy harvesting is possible using the proposed AEMM model, which is challenging to obtain using traditional phononic crystal based energy harvesters. It is shown that by setting a piezoelectric wafer inside the soft matrix of AEMM, significant electric potential can be recovered and the amount of power that can

be harvested from a unit cell with unit excitation, is significantly higher (~36μW against 10KΩ) compared to the existing low frequency harvesters of same kind. A multi-cell model for broadband energy scavenging is proposed which is a heuristic design to demonstrate the concept, but any application specific structure can be manufactured at sub wave length scale by applying the similar physics. It is shown that the systematic selection of the core mass, placement of piezoelectric wafer and coupling local, structural and matrix resonance in a multi-cell system could result a broadband energy scavenging device. It has been found that PZT geometry and orientation plays important role in manipulating vibration modes and additional local resonance modes can be introduced through altering PZT orientation. Since power output is one of the key features of the energy scavengers, hence various optimization approaches are proposed to optimize the power output from the proposed AEMM model. We believe that the proposed harvester possess enough potential, flexibility and novelty to be employed in many engineering applications.

# CHAPTER 8: APPLICATIONS OF AEMM HARVESTER

The proposed AEMM model can be applicable in various novel applications due to its enormous features and flexibilities. One of the key feature of the AEMM model is that, it is capable of harvesting energy at very low acoustic frequencies and keeping the geometry unchanged the harvesting frequency can easily be shifted toward high frequency level only varying the material properties. Though it is expected that the proposed model can be employed in wide variety of engineering applications, however in this study three possible novel applications of the AEMM based energy harvester is presented.

1. Highway traffic noise barrier
2. Powering low power electronics
3. Powering Pacemaker

## 8.1 Highway Traffic Noise Barrier

A sound occurs when an ear senses pressure variations or vibrations in the air. Noise is unwanted sound. The brain relates a subjective element to a sound, and an individual reaction is formed. Numerous studies have indicated that the most pervasive sources of noise in our environment today are those associated with transportation. Highway traffic noise tends to be a dominant noise source in our urban, as well as rural, environment. The control of noise in everyday life is very important. Unwanted noise can cause stress related

illness and severe noise can cause hearing damage. Hence noise barrier has found tremendous interest in recent years.

**What is Noise Barrier?**

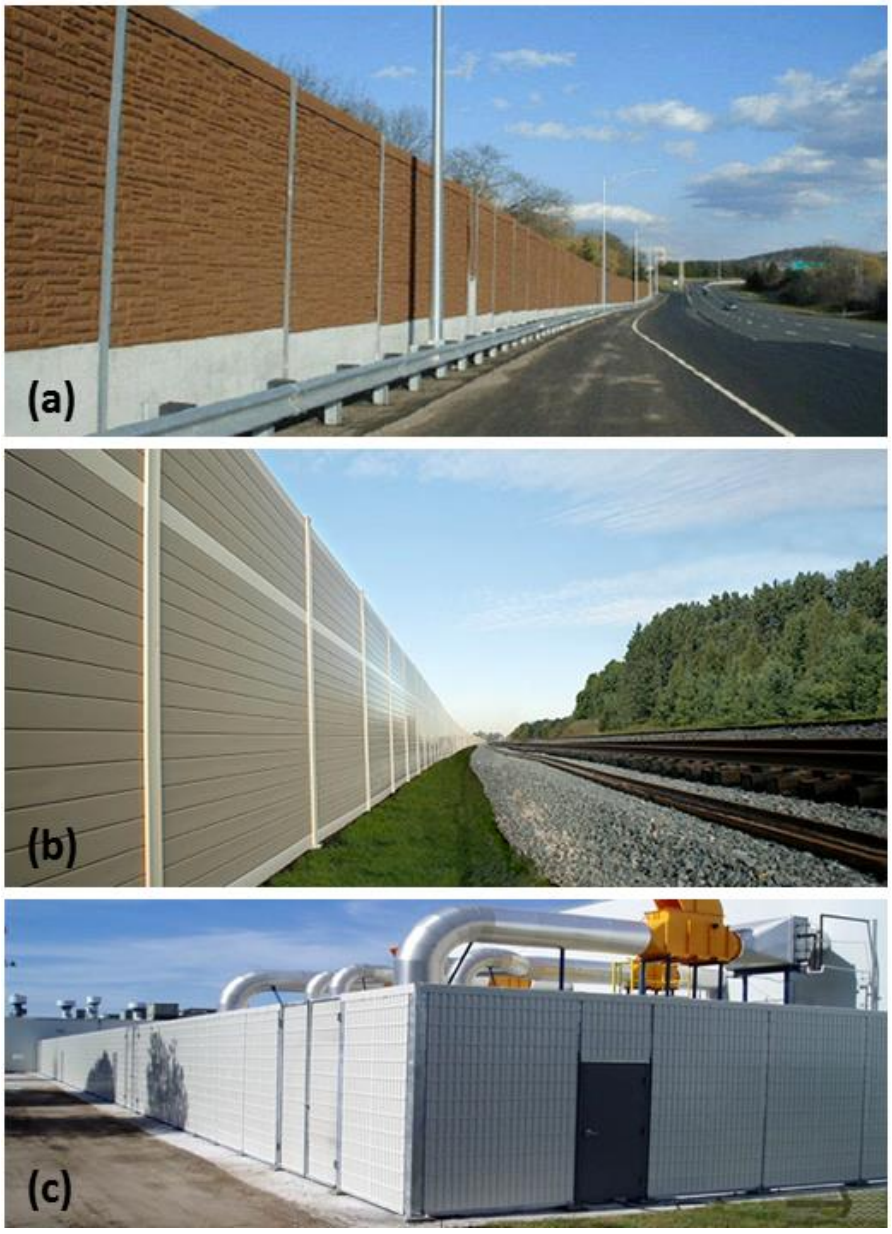


Figure 8.1: Typical noise barriers for (a) highway (b) railway and (c) industrial noise control.

A noise barrier (also called a soundwall, sound berm, sound barrier, or acoustical barrier) is an exterior structure designed to protect inhabitants of sensitive land use areas from noise pollution. Noise barriers (see Figure 8.1) are the most effective method of mitigating roadway, railway, and industrial noise sources other than interruption of the source activity or use of source controls [152].

Noise barriers are solid obstructions built between the highway and the homes along a highway. They do not completely block all noise they only reduce overall noise levels. Effective noise barriers typically reduce noise levels by 5 to 10 decibels (dB), cutting the loudness of traffic noise by as much as one half. For example, a barrier which achieves a 10-dB reduction can reduce the sound level of a typical tractor trailer pass-by to that of an automobile [153].

**How Noise Barrier Work?**

Noise barriers reduce the sound which enters a community from a busy highway by either absorbing the sound, transmitting it, reflecting it back across the highway, or forcing it to take a longer path over and around the barrier. A noise barrier must be tall enough and long enough to block the view of a highway from the area that is to be protected, the “receiver" (see Figure 8.2). Noise barriers provide very little benefit for homes on a hillside overlooking a highway or for buildings which rise above the barrier. A noise barrier can achieve a 5 dB noise level reduction, when it is tall enough to break the line-of-sight from the highway to the home or receiver. After it breaks the line-of-sight, it can achieve approximately 1.5dB of additional noise level reduction for each meter of barrier height [153].

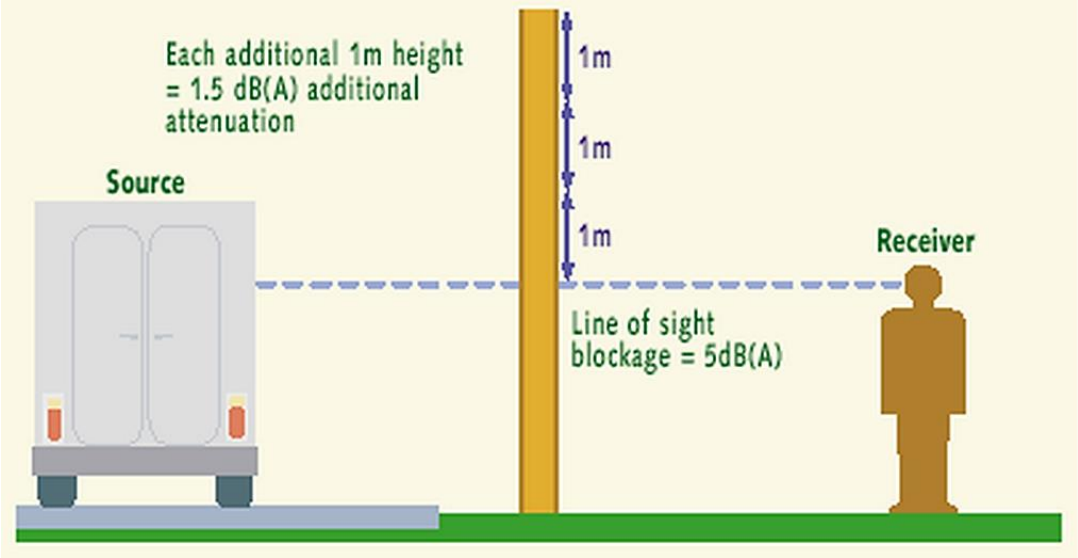


Figure 8.2: Noise barrier sound attenuation capacity considering its height

**Typical Materials for Noise Barrier**

Noise barriers can be constructed from earth, concrete, masonry, wood, metal, and other materials. To effectively reduce sound transmission through the barrier, the material chosen must be rigid and sufficiently dense (at least 20 kilograms/square meter). All noise barrier material types are equally effective, acoustically, if they have this density. There are no federal requirements specifying the materials to be used in the construction of highway traffic noise barriers. Individual State departments of transportation select the materials when building these barriers. The selection is normally made based on factors, such as aesthetics, durability, maintenance, cost, and the desires of the public.

**Noise Barrier Using AEMM**

It has been reported that, conventional noise barrier transmits, absorbs or reflects the acoustic wave in noise filtering process. Also note that the current noise barriers are not capable of fully filter the acoustic noise, whereas it just attenuates the noise db. Hence

in this study we propose to consider the AEMM structure as the potential material for the noise barrier. We expect that using the AEMM model, acoustic noise can be attenuated much more efficiently compared to the existent barriers. In stopping the acoustic noise, the AEMM built barrier is expected to absorb the acoustic energy precisely, where using the energy harvesting technique studied earlier, the absorbed energy can easily be converted to electric potential (see Figure 8.3). Hence the proposed AEMM noise barrier will perform duel operations (noise control and energy harvesting), simultaneously. Since thickness of the proposed unit AEMM is considerably small compared to the traditional noise barriers, hence multiple AEMM layer can be used in fabricating the wall for multi-layer and highly effective filtration process. With noise controlling process, the AEMM built wall is expected to generate significantly large power output since millions of unit AEMM may accommodate in a 100 meter long barrier.

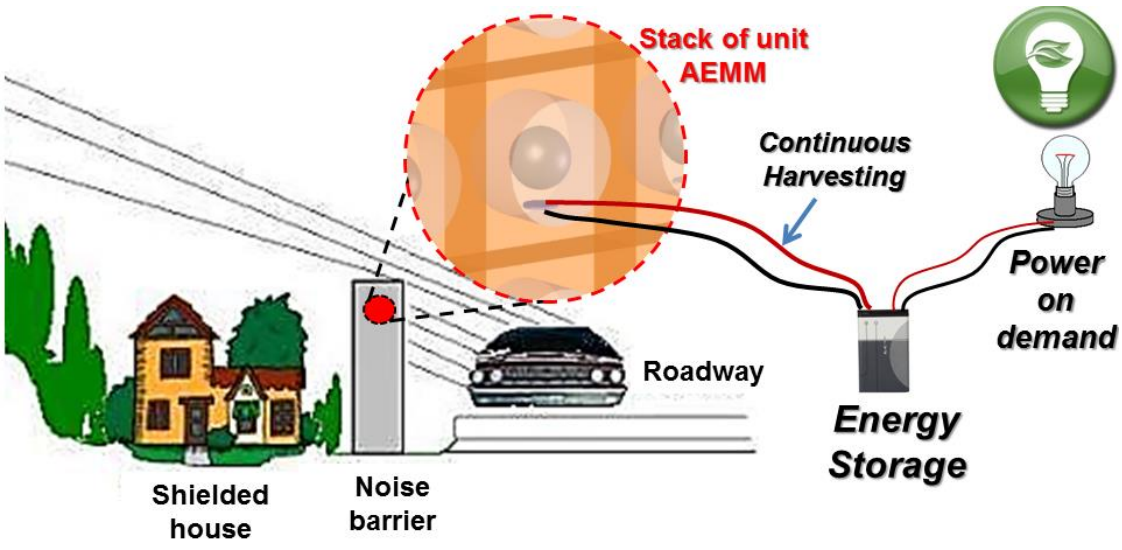


Figure 8.3: Schematic of simultaneous noise control and energy harvesting using AEMM

In addition with roadside noise filtration; control of noise and vibration is also very essential in industrial environments (Ref. Figure 8.1c) for health, safety and quality. The proposed AEMM model can be very effective for such industrial applications as well.

## 8.2 Powering Low Power Electronics

The increased use of cell phones, ipods, tablets, iPads throughout the world resulted surprisingly large energy footprint and according to 'International Energy Agency' (IEA), household energy demand has increased by 3.4% [154] since 1990. It is calculated that in US, only the usage of smart phones demands 1269000 Million Watt-hour of energy per years [155]. Hence, if such power demands can be satisfied by local powering devices through harvesting the energy from the abundant ambient noises, we could alleviate the power demands significantly. To circumvent the energy demand, local energy harvesters using multiple micro-cantilevers are proposed to scavenge energy from different alternate sources. Key motivation of the previous research was to introduce the self-powered wireless electronics systems such that the maintenance, replacement of the old batteries and the chemical waste from conventional batteries could be avoided [129]. Microcantilever low power energy harvesters are designed to operate at higher frequencies (between 20 KHz – 3 MHz) such that small (4 – 10 mm) size harvesters could be designed [130-133]. However, the physics of micro-cantilevers cannot be translated to harvest energy from low frequency ambient vibration (between 10 Hz – 3 KHz) due to their humongous size. For example to power a i-Phone one would need a table size harvester and which is impossible.

In this study we have established that, proposed AEMM based energy harvester is capable of harvesting at very low frequency level and it possess enormous flexibility to alter its operating frequency level only changing the constituent's material property or geometric configuration. Hence using the same hypothesis, here we argue that an AEMM energy harvester is possible to model for low power electronics (cell phone, i-pad etc.) that can scavenge electric potential from low frequency ambient vibrations (e.g. vibration during traveling in a car or jogging).

**Proposed Model**

In this proposal we envision to replace the back plate of the electronic item with the AEMM harvester, as shown in Figure 8.4. The modified AEMM unit cell consists of a relatively heavy core resonator, a very thin membrane and a flexible piezoelectric polymer. The flexible membrane is strongly attached to the mobile back plate and holds the core resonator and the piezoelectric polymer. Both resonator and piezoelectric polymers are firmly glued with the membrane. Dimension of the plate is considered as 120 mm X 60 mm X 1 mm.

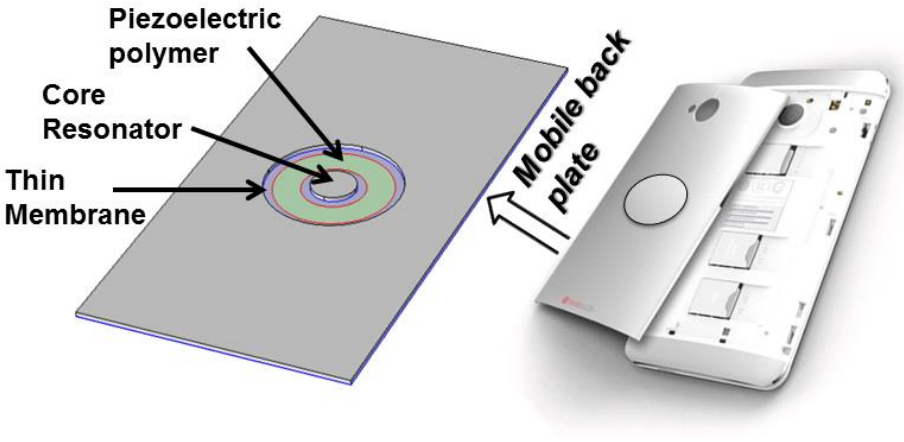


Figure 8.4: Proposed mobile back plate with the ability to scavenge energy.

For demonstration purpose, in this study steel, silicon and polyvinylidene fluoride (PVDF) are considered as the materials for core resonator, thin membrane and piezoelectric polymer, respectively. It is expected that, similar to proposed AEMM structure in **Figure 7.1**, the modified AEMM model is also capable of introducing low frequency local resonance modes. Though for demonstration purpose, only one cell is presented in Figure 8.4, however it is highly recommended to use as many cells as it can be accommodated with maintaining the acceptable minimum stiffness of the back plate. Each unit cell should contain variable geometric configurations. Hence it is expected to harvest electric energy at a wide range of ambient vibrations and maximize the power output. Figure 8.5 shows a sample back plate keeping six (6) unit cell where diameters of the biggest to the smallest cells are considered as 28mm to 8mm with 4mm decrement. Diameter of the core resonator in each cell is considered as 1/3.5 times of the cell diameter.

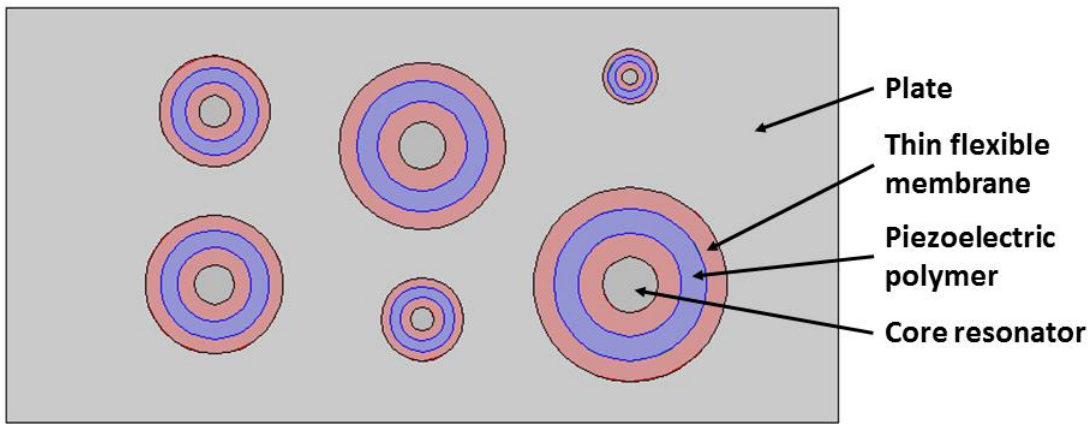


Figure 8.5: Envisioned multi-cell (6) electronic energy harvester

A numerical study is performed to investigate the feasibility of the proposal. It has been found that extremely low frequency local resonance modes can be achieved using the envisioned design. At local resonance modes, the thin membrane encounters oscillatory

motion due to the resonance behavior of the center mass. Such oscillation causes contraction and expansion in piezoelectric polymer and results electric potential. Energy can be harvested from ambient vibration of ~ 8 Hz from the biggest cell whereas other cells are offering energy scavenging capability at an increased frequency level with the decrease of cell geometry (see Figure 8.6). Table 8.1 lists the energy harvestable frequencies at different cells.

Table 8.1: Local resonance frequency at different cells

| Cell # | Diameter (mm) | Energy harvestable frequency (Hz) |
|---|---|---|
| 1 | 28 | ~ 8 |
| 2 | 24 | ~ 12 |
| 3 | 20 | ~ 20 |
| 4 | 16 | ~ 34 |
| 5 | 12 | ~ 82 |
| 6 | 8 | ~ 210 |

The proposed model confirms the possibility of multi-frequency energy harvesting from ambient vibration. Using the hypothesis it is possible to design the harvester for a wide variety of ambient frequency. Though in this study replacing a mobile back plate with AEMM energy harvester is proposed, however using the hypothesis it is quite possible to develop a much smaller portable energy harvester that can be inserted into the electronic device like a memory card.

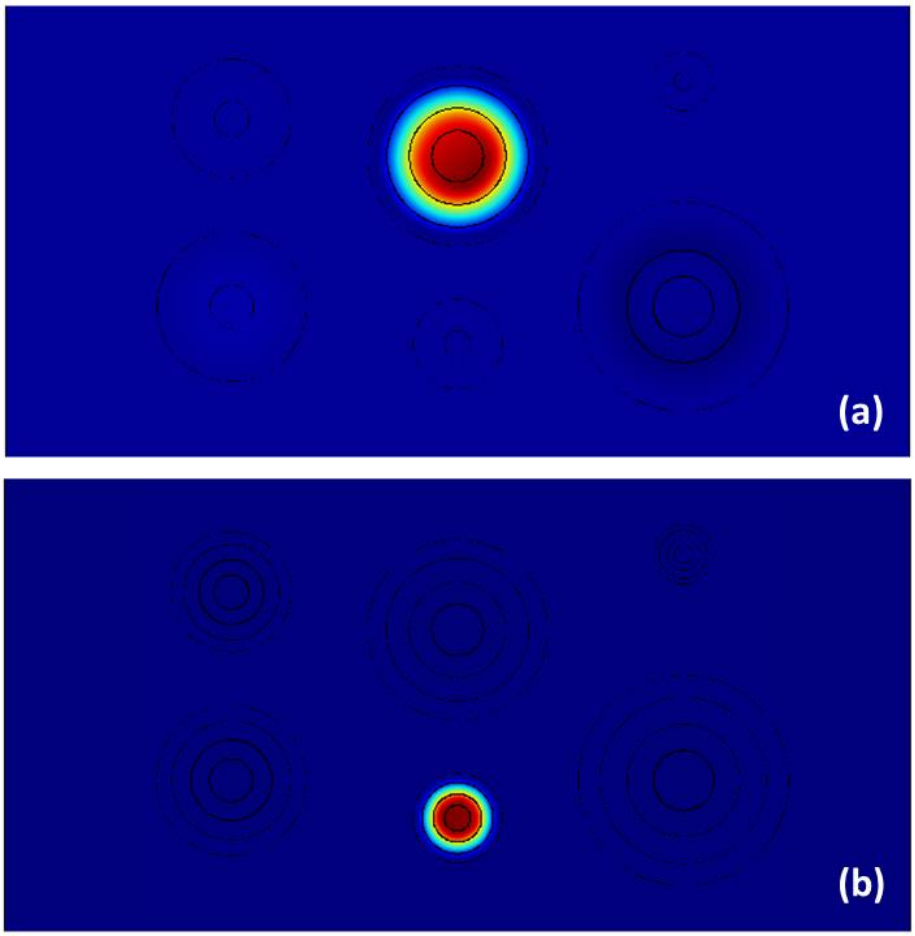


Figure 8.6: Local resonance at (a) 12 Hz (b) 82 Hz

## 8.3 Powering Pacemaker

Artificial cardiac pacemakers have made a noteworthy influence to control heartbeat using electrical impulses for contracting the heart muscles of people who suffer from sick sinus syndrome or heart block which causes abnormal heart rate, and may result in symptoms including syncope, angina, dizziness, and even heart failure or heart attack [156, 157]. However, due to the limited lifespan of the battery, replacement surgery for the artificial pacemaker implanted beneath chest skin should be made every 7 to 10 years (or even every 3 to 6 years for an implantable cardioverter defibrillator (ICD)) [158, 159]. This

poses a risk to elderly persons, particularly with regard to infection or bleeding during the surgical procedure [160]. Enhancing the battery lifetime is thus a critical issue to assure longer working time of the implanted pacemakers, and increase the replacement cycle. An attractive approach to address this challenge is to adopt self-powered systems, which potentially can provide low maintenance, independent operation, and sustainability for implantable biomedical devices [161, 162].

One of the applications of energy harvesters is powering implantable biomedical devices. Energy harvesting systems based on irregular vibrational motion and mechanical deformation are promising candidates for self-powered biomedical electronics [163-167]. Romero et al. [168] performed a detailed survey on energy harvesting devices designed for this purpose. The majority of vibrational energy harvesters that extract energy from human motion are attached to the limbs. If the biomedical device is intended to be implanted in the torso, it is preferred to include the energy harvesting device in the same package. There are three configurations in the literature for in vivo energy harvesting devices that can be utilized inside the torso. The first general configuration is microbial fuel cells, which utilize oxidation of glucose for generating power [169]. The second method is by harvesting energy from expansions of artery by wrapping a piezoelectric film around them [170]. The third solution is by printing piezoelectric ribbons onto rubber [171] and utilizing the expansion of the lungs in respiration.

In recent years battery free and self-powered pacemaker topic has found significant interest to the research community. Manipulating flexible piezoelectric energy harvesters (called nanogenerators (NGs)) inside the human body is of particularly medical interest,

because they can scavenge inexhaustible biomechanical energy such as cardiac motion, muscle contraction/relaxation, and blood circulation and convert it to electrical energy [172]. This could feasibly contribute to not only the operation of implantable heart rate monitoring and transmitting system, but also the development of a self-powered artificial pacemaker by directly recharging the battery or stimulating the heart [173]. Inspired from the capabilities of flexible piezoelectric materials, very recently Hwang et al. [174] and Dagdeviren et al. [175] proposed to place the piezoelectric membrane at the surface of the heart wall (see Figure 8.7) to harvest electric energy. However it is strongly suggested that, the energy harvester must not impede the heart beating action. Attachment of the energy harvester unit to the exterior of the heart, mass loads the heart and is therefore unacceptable. Moreover the proposed method requires open heart surgery to place the harvester. Since the process is really complicated, risky and expensive, placing energy harvesting unit at heart wall is extremely discouraged by the doctors.

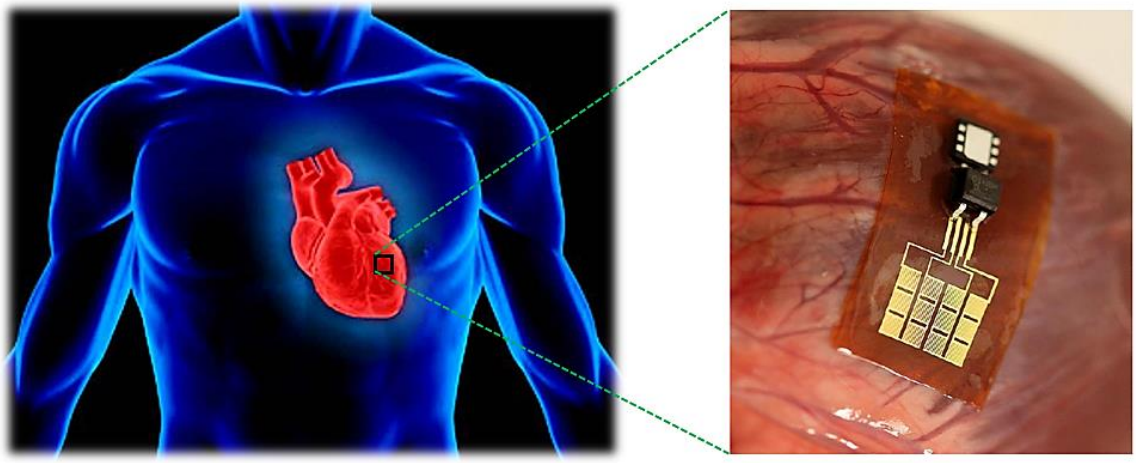

Figure 8.7: Placement of the piezoelectric membrane at the surface of the heart to harvest energy.

Keeping that in mind, in 2012, Karami et al. [176] proposed an energy scavenger utilizing the vibrations inside the chest area to power pacemakers and ICD. The most

significant vibrations inside the chest area are those caused by heartbeats. They investigated the possibility of recharging power efficient pacemakers with heartbeat-induced vibrations. Kanai et al. [177] performed the ultrasonic velocity measurements to estimate the vibrations in the vicinity of the heart due to the heartbeat (Figure 8.8). They measured the velocity of two points on the lower sides of the interventricular septum (the wall separating the left and right ventricles of the heart). Since the measurement points are close to the thoracic diaphragm, the velocity data are a safe estimate for the vibration of the part of the body close to heart area.

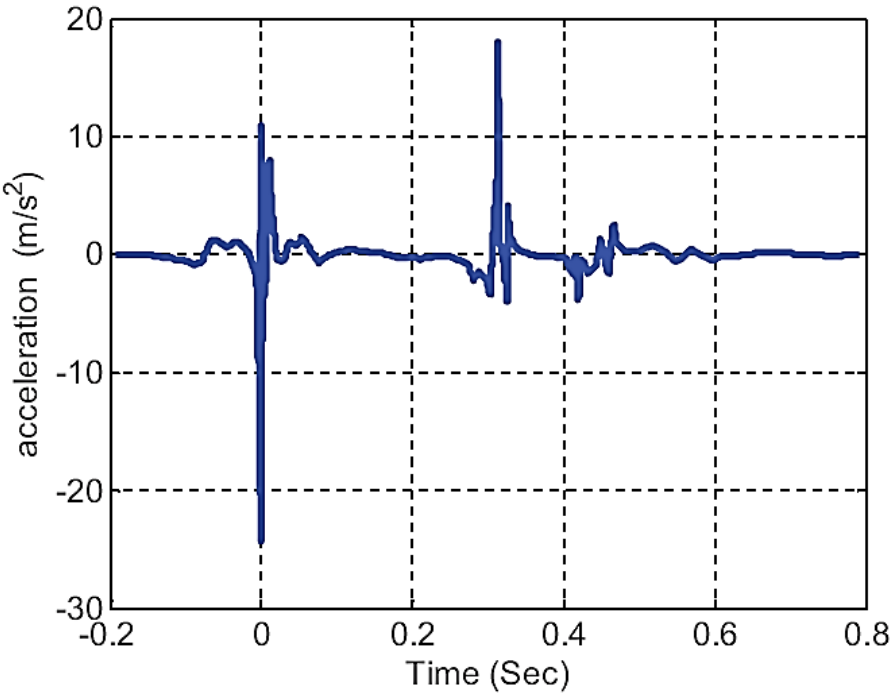


Figure 8.8: Frequency content at the vicinity of the heart wall measured by Kanai et al.[177]

The frequency spectrum of heart beat oscillations spread from fractions of a hertz to about 50 Hz. However the amplitude of the 39 Hz frequency component is relatively high and results better power production [176]. In designing the energy scavenger Karami

et al. [176] adopted the conventional cantilever beam based energy harvesting model. However the cantilever beam model was modified extensively and turned into zigzag beam model to capture low frequency contents of the heartbeat. The power requirement of pacemakers has been significantly reduced over the past years, and one microwatt is a reasonable upper estimate of the required power of modern pacemakers [178]. The size of a typical pacemaker is about 42mm X 51mm X 6mm (see Figure 8.9). Typically, the battery takes about 2/3 of the size of the pacemaker.


Figure 8.9: Typical pacemaker

**Proposed Model**

Inspired from Karami's work and outcome of our early studies, in this study we claim that it is possible to introduce an AEMM based energy harvester that can be placed inside the pacemaker that is capable of harvesting sufficient energy for powering

pacemaker. In our early studies it has been found that AEMM model is capable of harvesting energy at low frequency level. Harvesting frequency can be further decreased down to very low frequency simply changing the material properties or geometric configurations. In previous section (powering low power electronics), it has been confirmed that, energy can be scavenged at ~ 34 Hz using an AEMM cell of diameter 16 mm (Ref. Table 8.1). Hence here we propose that using the idea and similar model, a pacemaker energy harvester can be introduced to scavenge energy at ~ 39 Hz. It is expected that using the AEMM harvester pacemaker size can be reduced significantly since the proposed energy harvester (even without optimization) might not take more than ~ 1/3 portion of the regular pacemaker, whereas current pacemaker battery takes 2/3 portion of the system (Figure 8.10).

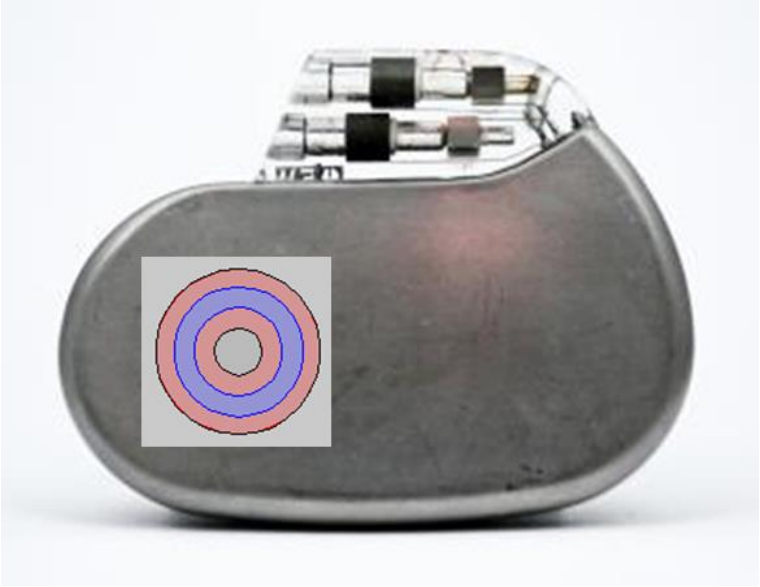

Figure 8.10: Conceptual representation of AEMM in pacemaker

# CHAPTER 9: MYCOTOXIN DETECTION SENSOR

Each year millions of food items have been demolished due to mycotoxin contamination. Mycotoxin is a toxic secondary metabolite produced by organisms of the fungus. However every mycotoxin aren't harmful for health (sometimes good for health), hence not essential to be discarded. To prevent needless dispose of the food items, a mycotoxin classification mechanism is crucial. In current state of the art, it requires expensive and time consuming laboratory operation to perform the test. However for a bulk or in-situ inspection a portable and cost effective test mechanism is required, which is a missing-link in the current state of the art. Such mycotoxins exhibit dynamic response upon infrared radiation and creates acoustic wave with specific frequency input. Frequency of the generated acoustic wave for each mycotoxin class is distinct. Hence in this work, we intend to propose a mechanical sensor that can classify mycotoxin type using the frequency content developed through photoacoustic wave.

## 9.1 What is Mycotoxin?

When certain types of fungus grow on food, they produce minute amounts of toxins called mycotoxins [179]. Mycotoxins are toxins produced by some species of mold (myco means

fungal) [180]. One mold species may produce many different mycotoxins, and the same mycotoxin may be produced by several species [181]. **Most fungi-produced mycotoxins are harmless, and even helpful**. For example, the antibiotic penicillin came from a fungus, and it is a mycotoxin [179]. Mycotoxins are secondary metabolites produced by microfungi that are capable of causing disease and death in humans and other animals. These metabolites constitute a toxigenically and chemically heterogeneous assemblage that are grouped together only because the members can cause disease and death in human beings and other vertebrates [182, 183]. Mycotoxins may be fatal or cause severe illness at very small concentrations, often measured in parts per million (ppm) or parts per billion (ppb). There may be thousands of mycotoxins on the planet earth, but only a small fraction of these toxic chemicals have the potential to cause plant and animal diseases. In nature, mycotoxins may act to disable host defense responses or to defend the fungus against other microorganisms [184].

## 9.2 Mycotoxins in Agriculture and Health

Mycotoxins are a big problem in agriculture. Over 25% of the world's agricultural production is contaminated by mycotoxins. Mycotoxins often grow on crops like corn, wheat and peanuts, for example. The mycotoxins can then end up in food. If crops like wheat are stored poorly after harvest, toxic molds can grow and contaminate the wheat with mycotoxins. There are limits set for the amount of mycotoxins in food. For example, the United States Food and Drug Administration limits the maximum amount of aflatoxin mycotoxins in food to 20 parts per billion. The limit set for milk is 0.5 parts per billion. To remove mycotoxins from food crops, binding agents are used [185].

However, there have still been incidents of people dying from eating mycotoxin-contaminated food. This occurs more often in third world countries. For example, 125 people died in 2004 in Kenya, after they ate food contaminated with aflatoxin mycotoxins. Many animals have also died from ingesting mycotoxins. Farm animals have died from eating feed contaminated with mycotoxins. There has also been cases of pets dying after eating pet food which contained mycotoxins [185].

The economic consequences of mycotoxin contamination are profound. Crops with large amounts of mycotoxins often have to be destroyed. Alternatively, contaminated crops are sometimes diverted into animal feed. Giving contaminated feeds to susceptible animals can lead to reduced growth rates, illness, and death. Moreover, animals consuming mycotoxin-contaminated feeds can produce meat and milk that contain toxic residues and biotransformation products.

National and international institutions and organisations, such as the European Commission (EC), the US Food and Drug Administration (FDA), the World Health Organisation (WHO) and the Food and Agriculture Organisation (FAO) of the United Nations, have recognized the potential health risks to animals and humans posed by food- and feed-borne mycotoxin intoxication and addressed this problem by adopting regulatory limits for major mycotoxin classes and selected individual mycotoxins. The FAO has compiled comprehensive worldwide regulations and directives regarding mycotoxins in food and feed as of December 2003. The Joint Expert Committee on Food Additives (JECFA), a scientific advisory body of FAO and WHO, provides mechanisms for assessing the toxicity of food additives, veterinary drug residues and contaminants, and has recently

evaluated the hazards related to several mycotoxins, including fumonisins B1, B2 and B3, ochratoxin A, deoxynivalenol, T-2 toxin, HT-2 toxin, and aflatoxin M1. The report explains the nature of each toxin, including its absorption and excretion, as well as toxicological studies, and it includes general considerations of analytical methods, sampling, associated intake issues and control mechanisms.

The EC has set maximum levels for some mycotoxins, including several aflatoxins, Ochratoxin A, patulin, deoxynivalenol and zearalenone, in certain foodstuffs. Maximum levels for fumonisins B1 and B2 came into force in October 2007. Consideration of a review of the maximum levels for deoxynivalenol, zearalenone and fumonisins B1 and B2 as well as the appropriateness of setting a maximum level for T-2 and HT-2 toxins in cereals and cereal products should be completed by July 2008.

The requirement to apply these regulatory limits has prompted the development of a vast number of analytical methods for the identification and quantification of mycotoxins in various samples, such as food, feed, and other biological matrices. The chemical diversity of mycotoxins and their varying concentration ranges in a wide range of agricultural commodities, foods and biological samples poses a great challenge to analytical chemists. The different chemical and physicochemical properties of the mycotoxins require specific extraction, cleanup, separation and detection methods. Therefore, most methods target only individual mycotoxins or at best a group of closely related mycotoxins. These methods are usually based on labour-intensive sample preparation protocols followed by traditional chromatographic separation (mostly liquid chromatography, LC). Gas chromatography (GC) either with electron capture detection

(ECD) or mass spectrometric (MS) detection is used in mycotoxin analysis, e.g. for trichothecene or patulin determination, but less frequently than alternative methods. In some cases, fast and accurate screening methods based on enzyme-linked immunosorbent assay (ELISA) are applied instead of the more labourintensive LC methods. Thin-layer chromatography (TLC) provides a cheaper alternative to LC-based methods and has an important role, especially in developing countries, for surveillance purposes and control of regulatory limits (Gilbert and Anklam 2002). Modern sample clean-up techniques, such as immunoaffinity columns (IAC) or solid-phase extraction (SPE) methods, help to simplify protocols, improve selectivity and, thus, performance characteristics.

To deal with the increasing number of sample matrices and mycotoxins of interest, fast and accurate analytical methods are needed. This demand has led to the development of rapid screening methods for single mycotoxins or whole mycotoxin classes based on immunochemical techniques (e.g. ELISA), biosensors (e.g. protein chips, antibody/protein-coated electrodes) and non-invasive optical techniques. On the other hand, highly sophisticated multi-mycotoxin methods based on LC coupled to multiple-stage MS are being developed to allow accurate and precise determination and unambiguous identification of mycotoxins without the need for tedious sample preparation and clean-up procedures.

## 9.3 Major Types of Mycotoxin

There are over 200 known types of mycotoxins. However there are some major and important type mycotoxins.

- Aflatoxin
- Ochratoxin
- Citrinin
- Ergot Alkaloids
- Patulin
- Fumonisins
- Trichothecenes
- Zearalenone

**Aflatoxin**

Aflatoxins are one of the most potent and dangerous groups of mycotoxins worldwide. Over four billion people in developing countries are repeatedly exposed to aflatoxins, contributing to greater than 40 percent of the disease burden in these countries. Aflatoxins are produced primarily by the fungi Aspergillus flavus and Aspergillus parasiticus. There are four main types of aflatoxins: B1, B2, G1, and G2. Aflatoxin B1 is the major toxin produced, and is regulated in the United States at 20 ppb in agricultural products that may be used in human food. The clinical effects of aflatoxins may include death, liver cancer, reproductive problems, anemia, immune system suppression, and jaundice. Nursing animals may be severely affected by a toxic derivative of aflatoxin (aflatoxin M1) that can be passed through milk [184].

Aflatoxin contamination is economically important in crops such as maize, peanuts, cottonseed, and tree nuts. Aspergillus flavus is commonly associated with a disease of maize known as Aspergillus ear rot (Figure 9.1a). Powdery, grey-green spores may develop

on the surface of maize ears, and aflatoxins may be produced by the fungus until the kernel moisture reaches about 15 percent. High temperatures, drought stress, and insect injury may contribute to increased aflatoxin contamination in maize. Aspergillus flavus and A. parasiticus may cause a disease of peanuts known as yellow mold (Figure 9.1b), and high levels of aflatoxin contamination may result following relatively high temperatures and moderate humidity. Cottonseed, an important food source for dairy cattle, may become contaminated with aflatoxins if the seed-bearing capsules (bolls) are damaged, followed by high humidity and warm temperatures before or after harvest. Tree nuts such as pistachios and almonds may become contaminated with aflatoxins during injury, such as the splitting of hulls [184].

Figure 9.1: Aflatoxin contaminated food items

**Ochratoxin**

Ochratoxin is a mycotoxin that comes in three secondary metabolite forms, A, B, and C. All are produced by Penicillium and Aspergillus species. The three forms differ in that Ochratoxin B (OTB) is a nonchlorinated form of Ochratoxin A (OTA) and that Ochratoxin C (OTC) is an ethyl ester form Ochratoxin A [186]. Aspergillus ochraceus is

found as a contaminant of a wide range of commodities including beverages such as beer and wine. Aspergillus carbonarius is the main species found on vine fruit, which releases its toxin during the juice making process [187]. OTA has been labeled as a carcinogen and a nephrotoxin, and has been linked to tumors in the human urinary tract, although research in humans is limited by confounding factors [186, 187].

**Citrinin**

Citrinin is a toxin that was first isolated from Penicillium citrinum, but has been identified in over a dozen species of Penicillium and several species of Aspergillus. Some of these species are used to produce human foodstuffs such as cheese (Penicillium camemberti), sake, miso, and soy sauce (Aspergillus oryzae). Citrinin is associated with yellow rice disease in Japan and acts as a nephrotoxin in all animal species tested. Although it is associated with many human foods (wheat, rice, corn, barley, oats, rye, and food colored with Monascus pigment) its full significance for human health is unknown. Citrinin can also act synergistically with Ochratoxin A to depress RNA synthesis in murine kidneys [181].

**Ergot Alkaloids**

Ergot Alkaloids are compounds produced as a toxic mixture of alkaloids in the sclerotia of species of Claviceps, which are common pathogens of various grass species. The ingestion of ergot sclerotia from infected cereals, commonly in the form of bread produced from contaminated flour, cause ergotism the human disease historically known as St. Anthony's Fire. There are two forms of ergotism: gangrenous, affecting blood supply to extremities, and convulsive, affecting the central nervous system. Modern

methods of grain cleaning have significantly reduced ergotism as a human disease, however it is still an important veterinary problem. Ergot alkaloids have been used pharmaceutically [181].

**Patulin**

Patulin is a toxin produced by the P. expansum, Aspergillus, Penicillium, and Paecilomyces fungal species. P. expansum is especially associated with a range of moldy fruits and vegetables, in particular rotting apples and figs [188, 189]. It is destroyed by the fermentation process and so is not found in apple beverages, such as cider. Although patulin has not been shown to be carcinogenic, it has been reported to damage the immune system in animals [189]. In 2004, the European Community set limits to the concentrations of patulin in food products. They currently stand at 50 μg/kg in all fruit juice concentrations, at 25 μg/kg in solid apple products used for direct consumption, and at 10 μg/kg for children's apple products, including apple juice [188, 189].

**Fusarium**

Fusarium toxins are produced by over 50 species of Fusarium and have a history of infecting the grain of developing cereals such as wheat and maize [190, 191]. They include a range of mycotoxins, such as: the fumonisins, which affect the nervous systems of horses and may cause cancer in rodents; the trichothecenes, which are most strongly associated with chronic and fatal toxic effects in animals and humans; and zearalenone, which is not correlated to any fatal toxic effects in animals or humans. Some of the other major types of Fusarium toxins include: beauvercin and enniatins, butenolide, equisetin, and fusarins [192].

## Trichothecenes

The trichothecenes are the largest group of mycotoxins known to date, consisting of more than 150 chemically-related toxic compounds. These mycotoxins are produced by several species of Fusarium, Stachybotrys, Trichoderma, and Trichothecium. The most important trichothecene mycotoxin in the United States is deoxynivalenol (DON), a common contaminant of wheat, barley, and maize. DON is sometimes called vomitoxin because of its deleterious effects on the digestive system of monogastric animals. Humans consuming flour made from wheat contaminated with DON often demonstrate symptoms of nausea, fever, headaches, and vomiting [184].

## Zearalenone

Zearalenone is a mycotoxin that mimics the reproductive hormone estrogen. This mycotoxin is produced primarily by the fungus Fusarium graminearum, the same fungus that produces deoxynivalenol in maize and small grains. Swine are the most commonly affected domestic animals, but cattle and poultry may also be affected. The clinical effects of zearalenone may include an enlarged uterus, swelling of the vulva and vagina (known as vulvovaginitis), enlarged mammary glands, anestrus (periods of infertility), and abortion. Zearalenone may be passed to nursing piglets through the mother's milk. A commercially available derivative of zearalenone (zeranol) has been used as a growth hormone to increase weight gain in beef cattle [184].

## 9.4 Mycotoxin Detection Techniques

### Analytical Techniques

#### *Conventional Analytical Techniques*

The term ''conventional method'' usually refers to a chromatographic separation coupled to a suitable detection system. The currently used quantitative methods for the determination of regulated mycotoxins, such as the fumonisins, zearalenone, type-A (e.g. T2-toxin) and -B trichothecenes (e.g. deoxynivalenol), ochratoxin A and the aflatoxins, in food and feed mainly use immunoaffinity clean-up with high-performance liquid chromatography (HPLC) or gas chromatography (GC) in combination with a variety of detectors, such as fluorescence detection (FLD) with either a pre- or post-column derivatisation step, UV detection, flame ionisation detection (FID), electron capture detection (ECD) or mass spectrometry (MS). Reviews of these methods have been summarized and published elsewhere [193-195]. From the multitude of available procedures, CEN is trying to standardize methods for mycotoxin analysis. CEN establishes performance criteria for mycotoxin methods usually on the basis of collaborative studies. CEN methods are official reference methods and are used for official control and surveillance and in cases of dispute. CEN–approved methods exist for aflatoxins, ochratoxin A, fumonisins, patulin and deoxynivalenol, for example, in various foods. Further methods for various mycotoxins in feed will be issued in the near future [196].

#### *Liquid Chromatography/Mass spectrometry (LC/MS)*

Within the last 10 years, liquid chromatography/mass spectrometry has become the universal approach for mycotoxin analysis, as more or less all potential analytes are

compatible with the conditions applied during separation and detection. Nevertheless, the breakthrough of this approach did not occur until the mid-1990s, when suitable interfaces, such as atmospheric pressure ionization, became accessible on a routine basis. Compared to conventional detection techniques, such as UV or fluorescence, mass spectrometry offers increased selectivity and sensitivity (although fluorescence detection might be more sensitive for certain mycotoxins, e.g. aflatoxins), unambiguous confirmation of the molecular identity of the analyte and the option to use isotopically labelled substances as internal standards. Furthermore, it is possible to investigate the molecular structure of metabolites and sugar conjugates (such as ‘‘masked mycotoxins’’; [197]) and to omit time consuming and error-prone derivatization and clean-up steps. However, it must be kept in mind that a reduction of the sample preparation inevitably emphasizes the Achille’s heel of LC/MS, i.e. relatively poor method accuracy and precision due to the irreproducible and unpredictable influence of co-eluting matrix components on the signal intensity of the analytes.

Due to the large number of LC/MS-based methods for the quantitative determination of single mycotoxin classes, their exhaustive examination goes beyond the scope of this work and, therefore, the interested reader is referred to the reviews of Zöllner and Mayer-Helm [198] and Sforza et al. [199].

**Multi-Mycotoxin Methods**

In the last few years, increased efforts have been made to develop analytical methods for the simultaneous determination of different classes of mycotoxins using LC–MS/MS. This trend is a result of the discovery of co-occurrence of different toxins and

related synergistic toxic effects that raise concerns about the health hazard from contaminated food and feed [200, 201]. In addition, it would be desirable to cover the toxins addressed by Commission Regulation 1881/2006 (aflatoxin B1, B2, G1, G2 and M1, Ochratoxin A, patulin, deoxynivalenol, zearalenone, fumonisins B1 and B2, HT-2 and T-2 toxin) with a single method as this increases sample throughput and decreases the costs per analysis. Although mass spectrometry offers sufficient selectivity (especially if tandem-mass spectrometry is applied) and multianalyte capabilities, its realization in the field of multi-mycotoxin analysis has been hampered mainly by the chemical diversity of the different toxin classes, which include acidic (fumonisins), basic (ergot alkaloids) as well as polar (moniliformin, nivalenol) and apolar (zearalenone, beauvericin) compounds. Therefore, compromises have to be made in the choice of extraction solvent and mobile phase, and the conditions may be far from optimal for certain analytes.

The initial stimulus for LC/MS-based multi-mycotoxin methods came from the field of mycology, where mass spectrometry is used to identify mold species according to their metabolite profile [202]. Beside the development of databases dealing with qualitative LC/MS of mycotoxins [203], this has led to early quantitative methods for the simultaneous determination of Aspergillus and Penicillium mycotoxins in building materials [204] and in an artificial food matrix [205]. While the former method suffered from low recoveries of some analytes, excellent accuracy and precision were obtained in the latter case through use of a de-fatting step applied to the raw extract, and use of matrix matched calibration to compensate for matrix effects. Some years later, this method was applied for the simultaneous determination of aflatoxins, ochratoxin A, mycophenolic acid, penicillic acid and roquefortine C [206] after a slight modification of the extraction solvent.

After this initial phase, the focus of multi-mycotoxin analysis shifted to Fusarium mycotoxins. Royer et al. [207] developed a method for the quantitative analysis of deoxynivalenol, fumonisin B1 and zearalenone in maize, including accelerated solvent extraction, a two-step SPE procedure and internal standards for each analyte. The LODs were below the maximum concentration levels permitted in the EU, but the method suffered from a low recovery for zearalenone. The next generation of methods included several A- and B- trichothecenes as well as zearalenone, and used Mycosep columns for clean-up of the raw extracts. Zearalanone was used as internal standard for zearalenone in the method of Berthiller et al. [197], and Biselli and Hummert [208] applied matrix matched calibration for this analyte. Cavaliere et al. [209] added α-zearalenol and three fumonisins to the list of analytes and performed de-fatting and solid-phase extraction of the raw extracts of corn meal. While the efficiency of the extraction step was greater than 84% for all analytes, matrix effects were still present and required matrix-matched calibration.

A method for the simultaneous determination of Fusarium, Aspergillus and Penicillium toxins (ochratoxin A, zearalenone, α- and β-zearalenol, fumonisins B1 and B2, T2- and HT2-toxin, T2-triol, mono- and diacetoxyscirpenol, deoxynivalenol, 3- and 15-acetyldeoxynivalenol, deepoxy-deoxynivalenol and aflatoxin M1) was reported by Sorensen and Elbaek [210]. Bovine milk samples were defatted and after adjustment of the pH, an SPE procedure was applied. Signal suppression/enhancement was minimized and recoveries 476% were obtained. However, the major drawback of this method was the necessity of using two chromatographic runs with different columns and eluents. The two most recent reports, which include a clean-up of the raw extract using MultiSep #226

cartridges, introduced instrumental improvements to multi-mycotoxin analysis in foodstuffs. A time-of-flight mass spectrometer was used by Tanaka et al. [211], while, in the method of Ren et al. [212], analysis time was significantly decreased through the application of ultra-performance liquid chromatography. In both methods, recoveries 470% were obtained for all analytes and no significant matrix effects were reported.

As all these methods rely on some sort of clean-up, certain toxin classes are excluded as they are not compatible with the clean-up and/or extraction conditions (for example, the fumonisins are not determined by the methods of Tanaka et al. [211] and Ren et al. [212]. In particular, neither ergot alkaloids, moniliformin, enniatins nor masked mycotoxins are included in any of these reports. To overcome these problems, some existing methods omit a clean-up of the sample and inject raw extracts into the LC/MS. This clearly increases the demands on the selectivity of the detector as well as on the investigation of matrix effects, especially if complicated food matrices are analysed. Spanjer et al. [213] determined 22 mycotoxins (including the ergot alkaloid ergotamine) in different food matrices. Samples were extracted with an acetonitrile/water mixture and were diluted with water prior to injection. Matrix effects were investigated for every analyte/matrix combination and validation data obtained that suggested that the analysis of diluted raw extracts is indeed feasible and at the same time sensitive enough for determining most mycotoxin levels set in the legislation. Our own contribution in this field was the quantitative determination of a set of 39 analytes (including moniliformin, beauvericin, enniatins and masked mycotoxins) in wheat and maize [214]. In both matrices, linear calibration curves were obtained (with the exception of moniliformin) after spiking blank matrices at multiple concentration levels, with coefficients of variance of the overall

process of <5.1 and <3.0%, respectively. Significant matrix effects were observed for maize, but these could be overcome by matrix-matched calibration. LODs ranged from 0.03 to 220 µg $kg^{-1}$ and the trueness of the method was confirmed for deoxynivalenol and zearalenone though the analysis of certified reference materials. Very recently, this method has been extended to the simultaneous determination of 87 mycotoxins and has successfully been applied to mouldy food samples [215].

In the near future, a strong trend towards multi-mycotoxin methods, which do not involve a clean-up of the sample, can be expected, as these methods can be relatively easily adapted to new analytes and matrices, and the obvious time- and cost-savings compensate for the expense of initial validation. Advances in the technology and in the instrumental design in mass spectrometry will further decrease the influence of matrix effects, which certainly constitute the main drawback of this approach at the moment.

## Fast Screening Methods

### *Immunochemical Techniques*

Rapid methods based on immunochemical techniques often have the advantage of not requiring any clean-up or analyte enrichment steps. ELISAs have become routinely used tools for rapid monitoring of most mycotoxins, especially for the screening of raw materials [196, 216]. Although ELISA tests may show a high matrix dependence and possible overestimation of levels, the advantages of the microtitre-plate format are speed, ease of operation, sensitivity and high sample throughput. ELISA test kits are commercially available for most of the major mycotoxins.

Alternatives to ELISAs include a number of immunosensors as well as upcoming methods using immunochemical platforms, such as fluorescence polarization immunoassays (FPI) [217] or surface plasmon resonance (SPR) with mycotoxin–protein conjugates immobilized onto a sensor chip surface [218]. Immunosensors are emerging as a cost-effective alternative for screening and quantitative determination of mycotoxins [219]. Array biosensors have been developed using competitive-based immunoassays for the simultaneous detection of multiple mycotoxins, including ochratoxin A, fumonisins B, aflatoxin B1, and deoxynivalenol, on a single waveguide surface by imaging the fluorescent pattern onto a CCD (charge-coupled device) camera [220]. Other formats with fluorescence detection include automated flow-through immunosensors with enzyme-labelled mycotoxin derivatives [221]. Electrochemical immunosensors with surface-adsorbed antibodies on screen-printed carbon electrodes have been fabricated for the detection of aflatoxin M1 in milk [222] and, in an array configuration, for the detection of aflatoxin B1 [223]. Affinity-based surface plasmon resonance sensors (SPR) have the advantage of not requiring any labelling of the target mycotoxin [218] and may become an alternative method for rapid screening, which also enables the simultaneous detection of multiple mycotoxins using serial connected flow cells [224]. In a further label-free immunochemical approach for the detection of aflatoxin B1 and ochratoxin A, optical waveguide lightmode spectroscopy (OWLS) was used with integrated optical waveguide sensor chips measuring the resonance incoupling angle of polarized light, thus determining the surface coverage [225].

A complementary tool for the screening of cereal samples may be DNA microarray-based chips using PCR followed by microarray colorimetric detection, which has been

developed for the fast detection and identification of 14 trichothecene- and moniliformin-producing Fusarium species occurring on cereals [226].

In recent years, interest in rapid membrane-based immunoassay methods, such as flow-through immunoassays and lateral flow devices (LFDs), has strongly increased due to the need for rapid on-site (pre)-screening. A flow-through enzyme immunoassay was developed for the detection of ochratoxin A in roasted coffee [227]. Requiring no sample preparation other than an extraction step, LFDs allow qualitative or semi-quantitative determination of mycotoxins on one-step strip tests within a few minutes. Such LFDs have been developed for selected mycotoxins, such as aflatoxin B1 [228] and fumonisin B1 [229]. The strong interest is furthermore reflected in the increasing number of commercially available test kits for field use, based mostly on direct competitive assays.

***Non-invasive Techniques***

Optical methods, such as Fourier Transform midinfrared spectroscopy with attenuated total reflection [230] or near-infrared transmittance spectroscopy [231], are promising techniques for the fast and non-destructive detection of mycotoxins in grains. The approaches allow sample preparation to be reduced to an absolute minimum and to be integrated into on-line monitoring systems. Nevertheless, since rapid data interpretation is based on the output of chemometric analysis, the high matrix dependence and the lack of appropriate calibration materials are still major restrictions.

Similarly, electronic noses, featuring an array of electronic chemical sensors with pattern recognition systems, have also been developed [232]. In this approach, volatile organic compounds of low molecular weight, which are released by many fungi as products

of secondary metabolism, are adsorbed onto the sensor surface and measured with a variety of transduction systems based on electrical-, optical-, or mass-transduction, such as metal oxide sensors (MOS) and surface acoustic wave sensors (SAW), for example [233].

**Photoacoustic Spectroscopy**

Photoacoustic spectroscopy (PAS) involves irradiating intermittent light onto a sample and then detecting the periodic temperature fluctuations in the sample as pressure fluctuations. Photoacoustic spectroscopy measurement is based on the photoacoustic effect. The photoacoustic effect was discovered by Alexander Graham Bell in 1880. This is the phenomenon whereby, when intermittent light is irradiated onto a substance, the substance emits acoustic waves of the same frequency as the light pulse frequency. With the development of highly-sensitive microphones and other advances in electronics, research progressed into the measurement of gas samples, in particular [234]. The photoacoustic spectroscopy uses Fourier transform infrared (FTIR) instruments in assessing the fungal contamination.

With FTIR-PAS as intact specimen is placed inside a closed cell containing a sensitive microphone. Infrared light is admitted through a window to irradiate the specimen. When the specimen absorbed the light, it became heated and warmed the surrounding layer of air or gas. The warm gas expanded, resulting in increased pressure in the cell returned to its original level. Chopping or periodic modulation of the light produced alternating heating and cooling of the specimen at the modulation frequency, resulting in gas pressure waves, which are detected as sound by the microphone. If the specimen absorbs infrared radiation, some of the absorbed energy will be converted to heat and

committed as acoustic waves. Since the amplitude and frequency of the acoustic waves emitted depend on the amount and frequency of the infrared energy absorbed, the photoacoustic signal reflects the infrared spectrum of the specimen. The signals from the microphone are acoustic interference waves. Applying Fourier transformation to these signals produces a spectrum similar to an absorption spectrum [234]. Schematic of the operating principle of the photoacoustic spectroscopy is shown is Figure 9.2. Because of the inherently surface-profiling signal of FTIR-PAS it is potentially sensitive detector of fungal infection on the surfaces of commodities. Gordon et al. [235] applied the technique to corn kernels classified as either bright greenish-yellow fluorescence (BGYF)-positive or negative. The technology has promise as a presumptive test for aflatoxin contamination, however application of the method is limited because available photoacoustic detectors can only accommodate a single kernel at a time [236].

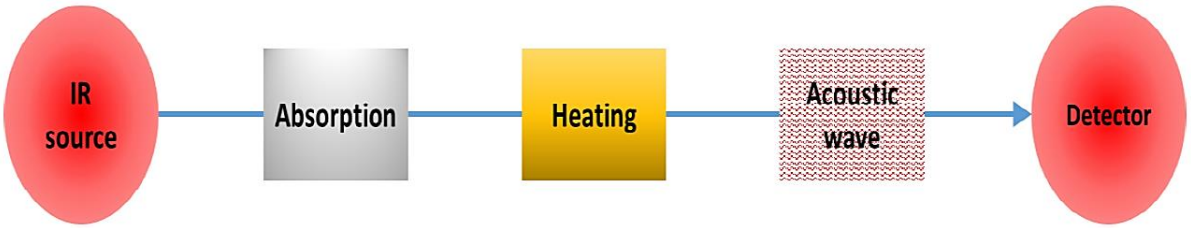


Figure 9.2: Working principle of Photoacoustic Spectroscopy method

The high demand for rapid screening methods for mycotoxin analysis reflects the need for fast and cost-effective on-site determination of the level of mycotoxin contamination in food and feed. Mycotoxin classification is essential to quantify its toxicity measure and harmfulness for the body. Current state of the art offers time consuming and expensive techniques. Hence, inspired from the outcome of our early studies and

capabilities of photoacoustic spectroscopy, in this study we propose a portable mechanical sensor for in-field characterization of mycotoxin in a fast and economic manner.

## 9.5 Proposed Model

The photoacoustic system is based on the excitation of molecules in a sample materials by infrared light. The excitation of molecules depends on the intensity and wavelength of the incoming light along with the absorption spectrum and the absorption area of the molecules. Molecules of different mycotoxin generates distinct frequencies upon infrared light. Hence a bio-inspired mechanical sensor is envisioned which can be used for characterizing multiple mycotoxins at a time. The proposed sensor avoid the requirement of any chemical testing and time-killing or expensive analysis.

The envisioned sensor is composed of a series of cantilever beams with linearly varying length from its base to apex end as shown in Figure 9.3. The sensor model is inspired from the basilar membrane study in chapter 5. It has been noticed that introducing a beam model, following the geometric configuration of basilar membrane, it is possible to select distinct frequency from each beam of the structure. Instead of fixed beams (as in chapter 5), the proposed mycotoxin sensor is consists of cantilever beams. Such modification is made to reduce the flexural stiffness of the beam since the acoustic wave amplitude generated by mycotoxin molecules could be significantly low to excite stiffer beams. Moreover it is evident that cantilever beam exhibits more pronounced deformation behavior than a fixed beam, which can be helpful in capturing the frequency content accurately. Each adjacent cantilever beam of the sensor is attached at opposite ends of the structure to allow substantial space for electrical connections in both ends. The proposed

sensor is comprise of 140 beams with 2 mm spacing. Width and thickness of each beam is considered as 2 mm and 0.1 mm, respectively. The smallest and longest cantilever beams of the model is 1.9 mm and 3.9 mm long, respectively, with 0.014 mm of decrement from base to apex end.

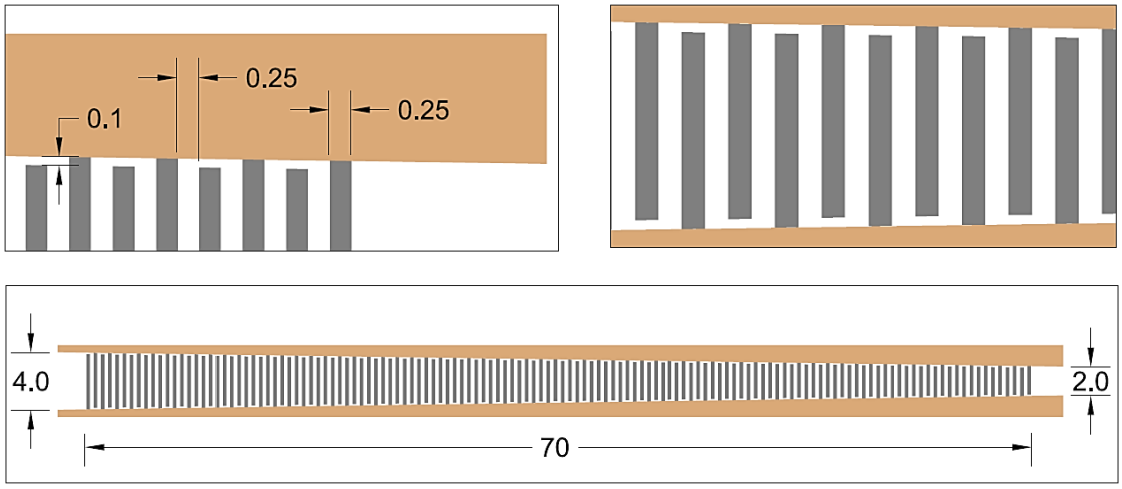


Figure 9.3: Proposed cantilever beam model for mycotoxin detection (dimensions are in mm)

Typically Silicon (Si) has been always considered as the prime material for sensor design. However application of Si has shown limitations in sensing applications at harsh environmental conditions. Silicon cannot be used for high temperature applications as it loses the electrical and mechanical reliability at high temperatures. Since infrared laser in photoacoustic spectroscopy is expected to generate significant heat in the system, hence silicon might not be a good choice for the beam material in the sensor. Instead of silicon, Gallium Nitrate (GaN) is considered for the beam material for its proven reliability and performance at high temperature environment. Also note that, GaN possess high young's modulus (181 GPa), which is essential to capture high frequency acoustic wave generated

by mycotoxin molecules. Material properties of the sensor constituents are listed in **Error! Not a valid bookmark self-reference.**.

Table 9.1: Material Properties of the mycotoxin cantilever beam sensor

| | **Material** | **Stiffness (GPa)** | **Density ($kg/m^3$)** | **Poisson's Ratio** |
|---|---|---|---|---|
| **Beam** | Gallium Nitrite | 181 | 6150 | 0.352 |
| **Support** | Aluminum | 69 | 2700 | 0.33 |

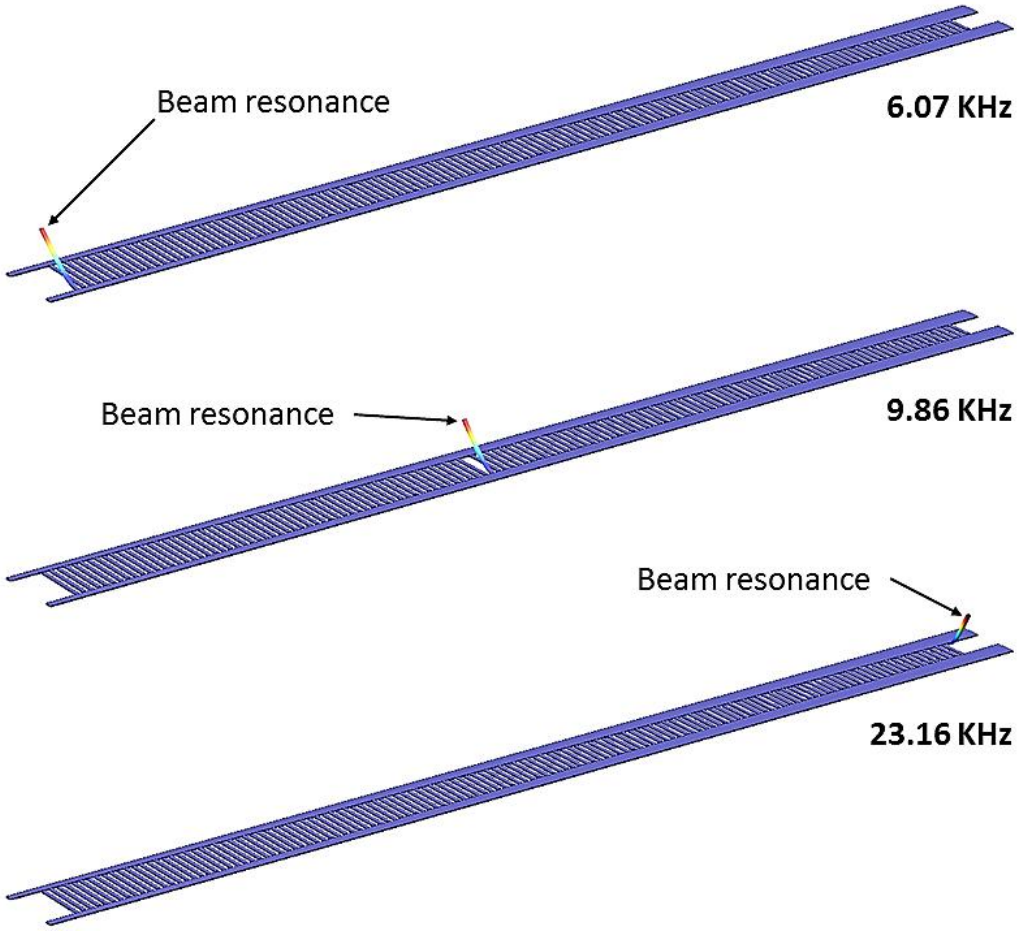


Figure 9.4: Local resonance of the cantilever beams at different frequencies.

A numerical study is performed to investigate the practicability of the proposed model. Eigenvalue analysis is performed using computational tool COMSOL multiphysics. Numerical computation confirms that, each cantilever beam resonates at a specific frequency with maximum frequency (23.16 KHz) at smallest beam to minimum frequency (6.07 KHz) at longest beam (see Figure 9.4). The proposed model in Figure 9.4 confirms the dynamic mechanical characteristic of the envisioned sensor with multi-frequency capturing capability. However the complete mycotoxin sensor requires a mycotoxin molecule bed and IR-PAS setup to excite the mycotoxin molecules, generate acoustic wave and resonate the selective sensor beam. The beam support at both ends of the sensor is suggested to extend, to use the extended portion as the test bed for the mycotoxin molecules. It is expected that, upon infrared ray, mycotoxin molecules will create acoustic wave which will propagate as surface wave to the cantilever beams. Highly sensitive piezoelectric strips are attached at the top surface of the GaN cantilever beam to capture the resonance response of the beam as electric potential.

## 9.6 Chapter Summary

When certain types of fungus grow on food, they produce minute amounts of toxins called mycotoxins. There are several types of mycotoxins in nature. Most of the mycotoxins are harmless for health, however few mycotoxins are really dangerous. Hence it is essential to detect the mycotoxin class to know its toxicity and importance to be destroyed. Each year millions of food items used to demolish due to fungal growth, but without knowing the toxicity level of the associated mycotoxins. Several mycotoxin detection techniques are available. However current methods are time consuming and

costly, hence not adequate for bulk or on-field application. Hence in this study we propose a mechanical mycotoxin detection sensor adopting the physics of basilar membrane and capabilities of Infrared Photoacoustic Spectroscopy. The proposed sensor is consists of a series of cantilever beams with varying length from its base to apex end. Gallium nitrite (GaN) beams are proposed instead of typically used silicon beams due to its (GaN) much reliable response at high temperature applications. The proposed model confirms its capability of exhibiting resonance response at a wide range of frequencies where each beam resonates at a distinct frequency. Using the IR-PAS along with the proposed model we expect that a cost effective portable mechanical sensor is possible to introduce which can be employed for in-filed bulk mycotoxin detection application.

# CHAPTER 10: ENERGY SCAVENGING USING PETTERENED PIEZOELECTRIC LAYERS

The piezoelectric transduction mechanism has significant applications in passive sensing, health monitoring and energy harvesting. Design of piezoelectric energy harvesters is typically restricted with cantilever beams or plates. Simply supported plate type energy harvesters are seldom used in printing machines, in cars to power localized MEMS sensors, but usually uncommon for energy harvesting purposes. Predominant reason for their limited use is that the amount of harvested energy is very small compared to cantilever beam harvesters. Although plate type harvesters are usually discouraged, with patterned electrodes and properly optimized shapes, they were found to be suitable for harvesting energy from wider band of frequencies. This is possible due to selective superposition of effective higher bending modes of the plates. This requires an effective mathematical model to understand their behavior. Consequently, these small harvesters can also be used as vibration sensors. In this study, a detained analytical model is presented to calculate the frequency response function (FRF) from a simply supported plate type energy harvester with patterned piezoelectric layers. A generalized mathematical form is presented for an arbitrary rectangular piezoelectric patch placed on a host plate. Strain rate damping mechanism is incorporated in the model for better and accurate results. First, a comparative study on the strain rate damping effect is presented by placing the piezoelectric layer on

the entire plate. It shows that without damping the estimation is quite inaccurate. Numerical simulation is also performed using Finite Element Method (FEM). Further a methodology through optimization is proposed to generate a required pattern of piezo layers for desired requirements or applications. With the proposed generalized model any particular shape and size of the layer can be obtained through optimization. The FRFs from two optimized electrode patterns are presented.

## 10.1 Background

Piezoelectric materials are increasingly used in vibration control, noise control and shape control of structures. In addition it has been found that piezoelectric materials are quite valuable for energy harvesting for low power devices. In this paper a predictive analytical model is proposed to harvest energy from a plate coated with designed piezoelectric layers with certain constrains. Predictive analytical model for piezoelectric sensors was first proposed in the field of structural health monitoring for sensing and actuation [237, 238]. In association with design and application of innovative piezoelectric devices, predictive model is equally or more important for better understanding of the physics and for adopting suitable design approaches. In the field of energy harvesting there has been significant advancement [78, 137, 239-246] in the design and application of energy harvesters. Recent advancements in low power electronics and piezoelectric materials have made vibration based energy harvesting more lucrative. On the other hand, a significant effort has been made to improve the circuit design for the energy storage [127, 151, 247-251]. It is evident that sometimes researcher adopt over-simplified model for explaining the physics of the harvesters [243, 252]. A comprehensive study of existing

models related to the piezoelectric (PZT) harvesters can be found in [151]. The inaccuracy in using the static expressions in fundamentally dynamic problems has been discussed in greater detail by Erturk et.al. [78, 244] & Banerjee, S. [137].

In this paper a simply-supported plate type harvester [137] with patterned piezoelectric layer is considered for energy harvesting. For the first time, a generalized predictive model is proposed to find the voltage output from a small rectangular patch of piezoelectric layer, analytically. The proposed predictive model could potentially be helpful to optimize the placement of such small segments of piezoelectric layers or electrodes in a required pattern as per design requirements (e.g. maximize the voltage output, maximize the resonance band, minimize the harvester weight or any coupled requirements). Such design approach would need an accurate mathematical model which can be used for predictive design of the customized harvesters. The proposed mathematical model is versatile enough to be formulated for different application e.g. sensors or actuators.

There are many structural components subject to vibration. Hence, energy harvesting from ambient vibration of the host structure using plate type harvester can be considered as a suitable candidate. Thin plate, metal sheets, diaphragms are frequently used in mechanical systems and vibrates by virtue of their design during their operation. Researchers and engineers are designing micro air vehicles (MAV) by mimicking the biological creatures. The wings are designed for flapping. Army combat operations are focusing on insect flights where in addition to the flapping (bending excitation), simultaneous excitation of the torsional degree-of-freedom is required [253, 254]. This

activity will require segmented and innovative placement of piezoelectric coating on the wing such that more control can be achieved. On the other hand, in this paper it can be seen that the orientation of the piezoelectric layer on the plate type harvester could perform better as a wideband energy scavenger. Hence, the idea of placing segmented piezoelectric layers is mutually beneficial.

In this paper, an effort has been made to model the energy output from a periodically deformable sandwich plate with distributed electrode or piezoelectric layer. First, the solution for the voltage output is calculated for arbitrary placement of electrode. Then the frequency response function (FRF) is superposed by varying the placement of the PZTs. The area under the curve (FRF) within a specific frequency band (wideband) is then maximized to get the PZT pattern on the plate. This study could be repeated for different load resistance because the current and the voltage output depend on the external load.

Analytically obtained Frequency Response Function (FRF) will be immensely valuable for energy harvester by virtue of patterning the piezoelectric layer in optimized fashion subjected to certain constrains. The concept of optimized placement of piezoelectric layer on a plate or a beam is not new in general [255-259]. Vibration control of lightweight structures has been seriously studied by the previous researchers using optimized [256] piezoelectric pattern. Most importantly, in the realm of vibration control, a numerical scheme using level set method [260] was proposed by Zhang, J. [261], where vibrating system with piezoelectric patches was analyzed to minimize the vibration frequency subjected to constraint on the patch geometry. Numerical analysis of simply supported plate for active vibration control with piezoelectric sensors and actuators is

presented by Narwall et.al. [262]. Recently, the optimal vibration control of plate structures is proposed by Ansari et.al. [263] using previously derived level set [260] topology optimization method but by using constrained layer damping patches in passive mode. Vibration control using simultaneously passive (constrained layer damping patches) and active (piezoelectric patches) elements was proposed by Lam et.al [264]. Dynamic passive controller for thin plate vibration was presented by Alessandroni et.al. [265]. Process of minimizing structural sound radiation passively through shunted piezoelectric material is described by Ozer et.al. [266]. Structural vibration reduction in passive mode by means of shunted piezoelectric patches is discussed by Ducarne, et.al. [267]. In this study a simple cantilever beam is considered to evaluate the dedicated modal electro-mechanical coupling factor as a function of material and piezoelectric layer geometry. Then particular to an eigen mode of the structure piezoelectric patch geometries are estimated using optimization by maximizing the modal electromechanical coupling factor [264, 267]. Such models are predominantly for vibration control of plate type structures by mode suppression. However, no such accurate mathematical model exists for plate type energy harvesters, which is proposed in this paper to calculate the Frequency response Function (FRF) for a plate as a function of piezoelectric patch geometry. The mathematical models for vibration control of plates (where certain vibration modes need to be suppressed by the piezoelectric counter effect or closed loop feedback control) and plate type energy harvesters (where voltage output from the piezoelectric layer has to be maximized to store power) are very different due to their different target applications. Predominantly for vibration control bimorph (piezoelectric layer on either side) plates are proposed whereas in this article to maximize the harvested energy unimorph (piezoelectric layer on one side) plate is proposed.

Moreover the pattern of the piezoelectric layer obtained for vibration control cannot be directly used for energy harvester. Thus a dedicated mathematical model for plate type harvester is necessary. In this paper such mathematical model for plates is proposed using correct physics by incorporating damping. Although the underlying philosophy of optimizing the piezoelectric layer subjected to constrains is similar, genetic algorithm is used in this paper as oppose to traditional level set method used for optimizing the geometry of piezoelectric layer for vibration control applications. Primary focus of this paper is to provide a predictive analytical tool to calculate Frequency response Function (FRF) for a plate type harvester as a function of arbitrary shaped piezoelectric patch geometry at arbitrary location on the plate (assuming piezoelectric layer is very thin compared to the plate). Such tool can be used any state-of-the-art optimization tool.

From our derivation two expressions for voltage frequency response function (FRF) is presented. One for the piezoelectric layer covering the entire plate and one for a small rectangular piezoelectric patch placed at any arbitrary location on the plate. It is shown that when the patch size is selected to cover the entire plate or any particular number of piezo patches that covers the entire plate, both expressions for FRF generated identical results. Hence, the second expression for FRF with a piezoelectric patch at any arbitrary location is absolutely generalized expression. The proposed closed form FRF expression can be easily used in any optimization program and which is a major contribution in this paper.

## 10.2 Mathematical Formulation

A generalized mathematical formulation is presented in the following paragraphs. A unimorph plate is considered with piezoelectric layer on the entire plate (see Fig. 1 (a))

and next a small rectangular segment of piezoelectric layer (see Fig. 1 (b)) is considered on the plate at any arbitrary location. The host structure can be divided in to several small rectangular segments. The piezoelectric coating is assumed to cover the rectangular segment only. In this derivation, we have assumed that the Love-Kirchhoff's assumptions are valid. The strain along the thickness direction of the plate is zero as a result of Love-Kirchhoff's assumptions. Thus, Mindlin's shear deformation theory [268-270] is ignored in this derivation. The electrode layer is assumed to be thin compared to the host structure. The mechanical damping is separated in two parts 1) internal strain rate damping (Kelvin–Voigt damping) associated with the piezoceramic layer 2) external environment (air) damping. The electrodes on either side of the piezoceramic layers are assumed to be perfectly conductive. Unlike earlier publications [243] the Kelvin-Voigt damping matrix is assumed to be coupled (a fully populated matrix) between two orthogonal directions x and y [137]. A resistive load ( $R_l$ ) is considered in the energy harvesting circuit (see Fig. 1) for developing the coupled governing equation. Hence, when piezoelectric patches are considered the total circuit resistance is assumed to be contributed through the parallel connection of effective resistance for individual patches. It is assumed that the electric field is bound to develop only along the z direction. Hence, the electric field strength developed along the x and y axes were zero. x, y, and z are analogous to $x_1$, $x_2$ and $x_3$, respectively. In Figure 10.1 (b) a small rectangular element between $x_i$ and $x_{i+1}$ along $x$ and between $y_i$ and $y_{i+1}$ along $y$ was considered in the forgoing derivation.

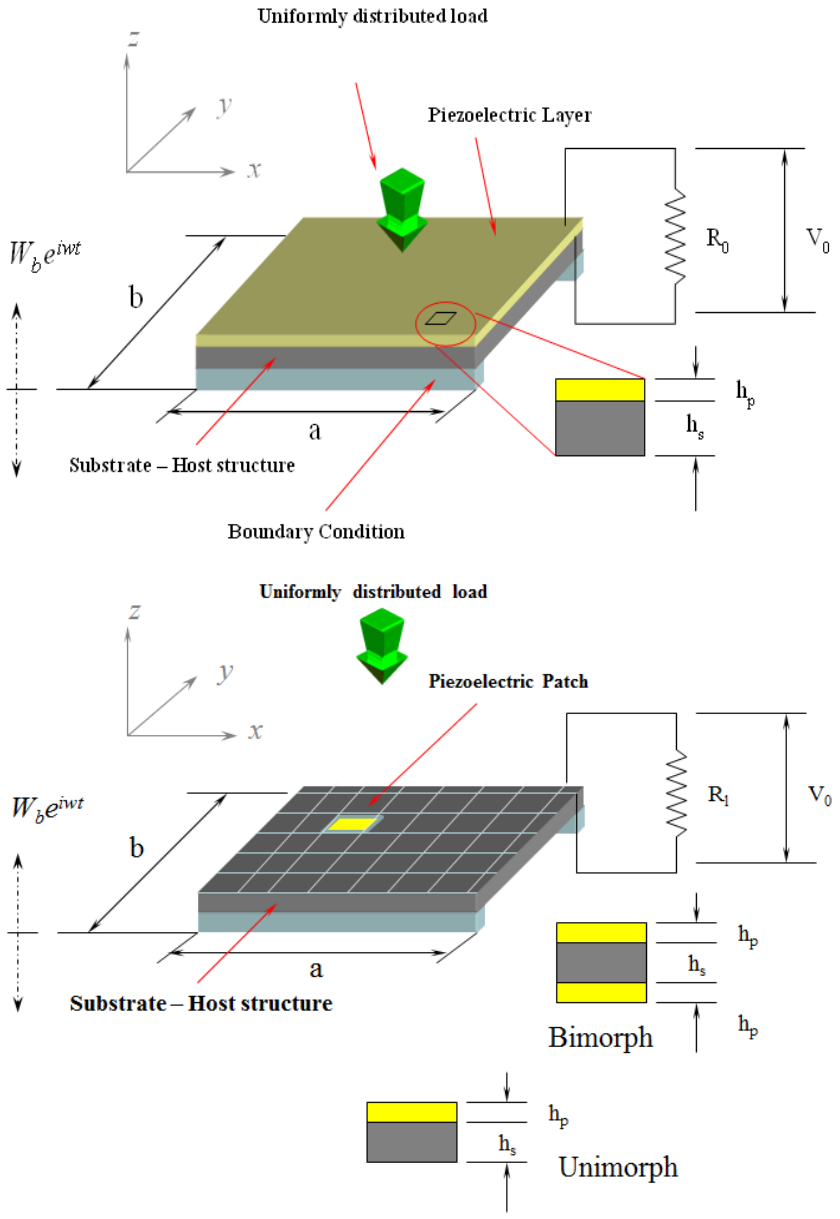


Figure 10.1: Schematics of plate type energy harvesters with discrete PZT patch a) covering the entire plate b) covering a small segment.

The Governing differential equation of a plate with transverse loading under dynamic condition can be written as

$$\frac{\partial^2 M_x}{\partial x^2} + 2\frac{\partial^2 M_{xy}}{\partial x \partial y} + \frac{\partial^2 M_y}{\partial y^2} + m\frac{\partial^2 w}{\partial t^2} = -m\frac{\partial^2 w_s}{\partial t^2} - L \qquad (10.1)$$

Where, $M_x$ is the moment per unit length about x axis and $M_y$ is the moment per unit length about y axis, $M_{xy}$ is the moment resulted from the shear stress. $L$ , m, w, $w_s$ are the transverse loading on the plate, mass density of the plate, relative transverse deflection and total external displacement of the plate, respectively. The moments ( $M_x$ , $M_y$ , $M_{xy}$ ) in equation (1) can be obtained by integrating the moment of the stress distribution over the cross-section of the plate. As an example, here the expression for the moment $M_x$ is written below.

$$M_x dy = \int_{-hs/2}^{+hs/2} \sigma_x^s dy.dz.z + \int_{+hs/2}^{hs/2+hp} \sigma_x^p dy.dz.z \qquad \text{or} \qquad M_x = T1 + T2 \tag{10.2}$$

Where, superscript p was used for the piezoelectric layer and s was used to represent the substrate layer. $h_s$ & $h_p$ are thickness of the substrate and the piezoelectric layer, respectively. The constitutive relation for piezoelectric materials can be written as [24].

$$\mathbf{S}^p = \left[\mathbf{s}^E\right]^p \{\mathbf{T}\}^p + [\mathbf{d}]^T \{\mathbf{E}\} \tag{10.3}$$

Where, $\mathbf{S}^p$ is strain tensor, $\{\mathbf{T}\}b^p$ is stress tensor, [**d**] is the matrix for direct piezoelectric effect consists of piezoelectric charge constants and [271] is the induced or generated electric filed strength. Using mathematical manipulation, expressions for the stress vector can be obtained as

$$\{\mathbf{T}\}^p = [\mathbf{C}]^p \mathbf{S}^p + [\mathbf{D}]^p \mathbf{S}^p - [\mathbf{C}]^p [\mathbf{d}]^T \{\mathbf{E}\} \tag{10.4}$$

[**C**]$^p$ is the constitutive matrix composed of elastic constant of the piezoelectric material, [**D**]$^p$ is the coupled strain rate damping matrix, and thus the matrix is not diagonal, which is assumed to be diagonal in [78, 244].

First, let's consider the plate with piezoelectric layer on the entire plate. After performing the integration and substituting the expressions for $M_x$, $M_y$ and $M_{xy}$ in equation (1) (assuming $e_{24} = 0$), viz.

$$\Psi_1 \frac{\partial^4 w}{\partial x^4} + \Psi_1 \frac{\partial^4 w}{\partial y^4} + \Psi_2 \frac{\partial^4 w}{\partial x^2 \partial y^2} + C_{srx}\left(\frac{\partial^5 w}{\partial x^4 \partial t} + \frac{\partial^5 w}{\partial y^4 \partial t}\right) + 2C_{sry} \frac{\partial^5 w}{\partial x^2 \partial y^2 \partial t} + C_{ax} \frac{\partial w}{\partial t} + C_{ay} \frac{\partial w}{\partial t} + m \frac{\partial^2 w}{\partial t^2}$$

$$-\left(V_{31} + V_{32}\right)\vartheta(t) = -m \frac{\partial^2 w_s}{\partial t^2} - C_{ax} \frac{\partial w_s}{\partial t} - C_{ay} \frac{\partial w_s}{\partial t} - L \qquad (10.5)$$

And the governing differential equation for a rectangular piezoelectric patch at any arbitrary location between $x_i$ and $x_{i+1}$ along $x$ and between $y_i$ and $y_{i+1}$ along $y$ the equation (1), viz.

$$\Psi_1 \frac{\partial^4 w}{\partial x^4} + \Psi_1 \frac{\partial^4 w}{\partial y^4} + \Psi_2 \frac{\partial^4 w}{\partial x^2 \partial y^2} + C_{srx}\left(\frac{\partial^5 w}{\partial x^4 \partial t} + \frac{\partial^5 w}{\partial y^4 \partial t}\right) + 2C_{sry} \frac{\partial^5 w}{\partial x^2 \partial y^2 \partial t} + C_{ax} \frac{\partial w}{\partial t} + C_{ay} \frac{\partial w}{\partial t} + m \frac{\partial^2 w}{\partial t^2}$$

$$-\left(V_{31} \frac{d^2}{dx^2} Sxy + V_{32} \frac{d^2}{dy^2} Sxy\right)\vartheta(t) = -m \frac{\partial^2 w_s}{\partial t^2} - C_{ax} \frac{\partial w_s}{\partial t} - C_{ay} \frac{\partial w_s}{\partial t} - L \qquad (10.6)$$

Where, $C_{ax}$ & $C_{ay}$ are the viscous air damping coefficients, $C_{srx} = \mathrm{Y}_p c_{srx}$ & $C_{sry} = \mathrm{Y}_p c_{sry}$ are the strain-rate damping coefficients, $\Psi_1 = \mathrm{Y}_s + \mathrm{Y}_p$, $\Psi_2 = 2\left(\mathrm{Y}_s \mu_s + \mathrm{Y}_p \mu_p + \mathrm{Y}_c\right)$, $\mathrm{Y}_s = -2D_s h_s^3$

$$Y_p = -\left(D_p(h_s + 2h_p)^3 - D_p h_s{}^3\right), \quad Y_c = -2D_s(1-\mu_s)h_s^3 - D_p(1-\mu_p)\left((h_s + 2h_p)^3 - h_s{}^3\right)$$

$$V_{31} = \frac{e_{31}}{2h_p}\left(h_p{}^2 + 2h_s h_p\right) \quad \& \quad V_{32} = \frac{e_{32}}{2h_p}\left(h_p{}^2 + 2h_s h_p\right)$$

$$Sxy = \left[H(x-x_i) - H(x-x_{i+1})\right]\left[H(y-y_i) - H(y-y_{i+1})\right], \quad H(x-a) \text{ is Heaviside}$$

step function reveals the value 1 only if $x > a$.

$D_s = \frac{E_s}{24(1-\mu_s{}^2)}$ and $D_p = \frac{E_p}{24(1-\mu_p{}^2)}$, $E_s$ and $E_p$ are Elastic Modulus of Substrate Structure and piezoelectric coating, respectively. $\mu_s$ and $\mu_p$ are Shear Modulus of Substrate Structure and piezoelectric coating, respectively. In the foregoing derivation two types of damping mechanisms are considered: viscous damping caused by air medium and the Kelvin–Voigt damping or strain rate damping, together they can be called as Rayleigh damping mechanism. Viscous air damping is a simple way of modeling the force acting on the plate due to the air particles displaced by the plate and strain-rate damping accounts for the structural damping due to the friction due to internal constitution of the plate [137, 151]. The equations (5) or (6) are dynamic equation for mechanical vibration with electrical coupling and hence, the electrical circuit equation with mechanical coupling must also be considered simultaneously in the proposed coupled problem. The electric charge density displacement of the PZT layer will be used in the following expressions. The electric charge density at the PZT layer can be represented by the Gauss Law

$$q(t) = \int_A \mathbf{D} \bullet \mathbf{n} dA = \int_{y_i}^{y_{i+1}} \int_{x_i}^{x_{i+1}} D_3 dx dy \qquad (10.7)$$

Where, A is the electrode area over the PZT layer and $q(t)$ is electric charge developed between the PZT electrodes

$$q(t) = -\int_{y_i}^{y_{i+1}} \int_{x_i}^{x_{i+1}} \left( C\left( h_{pc} \frac{\partial^2 w}{\partial x^2} + h_{pc} \frac{\partial^2 w}{\partial y^2} \right) \right) dxdy - \frac{\vartheta(t)\eta_{33} ab}{h_p} \qquad (10.8)$$

Assuming $C = d_{31}\left(C_{11} + C_{12}\right)$

Since the current expression given by the above equation includes the capacitance information of the PZT, in this model, it is convenient to connect the PZT directly to the resistive load as a current source without any external capacitive element as shown in Figure 10.1. Then, the differential equation for the voltage in the feed back loop becomes

$$\frac{d\vartheta(t)}{dt} \frac{\eta_{33} ab}{h_p} + \frac{\vartheta(t)}{R_l} = -\int_{y_i}^{y_{i+1}} \int_{x_i}^{x_{i+1}} \left( C\left( h_{pc} \frac{\partial^2}{\partial x^2}\left( \frac{dw}{dt} \right) + h_{pc} \frac{\partial^2}{\partial y^2}\left( \frac{dw}{dt} \right) \right) \right) dxdy \qquad (10.9)$$

Where, $\frac{\eta_{33} ab}{h_p}$ is the capacitance of the PZT layer and $R_l$ is the external load resistance.

## 10.3 Solution for the Dynamic Equation

Let us assume for the moment that the external loading on the plate is uniform (uniform pressure). Let us also assume that the maximum amplitude of the loading is $L_0$. As discussed in section 2.0, we assumed that the plate is simply supported all around and hence the vertical displacement ( $w$ ) and the moments ( $M_x, M_y$ ) are zero at the boundary.

Considering the time dependent vibration of the base, ( $w_s$ ) it is quite justifiable to assume Navier's solution [268, 270] for relative vertical displacement of the plate as $w(x,y,t)=\sum_{r=1}^{\infty}\sum_{s=1}^{\infty}B_{rs}X_r(x)Y_s(y)\mathrm{T}_{rs}(t)$ which can also satisfy the boundary condition of the plate. We could assume any suitable eigen functions $X_r(x)Y_s(y)$ satisfying the boundary conditions pertained to simply supported end, cantilever end or restrained end, respectively. Here in this paper we have assumed sinusoidal eigen functions satisfying the homogeneous boundary conditions. Substituting the expression for $w$ in equation (6) and enforcing the orthogonality conditions of the eigen functions we get

$$\Delta_{rs}B_{rs}\mathrm{T}_{rs}(t)+c_{rs}B_{rs}\frac{d\mathrm{T}_{rs}(t)}{dt}+mB_{rs}\frac{d^2\mathrm{T}_{rs}(t)}{dt^2}-\left[V_{31}Cox*Siy+V_{32}Six*Coy\right]\vartheta(t)$$

$$=\Gamma_{rs}^{m}(t)+\Gamma_{rs}^{d}(t)+\Gamma_{rs}^{e}(t) \qquad (10.10)$$

Where,

$$\Delta_{rs}=\left[\Psi_1\left(\left(\frac{r\pi}{a}\right)^4+\left(\frac{s\pi}{b}\right)^4\right)+\Psi_2\left(\frac{r\pi}{a}\right)^2\left(\frac{s\pi}{b}\right)^2\right]$$

$$c_{rs}=\left[C_{srx}\left(\left(\frac{r\pi}{a}\right)^4+\left(\frac{s\pi}{b}\right)^4\right)+2C_{sry}\left(\frac{r\pi}{a}\right)^2\left(\frac{s\pi}{b}\right)^2+C_a\right]$$

$$C_a=C_{ax}+C_{ay}$$

$$Cox=\left[\cos\left(\frac{\pi r x_{i+1}}{a}\right)-\cos\left(\frac{\pi r x_i}{a}\right)\right];\ Coy=\left[\cos\left(\frac{\pi s y_{i+1}}{b}\right)-\cos\left(\frac{\pi s y_i}{b}\right)\right];$$

$$Six = \left[ \sin\left( \frac{\pi r x_{i+1}}{a} \right) - \sin\left( \frac{\pi r x_i}{a} \right) \right];\ Siy = \left[ \sin\left( \frac{\pi s y_{i+1}}{b} \right) - \sin\left( \frac{\pi s y_i}{b} \right) \right]$$

Assuming pure vertical translation, the excitation force due to mass inertia can be written as $\Gamma_{rs}^{m}(t) = -m \frac{16}{\pi^2 rs} \frac{d^2 w_s(t)}{dt^2}$. Due to viscous damping, the effect on the external force will be $\Gamma_{rs}^{d}(t) = -C_a \frac{16}{\pi^2 rs} \frac{dw_s(t)}{dt}$. The time dependent external force due to varying pressure is $\Gamma_{rs}^{e}(t) = L(t) \frac{16}{\pi^2 rs}$. Let $\Gamma_{rs}(t)$ be the algebraic sum of these three forces.

Similarly, substituting the assumed expression for $w$ in equation (8) we get

$$\frac{d\vartheta(t)}{dt} \frac{\eta_{33} ab}{h_p} + \frac{\vartheta(t)}{R_l} = \sum_{r=1}^{\infty} \sum_{s=1}^{\infty} Ch_{pc} B_{rs} \frac{4ab}{\pi^2 rs} \left[ \left( \frac{r\pi}{a} \right)^2 + \left( \frac{s\pi}{b} \right)^2 \right] \frac{d\mathrm{T}_{rs}(t)}{dt} \qquad (10.11)$$

Henceforth, the $B_{rs}$ coefficients are consumed in the expression $\mathrm{T}_{rs}(t)$. Using homogeneous solution and the particular integral, the solution for $\vartheta(t)$ can be found from equation (11). After enforcing the initial condition $\vartheta(t) = 0$ at $t = 0$ we can write the expression

$$\vartheta(t) = \exp(-\theta t) . \int \exp(\theta t) \Theta(t) dt \qquad (10.12)$$

Where, $\theta = \frac{h_p}{R_l \eta_{33} ab}$ and $\Theta(t) = \sum_{r=1}^{\infty} \sum_{s=1}^{\infty} Ch_{pc} \frac{4ab}{\pi^2 rs} \left[ \left( \frac{r\pi}{a} \right)^2 + \left( \frac{s\pi}{b} \right)^2 \right] \frac{d\mathrm{T}_{rs}(t)}{dt}$.

## 10.4 Solution under Harmonic Condition and Random Vibration

If it can be assumed, that the harmonic external vibration is provided to the energy harvester then $w_s(t)$ can be assumed as $W_b e^{i\omega t}$, where $\omega$ is any arbitrary excitation frequency and $W_b$ is the amplitude of the transverse vibration. If $w_s(t)$ is the source of random vibration then $w_s(t)$ can be written as $w_s(t) = \int_{-\infty}^{\infty} W(\omega) e^{i\omega t}$, where $W(\omega)$ is the random complex valued spectrum. Assuming the proposed electro-mechanical system linear, the voltage output from the harvester will be harmonic under harmonic loading condition. If the maximum voltage across the load resistance $R_l$ is $V_0$ then, $\vartheta(t) = V_0 e^{i\omega t}$. The equation (10) can be modified and can be written as

$$m\frac{d^2 \mathrm{T}_{pq}(t)}{dt^2} + c_{pq}\frac{d\mathrm{T}_{pq}(t)}{dt} + k_{pq}\mathrm{T}_{pq}(t) = \left[\phi_{pq}\left[\mathrm{I}W_b e^{i\omega t} + L(t)\right] + \left(V_{31}Cox * Siy + V_{32}Six * Coy\right)\vartheta(t)\right] \quad (10.13)$$

Where, $c_{pq}$ includes both viscous and strain-rate damping terms; $k_{pq} = \Delta_{pq}$; $\phi_{pq} = \frac{16}{\pi^2 pq}$ ; $\mathrm{I} = \left[m\omega^2 - iC_a\omega\right]$

Hence, the natural frequency of the system can be written as $\omega_{pq} = \sqrt{\frac{k_{pq}}{m}}$ and the damped natural frequency is $\omega_{pq}{}^{d} = \omega_{pq}\sqrt{1-\xi_{pq}{}^{2}}$ where, $\xi_{pq} = \frac{c_{pq}}{2m\omega_{pq}}$. The forcing function in the dynamic equation (13) is

$$F(t) = \left[\phi_{pq}\left(\mathrm{I}W_b e^{i\omega t} + L(t)\right) + \left(VCS\right)V_0 e^{i\omega t}\right] \quad (10.14)$$

Where, $VCS = \left(V_{31} Cox * Siy + V_{32} Six * Coy\right)$, the steady state solution for $T_{pq}(t)$ can be obtained as

$$T_{pq}(t) = \frac{\left[\phi_{pq}\left(\mathrm{I} W_b e^{i\omega t} + L(t)\right) + \left(VCS\right) V_0 e^{i\omega t}\right]}{m\left(-\omega^2 + 2i\xi_{pq}\omega_{pq}\omega + \omega_{pq}^2\right)} \tag{10.15}$$

Substituting the feed-back-loop voltage expression in the equation (11) we get

$$V_0\left[i\omega\frac{\eta_{33}ab}{h_p} + \frac{1}{R_l}\right]e^{i\omega t} =$$

$$\sum_{r=1}^{\infty}\sum_{s=1}^{\infty} Ch_{pc}\frac{4ab}{\pi^2 rs}\left[\left(\frac{r\pi}{a}\right)^2 + \left(\frac{s\pi}{b}\right)^2\right]\frac{\left[\phi_{rs}\left(i\omega \mathrm{I} W_b e^{i\omega t} + \dot{L}(t)\right) + i\omega\left(VCS\right)V_0 e^{i\omega t}\right]}{m\left(-\omega^2 + 2i\xi_{rs}\omega_{rs}\omega + \omega_{rs}^2\right)} \tag{10.16}$$

Now the explicit expression for the current across the resistance can be written as

$$I(t) = \frac{\sum_{r=1}^{\infty}\sum_{s=1}^{\infty} Ch_{pc}\frac{4ab}{\pi^2 rs}\left[\left(\frac{r\pi}{a}\right)^2 + \left(\frac{s\pi}{b}\right)^2\right]\frac{\phi_{rs}\left[i\omega \mathrm{I} W_b e^{i\omega t} + \dot{L}(t)\right]}{\left(-m\omega^2 + c_{rs}i\omega + k_{rs}\right)}}{\left[i\omega\frac{\eta_{33}ab}{h_p}R_l + 1\right] - \sum_{r=1}^{\infty}\sum_{s=1}^{\infty} Ch_{pc}\frac{4ab}{\pi^2 rs}\left[\left(\frac{r\pi}{a}\right)^2 + \left(\frac{s\pi}{b}\right)^2\right]\frac{i\omega R_l\left(VCS\right)}{\left(-m\omega^2 + c_{rs}i\omega + k_{rs}\right)}} \tag{10.17}$$

In equation (16), the maximum voltage output across the load resistance will also depend on the external mechanical loading $L(t)$. A harmonic loading with a phase lag can be considered. It is clear from the expression in equation (16) that the uniform loading without any time dependence has no effect on the voltage output. Assuming $L(t) = q_0 e^{i(\omega t + \theta)}$ where $\theta$ is the phase difference between the vibration excitation and the

external vertical loading. Substituting the expression in equation (16), the maximum voltage output expression will become

$$V_0 = \frac{\sum_{r=1}^{\infty}\sum_{s=1}^{\infty} Ch_{pc}\frac{4ab}{\pi^2 rs}\left[\left(\frac{r\pi}{a}\right)^2+\left(\frac{s\pi}{b}\right)^2\right]\frac{i\omega\phi_{rs}\left[IW_b + q_0 e^{i\theta}\right]}{\left(-m\omega^2 + c_{rs}i\omega + k_{rs}\right)}}{\left[i\omega\frac{\eta_{33}ab}{h_p}+\frac{1}{R_l}\right]-\sum_{r=1}^{\infty}\sum_{s=1}^{\infty} Ch_{pc}\frac{4ab}{\pi^2 rs}\left[\left(\frac{r\pi}{a}\right)^2+\left(\frac{s\pi}{b}\right)^2\right]\frac{i\omega\phi_{rs}(VCS)}{\left(-m\omega^2 + c_{rs}i\omega + k_{rs}\right)}} \quad (10.18)$$

Hence, the maximum power output is $P_0 = \frac{{V_0}^2}{R_l}$

## 10.5 Calculation of Damping Coefficients

In this study, two types of damping are considered, 1) strain rate damping and 2) viscous damping. The damping term $c_{rs}$ in equation (10) has three damping coefficients. $C_{srx}$ and $C_{sry}$ are the strain rate damping coefficients pertaining to bending of the plate about x axis and y axis, respectively. $C_a$ is viscous damping coefficient. To derive the values of these coefficients, following steps are adopted. The damping coefficients for the first four vibration modes of the energy harvester ($\xi_{11}, \xi_{12}, \xi_{21}$ and $\xi_{22}$) are assumed to be 0.015, 0.02, 0.02 and 0.025. Using these known values of the $\xi_{pq}$, unknown values of $C_{srx}$, $C_{sry}$ and $C_a$ are calculated. Values of the strain rate damping and viscous damping coefficients are highly dependent on structural geometry of the energy harvester, such as the length, breath, the thickness of substrate and the thickness of the piezoelectric layer. In this paper, a geometric configuration is used and respective values of the damping coefficients are calculated and incorporated automatically in our MATLAB program.

## 10.6 Numerical Implementation

A MATLAB code is developed based on the equations derived in the previous section. The resistance (load) was varied to calculate the power output variation at different frequencies. From this study, resonant frequencies were identified at different load resistances. With certain requirements in mind the Optimization tool box in MATLAB is used to obtain pattern of piezoelectric patch on the energy harvester. Material properties for this analysis are assumed as follows, $E_s$ =98 GPa , $\mu_s$ =0.335 , $E_p$ =66 GPa , $\mu_p$ =0.30 , $m_s$ =7.20 gm/c.c , $m_p$=7.5 gm/ c.c , $d_{31}$ =-274 pm/V or pC/N , $\varepsilon_{p33}$ =3400*8.854 pF/m. We have assumed 8 different external load resistances to calculate the voltage output. Figure 10.2 shows the comparison between two mathematical modeling approaches, employing the strain rate damping (SRD) mechanism and neglecting the strain rate damping mechanism or zero damping (ZRD) mechanism. It can be seen that having 200 $\Omega$ and 1000 $\Omega$ load resistance in the harvesting circuit, the resonant frequencies around 13 KHz & 16.5 KHz are not present when strain rate damping mechanism is considered. Also the magnitudes of FRF at 3.3 KHz and 8.2 KHz resonant frequencies are significantly different for SRD and ZRD. Hence, it can be stated that for accurate estimation of power output from plate type harvesters, SRD is quite necessary. In the forgoing discussions and charts the SRD mechanism is considered in the mathematical model.

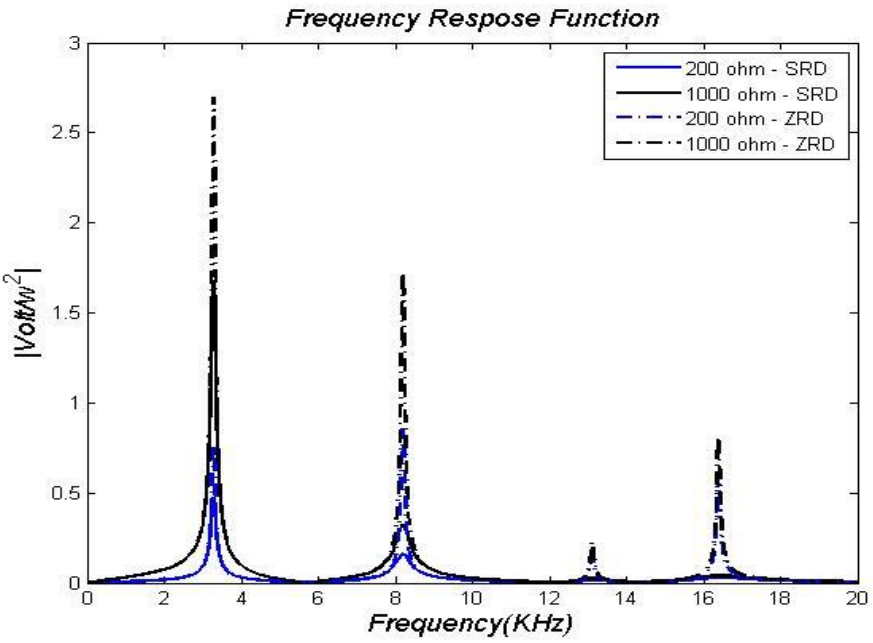


Figure 10.2: Comparison of FRF by using SRD and ZRD in the mathematical model

A parameter $V/\omega^2$ is formulated to presented which is designated as frequency response function (FRF). Two types of harvesters (square and rectangular plate) were investigated. First a 100 mm x 100 mm square harvester with 0.05 mm thick PZT on top of 1 mm thick substrate was considered. The plate is discretized in to 1000 x 1000 elements. For each individual placement of PZT patch the voltage expression from equation 18 was used to calculate the FRF. For this study we assumed that the entire plate is covered by piezoelectric layer. The FRF for entire piezoelectric layer was first obtained using the voltage expression presented in Reference [240]. Next the FRF function for the entire plate with element patches was obtained from each element of piezoelectric layer, using superposition theorem (considering load resistances connected in parallel). Identical results were obtained. It proves the accuracy of the mathematical expression in equation (18). Figure 10.3 shows the FRF function obtained by superposition. Total 8 load resistance

between 100 Ω to 20,000 Ω as shown in Figure 10.3 were considered. It can be seen that, higher resistances have slightly lower resonant frequencies.

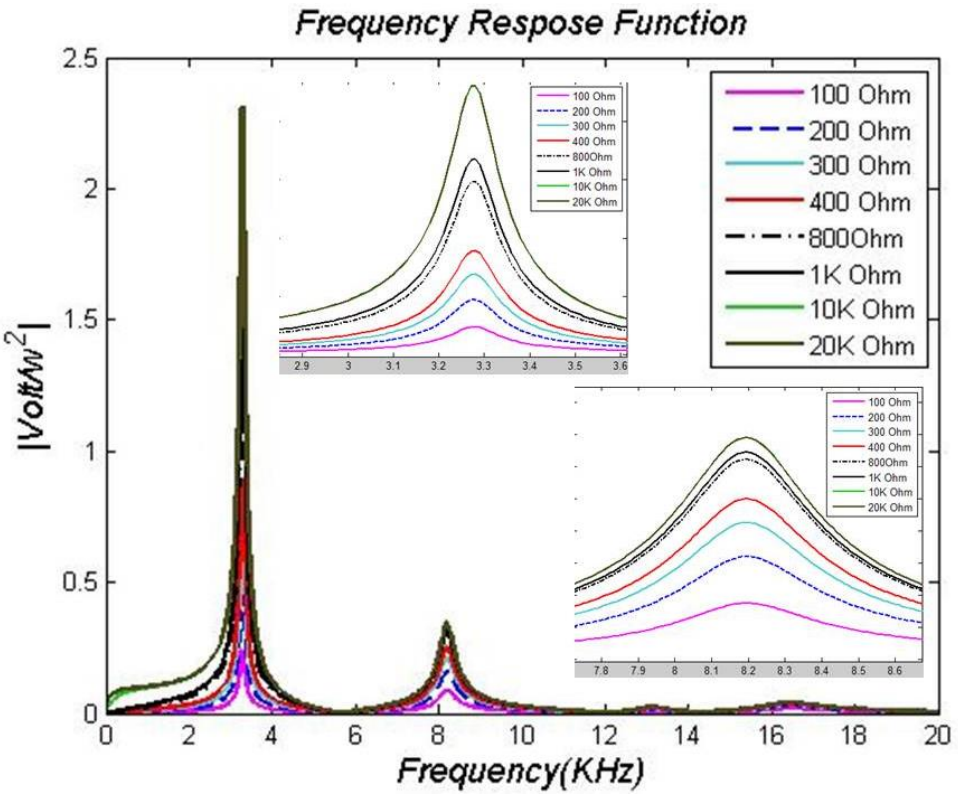


Figure 10.3: FRF function of a 100mm x 100mm square plate at different load resistance

Next a plate with 200 mm length and 100 mm width is considered. As shown in Figure 10.4 the FRF function has five consecutive resonant frequencies within 10 KHz band, unlike 2 resonant frequencies obtained from a square plate. This shows that the rectangular plate has higher energy output (higher area under the FRF curve) but within a narrow band. Hence, if many rectangular plates are arranged in a certain pattern then they could potentially harvest energy from wider band of frequencies. It is known that the energy could only be harvested from the area of the plate, where the piezoelectric patches are placed on the plate. Thus, many rectangular patterns of piezoelectric layer on a square

plate could also serve similar functionality. Keep this concept in mind optimization process was introduced to obtain different piezoelectric pattern for desired goal.

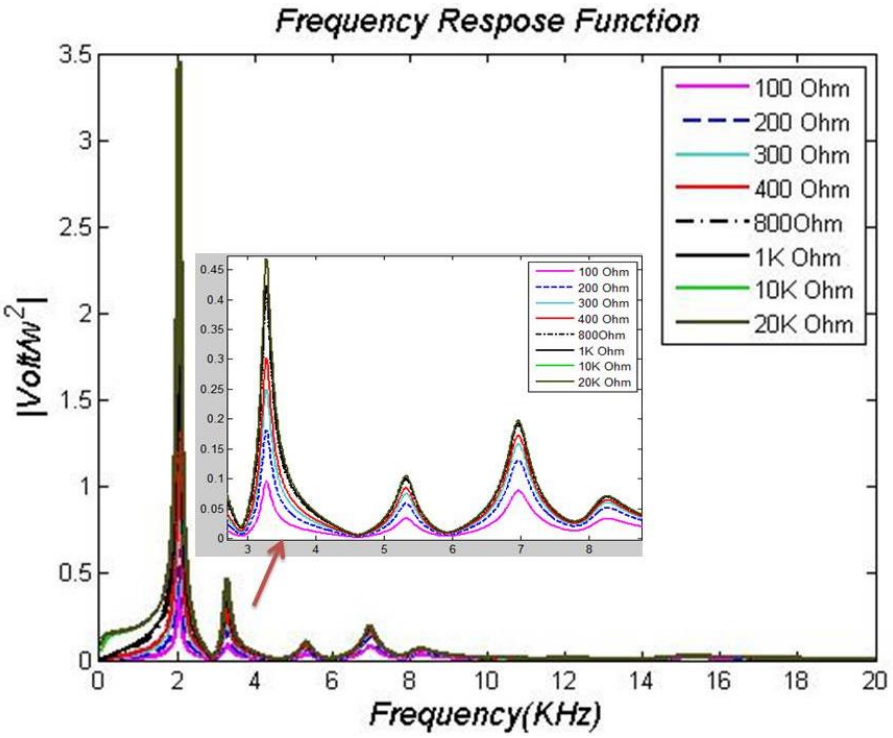


Figure 10.4: FRF function of a 200mm x 100mm square plate at different load resistance

## 10.7 Optimization Problem to Obtain PZT Pattern

The plate is assumed to be divided in to 1000x1000 elements. The placements of piezoelectric patch elements in certain pattern that can satisfy certain requirements of voltage output (e.g. maximize the voltage output at certain frequency, maximize the number of resonant frequency within a certain band of frequency etc.) can be obtained through multifunctional optimization, if the output voltage expression due to an element of piezoelectric patch is known. Hence, the explicit mathematical expression for voltage output has been obtained in the previous section (see equation (18)). Multifunction

optimization tool using Genetic Algorithm in MATLAB is used to calculate the design parameters. First the load resistance dependent (i.e. for fixed external load i.e. $400\,\Omega$) FRF for each piezoelectric patch between $x_i$ and $x_{i+1}$ along $x$ and between $y_i$ and $y_{i+1}$ along $y$ was obtained using the equation (18). The FRF was obtained for three different thicknesses of piezoelectric layer. Then each FRF function ($V/\omega^2$ as function of $\omega$) was treated as a chromosome in the forgoing genetic algorithm in MATLAB.

In the optimization program, following design parameters were considered, A. Total number of patches, B. length, width and location of the patches ($x_i$ and $x_{i+1}$ along $x$ and between $y_i$ and $y_{i+1}$ along $y$) on the energy harvester plate and C. thickness of each piezoelectric patch. The objective functions were specified in the code. To demonstrate the proposed process we have considered two optimization problems, 1) Maximize the area under the FRF function for broad band harvesting while covering only 50% of the plate using piezoelectric layer, 2) Maximize the amplitude of FRF function at 3KHz which is the first resonant frequency (refer Figure 10.3) while covering only 50% of the plate using piezoelectric layer. 3) Maximize the amplitude of FRF function at 3 KHz which is the first resonant frequency (refer Figure 10.3) while covering only 75% of the plate using piezoelectric layer. Hence, from two problems we received three patterns of piezoelectric layers. The patterns obtained from the optimization program are not exactly plausible or difficult to manufacture. Different thicknesses of the piezoelectric patches were reported at different locations of the plate from the optimization program, which is extremely difficult to fabricate. Hence, the closest geometrical patterns that are physically possible to manufacture were considered to obtain piezoelectric pattern on the harvester as

shown in Figure 10.5 a, b & c. We have enforced same thickness of the piezoelectric layer (i.e. 0.5 mm) for all the patches. All dimensions in the images are in mm.

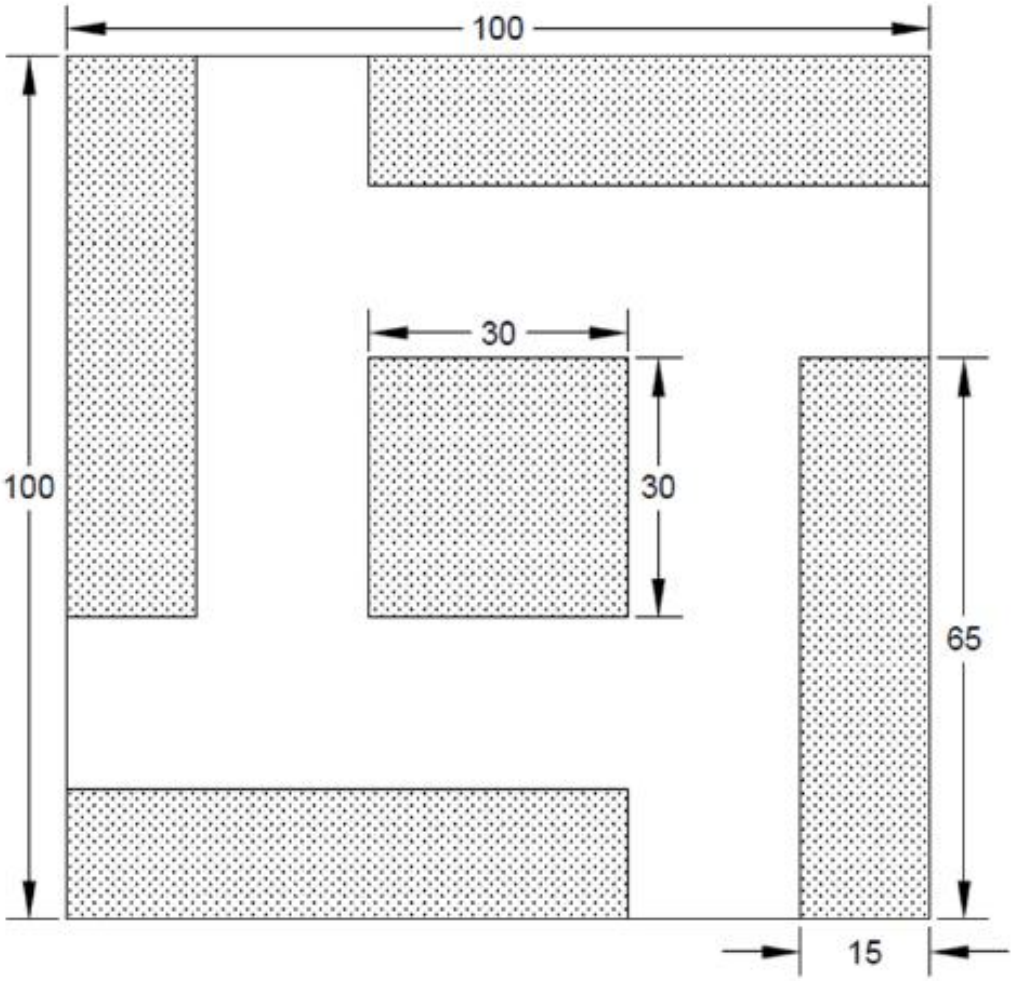


(a)

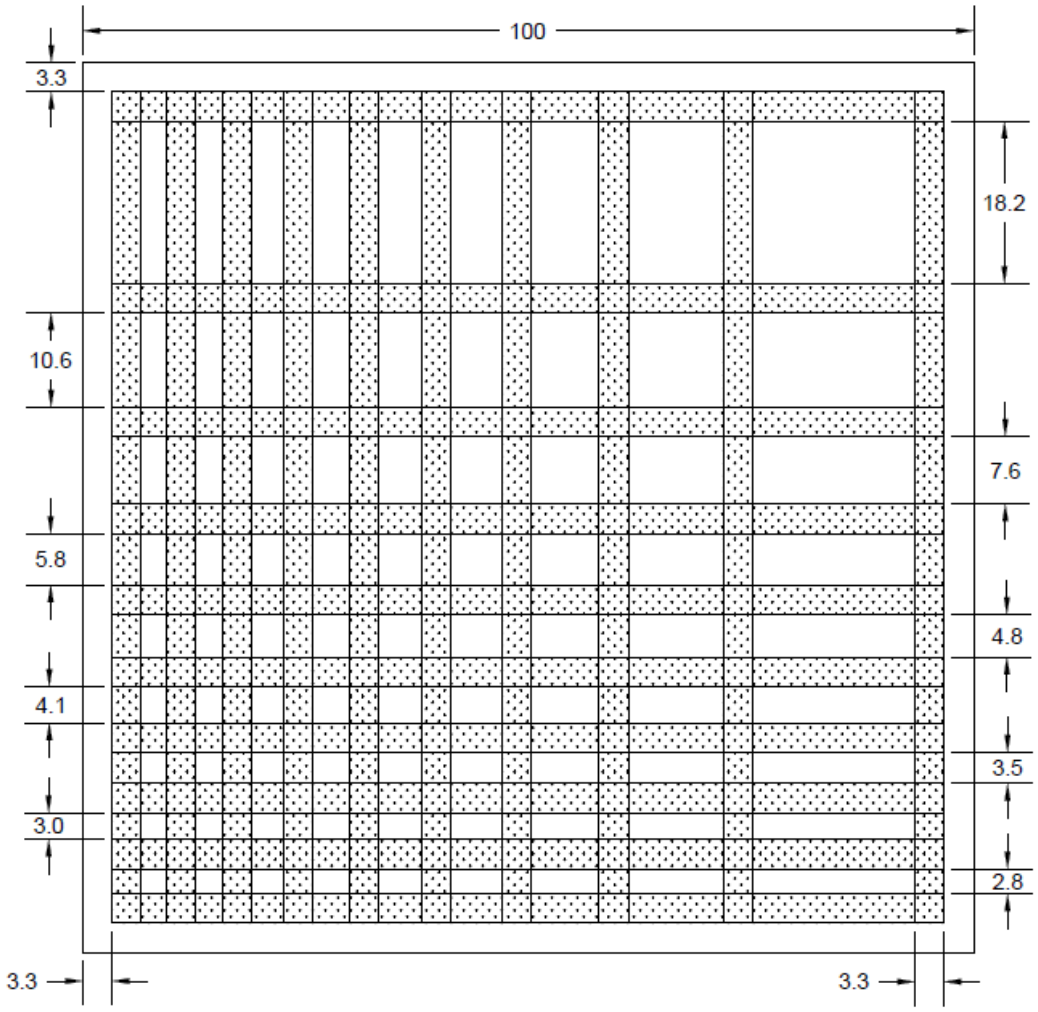


(b)

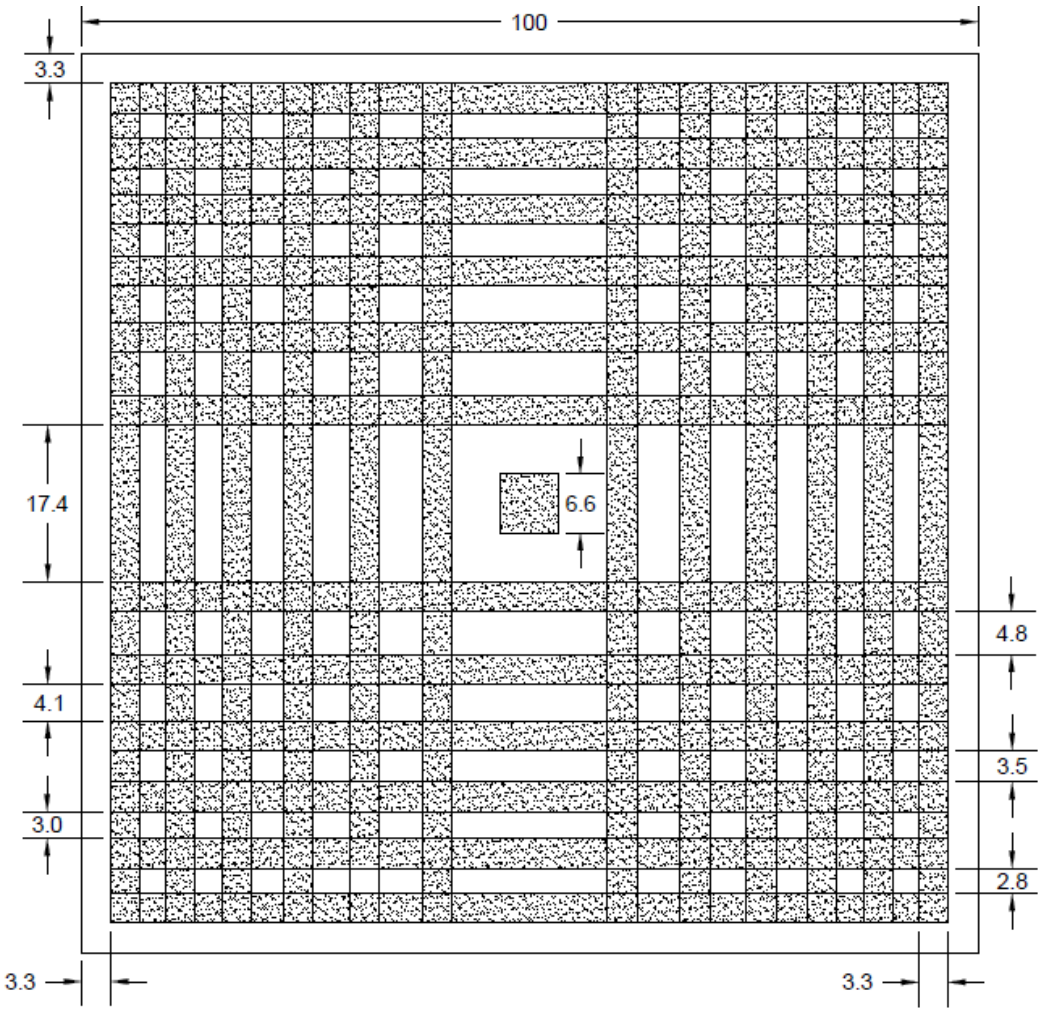


(c)

Figure 10.5: Piezoelectric layer pattern on square plate energy harvester: a) swastika pattern b) unsymmetrical logarithmic chirp pattern c) symmetric logarithmic chirp pattern

Finite Element Method (FEM) simulations with respective piezoelectric patterns were performed simultaneously with the analytical calculation to obtain the FRF. Figure 10.6 shows a qualitative comparison between FRF function obtained using Analytical method and using the FEM. For analytical calculation we have used 20Hz interval, however, due to cost of computation the FRF in FEM was calculated at every 200 Hz. Hence, the detailed pattern of the FRF curve was not captured by the FEM. But overall qualitative understanding can be easily referred. It was found that FEM provides quite close

approximation of the FRF function with respect to the analytical model. This proves the accuracy of the analytical expression that is obtained in equation (18). The deformation pattern of the plate with specific piezoelectric pattern is shown in Figure 10.7. Next, a similar study was conducted using another piezoelectric pattern (logarithmic) which was obtained by maximizing the amplitude of FRF function at around 3 KHz covering 50% and 75% of the plate. Figure 10.8 and Figure 10.10 shows the qualitative comparison of the FRF obtained from analytical and FEM model. For analytical calculation we have used 20Hz interval, however, due to cost of computation the FRF in FEM was calculated at every 200 Hz. Hence, the detailed pattern of the FRF curve was not captured by the FEM. The deformation pattern of the plate with logarithmic piezoelectric pattern are shown in Figure 10.9 and Figure 10.11. Comparing Figure 10.7, Figure 10.9 & Figure 10.11 it can be seen that the deformation pattern is quite different due to different pattern of piezoelectric layers and thus the output FRF.

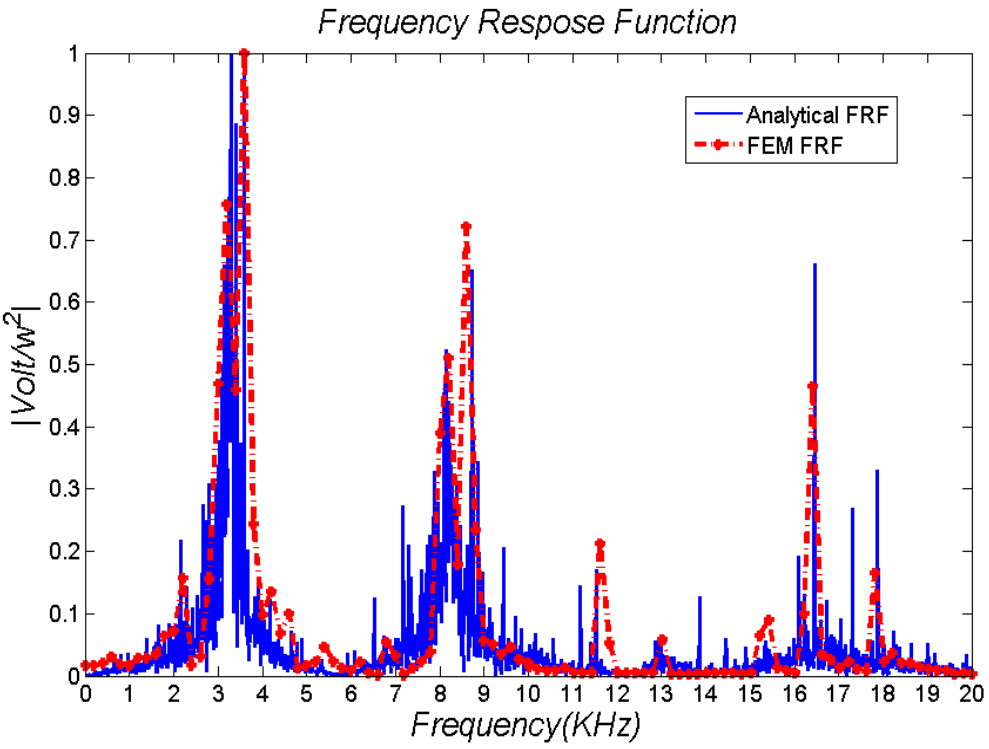


Figure 10.6: Qualitative comparison between analytical and simulation (FEM) results: FRF function of a 100mm x 100mm square plate with patterned patch

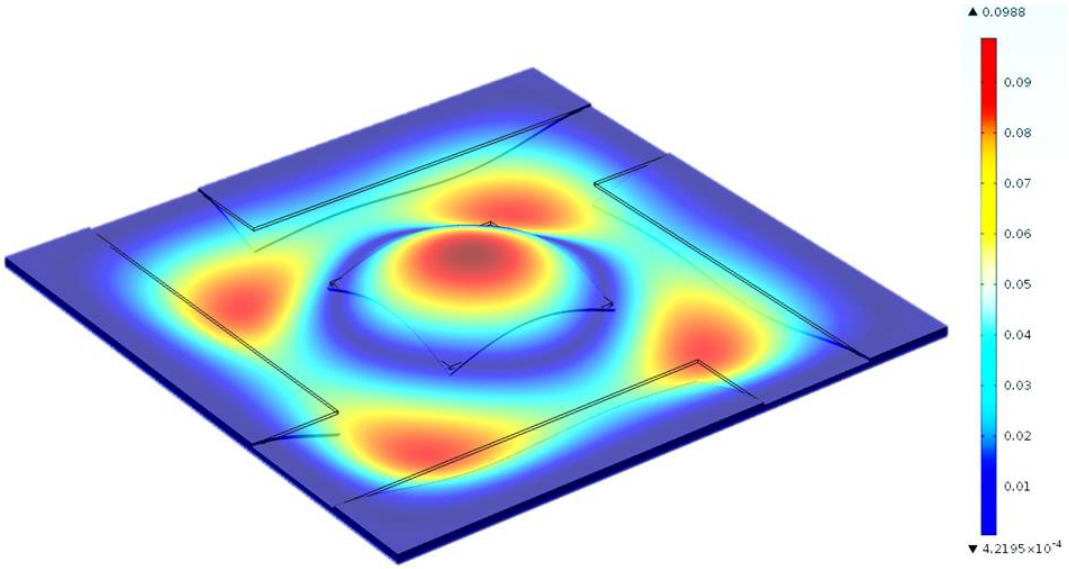


Figure 10.7: Deformation of the plate at 3.2 KHz

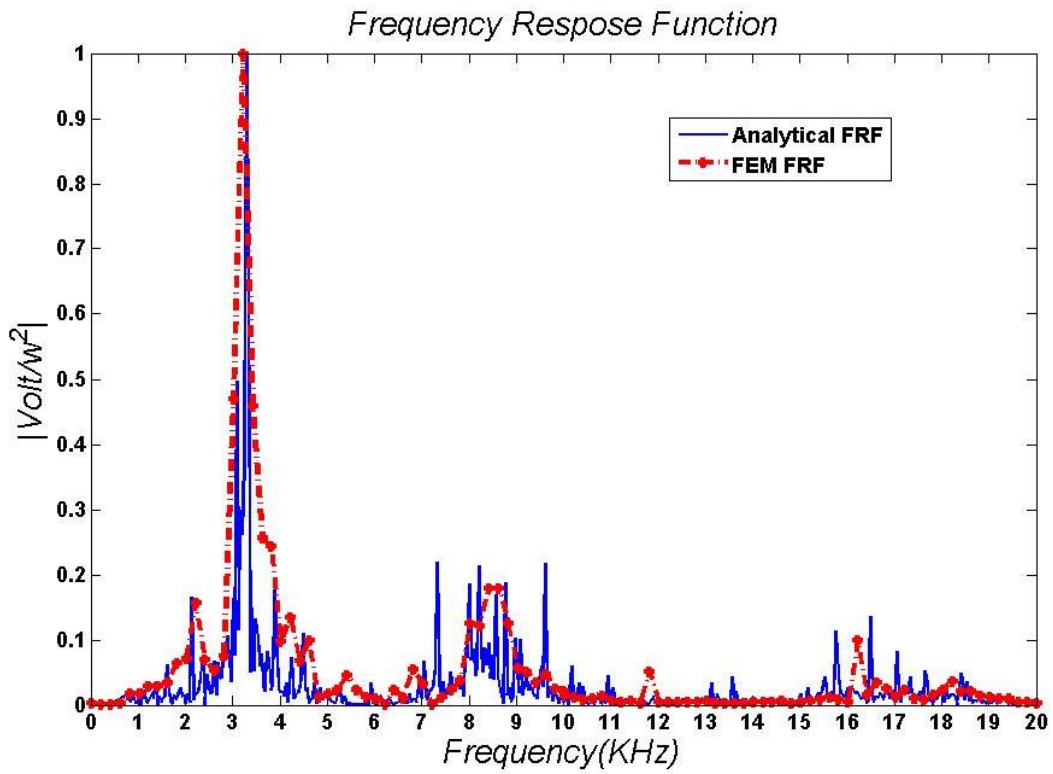


Figure 10.8: Qualitative comparison between analytical and simulation (FEM) results: FRF function of a 100mm x 100mm square plate with patterned patch (unsymmetrical logarithmic)

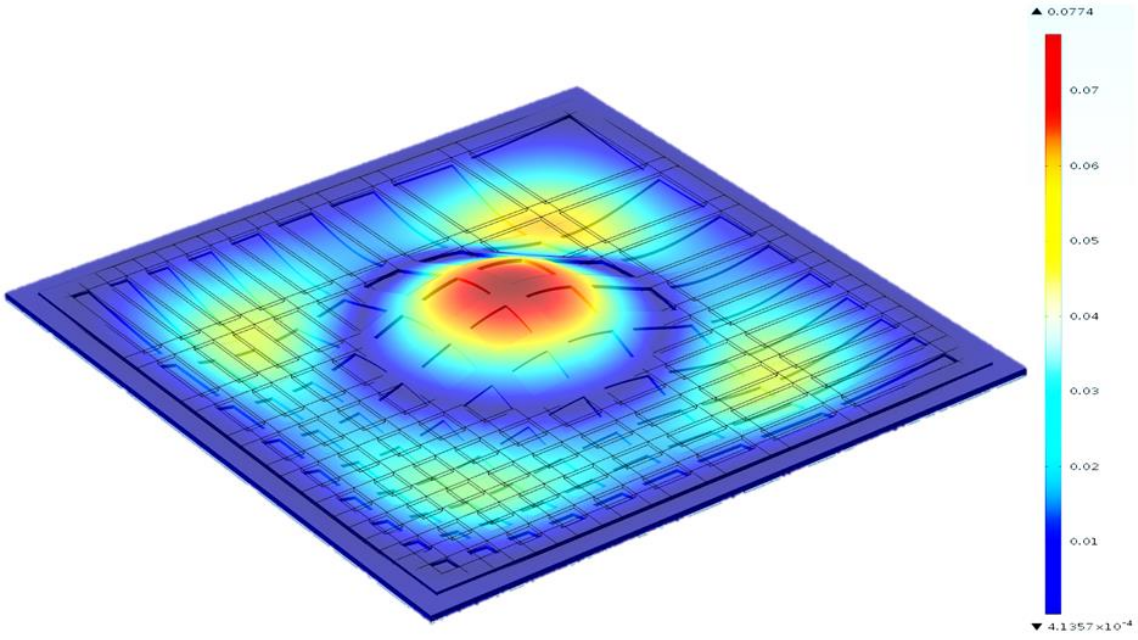


Figure 10.9: Deformation of the plate at 3.2 KHz

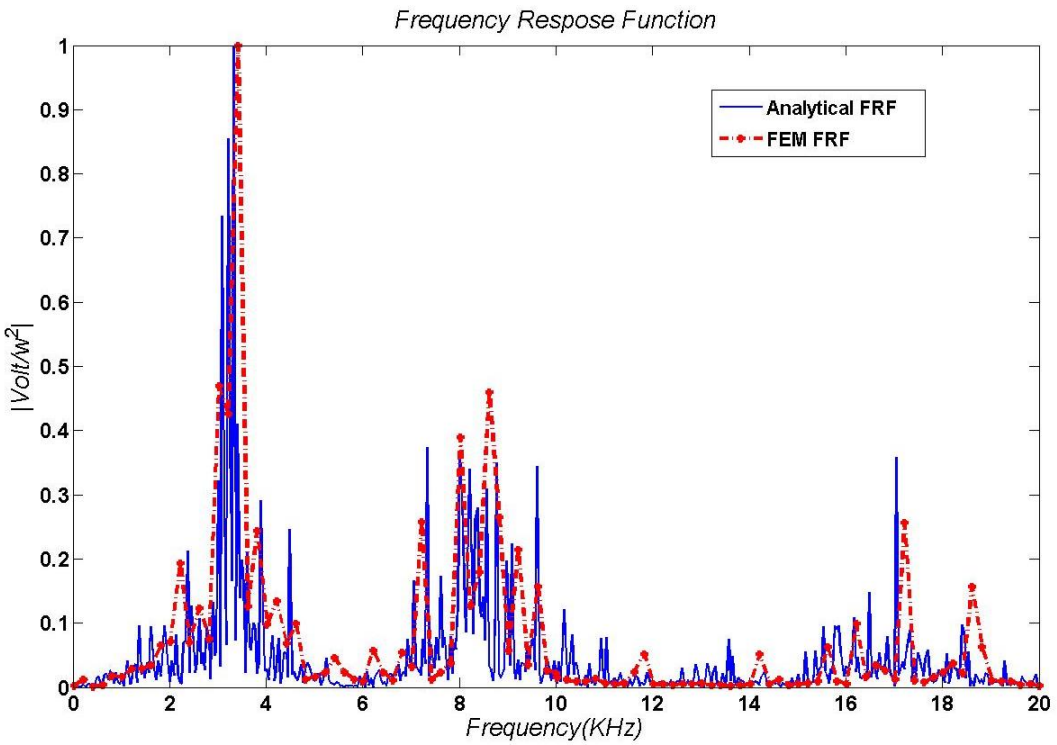


Figure 10.10: Qualitative comparison between analytical and simulation (FEM) results: FRF function of a 100mm x 100mm square plate with patterned patch (symmetrical logarithmic chirp)

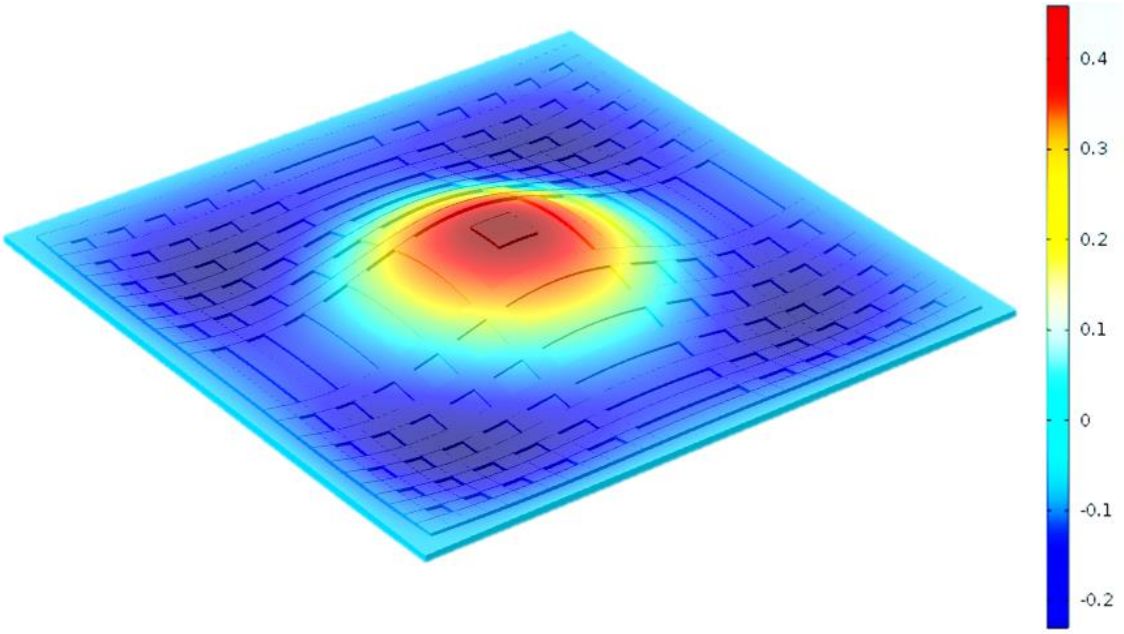


Figure 10.11: Deformation of the plate at 3.2 KHz

## 10.8 Chapter Summary

In this research, a mathematical derivation of power output and exact output voltage expressions are presented for plate type energy harvesters that are suitable for harvesting energy. The frequency response function produces peak values at certain band of frequencies. However, using the patterned patch in the model a wide band of resonance is achieved, although the amplitude is much lower than the actual resonance at a particular frequency. It can be seen that the resonant band also depends on load resistance. Thus if the target power output and the load resistances are known, through optimization, an effective energy harvester can be designed with a wider band of resonance frequency.

# CHAPTER 11: PHONON CONFINEMENT USING SPIRALLY DESIGNED ELASTIC RESONATORS IN DISCRETE CONTINUUM

Periodic and chiral orientation of microstructures, here we call phononic crystals, have extraordinary capabilities to facilitate the innovative design of new generation metamaterials. Periodic arrangements of phononic crystals are capable of opening portals of non-passing, non-dispersive mechanical waves. Defying conventional design of regular periodicity, in this work spirally periodic but chiral orientation of resonators are envisioned. Dynamics of the spirally connected resonators and the acoustic wave propagation through the spirally connected multiple local resonators are studied using fundamental physics. In present study the spiral systems with local resonators are assumed to be discrete media immersed in fluid. In this work it is assumed that acoustic or ultrasonic waves in fluid are propagated along the plane of the spiral resonators and thus only the longitudinal wave mode exists due to nonexistence of shear stress in the fluid. Lagrangian formulation of the spiral systems were employed to obtain the governing Euler-Lagrange equation of the system. Discrete element method was employed to verify the equation assuming nearest neighboring effect.

## 11.1 Background

The aim of this work is to demonstrate the possibility of phonon confinements in a set of spirally connected phononic crystals. In last few years, phononic crystals either in discrete or embedded in the acoustic materials have received significant attention [272, 273]. Band gap manipulation is increasingly important in periodic structures to diversify the applications of the novel materials and the phononic crystals. Tunabilitiy of frequency band structures in engineered materials are of significant interest due to their many practical applications [274]. Acoustic frequency filtration, vibration isolation, manufacturing of ultrasonic array transducers, improve clarity of acoustic imaging using photon-phonon coupling, micro to nano scale acoustic devices etc. are few applications where frequency manipulations are extremely valuable. Bragg scattering in periodic media is the most important phenomena that is used in both photonics and phononics for creating frequency band gaps. But in photonics there are some possibilities of non-Bragg type band gaps that are called polariton [275] band gaps originates from photon-phonon coupling. Similar phenomenon of phonon-photon coupling can also be found in superlattices. Also recently in phononics, additional frequency band gaps are reported by creating a local resonance effect [273]. In addition to the Bragg scattering, in the periodic structures made of embedded local resonators, negative bulk modulus and negative effective mass causes additional low frequency band gaps [276]. Mass-in-mass unit cells were proposed where the effective mass of the cell becomes negative at frequencies near the local resonance frequency of the resonators due to special decay of the wave amplitudes [277]. Low frequency can be controlled by introducing locally resonant components into the phononic crystals [278]. Based on the previous researches it is envisioned that there is a possibility

to open a new portals of low-frequency forbidden bands by arranging the local resonator (phononic crystal) in a certain geometric fashion. Band gaps can also be obtained by altering the geometry of the local resonator [279].

In 2003, Hirsekorn et al. [278] performed a numerical simulation of acoustic wave propagation through sonic crystals consisting of local resonators using the local interaction simulation approach (LISA). It was found that there are three strong attenuation bands at frequencies between 0.3 and 6.0 kHz, which does not depend on the periodicity of the crystals. With the Lamb waves, extremely low frequency band gaps (BG) can be obtained by periodically depositing single-layer or two-layer stubs on the surface of a thin homogeneous plate [280]. Caballero et al. [280] showed that by placing two-dimensional square and triangular lattices (made of rigid cylinders) in the air,absolute sonic band gaps are created. Such band gapscan be further increased by reducing the structure symmetry or by introducing chirality in the geometry. Based on the idea of localized resonant structures, Liu et al. [281] fabricated sonic crystals that exhibit spectral gaps with a lattice constant two orders of magnitude smaller than the relevant wavelength. Even after such magnificent efforts sonic bands are mostly limited to fewer (one or two) bands gaps with smaller band widths. Superposing the ideas of Liu et al. and Caballero et al. here we envision that geometric configuration of local resonators and there mode of intra-connections could result wider band gaps that would be lucrative for phononic applications and are yet to be explored. Hence, instead of creating stop bands, here we propose spiral system of resonators that are capable of creating selective pass bands by confining the phonons within a desired frequency band.

Naturally obtained spirals (e.g. Cochlea in human ear) shows great advantages in filtering desired frequency of sound waves. Significance of the physics of spiral is evident throughout our nature. Density waves in galaxies, geometrical configuration of the sensory system of the Cephalopodas, geometrical configuration in Cochlea of human ear and numerous botanical species demonstrate the spiral pattern [282]. Appearance of this spiral chirality is sufficiently diverse in nature (e.g. Archimedean, Logarithmic, Golden and Fermat's spiral patterns etc.).Few research can be found in the field of photonics, where guiding of electromagnetic wave by using spiral resonators [283, 284] were demonstrated. For most cases Archimedean spiral orientations were used. He et al. [285] proposed a three-dimensional chiral metamaterial consisting of arrays of the multi-layered mutually twisted metallic spirals which can exhibit negative refractive index at terahertz frequencies. Isik et al. [70] determined the electromagnetic response of the particles arranged in Archimedean spiral by using point group symmetry and the methods of crystallography. In 2011, Elford et al. [286] proposed a Bernoulli type spiral coil resonator to attenuate sound pressure level at low frequency region. They found three attenuation (greater than two) areas within the frequency range 0-2.2 kHz. They also illustrated that attenuation area can be shifted slightly by changing the number turns in the coil. Then a seashell resonator was also proposed, which is quite similar to naturally obtained nautilus shell that can attenuate sound pressure level at wide range of frequencies.

Inspired by nature, spirally arranged phononic crystals in fluid (air or liquid) is proposed in this study, where cylindrical local resonators are placed both in Archemedian and Logarithmic spiral orientation. To understand the fundamental physics a relatively simple physical model is proposed where all resonators are assumed to be discrete elastic

resonators connected via elastic springs (tangential springs). Also to keep the shape of the spiral configuration intact, it is assumed that all the resonators are connected with the central resonator placed at the center of the spiral configuration via another set of elastic springs (radial springs). Shadowing effect of spiral rings are ignored in this derivation, however, to be exact such consideration could be valuable and is under investigation. A parametric study was performed to understand the effect of the spring constants on wave dispersion phenomenon. Mass, radial spring constants and tangential spring constants were varied to see their effect on phonon confinement.

## 11.2 Mathematical Formulation

**Euler-Lagrange Equation**

Figure 11.1 shows the proposed phononic crystal system with spirally connected local resonators. Based on previous studies the local resonators are designed with hard metal coated with soft deformable material e.g. rubber. The proposed system is modeled as a discrete spring mass system. Damping is ignored in the forging derivation. All individual resonators are assumed to be connected with the neighboring resonators on either side, via elastic springs, in series. Simultaneously each resonator is also assumed to be connected with the origin of the spiral configuration, via a different spring to prevent the shape of the spiral. The proposed spring-mass system is shown in Figure 11.2 (a) and three representative resonators in spiral are depicted in Figure 11.2 (b). As shown in Figure 11.2 (b) each resonator (e.g. i-th resonator) is subjected to three forces$F_{i+1}$, $F_i$ & $Ft_i$. Displacements of the center of the i-th resonator are divided in to two components $x_i$&$y_i$. Similarly the displacements of the neighboring resonators are $x_{i+1}$, $y_{i+1}$&$x_{i-1}$, $y_{i-1}$ for i +

1-th and $i-1$-th resonators, respectively. Mass of the $i$ -th resonator is $m_i$. Hence, the Lagrangian of the spiral system can be written in the general form.

$$L = \frac{1}{2}\sum_{i=1}^{n} m_i(\dot{x_i}^2 + \dot{y_i}^2) - \sum_{i=1}^{n} U|x_i - x_{i-1}||y_i - y_{i-1}| + U|x_i - x_{i+1}||y_i - y_{i+1}| + U|x_i - x_0||y_i - y_0| \qquad (11.1)$$

Applying the principal of least action we achieve the Euler-Lagrange equation of motion as follows

$$\frac{\partial L}{\partial x_i} - \frac{d}{dt}\left(\frac{\partial L}{\partial \dot{x_i}}\right) = 0\ ;\ \frac{\partial L}{\partial y_i} - \frac{d}{dt}\left(\frac{\partial L}{\partial \dot{y_i}}\right) = 0 \qquad (11.2)$$

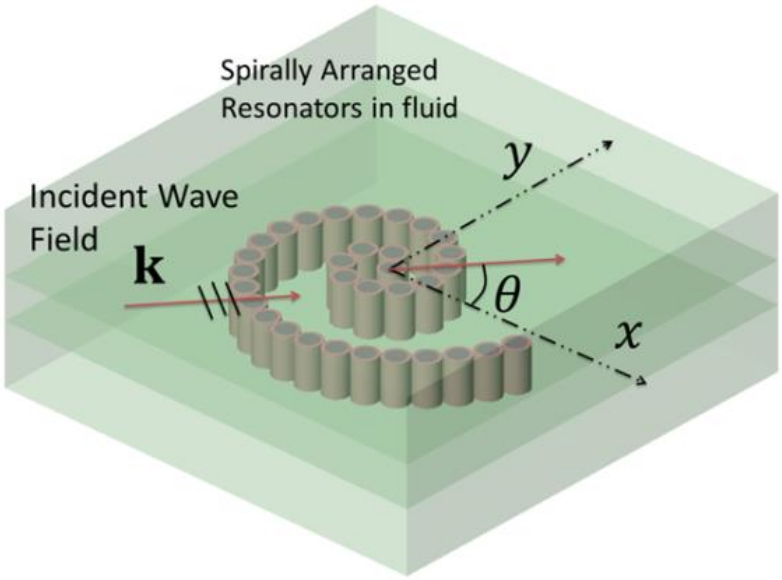


Figure 11.1: A possible arrangement of phononic crystal in Logarithmic spiral form. Individual resonators are connected to each other through epoxy strings casted together. The system is submerged in fluid to neglect the shear mode or rotation degrees of freedom.

The above equation has to satisfy at all the points in the trajectory of evolution during wave propagation. Let, $K_{i+1}$ be the spring constant connecting i-th and $i+1$ –th resonator and $K_{i-1}$ be the spring constant connecting $i-1$-th and i –th resonator. Let, $Kt_i$

be the spring constant for the spring connecting i-th resonator to the center of the spiral. Let, $n_i^j$ be the direction cosine between i-th and j-th resonator.$n_i^j = \widehat{n1}_i^j e_1 + \widehat{n2}_i^j e_2 + \widehat{n3}_i^j e_3$

After performing the derivatives in the above two equations we get the following equations of motion for the spiral system.

$$m_i \ddot{x}_i = x_i Kxx_i + y_i Kxy_i + x_{i+1} Kxx_{i+1} + x_{i-1} Kxx_{i-1} + y_{i+1} Kxy_{i+1} + y_{i-1} Kxy_{i-1} \quad (11.3)$$

$$m_i \ddot{y}_i = x_i Kyx_i + y_i Kyy_i + x_{i+1} Kyx_{i+1} + x_{i-1} Kyx_{i-1} + y_{i+1} Kyy_{i+1} + y_{i-1} Kyy_{i-1} \quad (11.4)$$

where,

$$Kxx_i = \left[-K_{i+1}\left(\widehat{n1}_i^{i+1}\right)^2 - K_{i-1}\left(\widehat{n1}_i^{i-1}\right)^2 - Kt_i\left(\widehat{n1}_i^0\right)^2\right]$$

$$Kxy_i = \left[-K_{i+1}\left(\widehat{n1}_i^{i+1}\right)\left(\widehat{n2}_i^{i+1}\right) - K_{i-1}\left(\widehat{n1}_i^{i-1}\right)\left(\widehat{n2}_i^{i-1}\right) - Kt_i\left(\widehat{n1}_i^{o}\right)\left(\widehat{n2}_i^{o}\right)\right]$$

$$Kxx_{i+1} = \left[K_{i+1}\left(\widehat{n1}_{i+1}^{i}\right)^2\right] Kxx_{i-1} = \left[K_{i-1}\left(\widehat{n1}_{i-1}^{i}\right)^2\right]$$

$$Kxx_{i+1} = \left[K_{i+1}\left(\widehat{n1}_{i+1}^{i}\right)^2\right] Kxx_{i-1} = \left[K_{i-1}\left(\widehat{n1}_{i-1}^{i}\right)^2\right] Kxy_{i+1} = \left[K_{i+1}\left(\widehat{n1}_{i+1}^{i}\right)\left(\widehat{n2}_{i+1}^{i}\right)\right],$$

$$Kxy_{i-1} = \left[K_{i-1}\left(\widehat{n1}_{i-1}^{i}\right)\left(\widehat{n2}_{i-1}^{i}\right)\right]$$

$$Kyx_i = \left[-K_{i+1}\left(\widehat{n1}_i^{i+1}\right)\left(\widehat{n2}_i^{i+1}\right) - K_{i-1}\left(\widehat{n1}_i^{i-1}\right)\left(\widehat{n2}_i^{i-1}\right) - Kt_i\left(\widehat{n1}_i^{o}\right)\left(\widehat{n2}_i^{o}\right)\right]$$

$$Kyy_i = \left[-K_{i+1}\left(\widehat{n2}_i^{i+1}\right)^2 - K_{i-1}\left(\widehat{n2}_i^{i-1}\right)^2 - Kt_i\left(\widehat{n2}_i^{0}\right)^2\right]$$

$$Kyx_{i+1} = \left[K_{i+1}\left(\widehat{n1}_{i+1}^{i}\right)\left(\widehat{n2}_{i+1}^{i}\right)\right] Kyx_{i-1} = \left[K_{i-1}\left(\widehat{n1}_{i-1}^{i}\right)\left(\widehat{n2}_{i-1}^{i}\right)\right],$$

$$Kyy_{i+1} = \left[K_{i+1}\left(\widehat{n2}^{i}_{i+1}\right)^2\right], Kxy_{i-1} = \left[K_{i-1}\left(\widehat{n2}^{i}_{i-1}\right)^2\right]$$

Considering n numbers of resonators (i runs between 1 to n) in the system, the governing equation of motion can be obtained by arranging the equation (11.3) and (11.4) in a matrix form. The generalized dynamic equation for n numbers of resonators in spiral pattern can be written as $\underline{M}\ddot{q} = \underline{K}q$

where, $\underline{M}$ the diagonal mass matrix, $\underline{K}$ the stiffness matrix and $q = \{x_1 \dots x_n \;\; y_1 \dots \;\; y_n\}^T$

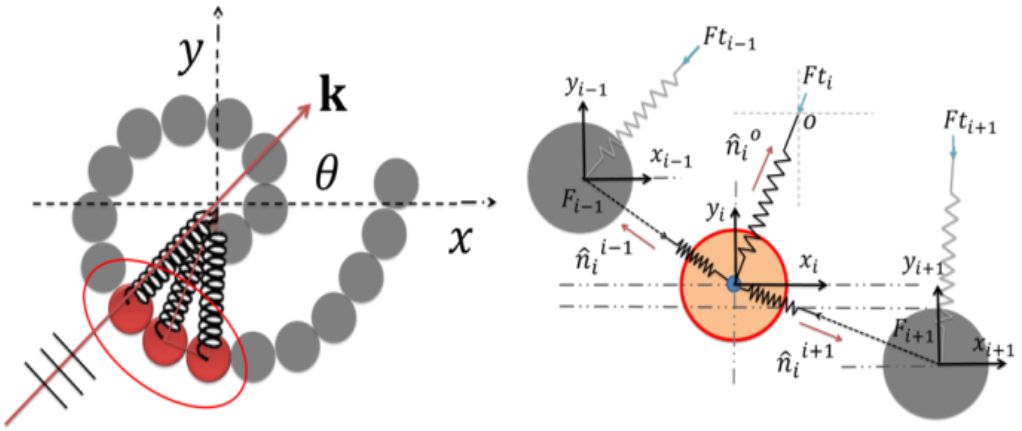


Figure 11.2: a) Schematic diagram of spirally connected phononic crystals for metamaterials; b) Representative spiral mass spring model using discrete elements

**Eigen Value Solution: Natural Frequencies and Dispersion**

Dynamical behavior of the spiral resonators is studied first. Assuming $x_i = A_i e^{-j\omega t} \& y_i = B_i e^{-j\omega t}$, we obtain an eigen value problem from the equation (11.6) which can be written as $\left[\underline{K} - \omega^2 \underline{M}\right]\lambda = 0$

Where, $\boldsymbol{\lambda} = \{A_1 \quad ... \quad A_n \quad B_1 \quad ... \quad B_{n-1} \quad B_n\}^T$eigen vector representing the mode shapes of the spiral system. The fundamental eigen frequencies are obtained by writing a computer program.

Next the displacement components of the resonators are assumed to have the wave number components in order to discover wave dispersion phenomenon through spirally connected resonators. Displacements $x_i = A_i e^{-j\omega t - j\mathbf{k}.\mathbf{r_i}}$ & $y_i = B_i e^{-j\omega t - j\mathbf{k}.\mathbf{r_i}}$ are assumed, where $k = k_x\hat{\imath} + k_y\hat{\jmath}$ is the wave number vector and $r_i = x_i\hat{\imath} + y_i\hat{\jmath}$ is spatial vector measures distance of the i-th resonator from the origin. Substituting the expressions for the displacements in equations (11.1) & (11.2) and intentionally dropping the time harmonic term we get

$$-\omega^2 m_i A_i = A_i Kxx_i + y_i Kxy_i + A_{i+1} e^{(j\mathbf{k}.\mathbf{r_{i+1}} - j\mathbf{k}.\mathbf{r_i})} Kxx_{i+1} + A_{i-1} e^{(j\mathbf{k}.\mathbf{r_{i-1}} - j\mathbf{k}.\mathbf{r_i})} Kxx_{i-1} + B_{i+1} e^{(j\mathbf{k}.\mathbf{r_{i+1}} - j\mathbf{k}.\mathbf{r_i})} Kxy_{i+1} + B_{i-1} e^{(j\mathbf{k}.\mathbf{r_{i-1}} - j\mathbf{k}.\mathbf{r_i})} Kxy_{i-1}$$

$$-\omega^2 m_i B_i = A_i Kyx_i + y_i Kyy_i + A_{i+1} e^{(j\mathbf{k}.\mathbf{r_{i+1}} - j\mathbf{k}.\mathbf{r_i})} Kyx_{i+1} + A_{i-1} e^{(j\mathbf{k}.\mathbf{r_{i-1}} - j\mathbf{k}.\mathbf{r_i})} Kyx_{i-1} + B_{i+1} e^{(j\mathbf{k}.\mathbf{r_{i+1}} - j\mathbf{k}.\mathbf{r_i})} Kyy_{i+1} + B_{i-1} e^{(j\mathbf{k}.\mathbf{r_{i-1}} - j\mathbf{k}.\mathbf{r_i})} Kyy_{i-1}$$

After arranging all the elements systematically the dispersion equation of the proposed system (spiral resonators) can be written as $\left[\underline{K}(k_x, k_y) - \omega^2 \underline{M}\right]\varphi = 0$

Where, $\varphi = \{A_1 \quad ... \quad A_n \quad B_1 \quad ... \quad B_{n-1} \quad B_n\}^T$are the eigen vectors (mode shapes) of the spiral system. The dispersion equations written above can be solved for ω by assuming digital values of $k_x$ & $k_y$. In this research 2 dimensional wave with wave number|k| is assumed to propagate along any arbitrary θ direction with respect to the x-

axis. $|k|$ is discretized between 0 to $\pi$ with wave number interval $\pi/100$. Thus $k_x = |k|\cos(\theta)$ and $k_y = |\mathbf{k}|\sin(\theta)$. A computer program was written to solve the dispersion equation and the spiral eigen modes were obtained.

**Problem Description**

Solution was obtained from two configurations of the resonators in Archimedean Spiral ($r = 5 + 2\theta$ and Logarithmic Spiral ($r = 5e^{0.2\theta}$), where dimensions are in mm. The angular distance between two consecutive resonators were $0.4\pi$. The eigen value problem can be solved for any geometrical configuration of the spirals. Problem can be solved for different material properties of the resonators and materials in which the resonators are placed. For example, individual mass of the resonators, individual spring constants between neighboring resonators and individual spring constants for the springs connecting the resonators to the origin the spiral, can be varied or can be designed as per the requirements. In this work, the local resonators are assumed to be lead cylinders of mass 5 gm ($m_0$) and are connected to each other by hard polymer string (source of spring constant$K_0 = 10.5e6\ N/m$). These resonators are then spirally connected with the center of the spiral (source of spring constant $Kt_0 = 10.5e6\ N/m$). The complete system is assumed to be submerged in fluid (air or liquid). In this research, three different problems are solved for each type of spirals. Problem 1: Mass of the resonators are assumed to be constant and the stiffness of the springs that connects the neighboring resonators are equal (i.e. $m_1 = m_i = m_n = m_0$, $K_{i-1} = K_i = K_{i+1} = K_0$, $Kt_{i-1} = Kt_i = Kt_{i+1} = K_0 = Kt_0$). These assumptions are made for both Archimedean and Logarithmic spirals. Problem 2: Masses of the resonators are increased by the ratio of their radial distance ($m_i = m_0(r(\theta))$) from the center, keeping spring constants constant. Problem 3: The spring Kt that connects

the resonators with the center of the spiral (radial springs), are increased by the ratio of the distance of the resonators ($Kt_i = Kt_0(r(\theta))$) from the center, keeping the mass of the resonators constant. Problem 4: The Kt spring that connects the resonators with the center of the spiral, are decreased by the ratio of the distance of the resonators ($Kt_i = Kt_0(1/r(\theta))$) from the center, keeping the mass of the resonators constant. Problem 5: Keeping equal mass and equal radial spring constants, $K_i$ is increased by the ratio of their distance from the center ($K_i = K_0(r(\theta))$). Problem 6: Keeping equal mass and equal radial spring constants of the resonators, $K_i$ are decreased by the ratio of the distance of the resonators ($K_i = K_0(1/r(\theta))$) from the center. Problem 7: Keeping the mass of the resonators constants spring constant for $K_i$ are considered 1/10 of the spring constant $Kt_i$ (i.e. $K_i = Kt_i/10$). This assumption is valid, especially when the resonators are coated with softer materials.

## 11.3 Results and Discussions

Natural frequencies of the Archimedean and Logarithmic spiral systems are shown is Figure 11.3 (a), obtained from Problem 1 and Problem 2. Figure 11.3 (b) shows the deformed or new position of the resonators oriented in Logarithmic spiral obtained from two consecutive vibration modes ($26^{th}$ and $27^{th}$ eigen vectors) where sudden jump in natural frequencies from 28 KHz to 60 KHz is apparent (from Figure 11.3 (a)). Although sudden jumps are evident from Figure 11.3 (a), such jumps are apparent, if the natural frequencies are plotted keeping track of correlation between the numbed of degrees of freedom and the identities of the resonators in spiral order. Factually no frequency jump in eigen modes were observed from Problem 1 and Problem 2. Maximum natural frequency of the spiral

system was found to be around 90 KHz. It is observed that a and b parameters in spiral equation ($r = a + b\theta$) or ($r = ae^{b\theta}$) play a key role in obtaining certain natural frequencies (not shown) in their vibrational modes. Similar study was performed in Problem 3 and Problem 4. Radial spring constants were increased (Problem 3) and then decreased (Problem 4) by the ratio of their radial distance and the natural frequencies obtained are plotted in Figure 11.4 (a). Figure 11.4 (b) shows the natural frequencies of the system when Problem 5 and Problem 6 are solved. From Figure 11.4 (a) it can be seen that there are no obvious gap in the natural frequencies of the system similar to Figure 11.3 (a), however, a narrow band gap in natural frequencies were observed in both Archimedean and Logarithmic spiral systems between 15 KHz – 85 KHz when the spring constants for the springs connecting the resonators to each other are increased or decreased, radially.

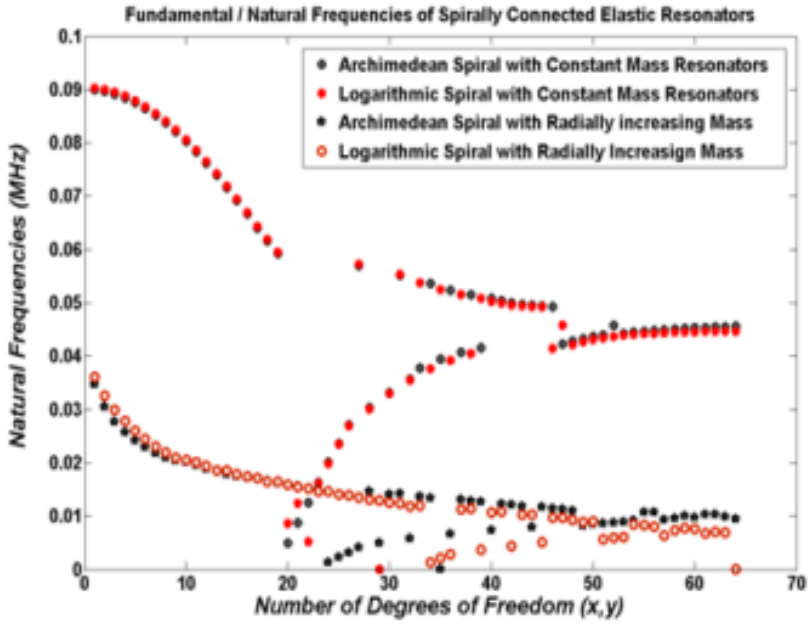

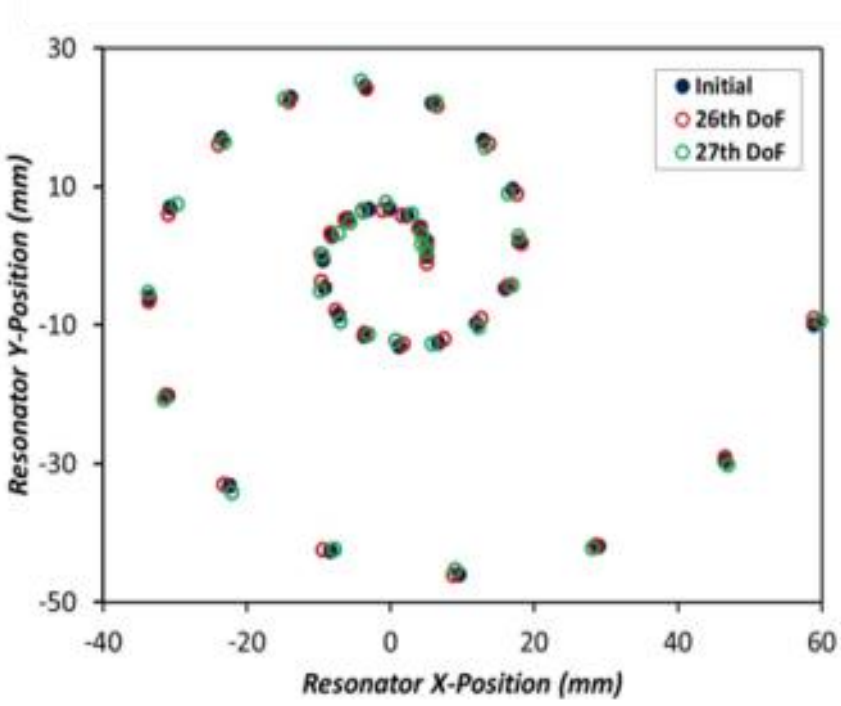


Figure 11.3: a) Natural vibrational frequencies in Discrete Archemedian and Logarithmic spiral system with constant and radially increasing mass; b) Displaced position of the centers of the resonators in Logarithmic spiral system for $26^{th}$ and $27^{th}$ vibrational mode where a sudden jump is in natural frequency is found.

Next the wave propagation through the proposed spiral system is studied. Here, $e^{i(\mathbf{k}.\mathbf{x}-\omega t)}$ plane wave incident was assumed and the dispersion equation was solved by discretizing the wave numbers to obtain the eigen frequencies. Figure 11.5 shows the frequency eigen modes within a band $0-\pi$ of the wave numbers obtained from Logarithmic spiral system. In Figure 11.5 (a) marking along the x axis (0-1, 1-2 & 2-3) represents the wave number between $0-\pi$ for the propagation of wave along $0^0$, $45^0$& $90^0$, respectively. It is apparent that all the possible eigen modes are confined within a specific band of the frequencies. The system is modeled as a discrete system and thus discrete numbers of eigen modes were obtained. All eigen modes were found to be confined within 20 KHz – 100 KHz when the mass of the resonators are kept constant (Problem 1).

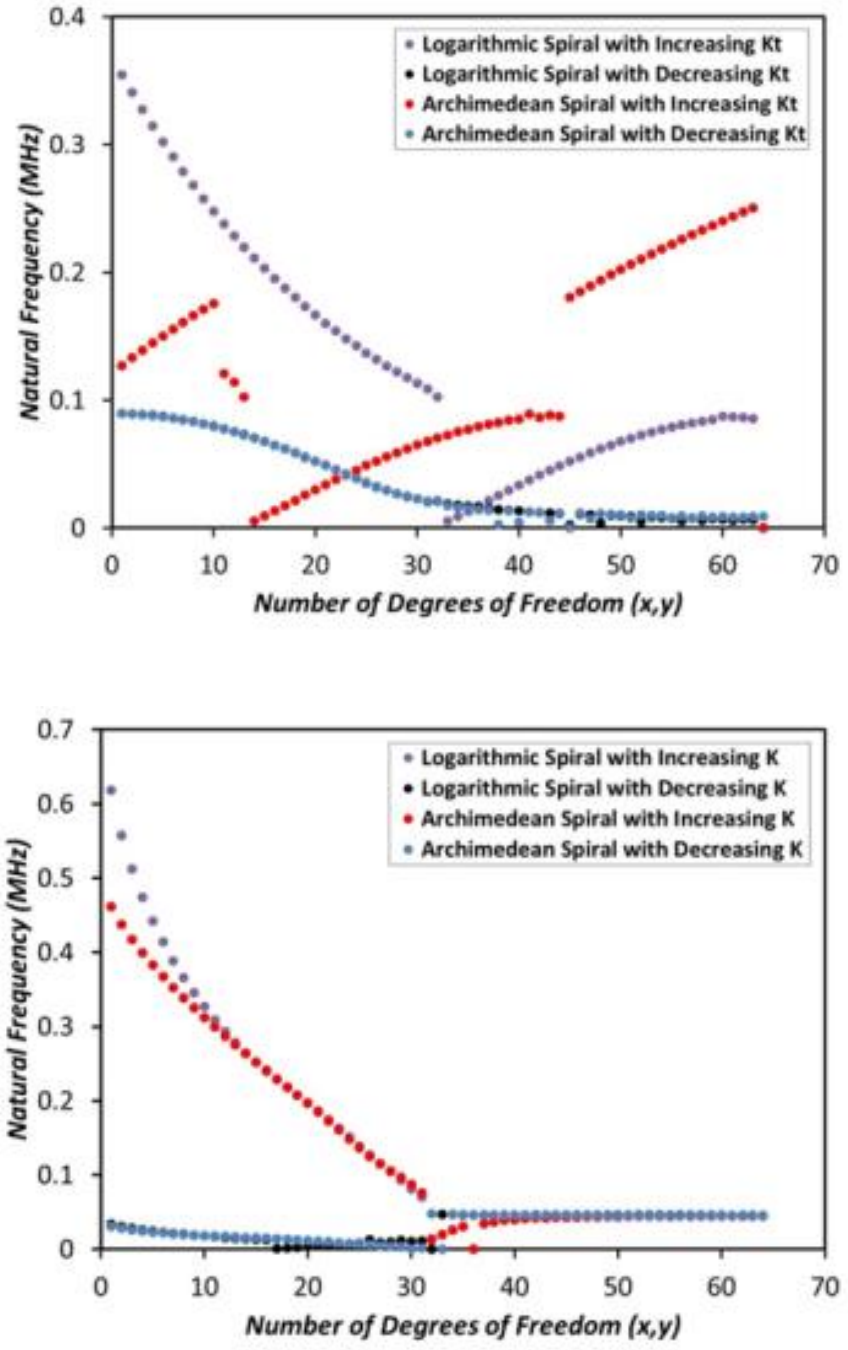


Figure 11.4: a) Natural vibrational frequencies in Discrete Archemedian and Logarithmic spiral system with constant mass, constant tangential spring constants but radially increasing / decreasing radial spring constants ; b) Natural vibrational frequencies in Discrete Archemedian and Logarithmic spiral system with constant mass, constant radial spring constants but radially increasing/decreasing tangential spring constants.

Similar confined band was obtained but shifted between 3 KHz - 25 KHz when the

mass of the resonators were increased gradually (Problem 2). Hence, by manipulating the resonator's mass, it is possible to change the governing pass band of the spiral resonator system. Further a closer investigation was carried out. The variation of eigen frequencies, with respect to the wave numbers between $-\pi$ to $\pi$ for the first two modes (wave propagation along $90^0$) are shown in the Figure 11.5 (b). It can be seen that there are many crossover zones between two modes. A closer view of the section marked in blue is shown in Figure 11.5 (c).

The radial spring constants are the design parameter of the spiral system and hence a study was conducted to understand their impact on eigen frequencies. Problem 2 and Problem 3 was solved and very complicated mode patterns were observed. Highly dispersive, weakly dispersive and nondispersive wave modes were generated simultaneously. In Figure 11.6 (a) marking along the x axis (0-1, 1-2 & 2-3) represents the wave number between $0-\pi$ for the propagation of wave along $0^0$, $45^0$&$90^0$, respectively. Completely new finding compared to Problem 1 and 2 was obtained when the radial spring constants are increased radially by the ratio of their radial distance. A definite pass band of frequencies between 35 KHz – 95 KHz was observed along with the nondispersive wave modes between 290 KHz – 355 KHz. However, all such modes were found to be dispersive within the wave number band 0 - 0.1. Jump between two consecutive wave modes were increasing with the increase in radial spring constant. Between frequencies 0 - 35 KHz no wave modes were found. Indication of modal crossovers (cross-talk) at higher frequencies were found (e.g. marked in red circle in Figure 11.6 (a)) when the wave propagated along the $45^0$ & $90^0$. Similar crossovers were apparent at lower frequencies (between 100 KHz – 120 KHz) when the wave propagated along the x axis

(propagation angle $0^0$). These crossovers appeared periodically along the wave number axis and that periodicity was varied with varying frequency. A closer view of the wave modes within in the black box (marked in Figure 11.6 (a)) is shown in Figure 11.6 (b). A mode was found to be symmetric about the wave number 0.5585, which is essentially the mode associated with x displacement of the 18th resonator at approximately $30^0$ angle with the x axis at a distance of 19.481 mm. Dividing the x component of the radial distance by the wave number 0.5585, it can be seen that approximately 30 full wave form can fit within the radial distance of the 18th resonator. Similar phenomena are evident in many places in the dispersion curves. After solving Problem 4 (the radial spring constants were decreased radially) it was found that the stop band was reduced to 0-8 KHz keeping the upper limit of the mode confinements within 95 KHz.

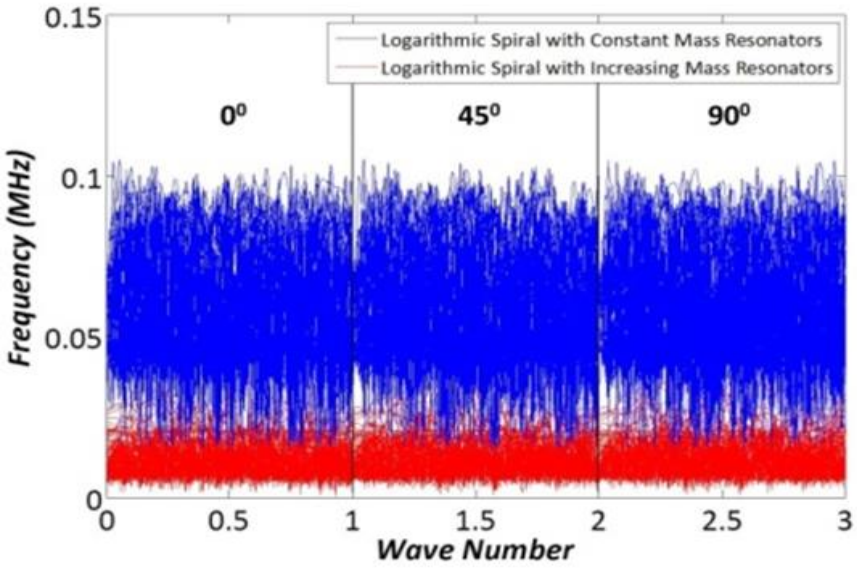

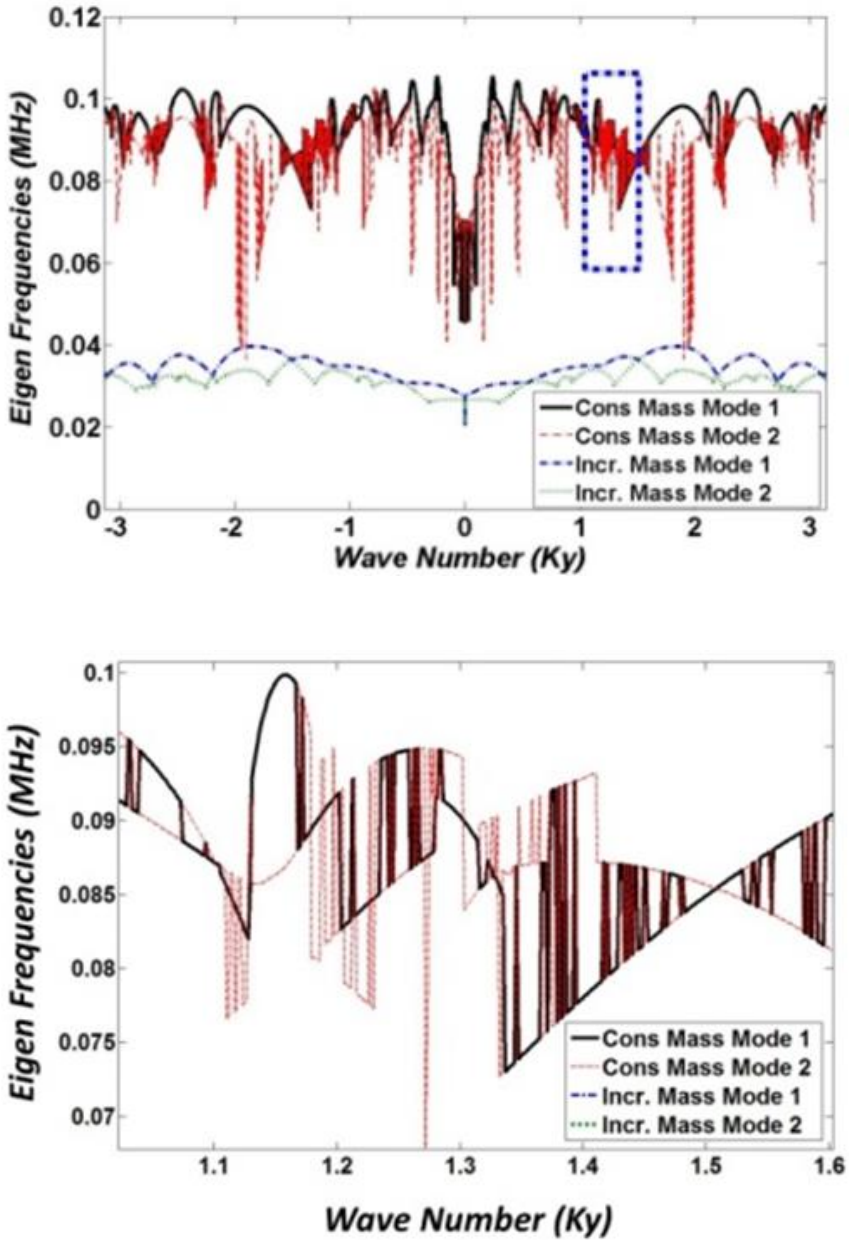


Figure 11.5: Evidence of phonon confinement (all possible real modes) in discrete Logarithmic spiral system with constant and radially increasing mass; middle) Real modes 1st and 2nd modes between wave number $-2\pi$ to $2\pi$ in discrete Logarithmic spiral system with constant and radially increasingmass ; bottom) Zoomed view within the blue box : Real modes 1st and 2nd modes between wave number $-2\pi$ to $2\pi$ in discrete Logarithmic spiral system with constant and radially increasing mass

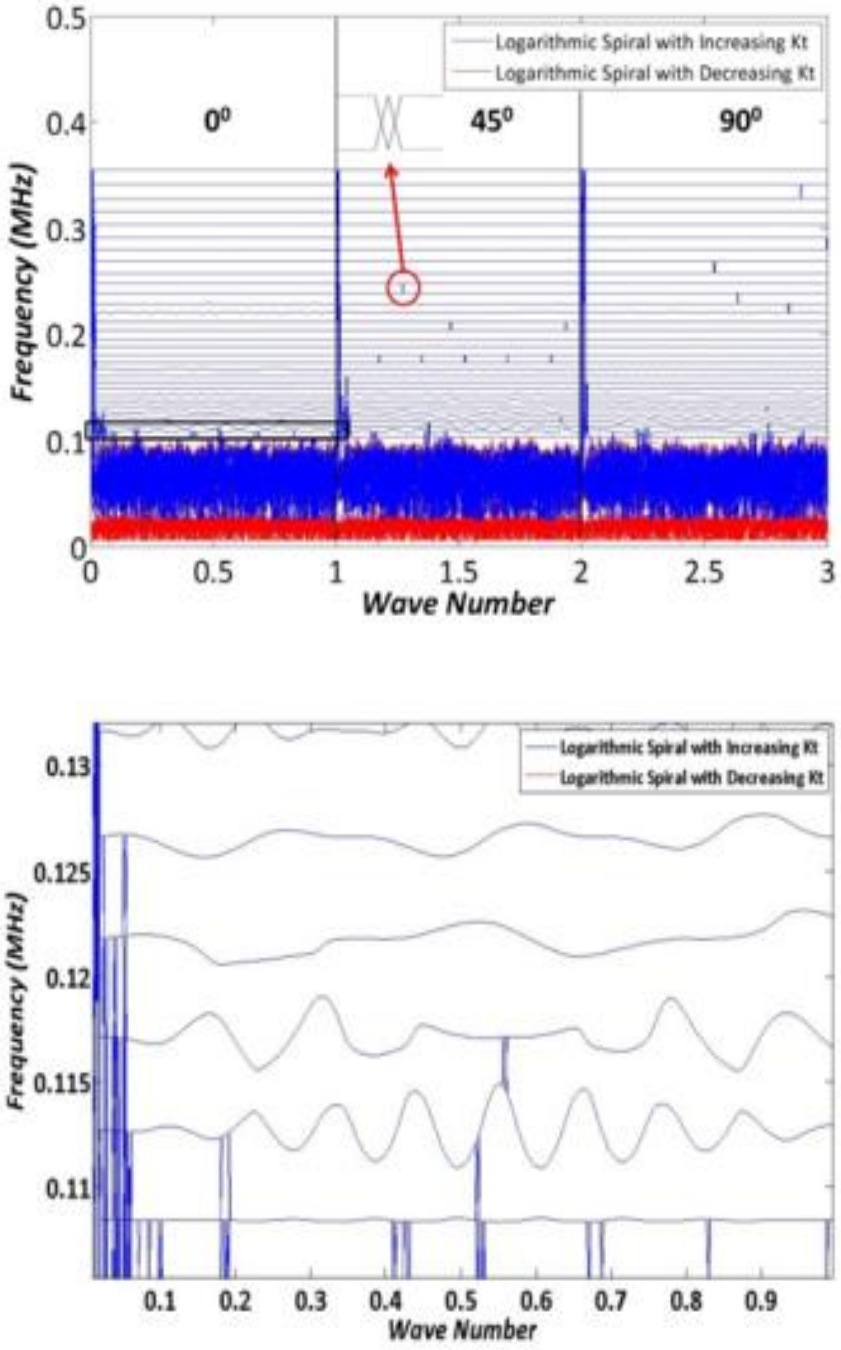


Figure 11.6: a) Evidence of phonon confinement (all possible real modes – nondispersive wave modes were found that results zero group velocity) in discrete Logarithmic spiral system with radially increasing/decreasing radial spring constant; b) Zoomed view within the black box in Figure 6(a)

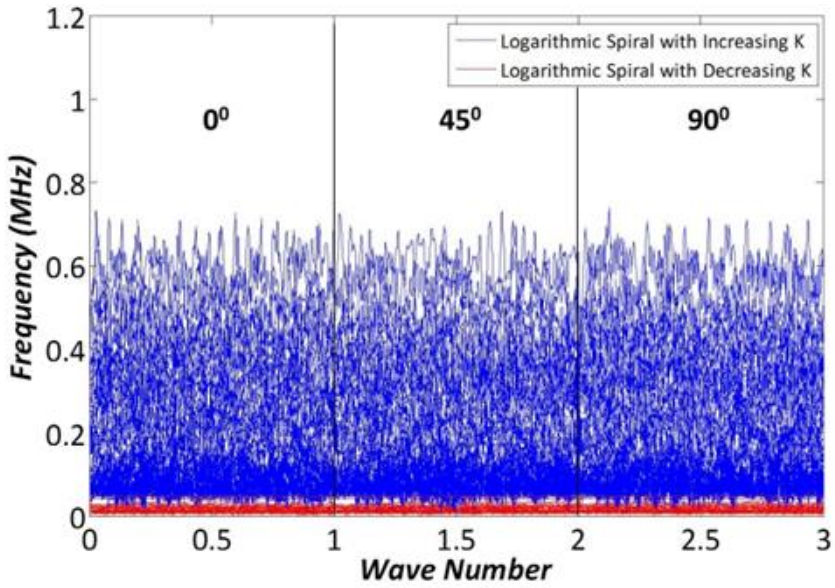


Figure 11.7: Evidence of phonon confinement (all possible real modes) in discrete Logarithmic spiral system with radially increasing/decreasing tangential spring constant; b) Zoomed view within the black box in Figure 11.6 (a)

Problem 6 and 7 were studied where the spring constants of the springs connecting two consecutive resonators are increased and decreased, respectively. Figure 11.7 (a) shows the dispersion phenomenon demonstrated by the Problem 6 and Problem 7. When the spring constants ($K_i$) are increased as per the problem description in Problem 6 the wave confinement were found to be within 20 KHz to 700 KHz. Hence, below 20 KHz no wave modes were found. Similarly, when the spring constants are decreased by the ratio of the radial distance of the resonators, wave confinement were separated in to two zones, zone 1, is wider band between 5 KHz – 25 KHz and zone 2, a narrow band between 45 KHz – 47 KHz. Multiple modal crossover points between these two zones were identified similar to the points shown in Figure 11.6 (a). Hence between 25 KHz – 45 KHz, no modes were found along the wave number axis except at the point of crossovers.

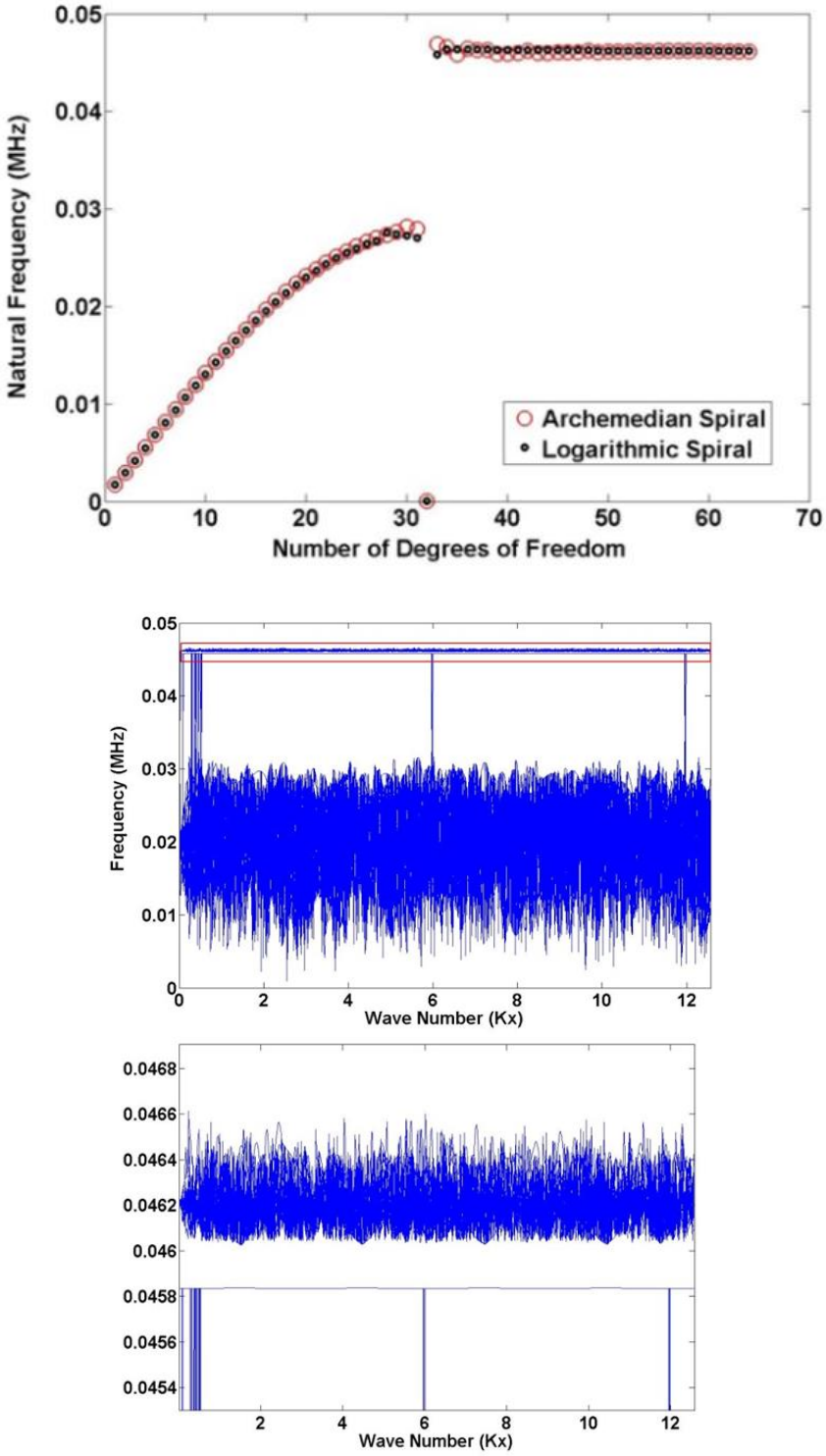


Figure 11.8: a) Natural vibrational frequencies in Discrete Archemedian and Logarithmic spiral system when tangential spring constants are 10 times less than the radial spring constants. b) Wave dispersion through the system showing existence of two pass bands between a stop band c) zoomed view of the modes within the red window in Figure 11.8(b)

Another interesting phenomenon that was observed, after solving the Problem 7, is shown in Figure 11.8. Figure 11.8 (a) shows the natural frequencies of the spiral system obtained when the tangential springs constants are ten time less than the radial spring constants. Such parametric variation created a band of frequencies which are not possible to be the natural frequency of the spiral system and then almost half of the wave modes found to be nondispersive. Next, wave propagation through the Logarithmic spiral system was studied (wave propagating along x direction (see Figure 11.8 (b) & Figure 11.8 (c))). A clear band gap at lower frequencies (similar to the above examples) was observed and another band gap between 30 KHz – 45 KHz was found. Just above this band gap another narrow pass band between 46 KHz – 46.6 KHz was observed. The band gap between 30 KHz – 45 KHz were found to be dependent on the ratio of tangential and radial spring constants. Hence, softer springs between resonators along the tangential direction are capable of creating larger band gaps at lower frequencies. Modal crossover points every $2\pi$ interval were evident as discussed before. These modal crossovers act as bridge between two pass bands at certain wave number zone. Hence, there are significant possibilities of manipulating these behaviors for practical use in frequency filtration.

## 11.4 Chapter Summary

From the above study the following comments can be made. Spiral modal behavior is geometry dependent. Archimedean and Logarithmic Spirals have similar phenomena but different frequency responses. In the vibration analysis of the Logarithmic spirals, the nonexistence of the natural frequencies is correlated with the frequency band gaps that are obtained when the wave propagation through the spiral system was studied. Increasing

spring constants increased the frequencies of the passing band of the wave modes, whereas increased mass ($m_i$) decreased the frequency bands of the wave modes. Different spring constants for radial springs ($Kt_i$) and tangential springs ($K_i$) could potentially result in separation of band structures with multiple pass bands. However, it is affirmative from the results that low frequency non passing zone can be created and all the possible wave modes can be confined within certain band of frequencies. Suitable selection of material for the resonators and materials for the springs will provide extreme design flexibility for frequency control and wave guiding.

# CHAPTER 12: CONCLUSION

In present state-of-the-art technologies, electronic and mechanical sensors are widely employed in industrial applications for selecting user defined frequencies. Cantilever beam models are the most popular designs for the mechanical sensors. However, cantilever beam models are typically designed for high frequency (usually > 10 KHz) applications since resonance phenomenon is the driving mechanism in selecting target frequencies using such sensors. Resonance frequency of the structural resonance primarily depends on structural geometry, stiffness and mass of the system. Thus dimension of the structure is the governing factor. Hence in this research, we proposed an alternative but novel mechanical frequency selection method that can be employed in a wide variety of frequencies maintaining the required smaller geometric configurations.

After rigorous study, it found that, the human cochlea is the most developed band pass sensor in nature, where it selects only the sonic frequency band (20 Hz – 20 KHz) and filters all the infrasonic and ultrasonic frequencies using only a ~35 mm effective structure length. The Basilar Membrane (BM) in the cochlea is naturally designed but based on the variable stiffness model, starting from the base to the apex of the cochlea. While cantilever beam uses the structural resonance phenomenon to select the target frequencies, basilar membrane performs bases on local resonance phenomena to do the same.

Two models have been proposed in this research considering the ability to introduce local resonance feature, a) the Acousto-Elastic MetaMaterial (AEMM) model and b) the Basilar Membrane (BM) model. AEMM's are traditionally employed for filtering acoustic waves. However, in this research, for the very first time AEMM's are proposed for the purpose of the frequency selection. Initially, stop band technique (SBT) is considered to model the AEMM based mechanical sensor. Upon unsuccessful attempts using SBT, band pass technique (PBT) is adopted. It has been found that, using the PBT, AEMM can perform as the targeted mechanical sensor. A specific frequency can be selected precisely from a unit cell AEMM, while remaining frequencies of this system can be filtered. Since each unit cell is capable of selecting a distinct frequency, multi-cell AEMM model, with systemic selection of material properties in each cell, is further proposed to sense a band of frequencies. It has been reported that, since in the AEMM model, local resonance frequency is a function of material properties instead of model geometry, it is possible to manipulate the target frequency keeping the model geometry unchanged. Such flexibility allows the AEMM model to be designed for a wide range of frequencies.

In Basilar Membrane model, geometric configuration of the real basilar membrane is mimicked to replicate its functionalities. A considerable number of studies have been performed in recent years to present mechanical frequency sensors/filters mimicking the basilar membrane. However, a comprehensive and comparatively fast predictive model is missing. Such model is the utmost necessity to conduct optimization study before any design proposal. Hence, in this research, a predictive model for the band pass frequency sensor is developed so that the frequency band and the model parameters can be selected predictively. It is expected that the developed predictive model can boost the artificial

cochlea technology since the human cochlea also performs as band pass frequency sensor, naturally. Following the geometry of the basilar membrane, trapezoidal structure is suggested for the sensor device. The predictive model is developed with utmost flexibility that not only can manage homogeneous but also the functionally graded model parameters. The model is flexible enough to adopt different types of boundary conditions.

Two designs of the BM based mechanical sensor are proposed, i) the plate model and ii) the beam model. The plate model is designed where a band of frequencies is necessary without missing any frequency within the band. Using the plate model and homogeneous model parameters, it has been found that a specific band of frequency can be selected from a distinct segment of the model. It is possible to shift, wide or narrow the length segment using functionally graded structure towards selecting the same frequency band. The beam model is proposed where distinct frequencies are require to be selected within a frequency band. The beam model suggests that a band of frequency can be sensed using the proposed model and it is possible to manipulate the frequency selection capacity of the model altering the material properties. Both the predictive models are numerically validated using the simulation tool COMSOL Multiphysics and it has been found that the proposed models are couple of order faster than its counter FEM technique. Though, in this work, deflection amplitude is referred as sensing parameters, the deflection amplitude can easily be converted to electrical signals through implementing smart materials, specifically piezoelectric material. The predictive models can be linked to any optimization tool to get the user required optimized geometry for any target frequency band.

In addition to the introduction of mechanical frequency selection method, in this research we envisioned few novel applications of the proposed models. Since the proposed

AEMM sensor uses electric potential as the sensing parameter, we further recommend AEMM model for energy harvesting application. We report that, the proposed unit AEMM structure with sub-wavelength geometry (< 5 cm) is capable to generate ~ 36 μW power at low frequency level (<1 KHz), which is significantly higher compared to the existing harvesters of same kind. We further suggest three novel applications (please refer chapter 7) of the AEMM based harvester. In this research, we also propose BM cantilever beam model as the mycotoxin detection sensor.

In spite of the key objectives of this dissertation, couple of supporting researches have also been performed, such as, energy scavenging using patterned piezoelectric layer, phonon confinement using spirally oriented elastic resonators (please see chapter 10 and 11).

## 12.1 Major contributions

1. A universal mechanical band pass frequency sensing mechanism is developed using the local resonance phenomena. The proposed frequency selection method provides the flexibility to be employed for both the low and the high frequencies with controlled geometric configuration.
2. Two designs (AEMM and BM) are proposed to model the targeted frequency sensors mimicking the operation of the human cochlea.
3. For the very first time AEMM is presented to read the trapped frequencies inside the metamaterial in oppose to the filtration of acoustic wave using band gap phenomena. It has been confirmed that the proposed design of AEMM is

capable of performing as the targeted frequency sensor. Each unit cell selects a unique frequency.

4. Comprehensive predictive model for the BM based frequency sensor is developed. Two predictive models are developed corresponding to the envisioned plate type and beam type BM sensors. The predictive models are significantly faster (~3 times) than its counter FEM approach.
5. AEMM based energy scavenging procedure is presented. Significantly higher power output is recorded compared to the existing harvesters of the similar type.
6. Additional novel applications of the AEMM and BM models are proposed.

## 12.2 Future Recommendations

1. Using the developed predictive models, scaling down of the AEMM and BM sensors to micro and nano scale for a specific target frequency are possible. Development of a low frequency sensor with micro/nano scale geometry is challenging but could be a future direction of research.
2. Optimize the precise frequency selection ability of the proposed models.
3. The BM predictive model could boost the development of the artificial mechanical cochlea.
4. Development of the ultrasonic cochlea for robots can be envisioned using the BM model.
5. Further study is necessary to avoid the tail peaks in the BM plate model.

6. Perform necessary study to implement the AEMM and BM models in respective novel applications those are proposed in this dissertation.

# REFERENCES


1. Taylor, J., M. Discotty, and D. Dornfeld, *Investigation of Acoustic Emission for Use as a Wheel-to-Workpiece Proximity Sensor in Fixed-Abrasive Grinding, Lawrence Livermore National Laboratory, CA,* 1995, UCRL-JC-121689.

2. Hwang, K.S., et al., *In-situ quantitative analysis of a prostate-specific antigen (PSA) using a nanomechanical PZT cantilever.* Lab on a Chip, 2004. **4**(6): p. 547-552.

3. Shen, Z., W.Y. Shih, and W.-H. Shih, *Self-exciting, self-sensing PbZr0.53Ti0.47O3/SiO2 piezoelectric microcantilevers with femtogram/Hertz sensitivity.* Applied physics letters, 2006. **89**(2): p. 023506.

4. Zhu, Q., W.Y. Shih, and W.-H. Shih, *In situ, in-liquid, all-electrical detection of Salmonella typhimurium using lead titanate zirconate/gold-coated glass cantilevers at any dipping depth.* Biosensors and Bioelectronics, 2007. **22**(12): p. 3132-3138.

5. Hierlemann, A. and H. Baltes, *CMOS-based chemical microsensors.* Analyst, 2003. **128**(1): p. 15-28.

6. Lee, J.H., et al., *Immunoassay of prostate-specific antigen (PSA) using resonant frequency shift of piezoelectric nanomechanical microcantilever.* Biosensors and Bioelectronics, 2005. **20**(10): p. 2157-2162.

7. Moulin, A., S. O'shea, and M. Welland, *Microcantilever-based biosensors.* Ultramicroscopy, 2000. **82**(1): p. 23-31.

8. Gopel, W., et al., *Sensors: a comprehensive survey. chemical and biochemical sensors, Part 2*1992: VCH.

9. Battiston, F., et al., *A chemical sensor based on a microfabricated cantilever array with simultaneous resonance-frequency and bending readout.* Sensors and Actuators B: Chemical, 2001. **77**(1): p. 122-131.

10. Lang, H., et al., *A chemical sensor based on a micromechanical cantilever array for the identification of gases and vapors.* Applied Physics A: Materials Science & Processing, 1998. **66**: p. S61-S64.

11. Capobianco, J.A., W.Y. Shih, and W.-H. Shih, *Methyltrimethoxysilane-insulated piezoelectric microcantilevers for direct, all-electrical biodetection in buffered aqueous solutions.* Review of Scientific Instruments, 2006. **77**(12): p. 125105.

12. Raiteri, R., et al., *Micromechanical cantilever-based biosensors.* Sensors and Actuators B: Chemical, 2001. **79**(2): p. 115-126.

13. Carrascosa, L.G., et al., *Nanomechanical biosensors: a new sensing tool.* TrAC Trends in Analytical Chemistry, 2006. **25**(3): p. 196-206.

14. Zhu, Q., W.Y. Shih, and W.-H. Shih, *Mechanism of flexural resonance frequency shift of a piezoelectric microcantilever sensor during humidity detection.* Applied physics letters, 2008. **92**(18): p. 183505.

15. Hodnett, M., R. Chow, and B. Zeqiri, *High-frequency acoustic emissions generated by a 20 kHz sonochemical horn processor detected using a novel broadband acoustic sensor: a preliminary study.* Ultrasonics sonochemistry, 2004. **11**(6): p. 441-454.

16. Watts, L., *Cochlear Mechanics: Analysis and Analog VLSI.* PhD Thesis, California Institute of Technology, 1992.

17. Diependaal, R.J. and M.A. Viergever, *Nonlinear and active two-dimensional cochlear models: time-domain solution.* J Acoust Soc Am, 1989. **85**(2): p. 803-12.

18. Kolston, P.J., et al., *Realistic mechanical tuning in a micromechanical cochlear model.* The Journal of the Acoustical Society of America, 1989. **86**(1): p. 133-140.

19. Sondhi, M.M., *Method for computing motion in a two-dimensional cochlear model.* The Journal of the Acoustical Society of America, 1978. **63**(5): p. 1468-1477.

20. de Boer, E. and E. van Bienema, *Solving cochlear mechanics problems with higher-order differential equations.* The Journal of the Acoustical Society of America, 1982. **72**(5): p. 1427-1434.

21. Holmes, M., *Low Frequency Asymptotics for a Hydroelastic Model of the Cochlea.* SIAM Journal on Applied Mathematics, 1980. **38**(3): p. 445-456.

22. Holmes, M.H., *An analysis of a low-frequency model of the cochlea.* The Journal of the Acoustical Society of America, 1980. **68**(2): p. 482-488.

23. Holmes, M.H., *Study of the transient motion in the cochlea.* The Journal of the Acoustical Society of America, 1981. **69**(3): p. 751-759.

24. Guenneau, S., et al., *Acoustic metamaterials for sound focusing and confinement.* New Journal of physics, 2007. **9**(11): p. 399.

25. *Acoustic Metamaterials.* http://en.wikipedia.org/wiki/Acoustic_metamaterials.

26. Krowne, C.M. and Y. Zhang, *Physics of negative refraction and negative index materials: optical and electronic aspects and diversified approaches*. Vol. 98. 2007: Springer.

27. Huang, H.H., C.T. Sun, and G.L. Huang, *On the negative effective mass density in acoustic metamaterials.* International Journal of Engineering Science, 2009. **47**(4): p. 610-617.

28. Huang, G.L. and C.T. Sun, *Band Gaps in a Multiresonator Acoustic Metamaterial.* Journal of Vibration and Acoustics, 2010. **132**(3): p. 031003-031003.

29. Krynkin, A., et al., *Predictions and measurements of sound transmission through a periodic array of elastic shells in air.* The Journal of the Acoustical Society of America, 2010. **128**(6): p. 3496-3506.

30. Oudich, M., et al., *A sonic band gap based on the locally resonant phononic plates with stubs.* New Journal of Physics, 2010. **12**(8): p. 083049.

31. Hsu, J.-C., *Local resonances-induced low-frequency band gaps in two-dimensional phononic crystal slabs with periodic stepped resonators.* Journal of Physics D: Applied Physics, 2011. **44**(5): p. 55401-55409.

32. Fan, L., S.-y. Zhang, and H. Zhang, *Transmission characteristics of double negativity acoustic metamaterials studied with fluid impedance theory.* The Journal of the Acoustical Society of America, 2011. **129**(4): p. 2483.

33. Norris, A., *Periodic metal structures for acoustic wave control.* The Journal of the Acoustical Society of America, 2011. **130**(4): p. 2359.

34. Chesnais, C., C. Boutin, and S. Hans, *Effects of the local resonance on the wave propagation in periodic frame structures: Generalized Newtonian mechanics.* The Journal of the Acoustical Society of America, 2012. **132**(4): p. 2873-2886.

35. Riaz, A. and S. Banerjee, *Wave Propagation in Metamaterial Using Multiscale Resonators by Creating Local Anisotropy* International Journal of Modern Engineering, 2013. **13**(2): p. 9.

36. El-Bahrawy, A., *Stopbands and Passbands for Symmetric Rayleigh-Lamb Modes in a Plate With Corrugated Surfaces.* Journal of Sound and Vibration, 1994. **170**(2): p. 145-160.

37. El-Bahrawy, A., *Point force excitation of surface waves along the doubly corrugated traction-free boundary of an elastic half-space.* The Journal of the Acoustical Society of America, 1994. **96**(5): p. 3167-3176.

38. Banerjee, S. and T. Kundu, *Elastic wave propagation in sinusoidally corrugated waveguides.* The Journal of the Acoustical Society of America, 2006. **119**(4): p. 2006-2017.

39. Banerjee, S. and T. Kundu, *Symmetric and anti-symmetric Rayleigh–Lamb modes in sinusoidally corrugated waveguides: An analytical approach.* International Journal of Solids and Structures, 2006. **43**(21): p. 6551-6567.

40. Veselago, V.G., *The electrodynamics of substances with simultaneously negative values of ε and μ.* Physics-Uspekhi, 1968. **10**(4): p. 509-514.

41. Smith, D.R., J.B. Pendry, and M.C.K. Wiltshire, *Metamaterials and Negative Refractive Index.* Science, 2004. **305**(5685): p. 788-792.

42. Pendry, J.B., et al., *Magnetism from conductors and enhanced nonlinear phenomena.* Microwave Theory and Techniques, IEEE Transactions on, 1999. **47**(11): p. 2075-2084.

43. Smirnova, E.I., et al., *Fabrication and cold test of photonic band gap resonators and accelerator structures.* Physical Review Special Topics - Accelerators and Beams, 2005. **8**(9): p. 091302.

44. Liu, Z., C.T. Chan, and P. Sheng, *Analytic model of phononic crystals with local resonances.* Physical Review B, 2005. **71**(1): p. 014103.

45. Mei, J., et al., *Effective Mass Density of Fluid-Solid Composites.* Physical Review Letters, 2006. **96**(2): p. 024301.

46. Wu, Y., Y. Lai, and Z.-Q. Zhang, *Effective medium theory for elastic metamaterials in two dimensions.* Physical Review B, 2007. **76**(20): p. 205313.

47. Sigalas, M.M. and E.N. Economou, *Elastic and acoustic wave band structure.* Journal of Sound and Vibration, 1992. **158**(2): p. 377-382.

48. Poulton, C.G., et al., *Eigenvalue problems for doubly periodic elastic structures and phononic band gaps.* Proceedings of the Royal Society of London. Series A: Mathematical, Physical and Engineering Sciences, 2000. **456**(2002): p. 2543-2559.

49. Caballero, D., et al., *Large two-dimensional sonic band gaps.* Physical Review E, 1999. **60**(6): p. R6316-R6319.

50. Phani, A.S., J. Woodhouse, and N.A. Fleck, *Wave propagation in two-dimensional periodic lattices.* The Journal of the Acoustical Society of America, 2006. **119**(4): p. 1995-2005.

51. Hirsekorn, M., et al., *Modelling and simulation of acoustic wave propagation in locally resonant sonic materials.* Ultrasonics, 2004. **42**(1–9): p. 231-235.

52. Li, J. and C.T. Chan, *Double-negative acoustic metamaterial.* Physical Review E, 2004. **70**(5): p. 055602.

53. Milton, G.W. and J.R. Willis, *On modifications of Newton's second law and linear continuum elastodynamics.* Proceedings of the Royal Society A: Mathematical, Physical and Engineering Science, 2007. **463**(2079): p. 855-880.

54. Huang, H.H. and C.T. Sun, *Anomalous wave propagation in a one-dimensional acoustic metamaterial having simultaneously negative mass density and Young's modulus.* The Journal of the Acoustical Society of America, 2012. **132**(4): p. 2887-2895.

55. Naify, C.J., et al., *New directions for manipulation of sound using acoustic metamaterials.* The Journal of the Acoustical Society of America, 2012. **132**(3): p. 2012.

56. Yao, *Experimental study on negative effective mass in a 1D mass-spring system.* New Journal of Physics, 2008. **10**(4): p. 043020.

57. Park, J., et al., *Determination of effective mass density and modulus for resonant metamaterials.* The Journal of the Acoustical Society of America, 2012. **132**(4): p. 2793-2799.

58. Liu, Z., et al., *Locally Resonant Sonic Materials.* Science, 2000. **289**(5485): p. 1734-1736.

59. Guenneau, S., et al., *Acoustic metamaterials for sound focusing and confinement* New Journal of Physics, 2007. **9**: p. 399.

60. Movchan, A.B. and S. Guenneau, *Split-ring resonators and localized modes.* Physical Review B, 2004. **70**(12): p. 125116.

61. Nemer, S., et al., *Modelling resonance frequencies of a multi-turn spiral for metamaterial applications.* Progress In Electromagnetics Research C, 2011. **20**(31-42).

62. Guven, K., et al., *Electromagnetic cloaking with canonical spiral inclusions.* New Journal Physics, 2008. **10**(11): p. 115037.

63. Anlage, S.M., *The physics and applications of superconducting metamaterials.* Journal of Optics, 2011. **13**(2): p. 024001.

64. Massaoudi, S. and I. Huynen, *Multiple resonances in arrays of spiral resonators designed for magnetic resonance imaging.* Microwave and Optical Technology Letters, 2008. **50**(7): p. 1945-1950.

65. Bilotti, F., A. Toscano, and L. Vegni, *Design of Spiral and Multiple Split-Ring Resonators for the Realization of Miniaturized Metamaterial Samples.* Antennas and Propagation, IEEE Transactions on, 2007. **55**(8): p. 2258-2267.

66. Isik, O. and K.P. Esselle, *Backward Wave Microstrip Lines With Complementary Spiral Resonators.* Antennas and Propagation, IEEE Transactions on, 2008. **56**(10): p. 3173-3178.

67. Ma, X., et al., *Multi-band circular polarizer using planar spiral metamaterial structure.* Optics Express, 2012. **20**(14): p. 16050-16058.

68. Baena, J.D., et al., *Artificial magnetic metamaterial design by using spiral resonators.* Physical Review B, 2004. **69**(1): p. 014402.

69. He, M., et al., *Negative refractive index in chiral spiral metamaterials at terahertz frequencies.* Optik - International Journal for Light and Electron Optics, 2011. **122**(18): p. 1676-1679.

70. Isik, O. and K.P. Esselle, *Analysis of spiral metamaterials by use of group theory.* Metamaterials, 2009. **3**(1): p. 33-43.

71. ELFORD, D.P., et al., *ACOUSTIC BAND GAP FORMATION IN METAMATERIALS.* International Journal of Modern Physics B, 2010. **24**(25n26): p. 4935-4945.

72. COMSOL Multiphysics 4.3 Manual. **Stockholm, Sweden**.

73. Hussein, M., *Band Structure Calculations by Modal Analysis*, in *IUTAM Symposium on Recent Advances of Acoustic Waves in Solids*, T.-T. Wu and C.-C. Ma, Editors. 2010, Springer Netherlands. p. 319-324.

74. Brillouin, L., *Wave Propagation in Periodic Structures.* Dover Publications, Inc., New York, 1953: p. 255.

75. Huang, R., *Periodic Structures.* John Wiley & Sons, Singapore, 2012. **Ch.3**.

76. Deymier, P., *Acoustic Metamaterial and Phononic Crystals.* Springer series in solid state sciences, 2013. **173**: p. Ch. 1-5.

77. Sheng, P., *Introduction to Wave Scattering, Localization and Mesoscopic Phenomena.* Springer Series in Material Science, 1995: p. 333.

78. Erturk, A. and D.J. Inman, *An experimentally validated bimorph cantilever model for piezoelectric energy harvesting from base excitation.* Smart Mater Struct. , 2009. **18**(025009).

79. Tan, K.T., H.H. Huang, and C.T. Sun, *Optimizing the band gap of effective mass negativity in acoustic metamaterials.* Applied Physics Letters, 2012. **101**(24): p. -.

80. Liu, A.P., et al., *Multi-displacement microstructure continuum modeling of anisotropic elastic metamaterials.* Wave Motion, 2012. **49**(3): p. 411-426.

81. Von Békésy, G., *Hearing theories and complex sounds.* The Journal of the Acoustical Society of America, 1963. **35**(4): p. 588-601.

82. Chen, F., et al., *A hydromechanical biomimetic cochlea: experiments and models.* The Journal of the Acoustical Society of America, 2006. **119**(1): p. 394-405.

83. Tanaka, K., M. Abe, and S. Ando, *A novel mechanical cochlea “Fishbone” with dual sensor/actuator characteristics.* Mechatronics, IEEE/ASME Transactions on, 1998. **3**(2): p. 98-105.

84. Wittbrodt, M.J., C.R. Steele, and S. Puria, *Developing a physical model of the human cochlea using micro-fabrication methods.* Audiol Neurootol, 2006. **11**(2): p. 104-12.

85. Shintaku, H., et al., *Wide-range frequency selectivity in an acoustic sensor fabricated using a microbeam array with non-uniform thickness.* Journal of Micromechanics and Microengineering, 2013. **23**(11): p. 115014.

86. Tanujaya, H., et al., *Experimental and Analytical Study Approach of Artificial Basilar Membrane Prototype (ABMP).* Journal of Engineering and Technological Science, 2013. **45**: p. 61-72.

87. White, R.D. and K. Grosh, *Microengineered hydromechanical cochlear model.* Proceedings of the National Academy of Sciences of the United States of America, 2005. **102**(5): p. 1296-1301.

88. Kim, S., et al., *Mechanical frequency selectivity of an artificial basilar membrane using a beam array with narrow supports.* Journal of Micromechanics and Microengineering, 2013. **23**(9): p. 095018.

89. Jang, J., et al., *MEMS piezoelectric artificial basilar membrane with passive frequency selectivity for short pulse width signal modulation.* Sensors and Actuators A: Physical, 2013. **203**: p. 6-10.

90. Bekesy, G.V., *Experiments in Hearing.* Acoustical Society of Amer, 1989.

91. Dallos, P., *Biophysics of the cochlea.* Handbook of Perception, 1978. **4**: p. 125-162.

92. Evans, E., *Functional anatomy of the auditory system.* The Senses. Cambridge University Press, Cambridge, 1982: p. 251-306.

93. Kessel, R.G. and R.H. Kardon, *Tissues and organs: a text-atlas of scanning electron microscopy*1979: WH Freeman San Francisco.

94. Miller, J.M. and A.L. Towe, *Audition: structural and acoustical properties.* Physiology and Biophysics, The Brain and Neural Function, 1979: p. 339-75.

95. Shepherd, G.M., *Neurobiology*1988: Oxford University Press.

96. Schubert, E.D., *History of research on hearing.* Handbook of perception. New York: Academic Press, IV, 1978: p. 41-80.

97. Cole, J.D. and R.S. Chadwick, *An approach to mechanics of the cochlea.* Zeitschrift für angewandte Mathematik und Physik ZAMP, 1977. **28**(5): p. 785-804.

98. Iurato, S., *Functional implications of the nature and submicroscopic structure of the tectorial and basilar membranes.* The Journal of the Acoustical Society of America, 1962. **34**(9B): p. 1386-1395.

99. Davis, H., *Energy into nerve impulses: the inner ear.* Adv. Sci, 1953. **9**: p. 420-425.

100. Bodian, D., *Electron microscopic atlas of the simian cochlea.* Hearing research, 1983. **9**(2): p. 201-246.

101. Brownell, W. and W. Shehata, *The effect of cytoplasmic turgor pressure on the static and dynamic mechanical properties of outer hair cells*, in *The Mechanics and Biophysics of Hearing*1990, Springer. p. 52-60.

102. *Hair Cell.* http://livelovehear.tumblr.com/post/6855236397/dancinghaircell.

103. Moller, A., *Auditory physiology*1982: Elsevier.

104. Von Békésy, G. and E.G. Wever, *Experiments in hearing*. Vol. 8. 1960: McGraw-Hill New York.

105. Fletcher, H., *The mechanism of hearing as revealed through experiment on the masking effect of thermal noise.* Proceedings of the National Academy of Sciences of the United States of America, 1938. **24**(7): p. 265.

106. Lyon, R. and C. Mead, *Cochlear hydrodynamics demystified.* Caltech Computer Science Tech. Rept., Caltech-CS-TR-884, 1988.

107. Loh, C.H., *Multiple scale analysis of the spirally coiled cochlea.* The Journal of the Acoustical Society of America, 1983. **74**(1): p. 95-103.

108. Steele, C.R. and J.G. Zais, *Effect of coiling in a cochlear model.* The Journal of the Acoustical Society of America, 1985. **77**(5): p. 1849-1852.

109. Evans, B.N., R. Hallworth, and P. Dallos, *The nonlinearity of outer hair cell motility: Implications for cochlear physiology and pathology*, in *The Mechanics and Biophysics of Hearing*1990, Springer. p. 61-68.

110. Ashmore, J., *A fast motile response in guinea-pig outer hair cells: the cellular basis of the cochlear amplifier.* The Journal of Physiology, 1987. **388**(1): p. 323-347.

111. Brownell, W.E., et al., *Evoked mechanical responses of isolated cochlear outer hair cells.* Science, 1985. **227**(4683): p. 194-196.

112. Zurek, P. and W. Clark, *Narrow-band acoustic signals emitted by chinchilla ears after noise exposure.* The Journal of the Acoustical Society of America, 1981. **70**(2): p. 446-450.

113. Kemp, D.T., *Stimulated acoustic emissions from within the human auditory system.* The Journal of the Acoustical Society of America, 1978. **64**(5): p. 1386-1391.

114. Santos-Sacchi, J., *Fast outer hair cell motility: how fast is fast?*, in *The Mechanics and Biophysics of Hearing*1990, Springer. p. 69-75.

115. Hubbard, A.E. and D.C. Mountain, *Haircell forward and reverse transduction: Differential suppression and enhancement.* Hearing research, 1990. **43**(2): p. 269-272.

116. Steele, C., *A possibility for sub-tectorial membrane fluid motion.* Basic mechanisms in hearing, 1973: p. 69-93.

117. Taber, L.A. and C.R. Steele, *Cochlear model including three-dimensional fluid and four modes of partition flexibility.* The Journal of the Acoustical Society of America, 1981. **70**(2): p. 426-436.

118. Manley, G.A., *Cochlear mechanisms from a phylogenetic viewpoint.* Proceedings of the National Academy of Sciences, 2000. **97**(22): p. 11736-11743.

119. Hinchcliffe, R.H., *Scientific foundations of otolarynogology*. 1976.

120. West, C.D., *The relationship of the spiral turns of the cochlea and the length of the basilar membrane to the range of audible frequencies in ground dwelling mammals.* The Journal of the Acoustical Society of America, 1985. **77**(3): p. 1091-1101.

121. Cai, H., D. Manoussaki, and R. Chadwick, *Effects of coiling on the micromechanics of the mammalian cochlea.* Journal of the Royal Society Interface, 2005. **2**(4): p. 341-348.

122. Manoussaki, D., E. Dimitriadis, and R. Chadwick, *Cochlea's graded curvature effect on low frequency waves.* Physical Review Letters, 2006. **96**(8): p. 088701.

123. Rayleigh, J.W.S.B., *The theory of sound*. Vol. 2. 1896: Macmillan.

124. Manoussaki, D., et al., *The influence of cochlear shape on low-frequency hearing.* Proceedings of the National Academy of Sciences, 2008. **105**(16): p. 6162-6166.

125. Beeby, S.P., M.J. Tudor, and N.M. White, *Energy harvesting vibration sources for microsystems applications.* Measurement Science and Technology, 2006. **17**(12): p. R175.

126. Anton, S.R. and H.A. Sodano, *A review of power harvesting using piezoelectric materials (2003–2006).* Smart Materials and Structures, 2007. **16**(3): p. R1.

127. Priya, S., *Advances in energy harvesting using low profile piezoelectric transducers.* Journal of Electroceramics, 2007. **19**(1): p. 167-184.

128. Cook-Chennault, K.A., N. Thambi, and A.M. Sastry, *Powering MEMS portable devices—a review of non-regenerative and regenerative power supply systems with special emphasis on piezoelectric energy harvesting systems.* Smart Materials and Structures, 2008. **17**(4): p. 043001.

129. Cunefare, K.A., et al., *Energy harvesting from hydraulic pressure fluctuations.* Smart Materials and Structures, 2013. **22**(2): p. 025036.

130. Choi, W.J., et al., *Energy harvesting MEMS device based on thin film piezoelectric cantilevers.* Journal of Electroceramics, 2006. **17**(2-4): p. 543-548.

131. Zhuo, W. and Y. Xu, *Vibration energy harvesting device based on air-spaced piezoelectric cantilevers.* Applied Physics Letters, 2007. **90**(26): p. 263512-263512-3.

132. Shen, D., et al., *The design, fabrication and evaluation of a MEMS PZT cantilever with an integrated Si proof mass for vibration energy harvesting.* Journal of Micromechanics and Microengineering, 2008. **18**(5): p. 055017.

133. Erturk, A. and D.J. Inman, *An experimentally validated bimorph cantilever model for piezoelectric energy harvesting from base excitations.* Smart Materials and Structures, 2009. **18**(2): p. 025009.

134. Chen, Z., et al., *Broadband characteristics of vibration energy harvesting using one-dimensional phononic piezoelectric cantilever beams.* Physica B: Condensed Matter, 2013. **410**: p. 5-12.

135. Gonella, S., A.C. To, and W.K. Liu, *Interplay between phononic bandgaps and piezoelectric microstructures for energy harvesting.* Journal of the Mechanics and Physics of Solids, 2009. **57**(3): p. 621-633.

136. Ahmed, R. and S. Banerjee, *Predictive Electromechanical Model for Energy Scavengers using Patterned Piezoelectric Layers.* Journal of Engineering Mechanics, 2014. **(In press)**.

137. Banerjee, S., *Electromechanical Model for a plate type energy harvester using coupled strain rate damping mechanism.* JP Journal of Solids and Structures, 2011. **5**(2): p. 75 – 105.

138. Carrara, M., et al., *Metamaterial-inspired structures and concepts for elastoacoustic wave energy harvesting.* Smart Materials and Structures, 2013. **22**(6): p. 065004.

139. Chen, Z., et al., *Metamaterials-based enhanced energy harvesting: A review.* Physica B: Condensed Matter, 2014. **438**(0): p. 1-8.

140. Lv, H., et al., *Vibration energy harvesting using a phononic crystal with point defect states.* Applied Physics Letters, 2013. **102**(3): p. -.

141. Mikoshiba, K., J.M. Manimala, and C. Sun, *Energy harvesting using an array of multifunctional resonators.* Journal of Intelligent Material Systems and Structures, 2013. **24**(2): p. 168-179.

142. Wu, L.-Y., L.-W. Chen, and C.-M. Liu, *Acoustic energy harvesting using resonant cavity of a sonic crystal.* Applied Physics Letters, 2009. **95**(1): p. -.

143. Ahmed, R. and S. Banerjee, *Wave Propagation in Metamaterial Using Multiscale Resonators by Creating Local Anisotropy.* International Journal of Modern Engineering, 2013. **13**(2): p. 51-59.

144. Carrara, M., et al., *Dramatic enhancement of structure-borne wave energy harvesting using an elliptical acoustic mirror.* Applied Physics Letters, 2012. **100**(20): p. -.

145. Wu, L.-Y., L.-W. Chen, and C.-M. Liu, *Acoustic pressure in cavity of variously sized two-dimensional sonic crystals with various filling fractions.* Physics Letters A, 2009. **373**(12–13): p. 1189-1195.

146. Wu, L.-Y., L.-W. Chen, and C.-M. Liu, *Experimental investigation of the acoustic pressure in cavity of a two-dimensional sonic crystal.* Physica B: Condensed Matter, 2009. **404**(12–13): p. 1766-1770.

147. Yeh, J.-Y., *Application and analysis of phononic crystal energy harvesting devices.* 2013.

148. Huang, H., C. Sun, and G. Huang, *On the negative effective mass density in acoustic metamaterials.* International Journal of Engineering Science, 2009. **47**(4): p. 610-617.

149. Zhang, S. and J.H. Wu. *Low-Frequency Broadband Energy Harvesting Based on Locally Resonant Phononic Crystals*. in *ASME 2013 International Mechanical Engineering Congress and Exposition*. 2013. American Society of Mechanical Engineers.

150. Sheng, P., et al., *Locally resonant sonic materials.* Physica B: Condensed Matter, 2003. **338**(1–4): p. 201-205.

151. Priya, S. and D.J. Inman, *Energy Harvesting Technologies.* Springer, 2009. **ISBN: 978-0-387-76463-4.** .

152. *Noise Barrier*. http://en.wikipedia.org/wiki/Noise_barrier.

153. *Highway Traffic Noise.* https://www.fhwa.dot.gov/environment/noise/noise_barriers/design_construction/keepdown.cfm.

154. *International Energy Agency.* http://www.treehugger.com/corporate-responsibility/energy-usage-increases-despite-efficiency-efforts.html.

155. *Forbes.com.* http://www.forbes.com/sites/christopherhelman/2013/09/07/how-much-energy-does-your-iphone-and-other-devices-use-and-what-to-do-about-it/.

156. Mond, H.G., J.G. Sloman, and R.H. Edwards, *The First Pacemaker*. Pacing and Clinical Electrophysiology, 1982. **5**(2): p. 278-282.

157. Nelson, G.D., *A brief history of cardiac pacing.* Tex Heart Inst J, 1993. **20**(1): p. 12-8.

158. Mallela, V.S., V. Ilankumaran, and N.S. Rao, *Trends in cardiac pacemaker batteries.* Indian Pacing Electrophysiol J, 2004. **4**(4): p. 201-12.

159. Horlbeck, F.W., et al., *Real-World Data on the Lifespan of Implantable Cardioverter-Defibrillators Depending on Manufacturers and the Amount of Ventricular Pacing.* Journal of Cardiovascular Electrophysiology, 2012. **23**(12): p. 1336-1342.

160. Wilhelm, M.J.M.D., et al., *Cardiac Pacemaker Infection: Surgical Management With and Without Extracorporeal Circulation.* The Annals of Thoracic Surgery. **64**(6): p. 1707-1712.

161. Wang, Z.L., *Self-Powered Nanosensors and Nanosystems.* Advanced Materials, 2012. **24**(2): p. 280-285.

162. Park, K.-I., et al., *Flexible Nanocomposite Generator Made of BaTiO3 Nanoparticles and Graphitic Carbons.* Advanced Materials, 2012. **24**(22): p. 2999-3004.

163. Xu, S., et al., *Self-powered nanowire devices.* Nat Nano, 2010. **5**(5): p. 366-373.

164. Wang, L.C., *Changing patterns in intestinal parasitic infections among Southeast Asian laborers in Taiwan.* Parasitol Res, 2004. **92**(1): p. 18-21.

165. Dagdeviren, C., et al., *Transient, Biocompatible Electronics and Energy Harvesters Based on ZnO.* Small, 2013. **9**(20): p. 3398-3404.

166. Park, K.-I., et al., *Flexible and Large-Area Nanocomposite Generators Based on Lead Zirconate Titanate Particles and Carbon Nanotubes.* Advanced Energy Materials, 2013. **3**(12): p. 1539-1544.

167. Jeong, C.K., et al., *Virus-Directed Design of a Flexible BaTiO3 Nanogenerator.* ACS Nano, 2013. **7**(12): p. 11016-11025.

168. Romero, E., R.O. Warrington, and M.R. Neuman, *Energy scavenging sources for biomedical sensors.* Physiological Measurement, 2009. **30**(9): p. R35.

169. Franks, A.E. and K.P. Nevin, *Microbial Fuel Cells, A Current Review.* Energies, 2010. **3**(5): p. 899-919.

170. Potkay, J. and K. Brooks, *The 2nd International Conference on Bioinformatics and Biomedical Engineering, 2008.* ICBBE, 2008. **2008**: p. 1580.

171. Qi, Y., et al., *Piezoelectric Ribbons Printed onto Rubber for Flexible Energy Conversion.* Nano Letters, 2010. **10**(2): p. 524-528.

172. Wang, Z.L. and J. Song, *Piezoelectric Nanogenerators Based on Zinc Oxide Nanowire Arrays.* Science, 2006. **312**(5771): p. 242-246.

173. Hu, Y., et al., *Self-Powered System with Wireless Data Transmission.* Nano Letters, 2011. **11**(6): p. 2572-2577.

174. Hwang, G.-T., et al., *Self-Powered Cardiac Pacemaker Enabled by Flexible Single Crystalline PMN-PT Piezoelectric Energy Harvester.* Advanced Materials, 2014. **26**(28): p. 4880-4887.

175. Dagdeviren, C., et al., *Conformal piezoelectric energy harvesting and storage from motions of the heart, lung, and diaphragm.* Proceedings of the National Academy of Sciences, 2014. **111**(5): p. 1927-1932.

176. Amin Karami, M. and D.J. Inman, *Powering pacemakers from heartbeat vibrations using linear and nonlinear energy harvesters.* Applied Physics Letters, 2012. **100**(4): p. -.

177. Kanai, H., et al., *Transcutaneous measurement and spectrum analysis of heart wall vibrations.* Ultrasonics, Ferroelectrics, and Frequency Control, IEEE Transactions on, 1996. **43**(5): p. 791-810.

178. Ohm, O.L.E.J. and D. Danilovic, *Improvements in Pacemaker Energy Consumption and Functional Capability: Four Decades of Progress.* Pacing and Clinical Electrophysiology, 1997. **20**(1): p. 2-9.

179. *Aflatoxins in Food.* https://www.wellvet.com/cgi-bin/commerce.cgi?preadd=action&key=ART_AFLATOX.

180. *Mycotoxins.* http://blackmold.awardspace.com/mycotoxins.html.

181. *Mycotoxin.* http://en.wikipedia.org/wiki/Mycotoxin.

182. Bennett, J.W., *Mycotoxins, mycotoxicoses, mycotoxicology and Mycopathologia*: Mycopathologia. 1987 Oct;100(1):3-5.

183. Bennett, J.W. and M. Klich, *Mycotoxins.* Clinical Microbiology Reviews, 2003. **16**(3): p. 497-516.

184. *Mycotoxins in Crops: A Threat to Human and Domestic Animal Health.* http://www.apsnet.org/edcenter/intropp/topics/Mycotoxins/Pages/default.aspx.

185. *Mycotoxins.* http://blacktoxicmolds.com/mycotoxins-mold.php.

186. Bayman, P. and J. Baker, *Ochratoxins: A global perspective.* Mycopathologia, 2006. **162**(3): p. 215-223.

187. Mateo, R., et al., *An overview of ochratoxin A in beer and wine.* International Journal of Food Microbiology, 2007. **119**(1–2): p. 79-83.

188. Trucksess, M.W. and P.M. Scott, *Mycotoxins in botanicals and dried fruits: A review.* Food Additives & Contaminants: Part A, 2008. **25**(2): p. 181-192.

189. Moss, M.O., *Fungi, quality and safety issues in fresh fruits and vegetables.* Journal of Applied Microbiology, 2008. **104**(5): p. 1239-1243.

190. Cornely, O.A., *Aspergillus to Zygomycetes: Causes, Risk Factors, Prevention, and Treatment of Invasive Fungal Infections.* Infection, 2008. **36**(4): p. 296-313.

191. Schaafsma, A.W. and D.C. Hooker, *Climatic models to predict occurrence of Fusarium toxins in wheat and maize.* International Journal of Food Microbiology, 2007. **119**(1–2): p. 116-125.

192. Desjardins, A.E. and R.H. Proctor, *Molecular biology of Fusarium mycotoxins.* International Journal of Food Microbiology, 2007. **119**(1–2): p. 47-50.

193. Krska, R., S. Baumgartner, and R. Josephs, *The state-of-the-art in the analysis of type-A and -B trichothecene mycotoxins in cereals.* Fresenius J Anal Chem, 2001. **371**(3): p. 285-99.

194. Krska, R., et al., *Advances in the analysis of mycotoxins and its quality assurance.* Food Addit Contam, 2005. **22**(4): p. 345-53.

195. Krska, R. and R. Josephs, *The state-of-the-art in the analysis of estrogenic mycotoxins in cereals.* Fresenius' Journal of Analytical Chemistry, 2001. **369**(6): p. 469-476.

196. Gilbert, J. and E. Anklam, *Validation of analytical methods for determining mycotoxins in foodstuffs.* TrAC Trends in Analytical Chemistry, 2002. **21**(6–7): p. 468-486.

197. Berthiller, F., et al., *Masked mycotoxins: determination of a deoxynivalenol glucoside in artificially and naturally contaminated wheat by liquid chromatography-tandem mass spectrometry.* J Agric Food Chem, 2005. **53**(9): p. 3421-5.

198. Zöllner, P. and B. Mayer-Helm, *Trace mycotoxin analysis in complex biological and food matrices by liquid chromatography–atmospheric pressure ionisation mass spectrometry.* Journal of Chromatography A, 2006. **1136**(2): p. 123-169.

199. Sforza, S., C. Dall'Asta, and R. Marchelli, *Recent advances in mycotoxin determination in food and feed by hyphenated chromatographic techniques/mass spectrometry.* Mass Spectrometry Reviews, 2006. **25**(1): p. 54-76.

200. Creppy, E.E., et al., *Synergistic effects of fumonisin B1 and ochratoxin A: are in vitro cytotoxicity data predictive of in vivo acute toxicity?* Toxicology, 2004. **201**(1–3): p. 115-123.

201. Speijers, G.J. and M.H. Speijers, *Combined toxic effects of mycotoxins.* Toxicol Lett, 2004. **153**(1): p. 91-8.

202. Smedsgaard, J. and J.C. Frisvad, *Using direct electrospray mass spectrometry in taxonomy and secondary metabolite profiling of crude fungal extracts.* Journal of Microbiological Methods, 1996. **25**(1): p. 5-17.

203. Nielsen, K.F. and J. Smedsgaard, *Fungal metabolite screening: database of 474 mycotoxins and fungal metabolites for dereplication by standardised liquid chromatography–UV–mass spectrometry methodology.* Journal of Chromatography A, 2003. **1002**(1–2): p. 111-136.

204. Tuomi, T., et al., *Detection of aflatoxins (G, B), sterigmatocystin, citrinine and ochratoxin A in samples contaminated by microbes.* Analyst, 2001. **126**(9): p. 1545-1550.

205. Rundberget, T. and A.L. Wilkins, *Determination of Penicillium mycotoxins in foods and feeds using liquid chromatography–mass spectrometry.* Journal of Chromatography A, 2002. **964**(1–2): p. 189-197.

206. Kokkonen, M., M. Jestoi, and A. Rizzo, *Determination of selected mycotoxins in mould cheeses with liquid chromatography coupled to tandem with mass spectrometry.* Food Addit Contam, 2005. **22**(5): p. 449-56.

207. Royer, D., H.U. Humpf, and P.A. Guy, *Quantitative analysis of Fusarium mycotoxins in maize using accelerated solvent extraction before liquid chromatography/atmospheric pressure chemical ionization tandem mass spectrometry.* Food Addit Contam, 2004. **21**(7): p. 678-92.

208. Biselli, S. and C. Hummert, *Development of a multicomponent method for Fusarium toxins using LC-MS/MS and its application during a survey for the content of T-2 toxin and deoxynivalenol in various feed and food samples.* Food Addit Contam, 2005. **22**(8): p. 752-60.

209. Cavaliere, C., et al., *Development of a multiresidue method for analysis of major Fusarium mycotoxins in corn meal using liquid chromatography/tandem mass spectrometry.* Rapid Communications in Mass Spectrometry, 2005. **19**(14): p. 2085-2093.

210. Sorensen, L.K. and T.H. Elbaek, *Determination of mycotoxins in bovine milk by liquid chromatography tandem mass spectrometry.* J Chromatogr B Analyt Technol Biomed Life Sci, 2005. **820**(2): p. 183-96.

211. Tanaka, H., et al., *Development of a liquid chromatography/time-of-flight mass spectrometric method for the simultaneous determination of trichothecenes, zearalenone and aflatoxins in foodstuffs.* Rapid Communications in Mass Spectrometry, 2006. **20**(9): p. 1422-1428.

212. Ren, Y., et al., *Simultaneous determination of multi-component mycotoxin contaminants in foods and feeds by ultra-performance liquid chromatography tandem mass spectrometry.* Journal of Chromatography A, 2007. **1143**(1–2): p. 48-64.

213. Spanjer, M.C., P.M. Rensen, and J.M. Scholten, *LC-MS/MS multi-method for mycotoxins after single extraction, with validation data for peanut, pistachio, wheat, maize, cornflakes, raisins and figs.* Food Addit Contam Part A Chem Anal Control Expo Risk Assess, 2008. **25**(4): p. 472-89.

214. Sulyok, M., et al., *Development and validation of a liquid chromatography/tandem mass spectrometric method for the determination of 39 mycotoxins in wheat and maize.* Rapid Commun Mass Spectrom, 2006. **20**(18): p. 2649-59.

215. Sulyok, M., R. Krska, and R. Schuhmacher, *A liquid chromatography/tandem mass spectrometric multi-mycotoxin method for the quantification of 87 analytes and its application to semi-quantitative screening of moldy food samples.* Analytical and Bioanalytical Chemistry, 2007. **389**(5): p. 1505-1523.

216. Fremy, J.M. and E. Usleber, *Policy on characterization of antibodies used in immunochemical methods of analysis for mycotoxins and phycotoxins.* J AOAC Int, 2003. **86**(4): p. 868-71.

217. Ngundi, M.M., et al., *Array biosensor for detection of ochratoxin A in cereals and beverages.* Anal Chem, 2005. **77**(1): p. 148-54.

218. Tüdös, A.J., E.R. Lucas-van den Bos, and E.C.A. Stigter, *Rapid Surface Plasmon Resonance-Based Inhibition Assay of Deoxynivalenol.* Journal of Agricultural and Food Chemistry, 2003. **51**(20): p. 5843-5848.

219. Maragos, C.M., *Emerging technologies for mycotoxin detection.* Toxin Reviews, 2004. **23**(2-3): p. 317-344.

220. Sapsford, K.E., et al., *Rapid detection of foodborne contaminants using an Array Biosensor.* Sensors and Actuators B: Chemical, 2006. **113**(2): p. 599-607.

221. Urraca, J.L., et al., *Analysis of Zearalenone in Cereal and Swine Feed Samples Using an Automated Flow-Through Immunosensor.* Journal of Agricultural and Food Chemistry, 2005. **53**(9): p. 3338-3344.

222. Micheli, L., et al., *An electrochemical immunosensor for aflatoxin M1 determination in milk using screen-printed electrodes.* Biosensors and Bioelectronics, 2005. **21**(4): p. 588-596.

223. Pemberton, R.M., et al., *Studies Towards the Development of a Screen-Printed Carbon Electrochemical Immunosensor Array for Mycotoxins: A Sensor for Aflatoxin B1.* Analytical Letters, 2006. **39**(8): p. 1573-1586.

224. van der Gaag, B., et al., *Biosensors and multiple mycotoxin analysis.* Food Control, 2003. **14**(4): p. 251-254.

225. Adányi, N., et al., *Development of immunosensor based on OWLS technique for determining Aflatoxin B1 and Ochratoxin A.* Biosensors and Bioelectronics, 2007. **22**(6): p. 797-802.

226. Kristensen, R., et al., *DNA microarray to detect and identify trichothecene- and moniliformin-producing Fusarium species.* Journal of Applied Microbiology, 2007. **102**(4): p. 1060-1070.

227. Sibanda, L., et al., *Development of a solid-phase cleanup and portable rapid flow-through enzyme immunoassay for the detection of ochratoxin A in roasted coffee.* Journal of Agricultural and Food Chemistry, 2002. **50**(24): p. 6964-6967.

228. Delmulle, B.S., et al., *Development of an Immunoassay-Based Lateral Flow Dipstick for the Rapid Detection of Aflatoxin B1 in Pig Feed.* Journal of Agricultural and Food Chemistry, 2005. **53**(9): p. 3364-3368.

229. Wang, S., et al., *Rapid Determination of Fumonisin B1 in Food Samples by Enzyme-Linked Immunosorbent Assay and Colloidal Gold Immunoassay.* Journal of Agricultural and Food Chemistry, 2006. **54**(7): p. 2491-2495.

230. Kos, G., H. Lohninger, and R. Krska, *Development of a Method for the Determination of Fusarium Fungi on Corn Using Mid-Infrared Spectroscopy with Attenuated Total Reflection and Chemometrics.* Analytical Chemistry, 2003. **75**(5): p. 1211-1217.

231. Pettersson, H. and L. Åberg, *Near infrared spectroscopy for determination of mycotoxins in cereals.* Food Control, 2003. **14**(4): p. 229-232.

232. Logrieco, A., et al., *DNA arrays, electronic noses and tongues, biosensors and receptors for rapid detection of toxigenic fungi and mycotoxins: a review.* Food Addit Contam, 2005. **22**(4): p. 335-44.

233. Olsson, J., et al., *Detection and quantification of ochratoxin A and deoxynivalenol in barley grains by GC-MS and electronic nose.* International Journal of Food Microbiology, 2002. **72**(3): p. 203-214.

234. *ABC's of Photoacoustic Spectroscopy.* http://www.shimadzu.com/an/ftir/support/ftirtalk/talk7/intro.html.

235. Gordon, S., et al., *Identification of Fourier transform infrared photoacoustic spectral features for detection of< i> Aspergillus flavus</i> infection in corn.* International Journal of Food Microbiology, 1997. **35**(2): p. 179-186.

236. Greene, R.V., et al., *Detection of fungal contamination in corn: potential of FTIR-PAS and-DRS.* Journal of Agricultural and Food Chemistry, 1992. **40**(7): p. 1144-1149.

237. Giurgiutiu, V., *Lamb Wave Generation with Piezoelectric Wafer Active Sensors for Structural Health Monitoring.* SPIE's 10th Annual International Symposium on Smart Structures and Materials and 8th Annual International Symposium on NDE for Health Monitoring and Diagnostics, San Diego, CA, 2002.

238. Giurgiutiu, V., A. Zagrai, and J. Jing Bao, *Piezoelectric Wafer Embedded Active Sensors for Aging Aircraft Structural Health Monitoring.* Structural Health Monitoring, 2002. **1**(1): p. 41-61.

239. Anton, S.R. and H.A. Sodano, *A review of power harvesting using piezoelectric materials (2003–2006).* Smart Mater. Struct. , 2007. **16 R1–21**.

240. Arnold, D.P., *Review of Microscale Magnetic Power Generation.* Magnetics, IEEE Transactions on, 2007. **43**(11): p. 3940-3951.

241. Beeby, S.P., M.J. Tudor, and N.M. White, *Energy harvesting vibration sources for microsystems applications.* Measurement Science and Technology, 2006. **17 R175**.

242. Cook-Chennault, K.A., N. Thambi, and A.M. Sastry, *Powering MEMS portable devices—a review of non-regenerative and regenerative power supply systems with emphasis on piezoelectric energy harvesting systems.* Smart Mater. Struct. , 2008. **17 043001**.

243. Dutoit, N.E., B.L. Wardle, and S.-G. Kim, *DESIGN CONSIDERATIONS FOR MEMS-SCALE PIEZOELECTRIC MECHANICAL VIBRATION ENERGY HARVESTERS.* Integrated Ferroelectrics, 2005. **71**(1): p. 121-160.

244. Erturk, A. and D.J. Inman, *On Mechanical Modeling of Cantilevered Piezoelectric Vibration Energy Harvesters.* Journal of Intelligent Material Systems and Structures, 2008. **19**(11): p. 1311-1325.

245. Glynne-Jones, P., et al., *An electromagnetic, vibration-powered generator for intelligent sensor systems.* Sensors and Actuators A: Physical, 2004. **110**(1–3): p. 344-349.

246. Guyomar, D., et al., *Toward energy harvesting using active materials and conversion improvement by nonlinear processing.* Ultrasonics, Ferroelectrics and Frequency Control, IEEE Transactions on, 2005. **52**(4): p. 584-595.

247. Guan, M.J. and W.H. Liao, *On the efficiencies of piezoelectric energy harvesting circuits towards storage device voltages.* Smart Mater. Struct. , 2007. **16** p. 498–505.

248. Ottman, G.K., et al., *Adaptive piezoelectric energy harvesting circuit for wireless remote power supply.* Power Electronics, IEEE Transactions on, 2002. **17**(5): p. 669-676.

249. Piguet, C., *Low Power Electronics Design.* CRC Press, New York, 2005.

250. Shu, Y.C. and I.C. Lien, *Analysis of power output for piezoelectric energy harvesting systems.* Smart Mater. Struct. , 2006. **15**: p. 1499.

251. Shu, Y.C., I.C. Lien, and W.J. Wu, *An improved analysis of the SSHI interface in piezoelectric energy harvesting.* Smart Mater. Struct. , 2007. **16** p. 2253–64.

252. Stephen, N.G., *On energy harvesting from ambient vibration.* Journal of Sound and Vibration, 2006. **293**(1–2): p. 409-425.

253. Hall, A.J. and J.C. Riddick. *Micro-electro-mechanical flapping wing technology for micro air vehicles*. 2012.

254. Riddick, J.C. and A. Hall. *Functionally modified bimorph PZT actuator for cm-scale flapping wing*. 2011.

255. Belloli, A. and P. Ermanni, *Optimum placement of piezoelectric ceramic modules for vibration suppression of highly constrained structures.* Smart Materials and Structures, 2007. **16**(5): p. 1662–1671.

256. Frecker, M.A., *Recent optimization of smart structures and actuators.* Journal of Intelligent Material Systems and Structures, 2003. **14**(4-5): p. 207–216.

257. Friswell, M.I. and S. Adhikari, *Sensor shape design for piezoelectric cantilever beams to harvest vibration energy.* Journal of Applied Physics, 2010. **108**(1): p. -.

258. Rosi, G., et al., *Optimization of piezoelectric patch positioning for passive sound radiation control of plates.* Journal of Vibration and Control, 2012.

259. Halim, D. and S.O. Reza Moheimani, *An optimization approach to optimal placement of collocated piezoelectric actuators and sensors on a thin plate.* Mechatronics, 2003. **13**(1): p. 27-47.

260. Osher, S. and J.A. Sethian, *Fronts propagating with curvature-dependent speed: Algorithms based on Hamilton-Jacobi formulations.* Journal of Computational Physics, 1988. **79**(1): p. 12-49.

261. Zhang, J., *Level set method for shape optimization of plate piezoelectric patches.* Methods and applications of analysis, 2003. **10**(2): p. 329–346.

262. Narwal, K. and D. Chhabra, *Analysis of simple supported plate for active vibration control with piezoelectric sensors and actuators* IOSR Journal of Mechanical and Civil Engineering, 2278-1684 2012. **1**(1): p. 26-39.

263. Ansari, M., A. Khajepour, and E. Esmailzadeh, *Application of level set method to optimal vibration control of plate structures.* Journal of Sound and Vibration, 2013. **332**(4): p. 687-700.

264. Lam, M.J., D.J. Inman, and W. Saunders, *Vibration control through passive constrained layer damping and active control.* Journal of Intelligent Material Systems and Structures, 1997. **3045**: p. 60–69.

265. Alessandroni, S., et al., *A passive electric controller for multimodal vibrations of thin plates.* Computers & Structures, 2005. **83**(15–16): p. 1236-1250.

266. Ozer, M.B. and T.J. Royston, *Passively minimizing structural sound radiation using shunted piezoelectric materials.* J Acoust Soc Am, 2003. **114**(4 Pt 1): p. 1934-46.

267. Ducarne, J., O. Thomas, and J.F. Deü, *Placement and dimension optimization of shunted piezoelectric patches for vibration reduction.* Journal of Sound and Vibration, 2012. **331**(14): p. 3286-3303.

268. Navier, C.L.M.H., *Extrait des recherches sur la flexion des plans elastiques, (Selected researches on bending of elastic plates).* Bull. Sci. Soc. Philomarhique de Paris, 1823. **5**: p. 95–102.

269. Timoshenko, S.P. and S. Woinowsky-Krieger, *Theory of Plates and Shells.* McGraw –Hill International Edition, 1959. **Second Edition**.

270. Wu, J.H., H.L. Chen, and A.Q. Liu, *Exact Solutions for Free-Vibration Analysis of Rectangular Plates Using Bessel Functions.* Journal of Applied Mechanics, 2005. **74**(6): p. 1247-1251.

271. Brownell, W., et al., *Evoked mechanical responses of isolated cochlear outer hair cells.* Science, 1985. **227**(4683): p. 194-196.

272. de Espinosa, F.M., E. Jimenez, and M. Torres, *Ultrasonic band gap in a periodic two-dimensional composite.* Physical Review Letters, 1998. **80**(6): p. 1208.

273. Li, X. and Z. Liu, *Coupling of cavity modes and guiding modes in two-dimensional phononic crystals.* Solid state communications, 2005. **133**(6): p. 397-402.

274. Poulton, C., et al. *Eigenvalue problems for doubly periodic elastic structures and phononic band gaps*. in *Proceedings of the Royal Society of London A: Mathematical, Physical and Engineering Sciences*. 2000. The Royal Society.

275. Xu, Y., C. Chen, and X. Tian, *Phonon-polariton and band structure of electro-magneto-acoustic SH wave propagation oblique to the periodic layered piezoelectric structures.* Physics Letters A, 2013. **377**(12): p. 895-902.

276. Li, J. and C. Chan, *Double-negative acoustic metamaterial.* Physical Review E, 2004. **70**(5): p. 055602.

277. Yao, S., X. Zhou, and G. Hu, *Experimental study on negative effective mass in a 1D mass–spring system.* New Journal of Physics, 2008. **10**(4): p. 043020.

278. Hirsekorn, M., et al., *Modelling and simulation of acoustic wave propagation in locally resonant sonic materials.* Ultrasonics, 2004. **42**(1): p. 231-235.

279. Hsu, J.-C., *Local resonances-induced low-frequency band gaps in two-dimensional phononic crystal slabs with periodic stepped resonators.* Journal of Physics D: Applied Physics, 2011. **44**(5): p. 055401.

280. Caballero, D., et al., *Large two-dimensional sonic band gaps.* Physical Review E, 1999. **60**(6): p. R6316.

281. Liu, Z., C. Chan, and P. Sheng, *Analytic model of phononic crystals with local resonances.* Physical Review B, 2005. **71**(1): p. 014103.

282. Mainzer, K., *Symmetries of Nature: a handbook for philosophy of nature and science*1996: Walter de Gruyter.

283. Nemer, S., et al., *Modelling resonance frequencies of a multi-turn spiral for metamaterial applications.* Progress In Electromagnetics Research C, 2011. **20**: p. 31-42.

284. Baena, J.D., et al., *Artificial magnetic metamaterial design by using spiral resonators.* Physical Review B, 2004. **69**(1): p. 014402.

285. He, M., et al., *Negative refractive index in chiral spiral metamaterials at terahertz frequencies.* Optik-International Journal for Light and Electron Optics, 2011. **122**(18): p. 1676-1679.

286. Elford, D.P., et al., *Acoustic band gap formation in metamaterials.* International Journal of Modern Physics B, 2010. **24**(25n26): p. 4935-4945.

# APPENDIX A: MATLAB CODE FOR BM PLATE MODEL

```
%%%%%%%%%%%%%%%%%%%%%%%%%%%%%%%%%%%%%%%%%%%
%%%%%%%% Predictive model for Basilar Membrane Plate Model%%%%%%%%%%

%%%%%%%%%%%%%%%%%%%%%%%%%%%%%%%%%%%%%%%%%%%



%%% This code possess the flexibility to alter model parameters, such as

%%% (model parameters can be defined as constant value or functional form)

%%%

%%% (1) Length [constant]

%%% (2) Width (Base width, Apex width) [constant]

%%% (3) Thicknessconstant/functional]

%%% (4) Stiffness [constant/functional]

%%% (5) Poissons Ratio [constant/functional]

%%% (6) Density [constant/functional]

%%% (7) Boundary condition [fixed/simply supported].

%%%

%%% Among four (4) boundaries of the model, 'Right' boundary always

%%% considered free, whereas other three (3) boundaries can be either

%%% 'Fixed' or 'Simply supported'. To change the boundary condition,

%%% uncommand equation for target bounday condition and command another.
```

```
clc
clear all

syms x;
syms y;

%% Defining Model Parameters

% E=8.963e6*(1+14.28571429*x);        % Functional stiffness
E=8.963e6;              % Fixed stiffness

% nu=0.48*(1-9.52380952380952*x);              % Functional poissons ratio
nu=0.48;                  % Fixed poissons ratio

% rho=1130*(1+14.28571429*x);         % Density of the model
rho=1130;                 % Density of the model

t=0.1e-3*(1+14.28571429*x);              % Functional thickness
% t=0.1e-3;                  % Fixed thickness

D=(E*t^3)/(12*(1-nu^2));
F=1e3;                    % Total vertical load
```

```
f=4500:10:5500;      % Frequency band
% f=1800;                % Frequency
omg=2*pi*f;
length=35e-3;              % Length of the model
wb=1e-3;                   % Base width of plate
wa=2e-3;                   % Apex width of plate

seg_x=200;                 % Finite difference segment along length (always even)
seg_y=10;                  % Finite difference segment along width (always even)

RowNum=seg_y-1;            % Node number along width
ColNum=seg_x;              % Node number along length
m=RowNum*ColNum;           % Total number of nodes
%% Calculation of distance between node points.
% "del_x" is constant, however "del_y" is varying over the length
for i=1:ColNum+3
   DyDecrement=(wb-wa)/ColNum;
   width(i)=wb-(i-1)*DyDecrement;
   dy(i)=width(i)/seg_y;
end

for i=1:RowNum
   for j=1:ColNum
```

```
        del_y((i-1)*ColNum+j)=dy(j+1);
    end
end

del_y_L1=dy(ColNum+2);  % del_y at fictitious line 1 on right boundary of the model
del_y_L2=dy(ColNum+3);  % del_y at fictitious line 2 on right boundary of the model

del_x=length/seg_x;

%% Pressure per unit area of the plate
for i=1:m
    p(i)=F/(del_x*del_y(i));     % pressure/area
end

%% Finding node cordinates

for i=1:ColNum+1
    xx(i)=(i-1)*del_x;
    for j=1:RowNum+2
        x_cord(j,i)=xx(i);    % x-coordinates of node points
    end
end
```

```
WidthDec=((wb/2)-(wa/2))/seg_x;   % Linear width decrement along length of the model

for i=1:seg_x+1
   y2(i)=-WidthDec*(i-1);
   for j=1:seg_y+1
      y1(j,i)=y2(i)-dy(i)*(j-1);

   end
end

for i=1:seg_x+1
   for j=1:seg_y+1
      y_cord(j,i)=y1(j,i)-y1((seg_y/2)+1,i);  % y-coordinates of the node points
   end
end

for i=1:RowNum
   for j=1:ColNum
      x_v(j+(i-1)*ColNum,1)=x_cord(i+1,j+1);  % x-coordinates in vector
      y_v(j+(i-1)*ColNum,1)=y_cord(i+1,j+1);  % y-coordinates in vector
   end
end
```

```
for i=1:m
   for j=1:m
      x_vec(i,j)=x_v(i);
      y_vec(i,j)=y_v(i);

   end
end

%% Angle calculation

for i=1:RowNum
   theta1(i)=atand((y_cord(i+1,ColNum)-y_cord(i+1,1))/(x_cord(i+1,ColNum)-
x_cord(i+1,1)));
   for j=1:ColNum
      theta(i,j)=theta1(i);
   end
end

for i=1:RowNum
   for j=1:ColNum
      CosT(i,j)=cosd(theta(i,j));          % Cos Theta
      SinT(i,j)=sind(theta(i,j));          % Sin Theta
   end
end
```

```
CoT=reshape(CosT',m,1);
SiT=reshape(SinT',m,1);

for j=1:m
   for i=1:m
      CT(i,j)=CoT(j);
      ST(i,j)=SiT(j);
   end
end

%% Calculating derivative terms related to model parameters
D_dx=diff(D,x);
D_dx2=diff(D_dx,x);

D_dy=diff(D,y);
D_dy2=diff(D_dy,y);

D_dxdy=diff(D_dx,y);

nu_dx=diff(nu,x);
nu_dx2=diff(nu_dx,x);
```

```
nu_dy=diff(nu,y);

nu_dy2=diff(nu_dy,y);


nu_dxdy=diff(nu_dx,y);


%%%%%% subs

t_1=double(subs(t,{x,y},{x_v,y_v}));

rho_1=double(subs(rho,{x,y},{x_v,y_v}));


D_1=double(subs(D,{x,y},{x_v,y_v}));

D_dx_1=double(subs(D_dx,{x,y},{x_v,y_v}));

D_dx2_1=double(subs(D_dx2,{x,y},{x_v,y_v}));

D_dy_1=double(subs(D_dy,{x,y},{x_v,y_v}));

D_dy2_1=double(subs(D_dy2,{x,y},{x_v,y_v}));

D_dxdy_1=double(subs(D_dxdy,{x,y},{x_v,y_v}));


nu_1=double(subs(nu,{x,y},{x_v,y_v}));

nu_dx_1=double(subs(nu_dx,{x,y},{x_v,y_v}));

nu_dx2_1=double(subs(nu_dx2,{x,y},{x_v,y_v}));

nu_dy_1=double(subs(nu_dy,{x,y},{x_v,y_v}));

nu_dy2_1=double(subs(nu_dy2,{x,y},{x_v,y_v}));

nu_dxdy_1=double(subs(nu_dxdy,{x,y},{x_v,y_v}));
```

```
for i=1:m
   for j=1:m
      t_2(i,j)=t_1(i);
      rho_2(i,j)=rho_1(i);

      D_2(i,j)=D_1(i);
      D_dx_2(i,j)=D_dx_1(i);
      D_dx2_2(i,j)=D_dx2_1(i);
      D_dy_2(i,j)=D_dy_1(i);
      D_dy2_2(i,j)=D_dy2_1(i);
      D_dxdy_2(i,j)=D_dxdy_1(i);

      nu_2(i,j)=nu_1(i);
      nu_dx_2(i,j)=nu_dx_1(i);
      nu_dx2_2(i,j)=nu_dx2_1(i);
      nu_dy_2(i,j)=nu_dy_1(i);
      nu_dy2_2(i,j)=nu_dy2_1(i);
      nu_dxdy_2(i,j)=nu_dxdy_1(i);
   end
end

%% Calculating coefficients for fictitious node points on free end
```

```
for i=1:ColNum+1
   alpha(i)=(del_x^2)/(dy(i+1).^2);
end

%%%%%% Line 1 dummy node coefficients

L1_C1=zeros(RowNum,m);    % 1st Coefficient of Line 1
L1_C2=zeros(RowNum,m);    % 2nd Coefficient of Line 1
L1_C3=zeros(RowNum,m);    % 3rd Coefficient of Line 1
L1_C4=zeros(RowNum,m);    % 4th Coefficient of Line 1

for i=1:RowNum;
   if i==1
      L1_C1(i,ColNum*i)=2+2*nu_2(ColNum,1)*alpha(ColNum);
      L1_C2(i,ColNum*i-1)=-1;
      L1_C4(i,ColNum*(i+1))=-nu_2(ColNum,1)*alpha(ColNum);
   elseif i==RowNum
      L1_C1(i,ColNum*i)=2+2*nu_2(ColNum,1)*alpha(ColNum);
      L1_C2(i,ColNum*i-1)=-1;
      L1_C3(i,ColNum*(i-1))=-nu_2(ColNum,1)*alpha(ColNum);
   else
      L1_C1(i,ColNum*i)=2+2*nu_2(ColNum,1)*alpha(ColNum);
      L1_C2(i,ColNum*i-1)=-1;
```

```
        L1_C3(i,ColNum*(i-1))=-nu_2(ColNum,1)*alpha(ColNum);

        L1_C4(i,ColNum*(i+1))=-nu_2(ColNum,1)*alpha(ColNum);

    end

end

L1=L1_C1+L1_C2+L1_C3+L1_C4;    % Line 1 coefficient matrix. Each row represents coefficients for a particular node


%%%%%% Calculating coefficients for additional Line 1 dummy nodes

L1_top=zeros(1,m);

L1_bottom=zeros(1,m);

L2_top=zeros(1,m);

L2_bottom=zeros(1,m);


% L1_top(:,ColNum)=0;                    %%% for simply supported top boundary

L1_top(:,ColNum)=-2*nu_2(ColNum,1)*alpha(ColNum);  %%% for fixed supported top boundary


% L1_bottom(:,m)=0;                    %%% for simply supported bottom boundary

L1_bottom(:,m)=-2*nu_2(ColNum,1)*alpha(ColNum);        %%% for fixed supported bottom boundary


% L2_top(:,ColNum)=0;                    %%% for simply supported top boundary

L2_top(:,ColNum)=-(4*nu_2(ColNum,1)*alpha(ColNum)...

    +8*nu_2(ColNum,1)*(2-nu_2(ColNum,1))*alpha(ColNum+1)*alpha(ColNum)...
```

```
   +4*(2-nu_2(ColNum,1))*alpha(ColNum+1));          %%% for fixed supported top boundary

L2_top(:,ColNum-1)=2*(2-nu_2(ColNum,1))*alpha(ColNum-1)...

   +2*(2-nu_2(ColNum,1))*alpha(ColNum+1);          %%% for fixed supported top boundary

L2_top(:,ColNum+ColNum)=2*nu_2(ColNum,1)*(2-nu_2(ColNum,1))...

   *alpha(ColNum+1)*alpha(ColNum);          %%% for fixed supported top boundary


% L2_bottom(:,m)=0;                    %%% for simply supported bottom boundary

L2_bottom(:,m)=-(4*nu_2(ColNum,1)*alpha(ColNum)...

   +8*nu_2(ColNum,1)*(2-nu_2(ColNum,1))*alpha(ColNum+1)*alpha(ColNum)...

   +4*(2-nu_2(ColNum,1))*alpha(ColNum+1));          %%% for fixed supported top boundary

L2_bottom(:,m-1)=2*(2-nu_2(ColNum,1))*alpha(ColNum-1)...

   +2*(2-nu_2(ColNum,1))*alpha(ColNum+1);          %%% for fixed supported top boundary

L2_bottom(:,m-ColNum)=2*nu_2(ColNum,1)*(2-nu_2(ColNum,1))...

   *alpha(ColNum+1)*alpha(ColNum);          %%% for fixed supported top boundary


%%%%%% Line 2 dummy node coefficients


L2_C1=zeros(RowNum,m);    % 1st Coefficient of Line 2

L2_C2=zeros(RowNum,m);    % 2nd Coefficient of Line 2

L2_C3=zeros(RowNum,m);    % 3rd Coefficient of Line 2

L2_C4=zeros(RowNum,m);    % 4th Coefficient of Line 2
```

```
L2_C5=zeros(RowNum,m);    % 5th Coefficient of Line 2

L2_C6=zeros(RowNum,m);    % 6th Coefficient of Line 2

L2_C7=zeros(RowNum,m);    % 7th Coefficient of Line 2

L2_C8=zeros(RowNum,m);    % 8th Coefficient of Line 2

L2_C9=zeros(RowNum,m);    % 9th Coefficient of Line 2


for i=1:RowNum;

   if i==1

%                                                    L2_C1(i,ColNum*i)=4+4*(2-
nu_2(ColNum,1))*alpha(ColNum+1)+4*nu_2(ColNum,1)*alpha(ColNum)...

%          +3*nu_2(ColNum,1)*(2-nu_2(ColNum,1))*alpha(ColNum)*alpha(ColNum+1);
%%% for simply supported top boundary

      L2_C1(i,ColNum*i)=4+4*(2-
nu_2(ColNum,1))*alpha(ColNum+1)+4*nu_2(ColNum,1)*alpha(ColNum)...

         +7*nu_2(ColNum,1)*(2-nu_2(ColNum,1))*alpha(ColNum)*alpha(ColNum+1);
%%% for fixed supported top boundary

      L2_C2(i,ColNum*i-1)=-(4+2*(2-nu_2(ColNum,1))*alpha(ColNum-1)...

         +2*(2-nu_2(ColNum,1))*alpha(ColNum+1));

      L2_C3(i,ColNum*i-2)=1;

      L2_C6(i,ColNum*(i+1))=-
(2*nu_2(ColNum,1)*alpha(ColNum)+4*nu_2(ColNum,1)*(2-nu_2(ColNum,1))...

         *alpha(ColNum)*alpha(ColNum+1)+2*(2-nu_2(ColNum,1))*alpha(ColNum+1));

      L2_C7(i,ColNum*(i+1)-1)=(2-nu_2(ColNum,1))*alpha(ColNum-1)+(2-
nu_2(ColNum,1))*alpha(ColNum+1);

      L2_C9(i,ColNum*(i+2))=nu_2(ColNum,1)*(2-
nu_2(ColNum,1))*alpha(ColNum)*alpha(ColNum+1);

   elseif i==2 && RowNum>=4
```

```
        L2_C1(i,ColNum*i)=4+4*(2-
nu_2(ColNum,1))*alpha(ColNum+1)+4*nu_2(ColNum,1)*alpha(ColNum)...

            +6*nu_2(ColNum,1)*(2-nu_2(ColNum,1))*alpha(ColNum)*alpha(ColNum+1);

        L2_C2(i,ColNum*i-1)=-(4+2*(2-nu_2(ColNum,1))*alpha(ColNum-1)...

            +2*(2-nu_2(ColNum,1))*alpha(ColNum+1));

        L2_C3(i,ColNum*i-2)=1;

        L2_C4(i,ColNum*(i-1))=-
(2*nu_2(ColNum,1)*alpha(ColNum)+4*nu_2(ColNum,1)*(2-nu_2(ColNum,1))...

            *alpha(ColNum)*alpha(ColNum+1)+2*(2-nu_2(ColNum,1))*alpha(ColNum+1));

        L2_C5(i,ColNum*(i-1)-1)=(2-nu_2(ColNum,1))*alpha(ColNum-1)+(2-
nu_2(ColNum,1))*alpha(ColNum+1);

        L2_C6(i,ColNum*(i+1))=-
(2*nu_2(ColNum,1)*alpha(ColNum)+4*nu_2(ColNum,1)*(2-nu_2(ColNum,1))...

            *alpha(ColNum)*alpha(ColNum+1)+2*(2-nu_2(ColNum,1))*alpha(ColNum+1));

        L2_C7(i,ColNum*(i+1)-1)=(2-nu_2(ColNum,1))*alpha(ColNum-1)+(2-
nu_2(ColNum,1))*alpha(ColNum+1);

        L2_C9(i,ColNum*(i+2))=nu_2(ColNum,1)*(2-
nu_2(ColNum,1))*alpha(ColNum)*alpha(ColNum+1);

    elseif i==2 && RowNum<4

        L2_C1(i,ColNum*i)=4+4*(2-
nu_2(ColNum,1))*alpha(ColNum+1)+4*nu_2(ColNum,1)*alpha(ColNum)...

            +6*nu_2(ColNum,1)*(2-nu_2(ColNum,1))*alpha(ColNum)*alpha(ColNum+1);

        L2_C2(i,ColNum*i-1)=-(4+2*(2-nu_2(ColNum,1))*alpha(ColNum-1)...

            +2*(2-nu_2(ColNum,1))*alpha(ColNum+1));

        L2_C3(i,ColNum*i-2)=1;

        L2_C4(i,ColNum*(i-1))=-
(2*nu_2(ColNum,1)*alpha(ColNum)+4*nu_2(ColNum,1)*(2-nu_2(ColNum,1))...
```

```
        *alpha(ColNum)*alpha(ColNum+1)+2*(2-nu_2(ColNum,1))*alpha(ColNum+1));

    L2_C5(i,ColNum*(i-1)-1)=(2-nu_2(ColNum,1))*alpha(ColNum-1)+(2-
nu_2(ColNum,1))*alpha(ColNum+1);

    L2_C6(i,ColNum*(i+1))=-
(2*nu_2(ColNum,1)*alpha(ColNum)+4*nu_2(ColNum,1)*(2-nu_2(ColNum,1))...

        *alpha(ColNum)*alpha(ColNum+1)+2*(2-nu_2(ColNum,1))*alpha(ColNum+1));

    L2_C7(i,ColNum*(i+1)-1)=(2-nu_2(ColNum,1))*alpha(ColNum-1)+(2-
nu_2(ColNum,1))*alpha(ColNum+1);

  elseif i==RowNum

%                                                   L2_C1(i,ColNum*i)=4+4*(2-
nu_2(ColNum,1))*alpha(ColNum+1)+4*nu_2(ColNum,1)*alpha(ColNum)...

%         +3*nu_2(ColNum,1)*(2-nu_2(ColNum,1))*alpha(ColNum)*alpha(ColNum+1);
%%% for simply supported bottom boundary

    L2_C1(i,ColNum*i)=4+4*(2-
nu_2(ColNum,1))*alpha(ColNum+1)+4*nu_2(ColNum,1)*alpha(ColNum)...

        +7*nu_2(ColNum,1)*(2-nu_2(ColNum,1))*alpha(ColNum)*alpha(ColNum+1);
%%% for fixed supported bottom boundary

    L2_C2(i,ColNum*i-1)=-(4+2*(2-nu_2(ColNum,1))*alpha(ColNum-1)...

        +2*(2-nu_2(ColNum,1))*alpha(ColNum+1));

    L2_C3(i,ColNum*i-2)=1;

    L2_C4(i,ColNum*(i-1))=-
(2*nu_2(ColNum,1)*alpha(ColNum)+4*nu_2(ColNum,1)*(2-nu_2(ColNum,1))...

        *alpha(ColNum)*alpha(ColNum+1)+2*(2-nu_2(ColNum,1))*alpha(ColNum+1));

    L2_C5(i,ColNum*(i-1)-1)=(2-nu_2(ColNum,1))*alpha(ColNum-1)+(2-
nu_2(ColNum,1))*alpha(ColNum+1);

    L2_C8(i,ColNum*(i-2))=nu_2(ColNum,1)*(2-
nu_2(ColNum,1))*alpha(ColNum)*alpha(ColNum+1);

  elseif i==RowNum-1
```

```
        L2_C1(i,ColNum*i)=4+4*(2-
nu_2(ColNum,1))*alpha(ColNum+1)+4*nu_2(ColNum,1)*alpha(ColNum)...

            +6*nu_2(ColNum,1)*(2-nu_2(ColNum,1))*alpha(ColNum)*alpha(ColNum+1);

        L2_C2(i,ColNum*i-1)=-(4+2*(2-nu_2(ColNum,1))*alpha(ColNum-1)...

            +2*(2-nu_2(ColNum,1))*alpha(ColNum+1));

        L2_C3(i,ColNum*i-2)=1;

        L2_C4(i,ColNum*(i-1))=-
(2*nu_2(ColNum,1)*alpha(ColNum)+4*nu_2(ColNum,1)*(2-nu_2(ColNum,1))...

            *alpha(ColNum)*alpha(ColNum+1)+2*(2-nu_2(ColNum,1))*alpha(ColNum+1));

        L2_C5(i,ColNum*(i-1)-1)=(2-nu_2(ColNum,1))*alpha(ColNum-1)+(2-
nu_2(ColNum,1))*alpha(ColNum+1);

        L2_C6(i,ColNum*(i+1))=-
(2*nu_2(ColNum,1)*alpha(ColNum)+4*nu_2(ColNum,1)*(2-nu_2(ColNum,1))...

            *alpha(ColNum)*alpha(ColNum+1)+2*(2-nu_2(ColNum,1))*alpha(ColNum+1));

        L2_C7(i,ColNum*(i+1)-1)=(2-nu_2(ColNum,1))*alpha(ColNum-1)+(2-
nu_2(ColNum,1))*alpha(ColNum+1);

        L2_C8(i,ColNum*(i-2))=nu_2(ColNum,1)*(2-
nu_2(ColNum,1))*alpha(ColNum)*alpha(ColNum+1);

    else

        L2_C1(i,ColNum*i)=4+4*(2-
nu_2(ColNum,1))*alpha(ColNum+1)+4*nu_2(ColNum,1)*alpha(ColNum)...

            +6*nu_2(ColNum,1)*(2-nu_2(ColNum,1))*alpha(ColNum)*alpha(ColNum+1);

        L2_C2(i,ColNum*i-1)=-(4+2*(2-nu_2(ColNum,1))*alpha(ColNum-1)...

            +2*(2-nu_2(ColNum,1))*alpha(ColNum+1));

        L2_C3(i,ColNum*i-2)=1;

        L2_C4(i,ColNum*(i-1))=-
(2*nu_2(ColNum,1)*alpha(ColNum)+4*nu_2(ColNum,1)*(2-nu_2(ColNum,1))...
```

```
        *alpha(ColNum)*alpha(ColNum+1)+2*(2-nu_2(ColNum,1))*alpha(ColNum+1));

    L2_C5(i,ColNum*(i-1)-1)=(2-nu_2(ColNum,1))*alpha(ColNum-1)+(2-
nu_2(ColNum,1))*alpha(ColNum+1);

    L2_C6(i,ColNum*(i+1))=-
(2*nu_2(ColNum,1)*alpha(ColNum)+4*nu_2(ColNum,1)*(2-nu_2(ColNum,1))...

        *alpha(ColNum)*alpha(ColNum+1)+2*(2-nu_2(ColNum,1))*alpha(ColNum+1));

    L2_C7(i,ColNum*(i+1)-1)=(2-nu_2(ColNum,1))*alpha(ColNum-1)+(2-
nu_2(ColNum,1))*alpha(ColNum+1);

    L2_C8(i,ColNum*(i-2))=nu_2(ColNum,1)*(2-
nu_2(ColNum,1))*alpha(ColNum)*alpha(ColNum+1);

    L2_C9(i,ColNum*(i+2))=nu_2(ColNum,1)*(2-
nu_2(ColNum,1))*alpha(ColNum)*alpha(ColNum+1);

  end

end

L2=L2_C1+L2_C2+L2_C3+L2_C4+L2_C5+L2_C6+L2_C7+L2_C8+L2_C9;


%% Calculating coefficients matrix for derivative terms


%%%%%%%% Calculating DX2 coefficients %%%%%%%%

%% DX2_C1 (i-1,j)

for i=1:m

  for j=1:m

    if rem((i-1)/ColNum,1)==0

      DX2_C1(i,j)=0;

    else

      DX2_C1(i,i-1)=1*(1/del_x^2);
```

```
        end
    end
end
%% DX2_C2 (i,j)
for i=1:m
    DX2_C2(i,i)=-2*(1/del_x^2);
end
%% DX2_C3 (i+1,j)
for i=1:m
    for j=1:m
        if rem(i/ColNum,1)==0
            DX2_C3(i,j)=1*L1(i/ColNum,j)*(1/del_x^2);
        else
            DX2_C3(i,i+1)=1*(1/del_x^2);
        end
    end
end

DX2=DX2_C1+DX2_C2+DX2_C3;

%%%%%%%% Calculating DX3 coefficients %%%%%%%%
%% DX3_C1 (i-2,j)
for i=1:m
```

```
    for j=1:m
        if rem((i-1)/ColNum,1)==0
%           DX3_C1(i,i)=-1*(-1/2)*(1/del_x^3);      %%% for simply supported left boundary
            DX3_C1(i,i)=1*(-1/2)*(1/del_x^3);          %%% for fixed left boundary
        elseif rem((i-2)/ColNum,1)==0
            DX3_C1(i,j)=0;
        else
            DX3_C1(i,i-2)=1*(-1/2)*(1/del_x^3);
        end
    end
end
%% DX3_C2 (i-1,j)
for i=1:m
    for j=1:m
        if rem((i-1)/ColNum,1)==0
            DX3_C2(i,j)=0;
        else
            DX3_C2(i,i-1)=1*(1/del_x^3);
        end
    end
end
%% DX3_C3 (i+1,j)
for i=1:m
```

```
    for j=1:m
        if rem(i/ColNum,1)==0
            DX3_C3(i,j)=-1*L1(i/ColNum,j)*(1/del_x^3);
        else
            DX3_C3(i,i+1)=-1*(1/del_x^3);
        end

    end
end
%% DX3_C4 (i+2,j)
for i=1:m
    for j=1:m
        if rem(i/ColNum,1)==0
            DX3_C4(i,j)=L2(i/ColNum,j)*(1/2)*(1/del_x^3);
        elseif rem((i+1)/ColNum,1)==0
            DX3_C4(i,j)=L1((i+1)/ColNum,j)*(1/2)*(1/del_x^3);
        else
            DX3_C4(i,i+2)=1*(1/2)*(1/del_x^3);
        end
    end
end

DX3=DX3_C1+DX3_C2+DX3_C3+DX3_C4;
```

```
%%%%%%%% Calculating DX4 coefficients %%%%%%%%
%% DX4_C1 (i-2,j)
for i=1:m
   for j=1:m
      if rem((i-1)/ColNum,1)==0
%           DX4_C1(i,i)=-1*(1/del_x^4);      %%% for simply supported left boundary
          DX4_C1(i,i)=1*(1/del_x^4);         %%% for fixed left boundary
      elseif rem((i-2)/ColNum,1)==0
          DX4_C1(i,j)=0;
      else
          DX4_C1(i,i-2)=1*(1/del_x^4);
      end
   end
end
%% DX4_C2 (i-1,j)
for i=1:m
   for j=1:m
      if rem((i-1)/ColNum,1)==0
          DX4_C2(i,j)=0;
      else
          DX4_C2(i,i-1)=-4*(1/del_x^4);
      end
```

```
    end
end
%% DX4_C3 (i,j)
for i=1:m
    DX4_C3(i,i)=6*(1/del_x^4);
end
%% DX4_C4 (i+1,j)
for i=1:m
    for j=1:m
        if rem(i/ColNum,1)==0
            DX4_C4(i,j)=-4*L1(i/ColNum,j)*(1/del_x^4);
        else
            DX4_C4(i,i+1)=-4*(1/del_x^4);
        end
    end
end
%% DX4_C5 (i+2,j)
for i=1:m
    for j=1:m
        if rem(i/ColNum,1)==0
            DX4_C5(i,j)=L2(i/ColNum,j)*(1/del_x^4);
        elseif rem((i+1)/ColNum,1)==0
            DX4_C5(i,j)=L1((i+1)/ColNum,j)*(1/del_x^4);
```

```
        else
            DX4_C5(i,i+2)=1*(1/del_x^4);
        end
    end
end

DX4=DX4_C1+DX4_C2+DX4_C3+DX4_C4+DX4_C5;

%%%%%%%% Calculating DY2 coefficients %%%%%%%%
%% DY2_C1 (i,j+1)
for i=1:m
    for j=1:m
        if (i/ColNum)<= 1
            DY2_C1(i,j)=0;
        else
            DY2_C1(i,i-ColNum)=1*(1/del_y(i)^2);
        end
    end
end
%% DY2_C2 (i,j)
for i=1:m
    DY2_C2(i,i)=-2*(1/del_y(i)^2);
end
```

```
%% DY2_C3 (i,j-1)
for i=1:m
   for j=1:m
      if i>(m-ColNum)
         DY2_C3(i,j)=0;
      else
         DY2_C3(i,i+ColNum)=1*(1/del_y(i)^2);
      end
   end
end

DY2=DY2_C1+DY2_C2+DY2_C3;

%%%%%%%% Calculating DY3 coefficients %%%%%%%%
%% DY3_C1 (i,j+2)
for i=1:m
   for j=1:m
      if (i/ColNum)<= 1
%            DY3_C1(i,i)=-1*(1/2)*(1/del_y(i)^3);      %%% for simply supported top boundary
         DY3_C1(i,i)=1*(1/2)*(1/del_y(i)^3);      %%% for fixed top boundary
      elseif (i/ColNum)> 1 && (i/ColNum)<= 2
         DY3_C1(i,j)=0;
      else
```

```
            DY3_C1(i,i-2*ColNum)=1*(1/2)*(1/del_y(i)^3);
        end
    end
end
%% DY3_C2 (i,j+1)
for i=1:m
    for j=1:m
        if (i/ColNum)<= 1
            DY3_C2(i,j)=0;
        else
            DY3_C2(i,i-ColNum)=-1*(1/del_y(i)^3);
        end
    end
end
%% DY3_C3 (i,j-1)
for i=1:m
    for j=1:m
        if i>(m-ColNum)
            DY3_C3(i,j)=0;
        else
            DY3_C3(i,i+ColNum)=1*(1/del_y(i)^3);
        end
    end
```

```
end
%% DY3_C4 (i,j-2)
for i=1:m
   for j=1:m
      if i>(m-ColNum)
%          DY3_C4(i,i)=-1*(-1/2)*(1/del_y(i)^3);      %%% for simply supported bottom boundary
         DY3_C4(i,i)=1*(-1/2)*(1/del_y(i)^3);      %%% for fixed bottom boundary
      elseif i<=(m-ColNum) && i>(m-2*ColNum)
         DY3_C4(i,j)=0;
      else
         DY3_C4(i,i+2*ColNum)=1*(-1/2)*(1/del_y(i)^3);
      end
   end
end

DY3=DY3_C1+DY3_C2+DY3_C3+DY3_C4;

%%%%%%%% Calculating DY4 coefficients %%%%%%%%
%% DY4_C1 (i,j+2)
for i=1:m
   for j=1:m
      if (i/ColNum)<= 1
%          DY4_C1(i,i)=-1*(1/del_y(i)^4);        %%% for simply supported top boundary
```

```
        DY4_C1(i,i)=1*(1/del_y(i)^4);          %%% for fixed top boundary
    elseif (i/ColNum)> 1 && (i/ColNum)<= 2
        DY4_C1(i,j)=0;
    else
        DY4_C1(i,i-2*ColNum)=1*(1/del_y(i)^4);
    end
  end
end
%% DY4_C2 (i,j+1)
for i=1:m
  for j=1:m
    if (i/ColNum)<= 1
        DY4_C2(i,j)=0;
    else
        DY4_C2(i,i-ColNum)=-4*(1/del_y(i)^4);
    end
  end
end
%% DY4_C3 (i,j)
for i=1:m
  DY4_C3(i,i)=6*(1/del_y(i)^4);
end
%% DY4_C4 (i,j-1)
```

```
for i=1:m
   for j=1:m
      if i>(m-ColNum)
         DY4_C4(i,j)=0;
      else
         DY4_C4(i,i+ColNum)=-4*(1/del_y(i)^4);
      end
   end
end
%% DY4_C5 (i,j-2)
for i=1:m
   for j=1:m
      if i>(m-ColNum)
%         DY4_C5(i,i)=-1*(1/del_y(i)^4);      %%% for simply supported bottom boundary
         DY4_C5(i,i)=1*(1/del_y(i)^4);         %%% for fixed bottom boundary
      elseif i<=(m-ColNum) && i>(m-2*ColNum)
         DY4_C5(i,j)=0;
      else
         DY4_C5(i,i+2*ColNum)=1*(1/del_y(i)^4);
      end
   end
end
```

```
DY4=DY4_C1+DY4_C2+DY4_C3+DY4_C4+DY4_C5;


%%%%%%%% Calculating DXDY coefficients %%%%%%%%
%% DXDY_C1 (i-1,j-1)
for i=1:m
   for j=1:m
      if rem((i-1)/ColNum,1)==0
         DXDY_C1(i,j)=0;
      elseif i>(m-ColNum)
         DXDY_C1(i,j)=0;
      else
         DXDY_C1(i,i+ColNum-1)=1*(1/(4*del_x*del_y(i-1)));
      end
   end
end
%% DXDY_C2 (i-1,j+1)
for i=1:m
   for j=1:m
      if rem((i-1)/ColNum,1)==0
         DXDY_C2(i,j)=0;
      elseif (i/ColNum)<= 1
         DXDY_C2(i,j)=0;
      else
```

```
            DXDY_C2(i,i-ColNum-1)=-1*(1/(4*del_x*del_y(i-1)));
        end
    end
end
%% DXDY_C3 (i+1,j-1)
for i=1:m
    for j=1:m
        if rem(i/ColNum,1)==0 && i~= m
            DXDY_C3(i,j)=-1*L1(i/ColNum+1,j)*(1/(4*del_x*del_y_L1));
        elseif i>(m-ColNum) && i~= m
            DXDY_C3(i,j)=0;
        elseif i == m
            DXDY_C3(i,j)=-1*L1_bottom(1,j)*(1/(4*del_x*del_y_L1));
        else
            DXDY_C3(i,i+ColNum+1)=-1*(1/(4*del_x*del_y(i+1)));
        end
    end
end
%% DXDY_C4 (i+1,j+1)
for i=1:m
    for j=1:m
        if rem(i/ColNum,1)==0 && i~= ColNum
            DXDY_C4(i,j)=L1(i/ColNum-1,j)*(1/(4*del_x*del_y_L1));
```

```
        elseif (i/ColNum)<= 1 && i~= ColNum
            DXDY_C4(i,j)=0;
        elseif i == ColNum
            DXDY_C4(i,j)=L1_top(1,j)*(1/(4*del_x*del_y_L1));
        else
            DXDY_C4(i,i-ColNum+1)=1*(1/(4*del_x*del_y(i+1)));
        end
    end
end

DXDY=DXDY_C1+DXDY_C2+DXDY_C3+DXDY_C4;

%%%%%%%% Calculating DX2DY coefficients %%%%%%%%
%% DX2DY_C1 (i-1,j-1)
for i=1:m
    for j=1:m
        if rem((i-1)/ColNum,1)==0
            DX2DY_C1(i,j)=0;
        elseif i>(m-ColNum)
            DX2DY_C1(i,j)=0;
        else
            DX2DY_C1(i,i+ColNum-1)=-1*(1/(2*(del_x^2)*del_y(i-1)));
        end
```

```
    end
end
%% DX2DY_C2 (i-1,j+1)
for i=1:m
    for j=1:m
        if rem((i-1)/ColNum,1)==0
            DX2DY_C2(i,j)=0;
        elseif (i/ColNum)<= 1
            DX2DY_C2(i,j)=0;
        else
            DX2DY_C2(i,i-ColNum-1)=1*(1/(2*(del_x^2)*del_y(i-1)));
        end
    end
end
%% DX2DY_C3 (i,j-1)
for i=1:m
    for j=1:m
        if i>(m-ColNum)
            DX2DY_C3(i,j)=0;
        else
            DX2DY_C3(i,i+ColNum)=1*(1/((del_x^2)*del_y(i)));
        end
    end
```

```
end
%% DX2DY_C4 (i,j+1)
for i=1:m
   for j=1:m
      if (i/ColNum)<= 1
         DX2DY_C4(i,j)=0;
      else
         DX2DY_C4(i,i-ColNum)=-1*(1/((del_x^2)*del_y(i)));
      end
   end
end
%% DX2DY_C5 (i+1,j-1)
for i=1:m
   for j=1:m
      if rem(i/ColNum,1)==0 && i~= m
         DX2DY_C5(i,j)=-1*L1(i/ColNum+1,j)*(1/(2*(del_x^2)*del_y_L1));
      elseif i>(m-ColNum) && i~= m
         DX2DY_C5(i,j)=0;
      elseif i == m
         DX2DY_C5(i,j)=-1*L1_bottom(1,j)*(1/(2*(del_x^2)*del_y_L1));
      else
         DX2DY_C5(i,i+ColNum+1)=-1*(1/(2*(del_x^2)*del_y(i+1)));
      end
```

```
    end
end
%% DX2DY_C6 (i+1,j+1)
for i=1:m
    for j=1:m
        if rem(i/ColNum,1)==0 && i~= ColNum
            DX2DY_C6(i,j)=L1(i/ColNum-1,j)*(1/(2*del_x^2*del_y_L1));
        elseif (i/ColNum)<= 1 && i~= ColNum
            DX2DY_C6(i,j)=0;
        elseif i == ColNum
            DX2DY_C6(i,j)=L1_top(1,j)*(1/(2*del_x^2*del_y_L1));
        else
            DX2DY_C6(i,i-ColNum+1)=1*(1/(2*del_x^2*del_y(i+1)));
        end
    end
end

DX2DY=DX2DY_C1+DX2DY_C2+DX2DY_C3+DX2DY_C4+DX2DY_C5+DX2DY_
C6;

%%%%%%%% Calculating DXDY2 coefficients %%%%%%%%
%% DXDY2_C1 (i-1,j-1)
for i=1:m
    for j=1:m
```

```
        if rem((i-1)/ColNum,1)==0
            DXDY2_C1(i,j)=0;
        elseif i>(m-ColNum)
            DXDY2_C1(i,j)=0;
        else
            DXDY2_C1(i,i+ColNum-1)=-1*(1/(2*del_x*(del_y(i-1))^2));
        end
    end
end
%% DXDY2_C2 (i-1,j)
for i=1:m
    for j=1:m
        if rem((i-1)/ColNum,1)==0
            DXDY2_C2(i,j)=0;
        else
            DXDY2_C2(i,i-1)=1*(1/(del_x*(del_y(i-1))^2));
        end
    end
end
%% DXDY2_C3 (i-1,j+1)
for i=1:m
    for j=1:m
        if rem((i-1)/ColNum,1)==0
```

```
        DXDY2_C3(i,j)=0;
    elseif (i/ColNum)<= 1
        DXDY2_C3(i,j)=0;
    else
        DXDY2_C3(i,i-ColNum-1)=-1*(1/(2*del_x*(del_y(i-1))^2));
    end

  end
end
%% DXDY2_C4 (i+1,j-1)
for i=1:m
  for j=1:m
    if rem(i/ColNum,1)==0 && i~= m
        DXDY2_C4(i,j)=L1(i/ColNum+1,j)*(1/(2*del_x*(del_y_L1)^2));
    elseif i>(m-ColNum) && i~= m
        DXDY2_C4(i,j)=0;
    elseif i == m
        DXDY2_C4(i,j)=L1_bottom(1,j)*(1/(2*del_x*(del_y_L1)^2));
    else
        DXDY2_C4(i,i+ColNum+1)=1*(1/(2*del_x*(del_y(i+1))^2));
    end
  end
end
```

```
%% DXDY2_C5 (i+1,j)
for i=1:m
   for j=1:m
      if rem(i/ColNum,1)==0
         DXDY2_C5(i,j)=-1*L1(i/ColNum,j)*(1/(del_x*(del_y_L1)^2));
      else
         DXDY2_C5(i,i+1)=-1*(1/(del_x*(del_y(i+1))^2));
      end
   end
end
%% DXDY2_C6 (i+1,j+1)
for i=1:m
   for j=1:m
      if rem(i/ColNum,1)==0 && i~= ColNum
         DXDY2_C6(i,j)=L1(i/ColNum-1,j)*(1/(2*del_x*(del_y_L1)^2));
      elseif (i/ColNum)<= 1 && i~= ColNum
         DXDY2_C6(i,j)=0;
      elseif i == ColNum
         DXDY2_C6(i,j)=L1_top(1,j)*(1/(2*del_x*(del_y_L1)^2));
      else
         DXDY2_C6(i,i-ColNum+1)=1*(1/(2*del_x*(del_y(i+1))^2));
      end
   end
```

```
end


DXDY2=DXDY2_C1+DXDY2_C2+DXDY2_C3+DXDY2_C4+DXDY2_C5+DXDY2_
C6;


%%%%%%%% Calculating DX2DY2 coefficients %%%%%%%%

%% DX2DY2_C1 (i-1,j-1)

for i=1:m

   for j=1:m

      if rem((i-1)/ColNum,1)==0

         DX2DY2_C1(i,j)=0;

      elseif i>(m-ColNum)

         DX2DY2_C1(i,j)=0;

      else

         DX2DY2_C1(i,i+ColNum-1)=1*(1/((del_x^2)*(del_y(i-1))^2));

      end

   end

end

%% DX2DY2_C2 (i-1,j)

for i=1:m

   for j=1:m

      if rem((i-1)/ColNum,1)==0

         DX2DY2_C2(i,j)=0;

      else
```

```
            DX2DY2_C2(i,i-1)=-2*(1/((del_x^2)*(del_y(i-1))^2));
        end
    end
end
%% DX2DY2_C3 (i-1,j+1)
for i=1:m
    for j=1:m
        if rem((i-1)/ColNum,1)==0
            DX2DY2_C3(i,j)=0;
        elseif (i/ColNum)<= 1
            DX2DY2_C3(i,j)=0;
        else
            DX2DY2_C3(i,i-ColNum-1)=1*(1/((del_x^2)*(del_y(i-1))^2));
        end
    end
end
%% DX2DY2_C4 (i,j-1)
for i=1:m
    for j=1:m
        if i>(m-ColNum)
            DX2DY2_C4(i,j)=0;
        else
            DX2DY2_C4(i,i+ColNum)=-2*(1/((del_x^2)*(del_y(i))^2));
```

```
        end
    end
end
%% DX2DY2_C5 (i,j)
for i=1:m
    DX2DY2_C5(i,i)=4*(1/((del_x^2)*(del_y(i))^2));
end
%% DX2DY2_C6 (i,j+1)
for i=1:m
    for j=1:m
        if (i/ColNum)<= 1
            DX2DY2_C6(i,j)=0;
        else
            DX2DY2_C6(i,i-ColNum)=-2*(1/((del_x^2)*(del_y(i))^2));
        end
    end
end
%% DX2DY2_C7 (i+1,j-1)
for i=1:m
    for j=1:m
        if rem(i/ColNum,1)==0 && i~= m
            DX2DY2_C7(i,j)=L1(i/ColNum+1,j)*(1/((del_x^2)*(del_y_L1)^2));
        elseif i>(m-ColNum) && i~= m
```

```
        DX2DY2_C7(i,j)=0;
    elseif i == m
        DX2DY2_C7(i,j)=L1_bottom(1,j)*(1/((del_x^2)*(del_y_L1)^2));
    else
        DX2DY2_C7(i,i+ColNum+1)=1*(1/((del_x^2)*(del_y(i+1))^2));
    end
  end
end
%% DX2DY2_C8 (i+1,j)
for i=1:m
  for j=1:m
    if rem(i/ColNum,1)==0
        DX2DY2_C8(i,j)=-2*L1(i/ColNum,j)*(1/((del_x^2)*(del_y_L1)^2));
    else
        DX2DY2_C8(i,i+1)=-2*(1/((del_x^2)*(del_y(i+1))^2));
    end
  end
end
%% DX2DY2_C9 (i+1,j+1)
for i=1:m
  for j=1:m
    if rem(i/ColNum,1)==0 && i~= ColNum
        DX2DY2_C9(i,j)=L1(i/ColNum-1,j)*(1/((del_x^2)*(del_y_L1)^2));
```

```
        elseif (i/ColNum)<= 1 && i~= ColNum
            DX2DY2_C9(i,j)=0;
        elseif i == ColNum
            DX2DY2_C9(i,j)=L1_top(1,j)*(1/((del_x^2)*(del_y_L1)^2));
        else
            DX2DY2_C9(i,i-ColNum+1)=1*(1/((del_x^2)*(del_y(i+1))^2));
        end
    end
end

DX2DY2=DX2DY2_C1+DX2DY2_C2+DX2DY2_C3+DX2DY2_C4+DX2DY2_C5+DX2DY2_C6...
    +DX2DY2_C7+DX2DY2_C8+DX2DY2_C9;

%%%%%%%% Calculating DX3DY coefficients %%%%%%%%
%% DX3DY_C1 (i-2,j-1)
for i=1:m
    for j=1:m
        if rem((i-1)/ColNum,1)==0 && i<=(m-ColNum)
%           DX3DY_C1(i,i+ColNum)=-1*(1/4)*(1/(del_x^3*del_y(i)));      %%% for simply supported left boundary
            DX3DY_C1(i,i+ColNum)=1*(1/4)*(1/(del_x^3*del_y(i)));          %%% for fixed left boundary
        elseif i>(m-ColNum)
            DX3DY_C1(i,j)=0;
```

```
        elseif rem((i-2)/ColNum,1)==0
            DX3DY_C1(i,j)=0;
        else
            DX3DY_C1(i,i+ColNum-2)=1*(1/4)*(1/(del_x^3*del_y(i-2)));
        end
    end
end
%% DX3DY_C2 (i-2,j+1)
for i=1:m
    for j=1:m
        if rem((i-1)/ColNum,1)==0 && (i/ColNum)> 1
%           DX3DY_C2(i,i-ColNum)=-1*(-1/4)*(1/(del_x^3*del_y(i)));      %%% for simply supported left boundary
            DX3DY_C2(i,i-ColNum)=1*(-1/4)*(1/(del_x^3*del_y(i)));          %%% for fixed left boundary
        elseif (i/ColNum)<= 1
            DX3DY_C2(i,j)=0;
        elseif rem((i-2)/ColNum,1)==0
            DX3DY_C2(i,j)=0;
        else
            DX3DY_C2(i,i-ColNum-2)=1*(-1/4)*(1/(del_x^3*del_y(i-2)));
        end
    end
end
```

```
%% DX3DY_C3 (i-1,j-1)
for i=1:m
   for j=1:m
      if rem((i-1)/ColNum,1)==0
         DX3DY_C3(i,j)=0;
      elseif i>(m-ColNum)
         DX3DY_C3(i,j)=0;
      else
         DX3DY_C3(i,i+ColNum-1)=1*(-1/2)*(1/(del_x^3*del_y(i-1)));
      end
   end
end
%% DX3DY_C4 (i-1,j+1)
for i=1:m
   for j=1:m
      if rem((i-1)/ColNum,1)==0
         DX3DY_C4(i,j)=0;
      elseif (i/ColNum)<= 1
         DX3DY_C4(i,j)=0;
      else
         DX3DY_C4(i,i-ColNum-1)=1*(1/2)*(1/(del_x^3*del_y(i-1)));
      end
   end
```

```
end
%% DX3DY_C5 (i+1,j-1)
for i=1:m
   for j=1:m
      if rem(i/ColNum,1)==0 && i~= m
         DX3DY_C5(i,j)=1*L1(i/ColNum+1,j)*(1/(2*del_x^3*del_y_L1));
      elseif i>(m-ColNum) && i~= m
         DX3DY_C5(i,j)=0;
      elseif i == m
         DX3DY_C5(i,j)=1*L1_bottom(1,j)*(1/(2*del_x^3*del_y_L1));
      else
         DX3DY_C5(i,i+ColNum+1)=1*(1/(2*del_x^3*del_y(i+1)));
      end
   end
end
%% DX3DY_C6 (i+1,j+1)
for i=1:m
   for j=1:m
      if rem(i/ColNum,1)==0 && i~= ColNum
         DX3DY_C6(i,j)=-1*L1(i/ColNum-1,j)*(1/(2*del_x^3*del_y_L1));
      elseif (i/ColNum)<= 1 && i~= ColNum
         DX3DY_C6(i,j)=0;
      elseif i == ColNum
```

```
            DX3DY_C6(i,j)=-1*L1_top(1,j)*(1/(2*del_x^3*del_y_L1));
        else
            DX3DY_C6(i,i-ColNum+1)=-1*(1/(2*del_x^3*del_y(i+1)));
        end
    end
end
%% DX3DY_C7 (i+2,j-1)
for i=1:m
    for j=1:m
        if rem(i/ColNum,1)==0 && i<=(m-ColNum)
            DX3DY_C7(i,j)=L2(i/ColNum+1,j)*(-1/(4*del_x^3*del_y_L2));
        elseif rem((i+1)/ColNum,1)==0 && (i+1)<=(m-ColNum)
            DX3DY_C7(i,j)=L1((i+1)/ColNum+1,j)*(-1/(4*del_x^3*del_y_L1));
        elseif i>(m-ColNum) && i<=m-2
            DX3DY_C7(i,j)=0;
        elseif i==m-1
            DX3DY_C7(i,j)=L1_bottom(1,j)*(-1/(4*del_x^3*del_y_L1));
        elseif i==m
            DX3DY_C7(i,j)=L2_bottom(1,j)*(-1/(4*del_x^3*del_y_L2));
        else
            DX3DY_C7(i,i+ColNum+2)=(-1/(4*del_x^3*del_y(i+2)));
        end
    end
```

```
end
%% DX3DY_C8 (i+2,j+1)
for i=1:m
   for j=1:m
      if rem(i/ColNum,1)==0 && (i/ColNum)> 1
         DX3DY_C8(i,j)=L2(i/ColNum-1,j)*(1/(4*del_x^3*del_y_L2));
      elseif rem((i+1)/ColNum,1)==0 && ((i+1)/ColNum)> 1
         DX3DY_C8(i,j)=L1((i+1)/ColNum-1,j)*(1/(4*del_x^3*del_y_L1));
      elseif i<=ColNum-2
         DX3DY_C8(i,j)=0;
      elseif i==ColNum-1
         DX3DY_C8(i,j)=L1_top(1,j)*(1/(4*del_x^3*del_y_L1));
      elseif i==ColNum
         DX3DY_C8(i,j)=L2_top(1,j)*(1/(4*del_x^3*del_y_L2));
      else
         DX3DY_C8(i,i-ColNum+2)=(1/(4*del_x^3*del_y(i+2)));
      end
   end
end

DX3DY=DX3DY_C1+DX3DY_C2+DX3DY_C3+DX3DY_C4+DX3DY_C5+DX3DY_
C6...    +DX3DY_C7+DX3DY_C8;
%%%%%%%% Calculating DXDY3 coefficients %%%%%%%%
%% DXDY3_C1 (i-1,j-2)
```

```
for i=1:m
   for j=1:m
      if rem((i-1)/ColNum,1)==0
         DXDY3_C1(i,j)=0;
      elseif i>(m-ColNum+1)
%           DXDY3_C1(i,i-1)=-1*(1/(4*del_x*del_y(i)^3));   %%% for simply supported bottom boundary
         DXDY3_C1(i,i-1)=1*(1/(4*del_x*del_y(i)^3));   %%% for fixed bottom boundary
      elseif i<=(m-ColNum) && i>(m-2*ColNum)
         DXDY3_C1(i,j)=0;
      else
         DXDY3_C1(i,i+2*ColNum-1)=(1/(4*del_x*del_y(i)^3));
      end
   end
end
%% DXDY3_C2 (i+1,j-2)
for i=1:m
   for j=1:m
      if rem(i/ColNum,1)==0 && i<=(m-2*ColNum)
         DXDY3_C2(i,j)=L1((i/ColNum)+2,j)*(-1/(4*del_x*del_y_L1^3));
      elseif i==(m-ColNum)
         DXDY3_C2(i,j)=L1_bottom(1,j)*(-1/(4*del_x*del_y_L1^3));
      elseif i==m
```

```
%           DXDY3_C2(i,j)=-1*L1((i/ColNum),j)*(-1/(4*del_x*del_y_L1^3));   %%% for simply supported bottom boundary

          DXDY3_C2(i,j)=1*L1((i/ColNum),j)*(-1/(4*del_x*del_y_L1^3));       %%% for fixed bottom boundary

       elseif i>(m-ColNum) && i~=m

%           DXDY3_C2(i,i+1)=-1*(-1/(4*del_x*del_y(i)^3));  %%% for simply supported bottom boundary

          DXDY3_C2(i,i+1)=1*(-1/(4*del_x*del_y(i)^3));       %%% for fixed bottom boundary

       elseif i>(m-2*ColNum) && i<(m-ColNum)

          DXDY3_C2(i,j)=0;

       else

          DXDY3_C2(i,i+2*ColNum+1)=(-1/(4*del_x*del_y(i)^3));

       end

    end

end

%% DXDY3_C3 (i-1,j-1)

for i=1:m

    for j=1:m

       if rem((i-1)/ColNum,1)==0

          DXDY3_C3(i,j)=0;

       elseif i>(m-ColNum)

          DXDY3_C3(i,j)=0;

       else

          DXDY3_C3(i,i+ColNum-1)=(-1/(2*del_x*del_y(i)^3));
```

```
        end
    end
end
%% DXDY3_C4 (i-1,j+1)
for i=1:m
    for j=1:m
        if rem((i-1)/ColNum,1)==0
            DXDY3_C4(i,j)=0;
        elseif (i/ColNum)<= 1
            DXDY3_C4(i,j)=0;
        else
            DXDY3_C4(i,i-ColNum-1)=(1/(2*del_x*del_y(i)^3));
        end
    end
end
%% DXDY3_C5 (i+1,j-1)
for i=1:m
    for j=1:m
        if rem(i/ColNum,1)==0 && i~= m
            DXDY3_C5(i,j)=L1(i/ColNum+1,j)*(1/(2*del_x*del_y_L1^3));
        elseif i>(m-ColNum) && i~= m
            DXDY3_C5(i,j)=0;
        elseif i == m
```

```
            DXDY3_C5(i,j)=L1_bottom(1,j)*(1/(2*del_x*del_y_L1^3));
        else
            DXDY3_C5(i,i+ColNum+1)=(1/(2*del_x*del_y(i+1)^3));
        end
    end
end
%% DXDY3_C6 (i+1,j+1)
for i=1:m
    for j=1:m
        if rem(i/ColNum,1)==0 && i~= ColNum
            DXDY3_C6(i,j)=L1(i/ColNum-1,j)*(-1/(2*del_x*del_y_L1^3));
        elseif (i/ColNum)<= 1 && i~= ColNum
            DXDY3_C6(i,j)=0;
        elseif i == ColNum
            DXDY3_C6(i,j)=L1_top(1,j)*(-1/(2*del_x*del_y_L1^3));
        else
            DXDY3_C6(i,i-ColNum+1)=(-1/(2*del_x*del_y(i+1)^3));
        end
    end
end
%% DXDY3_C7 (i-1,j+2)
for i=1:m
    for j=1:m
```

```
        if rem((i-1)/ColNum,1)==0
            DXDY3_C7(i,j)=0;
        elseif (i/ColNum)<= 1 && i~=1
%           DXDY3_C7(i,i-1)=-1*(-1/(4*del_x*del_y(i)^3));   %%% for simply supported top boundary
            DXDY3_C7(i,i-1)=1*(-1/(4*del_x*del_y(i)^3));   %%% for fixed top boundary
        elseif i>ColNum+1 && i<= 2*ColNum
            DXDY3_C7(i,j)=0;
        else
            DXDY3_C7(i,i-2*ColNum-1)=(-1/(4*del_x*del_y(i)^3));
        end
    end
end
%% DXDY3_C8 (i+1,j+2)
for i=1:m
    for j=1:m
        if rem(i/ColNum,1)==0 && i> 2*ColNum
            DXDY3_C8(i,j)=L1((i/ColNum)-2,j)*(1/(4*del_x*(del_y_L1)^3));
        elseif i== 2*ColNum
            DXDY3_C8(i,j)=L1_top(1,j)*(1/(4*del_x*(del_y_L1)^3));
        elseif i==ColNum
%           DXDY3_C8(i,j)=-1*L1((i/ColNum),j)*(1/(4*del_x*(del_y_L1)^3));   %%% for simply supported top boundary
            DXDY3_C8(i,j)=1*L1((i/ColNum),j)*(1/(4*del_x*(del_y_L1)^3));      %%%  for fixed top boundary
```

```
        elseif i<=ColNum-1

%           DXDY3_C8(i,i+1)=-1*(1/(4*del_x*(del_y_L1)^3));  %%% for simply supported
top boundary

            DXDY3_C8(i,i+1)=1*(1/(4*del_x*(del_y_L1)^3));  %%% for fixed top boundary

        elseif i>ColNum && i<2*ColNum

            DXDY3_C8(i,j)=0;

        else

            DXDY3_C8(i,i-2*ColNum+1)=(1/(4*del_x*(del_y_L1)^3));

        end

    end

end


DXDY3=DXDY3_C1+DXDY3_C2+DXDY3_C3+DXDY3_C4+DXDY3_C5+DXDY3_
C6...    +DXDY3_C7+DXDY3_C8;

%% Transformation to U-V (rotated) domain

for i=1:m

    for j=1:m

        DU2(i,j)=((1/(CT(i,j)^2))*DX2(i,j))-(((2*ST(i,j))/(CT(i,j)^2))...

            *DXDY(i,j))+(((ST(i,j)^2)/(CT(i,j)^2))*DY2(i,j));

        DU3(i,j)=((1/(CT(i,j)^3))*DX3(i,j))-(((3*ST(i,j))/(CT(i,j)^3))...

            *DX2DY(i,j))+(((3*ST(i,j)^2)/(CT(i,j)^3))*DXDY2(i,j))-...

            (((ST(i,j)^3)/(CT(i,j)^3))*DY3(i,j));

        DU4(i,j)=((1/(CT(i,j)^4))*DX4(i,j))-(((4*ST(i,j))/(CT(i,j)^4))...

            *DX3DY(i,j))+(((6*ST(i,j)^2)/(CT(i,j)^4))*DX2DY2(i,j))-...
```

```
        (((4*ST(i,j)^3)/(CT(i,j)^4))*DXDY3(i,j))+(((ST(i,j)^4)/...
        (CT(i,j)^4))*DY4(i,j));

    DV2(i,j)=DY2(i,j);
    DV3(i,j)=DY3(i,j);
    DV4(i,j)=DY4(i,j);

    DUDV(i,j)=((1/CT(i,j))*DXDY(i,j))-((ST(i,j)/CT(i,j))*DY2(i,j));
    DU2DV(i,j)=((1/(CT(i,j)^2))*DX2DY(i,j))-(((2*ST(i,j))/(CT(i,j)^2))...
        *DXDY2(i,j))+(((ST(i,j)^2)/(CT(i,j)^2))*DY3(i,j));
    DUDV2(i,j)=((1/CT(i,j))*DXDY2(i,j))-((ST(i,j)/CT(i,j))*DY3(i,j));
    DU2DV2(i,j)=((1/(CT(i,j)^2))*DX2DY2(i,j))-(((2*ST(i,j))/(CT(i,j)^2))...
        *DXDY3(i,j))+(((ST(i,j)^2)/(CT(i,j)^2))*DY4(i,j));
  end
end

%% Computing each term of the final plate deflection equation

%%%%% Derivative terms
T1=D_2.*DU4;
T2=2*D_2.*DU2DV2;
T3=D_2.*DV4;
T4=2*DU3.*D_dx_2;
```

```
T5=2*DV3.*D_dy_2;

T6=DU2.*D_dx2_2;

T7=DV2.*D_dy2_2;

T8=nu_2.*D_dx2_2.*DV2;

T9=nu_2.*D_dy2_2.*DU2;

T10=D_2.*nu_dx2_2.*DV2;

T11=D_2.*nu_dy2_2.*DU2;

T12=2*D_dx_2.*DUDV2;

T13=2*D_dy_2.*DU2DV;

T14=2*D_dx_2.*nu_dx_2.*DV2;

T15=2*D_dy_2.*nu_dy_2.*DU2;

T16=-2*nu_dx_2.*D_dy_2.*DUDV;

T17=-2*nu_dy_2.*D_dx_2.*DUDV;

T18=2*D_dxdy_2.*DUDV;

T19=-2*nu_2.*D_dxdy_2.*DUDV;

T20=-2*D_2.*nu_dxdy_2.*DUDV;


%%%%% Non derivative term

for j=1:numel(omg)
   for i=1:m
      T21(i,i,j)=-1*(omg(j).^2*(rho_2(i)*t_2(i)));
   end
end
```

```
%%%%% Forcing function


% b=ones(m,1);


for i=1:m

   b(i)=p(i);          % Pressure is applied on whole plate. Define pressure according to the
requirement

end


%% Calculating final coefficient matrix and node deflections

for j=1:numel(omg)

A(:,:,j)=T1+T2+T3+T4+T5+T6+T7+T8+T9+T10+T11+T12+T13+T14+T15+T16+T17...

      +T18+T19+T20+T21(:,:,j);     % Final coefficient matrix

   w(:,j)=inv(A(:,:,j))*b;         % Node deflection at different frequencies

end


for k=1:numel(omg)

   for i=1:RowNum

      for j=1:ColNum

         Zeta(i,j,k)=w(j+(i-1)*ColNum,k);

      end

   end
```

```
end

for k=1:numel(omg)
   for i=2:RowNum+1
      for j=2:ColNum+1
         Zm(i,j,k)=Zeta(i-1,j-1,k);  % Node deflection representation in
                                     % actual node discretization format
      end
   end
   Zm(RowNum+2,:,k)=0;
end

for k=1:numel(omg)
   for j=1:seg_x+1
      CenZm(k,j)=Zm((seg_y+2)/2,j,k); % Deflection of center line at different frequencies
      dB(k,j)=10*log10(CenZm(k,j));
   end
end

figure (1)

surf(x_cord,y_cord,Zm(:,:,1))     % plotting deflection pattern of the plate at discrete frequencies

% figure (2)
```

```
% plot(omg,abs(CenZm(:,1)))   % plotting deflection of 1st node of centerline at a band of frequencie


% figure (3)

% plot(abs(CenZm(1,:)))      % plotting deflection of centerline at discrete frequencies against node points


% figure (4)

% plot(x_cord(1,:),abs(CenZm(1,:)))  % plotting deflection of centerline at discrete frequencies against plate length
```

# APPENDIX B: MATLAB CODE FOR BM BEAM MODEL

```
%%%%%%%%%%%%%%%%%%%%%%%%%%%%%%%%%%%%%%%%%%%%%%
%%%%%%%%% Predictive model for Basilar Membrane Beam Model%%%%%%%%%%
%%%%%%%%%%%%%%%%%%%%%%%%%%%%%%%%%%%%%%%%%%%%%%

%%% This code possess the flexibility to alter model parameters, such as
%%% (model parameters can be defined as constant value or functional form)
%%%
%%% (1) Stiffness [constant/functional]
%%% (2) Beam width [constant/functional]
%%% (3) Beam thickness [constant/functional]
%%% (4) Beam length [constant/functional]
%%% (5) Density [constant/functional]
%%% (6) Beam number [constant]
%%% (7) Boundary condition [fixed/simply supported].
%%%
%%%To change the boundary condition,
%%% uncommand equation for target bounday condition and command another.
```

```
clc
clear

syms x
syms y

%% Defining Model Parameters
b=2e-3;      % Beam width
% b=2e-3*(1+4.16666666666667*x);

h=1e-3;          % Beam Thickness
% h=1e-3*(1+4.16666666666667*x);

l=20e-3*(1+4.16666666666667*x);   % beam length function

E=68.9e9;        % beam stiffness
% E=68.9e9*(1+4.16666666666667*x);

rho=2700;             % beam density
% rho=2700*(1+4.16666666666667*x);

BeamNum=20;    % Number of beams in the structure
NodeNum=51;    % Number of nodes in a beam (must be odd)
```

```
BeamDist=6e-3;  % Uniform distance between beams

TotalLength=(BeamNum-1)*BeamDist;   % Total length of the structure

f=100:50:8000;    % input frequency
omg=2*pi*f;
%%

I=(1/12)*b*h^3;
D=E*I;
A=b*h;      % cross-section area of beam

D_dx=diff(D,x);
D_dx2=diff(D_dx,x);

y_cord=0:BeamDist:TotalLength;    % defining y- coordinate

for i=1:length(y_cord)
   BeamLength(i)=double(subs(l,y_cord(i)));
   del_x(i)=BeamLength(i)/(NodeNum-1);
end

for i=1:length(y_cord)
```

```
    for j=1:NodeNum
        x_cord(i,j)=(j-1)*del_x(i);
    end
end

for i=1:length(y_cord)
    for j=1:NodeNum-2
        D1(i,j)=subs(D,y,y_cord(i));
        A1(i,j)=subs(A,y,y_cord(i));
        rho1(i,j)=subs(rho,y,y_cord(i));
        D_dx2_1(i,j)=subs(D_dx2,y,y_cord(i));

        D2(i,j)=double(subs(D1(i,j),x,x_cord(i,j+1)));
        A2(i,j)=double(subs(A1(i,j),x,x_cord(i,j+1)));
        rho2(i,j)=double(subs(rho1(i,j),x,x_cord(i,j+1)));
        D_dx2_2(i,j)=double(subs(D_dx2_1(i,j),x,x_cord(i,j+1)));
    end
end

m=length(y_cord)*(NodeNum-2);
n=NodeNum-2;

D3=reshape(D2',m,1);
```

```
A3=reshape(A2',m,1);
rho3=reshape(rho2',m,1);
D_dx2_3=reshape(D_dx2_2',m,1);

for i=1:m
   for j=1:n
      D4(i,j)=D3(i);
      A4(i,j)=A3(i);
      rho4(i,j)=rho3(i);
      D_dx2_4(i,j)=D_dx2_3(i);

   end
end

for i=1:length(y_cord)
   for j=1:(NodeNum-2)
      dx((i-1)*n+j)=del_x(i);
   end
end

%%%%%%%% Calculating DX2 coefficients %%%%%%%%
%% DX2_C1 (i-1,j)
for i=1:m
```

```
    for j=1:n
        if rem(i-1,n)==0
            DX2_C1(i,j)=0;
        elseif rem(i,n)==0
            DX2_C1(i,rem(i,n)+n-1)=1*(1/dx(i)^2);
        else
            DX2_C1(i,rem(i,n)-1)=1*(1/dx(i)^2);
        end
    end
end
%% DX2_C2 (i,j)
for i=1:m
    if rem(i,n)==0
        DX2_C2(i,rem(i,n)+n)=-2*(1/dx(i)^2);
    else
        DX2_C2(i,rem(i,n))=-2*(1/dx(i)^2);
    end
end
%% DX2_C3 (i+1,j)
for i=1:m
    for j=1:n
        if rem(i,n)==0
            DX2_C3(i,j)=0;
```

```
        else
            DX2_C3(i,rem(i,n)+1)=1*(1/dx(i)^2);
        end
    end
end

DX2=DX2_C1+DX2_C2+DX2_C3;

%%%%%%%% Calculating DX4 coefficients %%%%%%%%
%% DX4_C1 (i-2,j)
for i=1:m
    for j=1:n
        if rem(i-1,n)==0
%             DX4_C1(i,rem(i,n))=-1*(1/dx(i)^4);   %%% for simply supported bottom boundary
            DX4_C1(i,rem(i,n))=1*(1/dx(i)^4);  %%% for fixed supported bottom boundary
        elseif rem(i-2,n)==0
            DX4_C1(i,j)=0;
        elseif rem(i,n)==0
            DX4_C1(i,rem(i,n)+n-2)=1*(1/dx(i)^4);
        else
            DX4_C1(i,rem(i,n)-2)=1*(1/dx(i)^4);
        end
    end
```

```
end
%% DX4_C2 (i-1,j)
for i=1:m
   for j=1:n
      if rem(i-1,n)==0
         DX4_C2(i,j)=0;
      elseif rem(i,n)==0
         DX4_C2(i,rem(i,n)+n-1)=-4*(1/dx(i)^4);
      else
         DX4_C2(i,rem(i,n)-1)=-4*(1/dx(i)^4);
      end
   end
end
%% DX4_C3 (i,j)
for i=1:m
   if rem(i,n)==0
      DX4_C3(i,rem(i,n)+n)=6*(1/dx(i)^4);
   else
      DX4_C3(i,rem(i,n))=6*(1/dx(i)^4);
   end
end
%% DX4_C4 (i+1,j)
for i=1:m
```

```
    for j=1:n
        if rem(i,n)==0
            DX4_C4(i,j)=0;
        else
            DX4_C4(i,rem(i,n)+1)=-4*(1/dx(i)^4);
        end
    end
end
%% DX4_C5 (i+2,j)
for i=1:m
    for j=1:n
        if rem(i,n)==0
%           DX4_C5(i,rem(i,n)+n)=-1*(1/dx(i)^4);  %%% for simply supported top boundary
            DX4_C5(i,rem(i,n)+n)=1*(1/dx(i)^4);  %%% for fixed top boundary
        elseif rem(i+1,n)==0
            DX4_C5(i,j)=0;
        else
            DX4_C5(i,rem(i,n)+2)=1*(1/dx(i)^4);
        end
    end
end

DX4=DX4_C1+DX4_C2+DX4_C3+DX4_C4+DX4_C5;
```

```
for i=1:m
   for j=1:n
      for k=1:numel(omg)
         if rem(i,n)==0
            omg1(i,rem(i,n)+n,k)=omg(k);
         else
            omg1(i,rem(i,n),k)=omg(k);
         end
      end
   end
end

T1=D_dx2_4.*DX2;
T2=D4.*DX4;

for k=1:numel(omg)
   T3(:,:,k)=-rho4.*A4.*omg1(:,:,k).^2;
end

for k=1:numel(omg)
   Z(:,:,k)=T1+T2+T3(:,:,k);
end
```

```
%%%%% Forcing function
b=zeros(m,1);

for i=1:m
   b(i)=1;          % Uniform pressure on beam
end

for i=1:length(y_cord)
   for k=1:numel(omg)
      w(i,:,k)=inv(Z(((i-1)*n+1):(n*i),:,k))*b(((i-1)*n+1):(n*i));
   end
end

Zm=zeros(length(y_cord),NodeNum,numel(omg));

for i=2:NodeNum-1
   Zm(:,i,:)=w(:,i-1,:);
end

for i=1:BeamNum
   ZmMax(i)=max(abs(Zm(i,(NodeNum+1)/2,:)));
   for k=1:numel(omg)
```

```
        ZmNorm(i,k)=abs(Zm(i,(NodeNum+1)/2,k))/ZmMax(i);
    end
end

BeamCount=1:1:BeamNum;

for i=1:BeamNum
    for k=1:numel(omg)
        beam_cord(i,k)=BeamCount(i);
    end
end

for i=1:BeamNum
    for k=1:numel(omg)
        freq_cord(i,k)=f(k);
    end
end

col=1:numel(omg);

for i=1:BeamNum
    for j=1:numel(omg)
    c(i,j)=col(j);
```

```
    end
end

plot3(beam_cord',freq_cord',ZmNorm','LineWidth',2)

% plot(f,squeeze(abs(Zm(4,(NodeNum+1)/2,:)))), hold on
```